DESIGN REPORT

FOR THE

FERMILAB COLLIDER DETECTOR FACILITY

(CDF)

AUGUST, 1981

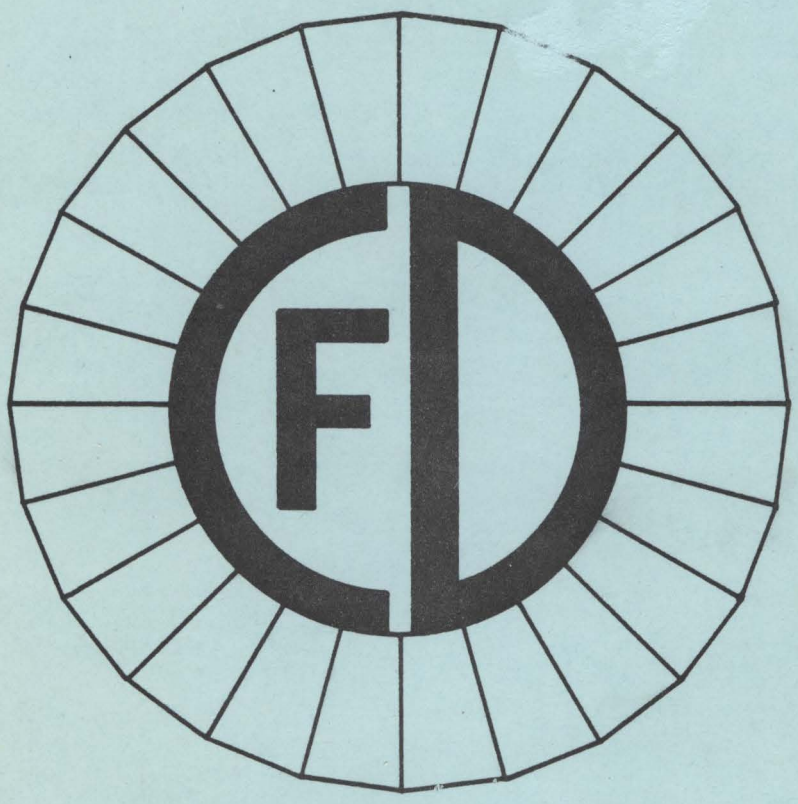

August, 1981

DESIGN REPORT

For the Fermilab Collider Detector Facility (CDF)

Argonne National Laboratory - D. Ayres, R. Diebold, E. May, B. Musgrave, L. Nodulman, J. Sauer, R. Wagner, A.B. Wicklund

University of Chicago - H. Frisch, C. Grosso-Pilcher, M. Shochet

Fermi National Accelerator Laboratory - M. Atac, F. Bedeschi, A. Brenner, T. Collins, T. Droege, J. Elias, J. Freeman, I. Gaines, J. Grimson, D. Gross, D. Hanssen, H. Jensen, R. Kadel, H. Kautzky, R. Kephart, M. Ono, R. Thatcher, D. Theriot, A. Tollestrup, R. Yamada, J. Yoh

Laboratori Nazionali dell' INFN - Frascati - S. Bertolucci, M. Cordelli, P. Giromini, P. Sermoneta

Harvard University - G. Brandenburg, R. Schwitters

University of Illinois - G. Ascoli, B. Eisenstein, L. Holloway, U. Kruse

KEK - S. Inaba, M. Mishina, K. Ogawa, F. Takasaki, Y. Watase

Lawrence Berkeley Laboratory - W. Carithers, W. Chinowsky, R. Kelly, K. Shinsky

University of Pisa - G. Bellettini, R. Bertani, L. Bosisio, C. Bradaschia, R. DelFabbro, E. Focardi, M.A. Giorgi, A. Menzione, L. Ristori, A. Scribano, G. Tonelli

Purdue University - V. Barnes, R.S. Christian, C. Davis, A.F. Garfinkel, A. Laasanen

Texas A & M - P. McIntyre, T. Meyer, R. Webb

Tsukuba University - Y. Asano, S. Kim, K. Kondo, S. Miyashita, H. Miyata, S. Mori, I. Nakano, Y. Takaiwa, K. Takikawa, Y. Yasu

University of Wisconsin - D. Cline, R. Loveless, R. Morse, L. Pondrom, D. Reeder, J. Rhoades, M. Sheaff

Table of Contents

ABSTRACT

The Collider Detector Facility (CDF) is planned to exploit the unique physics opportunities of the Fermilab Tevatron I project, where counterrotating beams of protons and antiprotons stored in the Tevatron will collide at 2 TeV in the center-of-mass. This will be the highest available energy in the world for particle physics experiments through at least the 1980's. A powerful, general purpose detector system is called for to explore fully this new energy range. The Collider Detector Facility, described in detail in this Design Report, is designed to meet that challenge.

The detector consists of electromagnetic and hadronic calorimetry over almost 4π solid angle around the interaction region. Fine-grain spatial segmentation has been matched to the large energies and high multiplicities characteristic of the high energy events expected. A large superconducting solenoidal magnet containing drift chambers measures the momentum of charged particles and gives a visual reconstruction of the event. Muon chambers around the perimeter of the central detector and iron toroidal magnets at one end identify muons.

The design, construction, and initial use of this facility is being carried out by a Fermilab-led consortium of physicists from six U.S. universities (University of Chicago, University of Illinois, Harvard, Purdue, Texas A&M, and the University of Wisconsin), Fermilab, two other U.S. national laboratories (Argonne National Laboratory and Lawrence Berkeley Laboratory), and physicists from Italy (Frascati and the University of Pisa), and Japan (KEK and the University of Tsukuba). A Caltech group also participated in the detector design presented here.

Chapter 1

PHYSICS MOTIVATION

INTRODUCTION

Beginning in 1984, the Fermilab $\bar{p}p$ collider will provide the highest energy collisions ever achieved in an accelerator. It is designed to reach a center-of-mass (c.m.) energy of 2000 GeV, about 30 times higher than any pre-1981 machine. Planned e^+e^- machines, while able to produce copiously and cleanly a 100 GeV/c^2 Z°, cannot explore this region at all. Experiments using the CERN SPS $\bar{p}p$ collider will begin by the end of 1981 with an energy of 540 GeV, about 1/4 that of the Fermilab collider. Thus, for a long time the collider will be the only place where collisions of the fundamental constituents of nature with c.m. energies ranging up to 2 TeV may be observed. It is in this unexplored region that particles with masses in the range 150-500 GeV/c^2 and jets with momentum transfers of 100-400 GeV/c can be uniquely investigated.

The large c.m. energy of the collider is also an asset at lower values of mass and momentum transfer. Our current theoretical understanding indicates that cross sections for large momentum transfer physics should be much higher at the Fermilab collider energy than at an energy of 500 GeV. The expected increase in cross section is a factor of about 10 for W or Z production, about 30 for heavy quark production, and over 100 for hard jets with p_T above 50 GeV/c. The factor of 10 for W production, for example, is equivalent to a hard-fought gain of an order of magnitude in luminosity.

This chapter of the Design Report will focus on the known physics processes of interest, their expected cross sections and signatures. To what extent this physics has determined the CDF detector design is delineated in Chapter 2. Details of the individual detector components are given in Chapters 3-9, and

examples of how the detector is actually expected to confront the physics are given in Chapter 10.

The organization of Chapter 1 is as follows: the expected production and decays of the W, Z, and Higgs particles in the standard electro-weak theory and alternative models are covered in Section 1.1. Section 1.2 discusses the expected production and decays of heavy quarks and heavy quarkonia. Section 1.3 describes possible production of other new particles and new threshold effects. The rate for jet and single particle production at large p_T from hadron constituent scattering is discussed in Section 1.4. Section 1.5 summarizes a few expectations for log s physics.

In the following sections, we will generally use the rates for an integrated luminosity of 10^{36} cm^{-2} or 1000 ev/nb as a measure of total sensitivity. This integrated luminosity corresponds to 12 days of continuous data taking at a luminosity of 10^{30} $cm^{-2}sec^{-1}$. Under realistic assumptions of overall operating efficiency, this integrated luminosity can be accumulated in less than one year of actual calendar time.

1.1 W, Z, AND OTHER GAUGE PARTICLES

The successes of the electro-weak theory (ref. 1.1) point to a synthesis of two of the four forces of nature, an advance that could be as significant as the combining of electricity with magnetism by Maxwell a century ago. Although all current experimental evidence points to the standard Weinberg-Salam theory (ref. 1.2) with $\sin^2(\theta_w)=.23$, it is crucial to observe directly the gauge bosons W and Z that mediate the electro-weak force. In this theory, the W and the Z have well predicted masses, widths and branching ratios. However, there are also other models (ref. 1.3) that are in agreement with existing low energy phenomenology but make different predictions. In particular, several alternatives have multiple W's and Z's. Thus, in order to establish the electro-weak theory, it is

essential to find these gauge bosons and study their properties.

Spontaneous symmetry breaking in electro-weak theories also predicts the existence of a scalar meson H (the Higgs particle). While the mass of this particle cannot be predicted, (ref. 1.4), production cross section and decay properties can be estimated once a mass value is assumed (ref. 1.5).

Properties of W and Z in Standard Electro-Weak Theory

The masses of the W and Z in the standard theory have been recently calculated including first order corrections to be 83 GeV/c^2 for the $W^{\pm}$ and 93 GeV/c^2 for the Z (ref. 1.6). If there are no charged Higgs particles with masses below half the Z mass, the Z is expected to decay predominantly into lepton pairs and quark pairs. In the standard model with 3 generations of quarks and leptons, the width of the Z is about 3 GeV, with di-electron and di-muon branching ratios of 3% each; decays into each flavor of quarks have branching ratios of about 12%. The W has comparable width but has leptonic branching ratios of about 8% each into $e + \nu$, $\mu + \nu$ and $\tau + \nu$; hadronic decay into quark-antiquark pairs gives branching ratios of about 25% each into $u + \bar{d}$, $c + \bar{s}$ and $t + \bar{b}$.

Production Cross Section of W and Z

Figure 1.1 shows the expected inclusive $W^{\pm}$ and Z production cross section in $\bar{p}p$ and pp collisions. In $\bar{p}p$ collisions at a c.m. energy of 2000 GeV, the cross sections are about 20 nb and 10 nb respectively and are about a factor of ten above the cross sections at c.m. energy of 540 GeV. This calculation assumes that the production mechanism is quark-antiquark annihilation as in dilepton production and includes scale breaking effects (ref. 1.7).

An integrated luminosity of 10^{36} cm^{-2} would produce about 20,000 W's of each sign and 10,000 Z's in this model. We will see below, however, that the backgrounds and branching ratios are such that detailed measurements of the W and Z are quite difficult, and that the expected statistics are still limited.

Leptonic Decays of the W and Z

The branching ratios of the W and Z to each dilepton mode are 8% and 3% respectively. Thus, for an integrated luminosity of 10^{36} cm^{-2}, we should have 3200 $e + \nu$ and $\mu + \nu$ each from W decays, and 300 $e\bar{e}$ and $\mu\bar{\mu}$ each from Z decay.

Figure 1.2 shows the expected y dependence of the production of the W and of charged leptons from W decays. The dashed curve shows the distribution of those leptons with p_T greater than 20 GeV/c. Roughly half of the leptons will be between 40 to 140 degrees in polar angle (-1 to 1 in y).

Figure 1.3 shows the expected momentum distribution for leptons from W decays for several polar angles. Note that at each angle, the yield rises to a Jacobian peak near a p_T of half the W-mass. This peaking will be less pronounced if the W is produced with significant average p_T.

The single leptons from Z decay have very similar distributions to the leptons from W decay. The two leptons from Z° decay are not colinear since the Z is usually produced with significant momentum along the beam (the quark and anti-quark that annihilate to form the Z typically have different values of x). Table 1.1 shows the distribution of the angles of the two leptons. A large angular coverage is required in order to see most of the pairs.

Table 1.1

θ_1 \ θ_2	0^o- 15^o 165^o-180^o	15^o- 30^o 150^o-165^o	30^o-150^o
0^o-15^o 165^o-180^o	3%	8%	24%
15^o-30^o 150^o-165^o	—	4%	26%
30^o-150^o	—	—	33%

Lepton Asymmetry of W Decays

Figures 1.3 and 1.4 illustrate an important feature of the lepton distribution from W decays: there is a significant charge asymmetry. At low p_T the asymmetry favors negative leptons in the proton direction, an effect caused by parity violation in the weak interaction (ref. 1.8). Near the Jacobian peak in p_T, there are more particles with charge equal to that of the beam because the W^+ moves preferentially in the proton direction.

Figure 1.4 shows the charge asymmetry of leptons from W decays as a function of polar angle for 4 bins of p_T. For example, a significant asymmetry occurs below 20 degrees and below 30 GeV/c in p_T, see CDF-64. It is clear from these small cross sections that large angular coverage and good background rejection are absolutely essential.

Hadronic Decays of the W and Z

The predominant decays of the W and Z are into a pair of quarks producing two collimated jets. Figure 1.5 shows the expected cross section for two jets from W or Z decay. While the two jets balance p_T quite well, they usually have some combined momentum along the beam so that they are not back-to-back in polar angle.

Although the branching ratios of W or Z decay into two quark jets are larger than those for leptonic decays, the backgrounds are much higher. The dominant backgrounds are expected to be the QCD hard-scattering processes involving light quarks and gluons. The cross section for two jets, both with a p_T greater than 10 GeV/c, is shown in Figure 1.5; if these (model-dependent) predictions are correct, one will not be able to detect the light quark decays of the W and Z.

The branching ratios for decays involving heavy quarks, such as $W \to t\bar{b}$ and $Z \to t\bar{t}$, are expected to be the same as for the light quarks if the t mass is not too large. Rejection of the light quark QCD background in this decay mode then depends on distinguishing heavy quark jets from light quark jets. If this is possible (see CDF-70), the W mass can be reconstructed from the multi-jet decay. The problem of heavy quark detection is discussed further in Section 10.3.

The intrinsic background for the W and Z heavy quark decays from directly produced $t\bar{t}$ pairs is smaller, and is also shown in Figure 1.5.

Pair Production of Gauge Bosons W, Z, and Photon

A fundamental property of the electro-weak theory is the existence of the trilinear boson couplings such as WWZ and WWγ (ref. 1.9). At the Fermilab $\bar{p}p$ collider, final states such as WW (about 10 pb), WZ or ZZ (2 pb), and Wγ (300 pb) should be produced. The rates of these final states are at the level of 10^{-4} to 10^{-2} of the single W/Z production and are at the very limit of detection. Figure 1.6 shows the dependence of these cross sections on center-of-mass energy; the increase by a factor of about 30 between $\sqrt{s}$ = 500 GeV and $\sqrt{s}$ = 2000 GeV makes it likely that these processes will be first observed at Fermilab. The final state signature of 4 energetic jets with p_T up to 45 GeV/c each should be distinctive. Again a premium is placed on large solid angle coverage and on good jet detection.

Implications of Multiple W/Z Models

Alternative gauge models that are consistent with low energy phenomena (ref. 1.3) exist, but they have radically different high q^2 behavior compared to the standard electro-weak theory. Such models have, in general, several W's and/or several Z's and most have at least one W/Z below the mass of the standard electro-weak W/Z. The presence of several W/Z's will result in several peaks in the lepton p_T spectrum. Observation of multiple W/Z's would be a startling development. In particular, right handed currents could exist. The increased energy available at the Fermilab collider is of great importance because if there are W's or Z's heavier than about 150 GeV/c^2, they will not be accessible to any other accelerator this decade.

Higgs and Other Gauge Bosons

Predictions of the masses and production cross sections of Higgs particles are much less reliable than those for the W or Z. Various models (ref. 1.4) give H masses from less than 10 GeV/c^2 to above 300 GeV/c^2. The H can be produced via gluon fusion (ref.1.5), with an expected cross section of the order of 10^{-34} to 10^{-36} cm^2 for masses in the range 10 to 100 GeV/c^2 (as shown in figure 1.7). Other production processes include W or Z decays, associated production with W or Z, and toponium decays into Higgs, all with expected cross sections less than that from gluon fusion (ref. 1.10). Unfortunately, the expected signatures of Higgs decays are not distinctive and it may be difficult to find these particles.

1.2 HEAVY FLAVORS

Since the November 1974 "revolution", two new heavy flavors of quarks (charmed c quark and bottom b quark) have been found and studied. Many of the interesting results in physics recently have involved particles with hidden or naked charm or bottom. The measurements of masses, widths and decay modes (both flavor changing weak decays and flavor conserving strong and electromagnetic decays) have increased our understanding of the dynamics of strong and weak interactions.

Currently, five flavors of quarks are known to exist. In most theoretical models (ref. 1.11), a sixth quark (called "top") should exist. Data from PETRA have already ruled out t quarks with masses less than 18 GeV/c^2 (ref. 1.12). If the mass of the t is less than 150 GeV/c^2, it can be produced with detectable rate at the Fermilab collider (ref. 1.13).

One mechanism for heavy quark pair production is through gluon fusion (ref. 1.14). Figure 1.8 shows the production rate as a function of quark mass as calculated by Halzen. The cross section for a quark mass of 25 GeV/c^2 is about 6 x 10^{-32} cm^2. Figure 1.8 also shows the rate of W decays into t quarks as function of the t mass.

Another possible mechanism for heavy quark pair production is suggested by recent data on diffractive charm production (ref. 1.15). The proton may have "intrinsic charm", i.e., a small admixture of the state $uud\bar{c}c$; the c quarks, having velocities comparable to the u/d quarks, would thus carry a large fraction of the momentum of the proton. Data from the ISR on diffractive strange and charm production suggest that the cross section is inversely proportional to the square of the quark mass. This could lead to large heavy quark diffractive production; for a t quark mass of 30 GeV/c^2, production at the Fermilab $\bar{p}p$ collider could exceed 10^{-31} cm^2, as shown in Figure 1.9.

If a massive top quark exists, the neutral vector bound state of $\bar{t}t$ could be produced in hadronic interactions and its subsequent decay into dilepton pairs would be a clean

signature. Unfortunately, for heavy top quarks, the extrapolated cross section for $\bar{t}t$ (quarkonium) production and decay, shown in Figure 1.10, suggests that the rate at the collider will be very small (ref. 1.13). Given an integrated luminosity of 10^{36} cm^{-2}, the ten event level corresponds to a $t\bar{t}$ mass of about 30 GeV/c^2, below the present limit set by PETRA. Unless the cross section is enhanced by some mechanism, the production rate of heavy quarkonium will be too small to be observed.

Several hundred dileptons from Upsilon decays should be produced; these events, in addition to being a physics measurement, serve as a check on the detector.

Final States of Heavy Quark Decays

We discuss here the signature of the decays of a pair of heavy quarks, each with mass about 30 GeV/c^2. Current models (ref. 1.16) suggest that such a heavy quark will fragment into a single heavy meson T with only a few other soft particles such as pions; the mass of the combined soft particles is estimated to be only about 1 GeV/c^2. The T meson will subsequently decay weakly into a lighter quark (probably b) and a virtual W; the W can either decay into 2 quark jets or a charged lepton plus a neutrino. Thus, the signature for a T meson will be either 3 hard jets or one jet plus one charged lepton at large transverse momentum with respect to the jet. For $\bar{t}t$ pairs, one could observe either 6 jets or 4 jets plus 1 lepton. Additional leptons could come from the cascade decay of b or c quarks.

Hard scattering processes involving light quarks or gluons could also lead to multiple jets through multiple gluon bremsstrahlung (ref. 1.17). At a particular q^2, the light quark or gluon interactions are several orders of magnitude more frequent than heavy quark pair production. However, heavy quark events with an energetic lepton far from any jet are likely to have a detectable signal to background ratio (see Section 10.3).

For quark masses above the W mass, the heavy quark will decay into a real W and a light quark giving final states with either 3 jets or 1 jet and 1 lepton. For the 3-jet decay, the additional constraint of the W mass for 2 of the 3 jets will improve the signal to background.

1.3 NEW THRESHOLDS AND NEW PARTICLE PRODUCTION

The tremendous increase in available center of mass energy provided by Tevatron I makes this machine a very attractive place to look for entirely new phenomena involving new particles perhaps with new interaction properties. Cosmic ray experiments already give hints that new particles or interactions may exist. The discovery of any one of these objects would alter our concepts of physics in a fundamental way and would change the direction of the field, just as did the discovery of the ψ a few years ago.

While Nature may well be even more imaginative when it comes to populating this new territory, we can still use current theoretical ideas for examples of the types of phenomena possible. For instance, ideas on dynamical symmetry breaking of the weak interaction lead to complex spectra of new particles possessing a new property of nature called technicolor. Some of these would be accessible for the first time at the Collider. Signatures for technicolor particles are discussed below. If quarks and leptons are made of simpler, smaller-yet building blocks, new types of interactions ("glints", for example) may occur at these energies - startling events with huge transverse momenta, multiplicity and acoplanarity. Other new particles may have lifetimes sufficiently long to allow the observation of their decay vertices. Alternatively they may simply appear as heavy slow particles with large momentum and energy; indeed, there are suggestions of such particles in cosmic ray experiments.

Whether or not our detector will be able to observe new particles convincingly depends upon their signature and production rate, and upon the abilities of the detector. In general, as the masses of particles increase, production cross sections decrease. Fortunately, as the mass increases, the particle signatures tend to become more and more distinctive, so that a handful of events will be conclusive in some cases.

Kinematics and the parton structure functions conspire to force the production of heavy objects to be more central as the mass increases. The exact form of the distribution depends on the production mechanism. For illustration we consider the case of two-gluon annihilation, with a gluon distribution function given by $G(x) = 3(1 - x)^5/x$. For production of a scalar particle with mass M, the simplest matrix element then gives

$$\frac{d\sigma}{dy} \propto G(x_1)\ G(x_2) \propto (1 - \sqrt{\tau}\ e^{y})^5\ (1 - \sqrt{\tau}\ e^{-y})^5$$

where $\sqrt{\tau} = M/\sqrt{s}$. At 90^o one has a factor $(1 - \sqrt{\tau})^{10}$, shown in Figure 1.11 for $\sqrt{s}$ = 2000 GeV; the variation of $d\sigma/dy$ with rapidity is shown in Figure 1.12. The distribution becomes narrower as the mass increases; for 200 GeV/c^2 mass at $\sqrt{s}$ = 2000 GeV the half height is at y = ±1 unit of rapidity.

Centauros - A New Hadronic Interaction?

Several events found by the Brazil-Japan cosmic ray collaboration (ref.1.18) have a high multiplicity ($\sim$80) of strongly interacting particles, but few or no γ rays from π^o decay. These events, called "Centauros", have been interpreted as fireballs decaying more or less isotropically into nucleons and antinucleons (ref.1.19). The observed energies of these events are 200 - 300 TeV, but this is only the electromagnetic energy deposited in the emulsion chambers by interactions of the incident hadrons. The total energy of these events has

been estimated to be roughly 1000 TeV, somewhat above the equivalent fixed-target CERN SPS collider energy of 150 TeV, and about equal to our equivalent energy of 2000 TeV.

These events could come from exotic components in the cosmic ray flux (ref.1.20), or could be some new form of interaction having a large cross section (>5% of the total). An example of the latter is the proposal (ref.1.21) that at these energies a small region of the colliding material is heated to a very high temperature such that quarks are able to escape.

If the Centauros are in fact a new type of interaction rather than a statistical fluctuation or a strange object entering the atmosphere, these events should be abundant and easy to detect at the Fermilab collider. The fireball has been estimated (ref.1.18) to have mass of about 200 GeV/c^2 and would have a rapidity less or equal to $y = \ln \sqrt{s}/m \simeq 2.3$.

Technicolor

There are a variety of predictions for the production of heavy particles that decay predominantly into two or more jets. The intermediate vector bosons and heavy quarks have already been discussed in the preceeding sections. Here we discuss some predictions of the dynamical symmetry breaking (DSB) approach. This model is an alternative to spontaneous breaking of the gauge symmetry of weak interactions with an elementary scalar field (the Higgs boson). There is not yet a complete DSB model, so that the predictions (ref.1.22) for masses and production cross sections are qualitative.

There are three natural mass scales on which particles occur in this model. The largest is the basic mass scale of the theory, which should be about 1 TeV to get the masses of the W and the Z correct. For example, there will be a colored technirho, ρ_T, with a mass of 900 GeV/c^2, produced with a cross section of order 10^{-35} cm^2 at $\sqrt{s}$ = 2000 GeV. Its dominant decays will be into gluon pairs, quark pairs or W pairs, all easily detectable and very dramatic at this mass.

The next mass scale contains bosons which would be massless, but which carry color and get mass through interaction with gluons. The ones with largest cross sections are the η-like color octet η_t^c, with a mass of 250 GeV/c^2. A lower limit on its cross section can be calculated from the triangle anomaly contribution, and is of order 10^{-34} cm^2, more than two orders of magnitude larger than for a fundamental Higgs boson of the same mass. The decays of these objects will be predominantly into pairs of the heaviest fermions kinematically allowed, again a distinctive experimental signature.

The third mass scale concerns those bosons that do not carry color and get mass from the electroweak (and even weaker extended technicolor) interactions. For example, the charged particles of this type would have mass $\simeq$8 GeV/c^2; if these charged bosons exist, they are expected to dominate the decays of the top quark, and may well be found at the same time as the t-quark is discovered.

Lepton And Quark Substructure

Three generations of quarks and leptons have been found. This proliferation suggests that these particles may have a composite nature with radius $r \sim \Lambda_g^{-1}$ ($\Lambda_g > 125$ GeV from our present knowledge). De Rujula (ref. 1.23) refers to these constituents as "gleeks".

Near threshold, De Rujula suggests that the multiplicity of such events would be roughly twice that for an ordinary QCD event and would increase with energy, perhaps to 4 times normal for $\Lambda_g = 0.5$ TeV and $\sqrt{s} = 2$ TeV. In addition, if the constituent gleeks are common to quarks and leptons, the quark debris will recombine into leptons as well as quarks, leading to multi-lepton events.

De Rujula has estimated the cross sections for such events using an analogy to QCD. Considering the distinctive nature of these events, we should be able to observe the effect even for

Λ_g = 6 TeV; extrapolating De Rujula's predictions gives a cross section in the range 10^{-31} to 10^{-35} cm^2 for this case.

Heavy Quasi-Stable Particles

It is possible that in this unexplored energy regime new heavy particles exist. For example, the startling results of Fairbank and collaborators (ref. 1.24) on the existence of fractional charge have not gone away in spite of detailed examinations. If correct, these results imply the existence of states of matter completely different from our present picture.

Fractional charged objects at a given value of p_T appear to have momenta higher than the true value by a factor of 3 for charge 1/3, and 3/2 for charge 2/3. Because the spectrum for charged particles falls steeply with p_T, the background for fractional charge is suppressed. The identification of a fractionally charged object, of course, rests on the measurements of the specific ionization.

There is always a long "laundry list" of as yet undiscovered particles. The magnetic monopole, for example, has seemed attractive ever since Dirac's first suggestion in 1931. There are now also other new objects, such as heavy technibaryons, stable heavy leptons, and gauge bosons (see CDF-88, for example). The discovery of any of these hypothetical objects would change the direction of high energy physics.

1.4 HARD SCATTERING PROCESSES

High P_T processes in hadron-hadron collisions are attributed to short distance interactions between hadron constituents, quarks and gluons. Because of the extremely high c.m. energy of Tevatron I, a region of P_T much above that accessible with existing machines should be within reach. It is therefore expected that the high P_T quark and gluon jets

resulting from hard scattering will be easier to identify and measure at the Collider. Two-jet events, with one jet from each of the scattered constituents, are expected to occur with the highest rates, but hard-scattering events with three and more jets are also expected with lower rates. Hard gluon bremsstrahlung from the scattered quarks and gluons is one mechanism for producing such events.

We anticipate a large experimental program for CDF in this field.

Jets And Single Particles At Large Transverse Momentum

Figure 1.13 shows the expected jet and single particle cross section for two c.m. energies (ref.1.25). These calculations are based on extrapolation of leading-log QCD terms and should only be considered as order-of-magnitude guesses. Even so, there is a very clear qualitative prediction of large event rates at P_T's that are inaccessible at present machines. For an integrated luminosity of 10^{36} cm^{-2} this model predicts 1000 jets above 200 GeV/c in P_T and several jets near a P_T of 400 GeV/c.

High P_T jets will come from gluons or quarks of various types. Gluon jets are expected to be the dominant type at 90 degrees, at least up to P_T of 200 GeV/c. The model suggests that valence quarks are dominant at forward angles. Figure 1.14 shows the angular dependence of the jet cross section for several p_T values.

According to the QCD theory, the hard jet production rate is a function of the structure functions of the incident particles. These structure functions and the fragmentation functions are expected to show scale breaking (ref.1.26). A determination of these functions and their Q^2 dependences in the energy range of the collider will be extremely important.

The number of discrete jets in the final states of the hard scattering processes is an important parameter relevant to the QCD theory. The frequency of additional jets from gluon

bremsstrahlung will constrain the value of the strong coupling constant.

Figure 1.15 (1.16) shows for QCD two-jet production the expected y-distribution of the second jet when the first jet is near 90° (40°). Nearly all of the cross-section is contained in the region covered by the CDF detector (2°-178°). This large acceptance will permit a detailed comparison of the angular distributions with theoretical predictions. Finally, it must be remembered that the jet-jet origin of large P_T hadrons is still an unproved hypothesis. The CDF detector will be able to distinguish such a mechanism from either a more isotropic production or other proposed hard scattering mechanisms such as quark-meson scattering in which a high P_T jet is balanced by a single particle or resonance.

A naive QCD prediction is that the single particle invariant cross section should behave with energy and P_T as P_T^{-4} times $(1-X_T)^M$; low energy data prefer P_T^{-8} although the highest P_T data available now indicate that the power is decreasing (ref.1.27).

Direct Photons At Large Transverse Momentum

The cross section for the production of direct photons through quark-antiquark annihilation and quark-gluon Compton scattering is shown in Figure 1.17 (ref.1.28). In the region where the photon rate is observable (P_T less than 40 GeV/c), the photon to pi-zero ratio is expected to be several percent. Experience at existing machines suggests that the detection of direct photons at this level would be difficult, although not impossible. If, in contrast, the γ/π° ratio depends only on p_T, and not on x_T, then an effect as large as that observed at the ISR could be seen.

Dilepton Continuum Production

Dileptons with high mass could be produced by the Drell-Yan quark-antiquark annihilation. Data from Fermilab and ISR show that the cross sections follow scaling (ref.1.29). Extrapolation to the energy range of the Fermilab collider shows that we should see Drell-Yan dilepton pairs with masses up to 30 to 40 GeV/c^2 (CDF-82).

1.5 LOG S PHYSICS

We have discussed so far the importance of the collider for producing high-mass particles and high-transverse momentum interactions. These events will constitute only a minute fraction of the hadronic interactions. The majority of the events involve low momentum transfers and are collective interactions of the hadron constituents, a process not yet completely understood. A study of these events is important and will help us understand the nature and properties of the constituent matter. At the ISR, the study of log s physics has provided some surprises and has shown the onset of new phenomena (ref.1.30). This is encouraging since even in the early phases of the Fermilab collider with low luminosity, new aspects of physics may be uncovered.

Total And Elastic Cross-Sections

The rising total cross section of hadronic interactions which was established at ISR (ref.1.30) was an important development, indicative of contributions from new channels as well as increases in existing channels. It will be interesting to find out whether the trend continues. A naive extrapolation of existing data predicts a total cross section at the Collider of about 75 mb, as shown in Figure 1.18.

The measurement of the elastic scattering differential cross section is complementary to the measurement of the total cross section. Both the slope and the value at t = 0 must fit optical model predictions for our qualitative understanding of the global features of strong interactions to remain valid. Possible dips and peaks in the differential elastic cross section will give a better understanding of the absorption process (ref.1.31).

Multiparticle Production

Figure 1.19 shows extrapolations of the measured charged particle multiplicity from accelerator and cosmic ray experiments (ref.1.32). A mean charged multiplicity between 30 and 70 is expected.

At the ISR, the particle rapidity density was found to scale in the beam fragmentation region (ref. 1.33). In the central plateau region the density is found to rise (ref.1.34). At the ISR, where the central plateau is only 4 units of rapidity, the study of rapidity correlations and rapidity gaps has been quite fruitful (ref. 1.35); the Fermilab collider, providing 12 units of central plateau, should allow us to have even more rewarding studies on these topics.

Diffraction

Single and double diffraction constitute a significant fraction of the total cross section. At the ISR, masses as large as several percent of the beam energy can be diffractively excited, with cross sections of the same order of magnitude as the elastic cross section (ref.1.36). If this is true at the Fermilab collider, one could produce masses of 50 to 100 GeV/c^2 diffractively with huge cross sections. These heavy masses could be heavy flavors as discussed in section 1.2. There are already indications from data at the ISR (ref. 1.37) and from cosmic rays that these possibilities may in fact occur.

Implications For Cosmic Ray Physics

The interpretation of cosmic ray experiments is often made difficult by a lack of knowledge of the characteristics of high energy interactions. General information on multiplicity, average transverse momentum, etc., will be of great help in deducing other results from these experiments. As a specific example, Gaisser has considered the possible "softening" of interactions at high energies (ref.1.38). High energy cascades show a rapid attenuation in the atmosphere. This could be explained by a deviation from scaling in which the energy tends to be subdivided among many low energy particles rather than a few fast secondaries. An alternative explanation would be an increase in the fraction of heavy primary nuclei in the cosmic rays, but this has far-reaching astrophysical implications concerning their origin, acceleration, and propagation through the galaxy.

Gaisser took as a measure of softening the fraction of energy appearing above 1° from the beam direction. This was examined using the Wdowczyk-Wolfendale parametrization of the inclusive cross section (ref.1.38). It uses a parameter β, which gives scaling for $\beta = 1$ and a softer distribution for smaller β ($\beta>0$ by energy conservation). Figure 1.20 shows the distributions expected for $\beta = 1$ and $\beta = 0.62$; a simple measurement with CDF will clearly resolve these two possibilities.

References

1.1 C.J. Prescott, AIP Conference Proceedings (ed. G.H. Thomas) Argonne (1978) p. 202; Proc. Int. School of Physics "Enrico Fermi", Varenna (July 1977) Course #51 (ed. North Holland Publishing Company); E. Fiorini, p. 164; H. Faissner, p. 185.

1.2 S. Weinberg, Phys. Rev. Lett., 19 (1967) 1264; A. Salam, Proc. 8th Nobel Symposium, Aspenäsgården, 1968 (ed. N. Svartholm) p. 367; S.L. Glashow, J. Iliopoulos and L. Maiani, Phys. Rev. D2 (1970) 1285;

1.3 H. Georgi and S. Weinberg, Phys. Rev. D17 (1978) 275; E.H. De Groot, G.J. Gounaris and D. Schildknecht, Phys. Lett. 85B (1979) 399 and Phys. Lett. 90B (1980) 472; V. Barger, W.Y. Keung and E. Ma, Phys. Rev. Lett. 44 (1980) 1169 and Phys. Rev. D22 (1980) 727.

1.4 S. Coleman and E. Weinberg, Phys. Rev. D7 (1973) 1888; M. Veltman, Acta Phys. Pol. B8 (1977) 475.

1.5 H.M. Georgi, S.L. Glashow, M.E. Machacek and D.V. Nanopoulos, Phys. Rev. Lett. 40 (1978) 692.

1.6 W.J. Marciano and A. Sirlin, Proc. Cornell Z° Theory Workshop, Feb. 6-8, 1981 (ed. M.E. Peskin, S.H. Tye, p. 40.)

1.7 F. Paige, BNL-27066 Updated Estimates of W Production in pp and $\bar{p}p$ interactions. The cross sections shown in Figs. 1.1-1.4 are calculated using a version of the program written by F. Paige. An earlier paper which describes the same phenomena without scale breaking is: R.F. Peierls, T.L. Trueman, L.L. Wang, Phys. Rev. D, Vol. 16 No. 5 (1977) 1397.

1.8 C. Quigg, Rev. Mod. Phys. 49 (1977) 297.

1.9 R.W. Brown and K.O. Mikaelian, Phys. Rev. D19 (1979) 922; R.W. Brown, D. Sahdev and K.O. Mikaelian, Phys. Rev. D20 (1979) 1164.

1.10 S.L. Glashow, D.V. Nanopoulos and A. Yildiz, Phys. Rev. D18 (1978) 1724.

1.11 M. Kobayashi and Maskawa, Progr. Theor. Phys. 49 (1973) 652.

1.12 See for example: Jade Collaboration, W. Bartel et al, Phys. Lett. 88B (1979) 171 and Phys. Lett. 89B (1979) 136.

1.13 D.B. Cline, Cern $\bar{p}p$ note 65 (1980); S. Pakvasa et al., Phys. Rev. D20 (1979) 2862.

1.14 F. Halzen and D. Scott, Wisconsin Preprint, DOE-ER/00881-161 (1980).

1.15 S. Brodsky, private communication.

1.16 J.D. Bjorken, Phys. Rev. D17 (1978) 171 (ep, νp and e^+e^-).

1.17 T. Gottschalk and D. Sivers, Phys. Rev. D21 (1980) 102.

1.18 C.M.G. Lattes et al., Phys. Reports 65, 151 (1980).

1.19 See, for example, the review of T.K. Gaisser and G.B. Yodh, Ann. Rev. Nucl. Part. Sci. 30, 475 (1980).

1.20 J.D. Bjorken and L.D. McLerran, Phys. Rev. D 20, 2353 (1979).

1.21 D. Sutherland, Cosmic Rays and Particle Physics-1978 (Bartol Conf.), AIP Conf. Proc. 49, 503 (1979).

1.22 S. Dimopoulos, S. Raby, and G.L. Kane, Michigan preprint UM HE 80-22, to appear in Nucl. Phys.

1.23 A. De Rújula, "Glints: A Signature of Quarks and Lepton Substructure," Th. 2903-CERN (July, 1980).

1.24 G. LaRue et al., Phys. Rev. Lett. 46 (1981) 867.

1.25 See, for example: R.D. Field, DOE R&D Report, CALT-68-696; R. Horgan and M. Jacob, CERN TH 2824 (1980).

1.26 See for instance: H.L. Anderson, H.S. Matis and L.C. Myrianthopoulos, Phys. Rev. Lett. 40 (1978) 1061; Y. Watanabe et al, Phys. Rev. Lett. 35 (1975) 898.

1.27 A.L.S. Angelis et al. Phys. Lett. 79B (1978) 505, C. Kourkoumelis et al, Phys. Lett. 84B (1979) 271; M. Jacob and P.V. Landshoff, Phys. Rep. 48C (1978) 285.

1.28 I. Hinchliffe and R. Kelly, Photon and π° Production at the FNAL $\bar{p}p$ collider CDF-83.

1.29 C. Kourkoumelis et al, Phys. Lett. 91B (1980) 475; J.K. Yoh et al, Phys. Rev. Lett. 41 (1978) 684.

1.30 U. Amaldi et al. Phys. Lett. 44B (1973) 112; S.R. Amendolia et al. Phys. Lett. 44B (1973) 119.

1.31 G. Albeni and G. Goggi, Diffraction of Subnuclear Waves. (To be published in Physics Report C).

1.32 W. Thomé et al, Nucl. Phys. B129 (1979) 365; H. Fuchi et al., Proc 16th ICRC Kyoto 1979, 6:245; B.S. Chaudhary et al. Nucl. Phys. B 86, (1975) 360.

1.33 G. Bellettini et al. Phys. Lett. 45B (1973) 69.

1.34 K. Guettler et al. Phys. Lett 64B (19), 111.

1.35 S.R. Amendolia et al. Phys. Lett. 48B (1974) 359 and Nuovo Cimento 31A (1976) 17.

1.36 M.G. Albrow et al. Nucl. Phys. B108, 1 (1976).

1.37 K.L. Giboni et al., Phys. Lett. 85B, 437 (1979); D. Drijard et al., Phys. Lett. 85B, 452 (1979); W. Lockman et al., Phys. Lett. 85B, 443 (1979).

1.38 T.K. Gaisser, "Energy Flow in Hadronic Collisions around $\sqrt{s} \sim 1$ TeV", Fermilab, Pub 80/104 (Dec. 1980).

Figure Captions

Fig. 1.1 Predicted inclusive cross sections for W and Z° production in pp and $\bar{p}p$ collisions versus $\sqrt{s}/m$, where $\sqrt{s}$ is the c.m. energy. The calculated cross sections include scale breaking effects (ref. 1.7).

Fig. 1.2 Calculated $d\sigma/dy$ for W^- production and $W^- \rightarrow \ell^-\nu$ decay versus y at $\sqrt{s}$=2000 GeV (ref. 1.7). The distribution in θ for the decay leptons is also shown.

Fig. 1.3 Calculated $d\sigma/dpdy$ for leptons from W-decay at four angles relative to the proton beam direction. There is a charge asymmetry for $\theta \neq 90°$ (ref. 1.7).

Fig. 1.4 Calcuated $d\sigma/d\theta$ for leptons from W-decay as a function of angle for four different intervals in p_T at $\sqrt{s}$ = 2000 GeV (ref. 1.7). The finite statistics of the Monte Carlo calculation causes irregularities in the curves.

Fig. 1.5 Calculated invariant mass distributions of heavy quark pairs from W and Z decay and from gluon fusion. For the heavy quark pair signal, a mass of 30 GeV/c^2 for the t-quark is assumed. A mass distribution from light quark and gluon di-jets with a p_T cut of 10 GeV/c is also shown.

Fig. 1.6 Calculated cross sections for pair production of gauge bosons in $\bar{p}p$ collisions (ref. 1.9).

Fig. 1.7 Calculation of the cross section for $\bar{p}p \rightarrow H + X$ for different $\sqrt{s}$ in the gluon fusion model (ref. 1.5).

Fig. 1.8 Calculated cross section for heavy quark pair production in the gluon fusion model (Ref. 1.14). The production via W decay is also shown.

Fig. 1.9 $d\sigma/dx$ versus x for Λ and Λ_c production at the ISR. Also shown are the cross sections for Λ_b and Λ_t production assuming a m^{-2} scaling.

Fig. 1.10 Calculated cross section for dileptons from decay of heavy quarkonium states as a function of the mass of the state (ref. 1.13).

Fig. 1.11 Mass dependence for the y = 0 production of a heavy scalar object via gluon fusion for a simple model.

Fig. 1.12 Normalized rapidity dependence for gluon fusion using a scaling distribution function $G(x) = 3(1 - x)^5/x$.

Fig. 1.13 Predicted jet and single particle cross sections (ref. 1.25)

Fig. 1.14 Calculated angular dependence of the QCD jet cross section for several p_T-values.

Fig. 1.15 Calculated rapidity distributions of QCD jets in quark-quark ($q\bar{q}$), quark-gluon (qg) and gluon-gluon (gg) scattering. The rapidity distributions of jet 2 (the recoil jet) are shown when jet 1 falls in the range $85° \leq \theta \leq 95°$, $45\ \text{GeV/c} \leq P_T \leq 55\ \text{GeV/c}$. The calculations use QCD-corrected structure functions. For the case of gluon-quark scattering (gq), the results of a calculation using scaling structure functions are also shown.

Fig. 1.16 Calculated rapidity distributions similar to Fig. 1.15, except that jet 1 falls in the range $40° \leq \theta \leq 50°$, 45 GeV/c $\leq P_T \leq$ 55 GeV/c.

Fig. 1.17 Calculated inclusive cross sections for $\pi°$'s and direct photons versus p_T (ref. 1.28). The $\pi°$ curve is the same as in Figure 1.13.

Fig. 1.18 Naive extrapolation of the total cross section for $\bar{p}p$ interactions to the Fermilab collider energy of 2 TeV in the c.m.

Fig. 1.19 Extrapolations of the total charged multiplicity from fits to existing data (W. Thomé et al., ref 1.32). The two points are cosmic-ray data (the lowest from Chaudhary and Malhotra, ref. 1.32, the highest from H. Fuchi et al., ref. 1.32).

Fig. 1.20 Distribution of events as a function of the fraction of hadronic energy outside 1° from the beam direction versus the β parameter (ref. 1.38). Each histogram contains 1000 events.

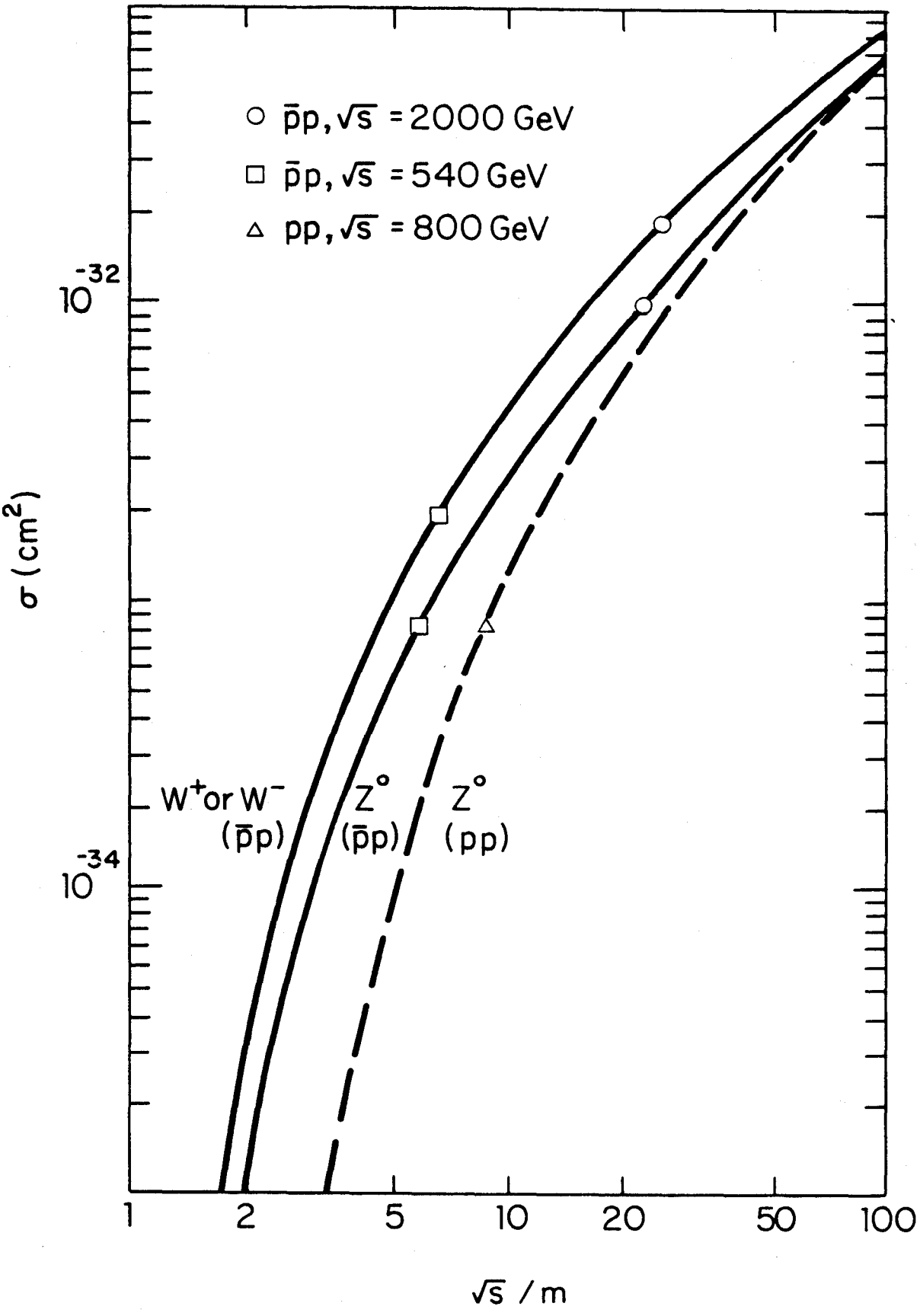
$\bar{p}p, \sqrt{s}$ = 2000 GeV
$\bar{p}p, \sqrt{s}$ = 540 GeV
$pp, \sqrt{s}$ = 800 GeV
10^{-32}
10^{-34}
σ (cm^2)
W^+ or W^- ($\bar{p}p$)
Z° ($\bar{p}p$)
Z° (pp)
1
2
5
10
20
50
100
$\sqrt{s}$ / m

FIG. 1.1

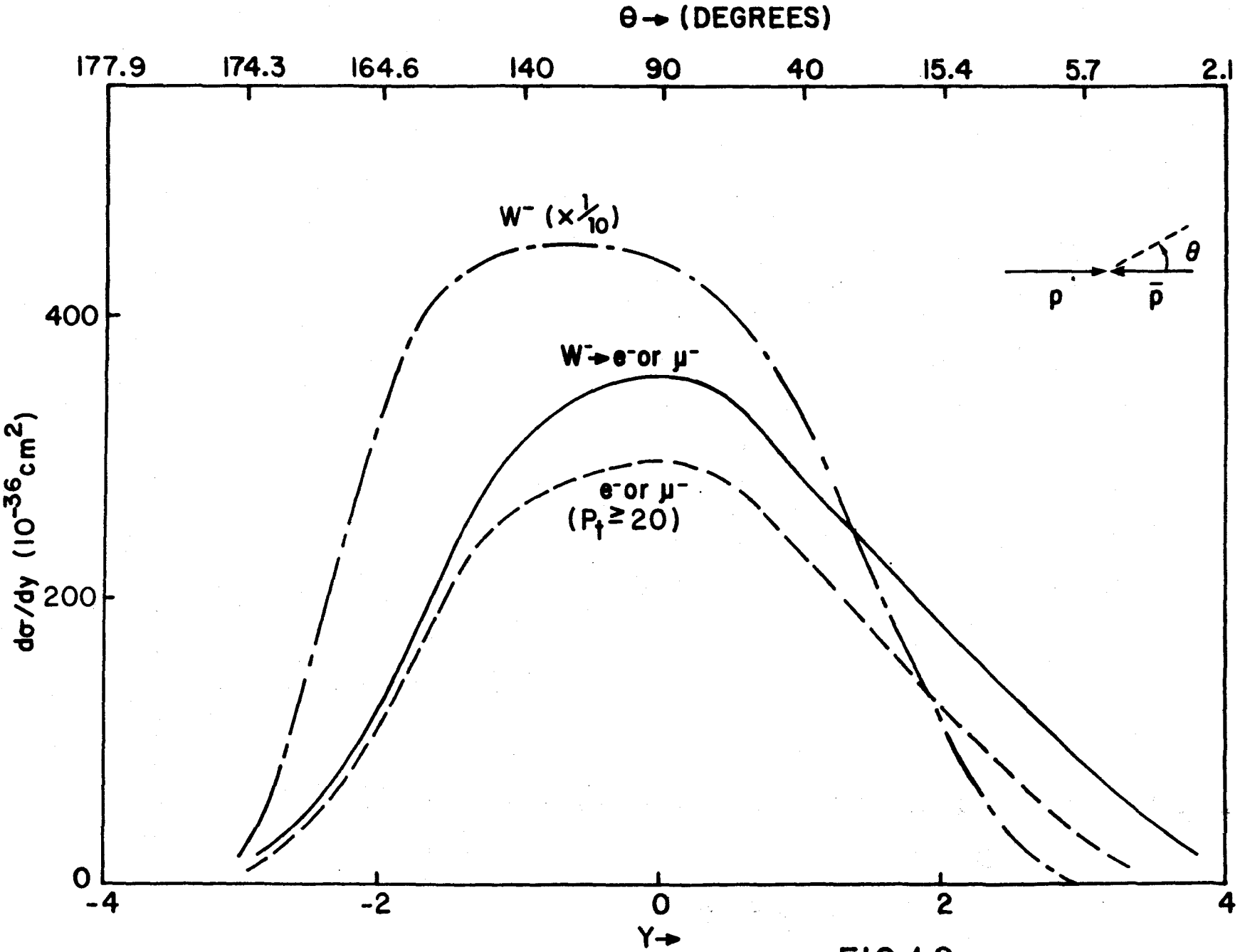
θ→ (DEGREES)
177.9
174.3
164.6
140
90
40
15.4
5.7
2.1
W⁻ (x 1/10)
W⁻→e⁻or μ⁻
e⁻or μ⁻
(P_t ≥ 20)
θ
p
p̄
400
200
0
dσ/dy (10⁻³⁶cm²)
-4
-2
0
2
4
Y→

FIG. 1.2

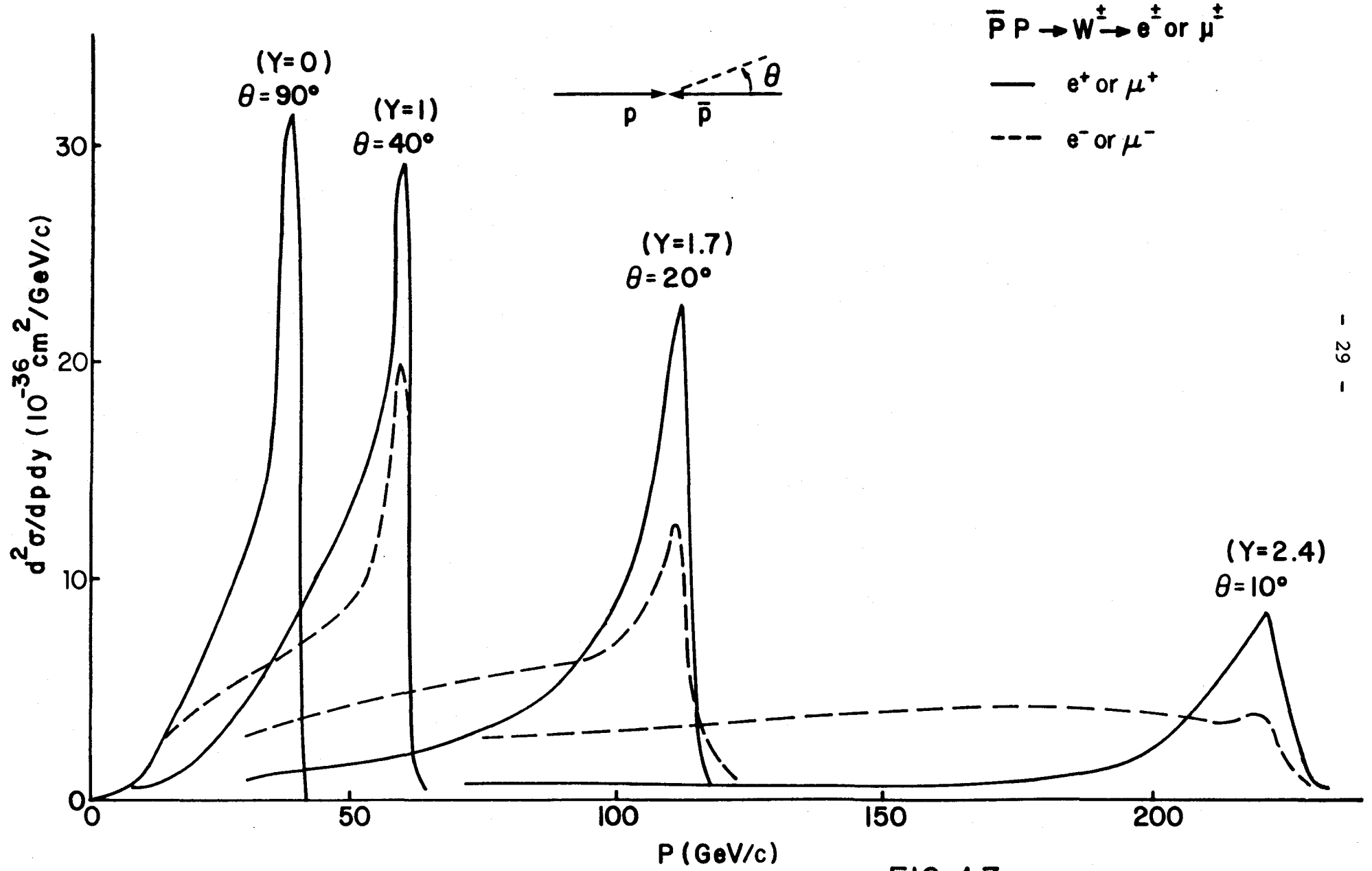
$\bar{P}P \rightarrow W^{\pm} \rightarrow e^{\pm}$ or $\mu^{\pm}$
e^+ or μ^+
e^- or μ^-
(Y=0)
θ=90°
(Y=1)
θ=40°
(Y=1.7)
θ=20°
(Y=2.4)
θ=10°
θ
p
$\bar{p}$
$d^2\sigma/dpdy$ (10^{-36} cm^2/GeV/c)
P (GeV/c)
0
10
20
30
0
50
100
150
200

FIG. 1.3

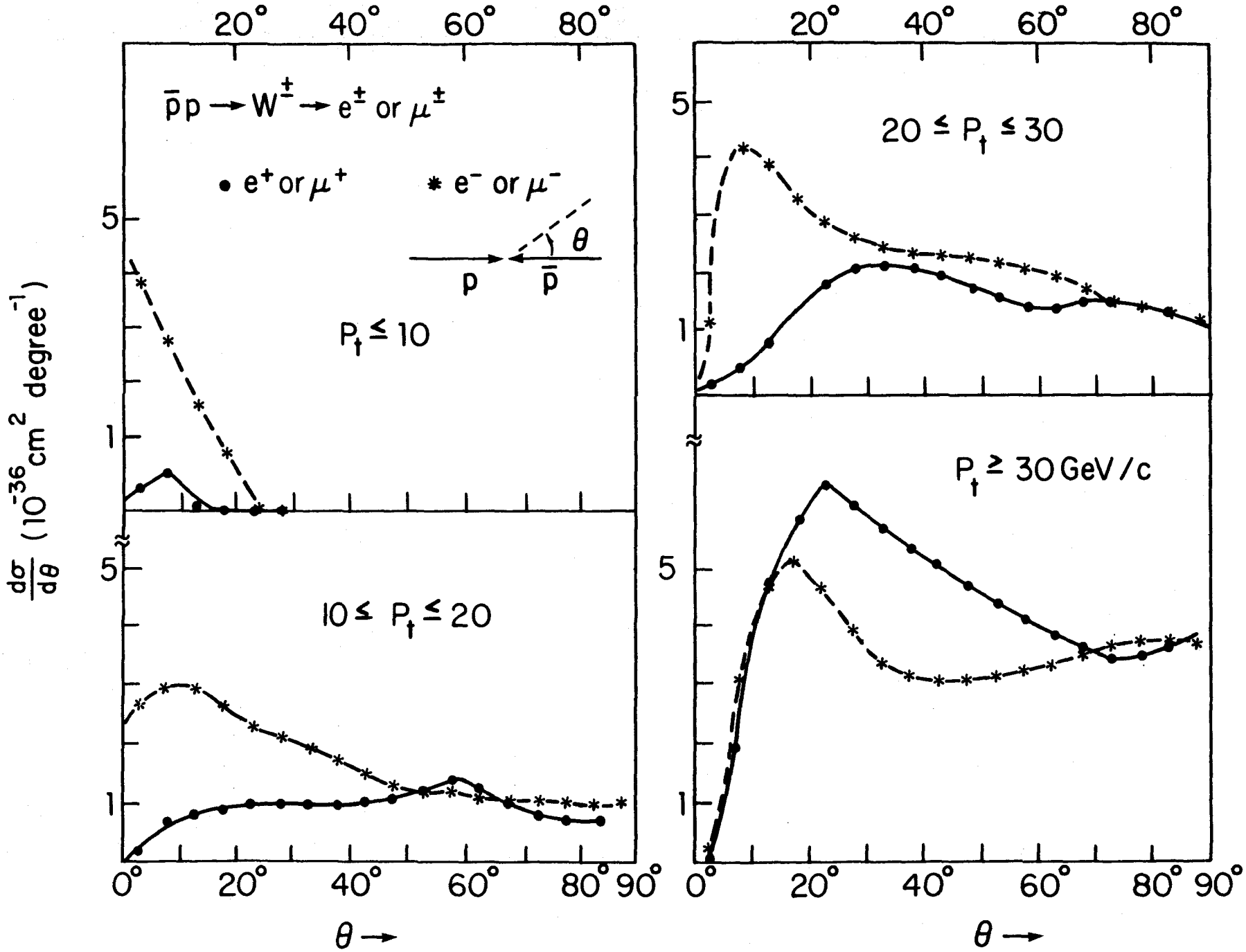
20° 40° 60° 80°
$\bar{p}p \rightarrow W^{\pm} \rightarrow e^{\pm}$ or $\mu^{\pm}$
• e^+ or μ^+
* e^- or μ^-
θ
p
$\bar{p}$
$P_t \leq 10$
$10 \leq P_t \leq 20$
$20 \leq P_t \leq 30$
$P_t \geq 30$ GeV/c
$\frac{d\sigma}{d\theta}$ (10^{-36} cm^2 degree^{-1})
5
1
0° 20° 40° 60° 80° 90°
θ →

FIG. 1.4

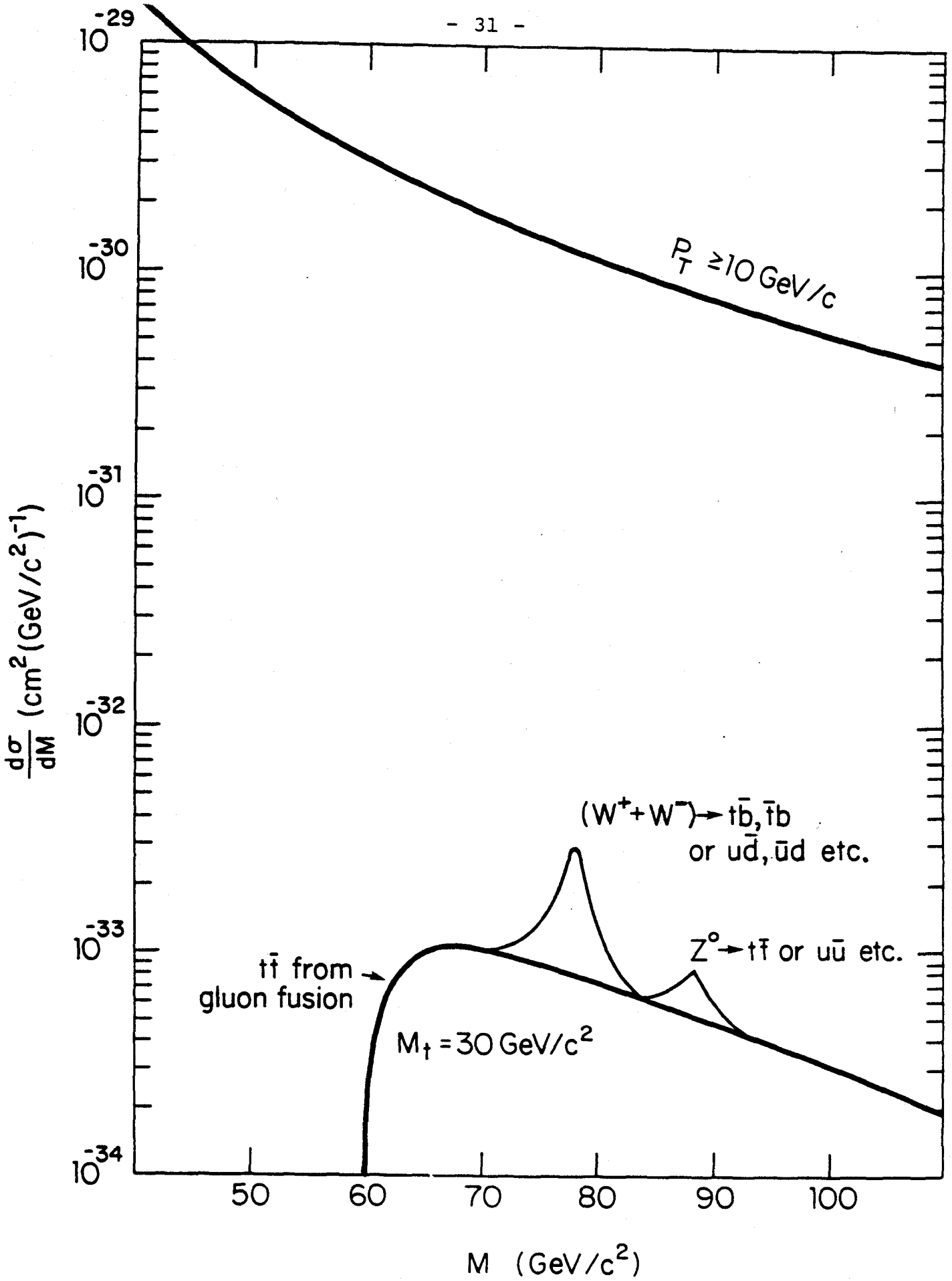
10^{-29}
10^{-30}
10^{-31}
10^{-32}
10^{-33}
10^{-34}
$\frac{d\sigma}{dM}$ (cm^2(GeV/c^2)$^{-1}$)
$P_T \geq 10$ GeV/c
$(W^+ + W^-) \rightarrow t\bar{b}, \bar{t}b$
or $u\bar{d}, \bar{u}d$ etc.
$Z^\circ \rightarrow t\bar{t}$ or $u\bar{u}$ etc.
$t\bar{t}$ from
gluon fusion
$M_t = 30$ GeV/c^2
50
60
70
80
90
100
M (GeV/c^2)

FIG. 1.5

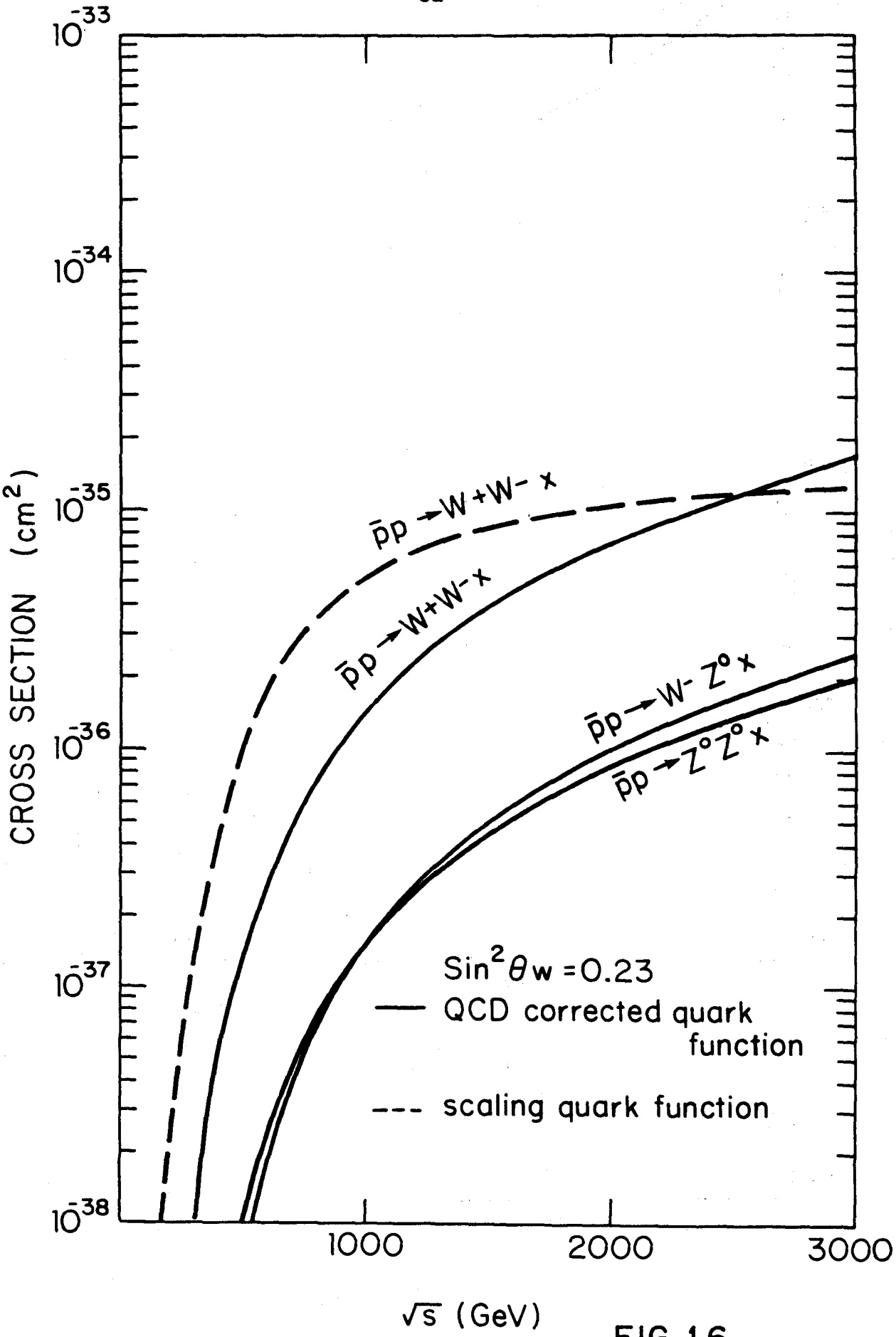
CROSS SECTION (cm²)
10⁻³³
10⁻³⁴
10⁻³⁵
10⁻³⁶
10⁻³⁷
10⁻³⁸
p̄p → W⁺W⁻ x
p̄p → W⁺W⁻ x
p̄p → W⁻ Z° x
p̄p → Z°Z° x
Sin²θw = 0.23
QCD corrected quark function
scaling quark function
1000
2000
3000
√s (GeV)

FIG. 1.6

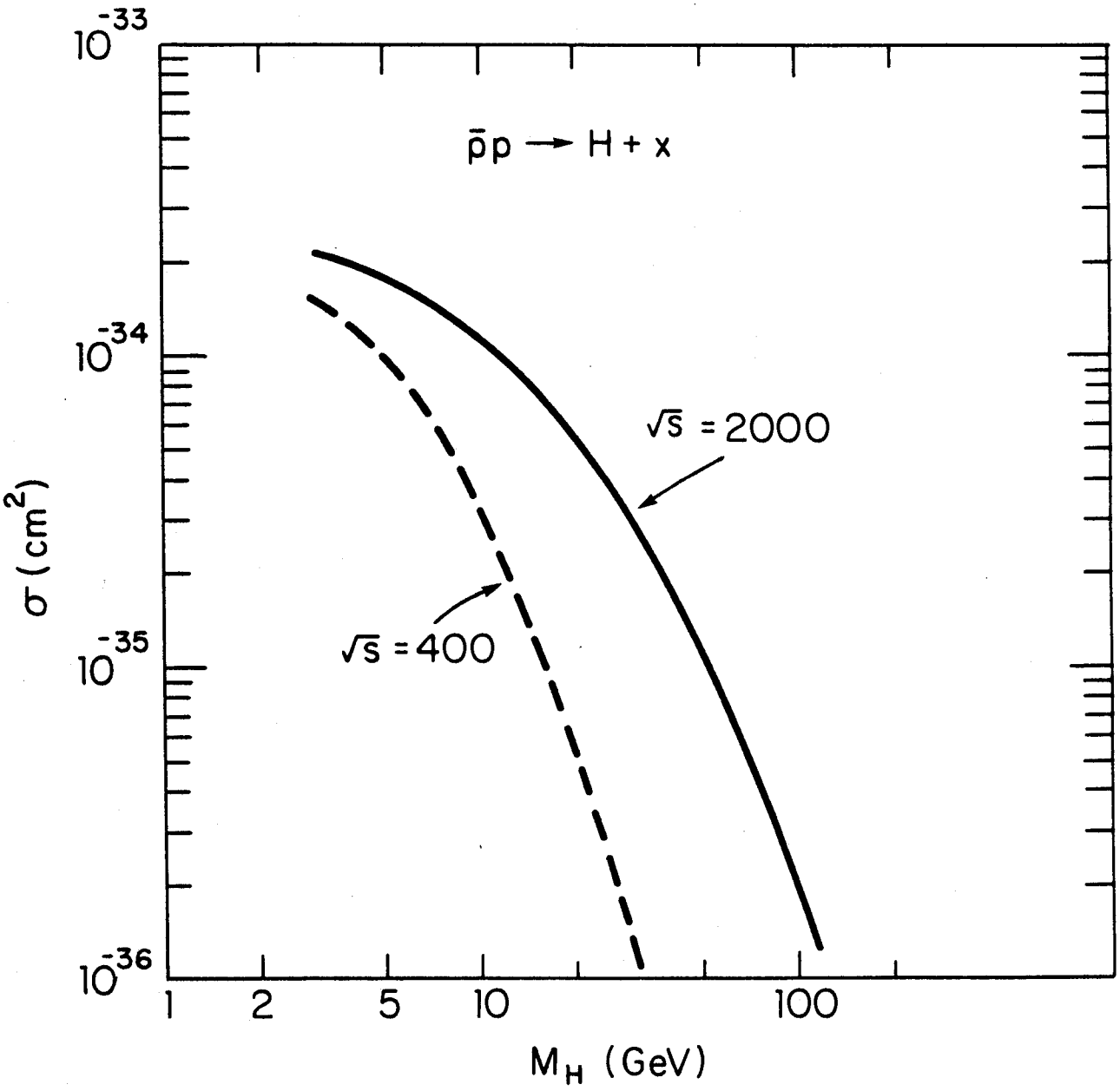
10^{-33}
10^{-34}
10^{-35}
10^{-36}
$\bar{p}p \rightarrow H + x$
$\sqrt{s} = 2000$
$\sqrt{s} = 400$
σ (cm^2)
1
2
5
10
100
M_H (GeV)

FIG. 1.7

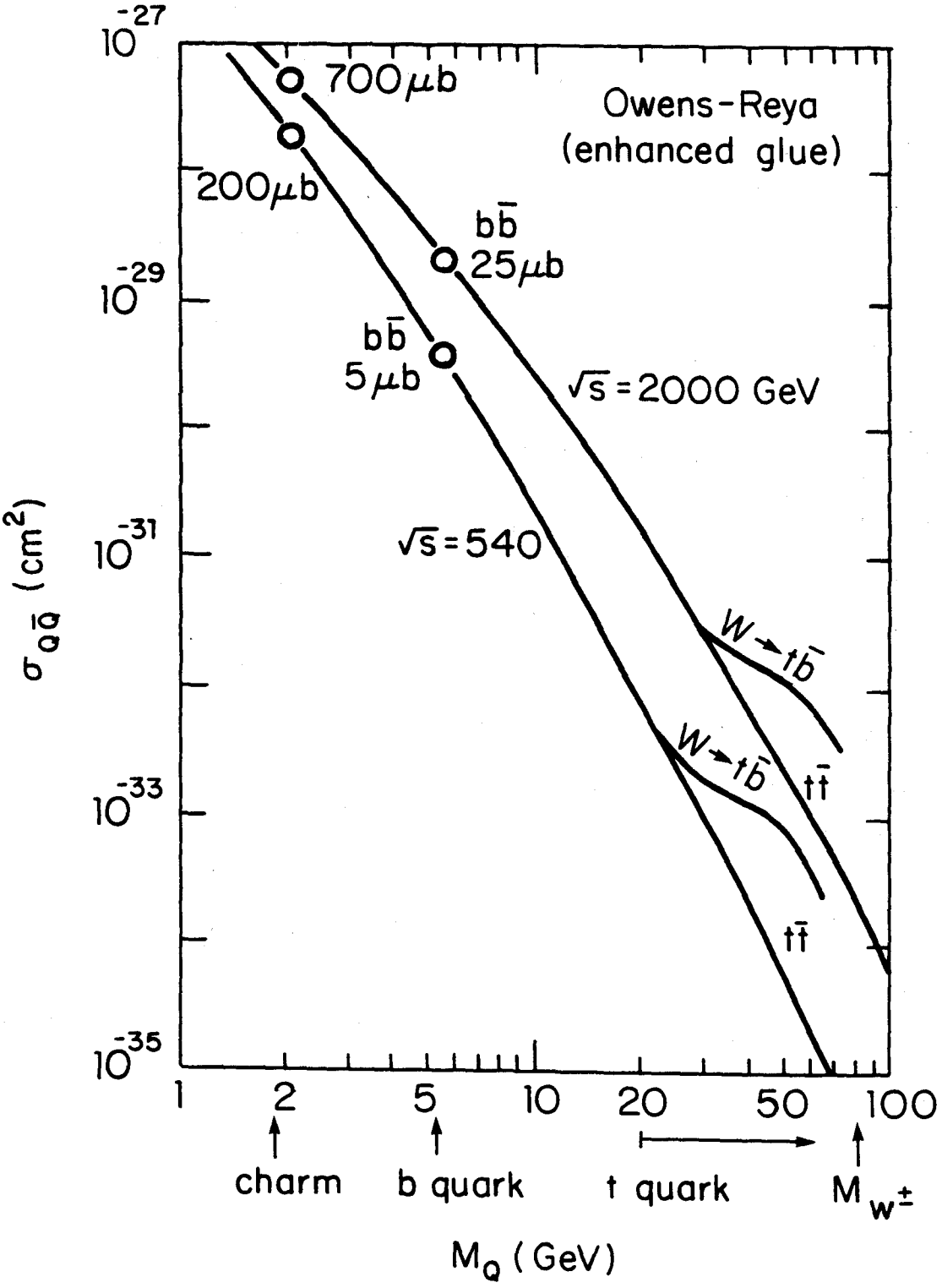
10^{-27}
10^{-29}
10^{-31}
10^{-33}
10^{-35}
$\sigma_{Q\bar{Q}}$ (cm^2)
700μb
200μb
Owens-Reya
(enhanced glue)
$b\bar{b}$
25μb
$b\bar{b}$
5μb
$\sqrt{s}$ = 2000 GeV
$\sqrt{s}$ = 540
$W \to t\bar{b}$
$W \to t\bar{b}$
$t\bar{t}$
$t\bar{t}$
1
2
5
10
20
50
100
charm
b quark
t quark
$M_{W^\pm}$
M_Q (GeV)

FIG. 1.8

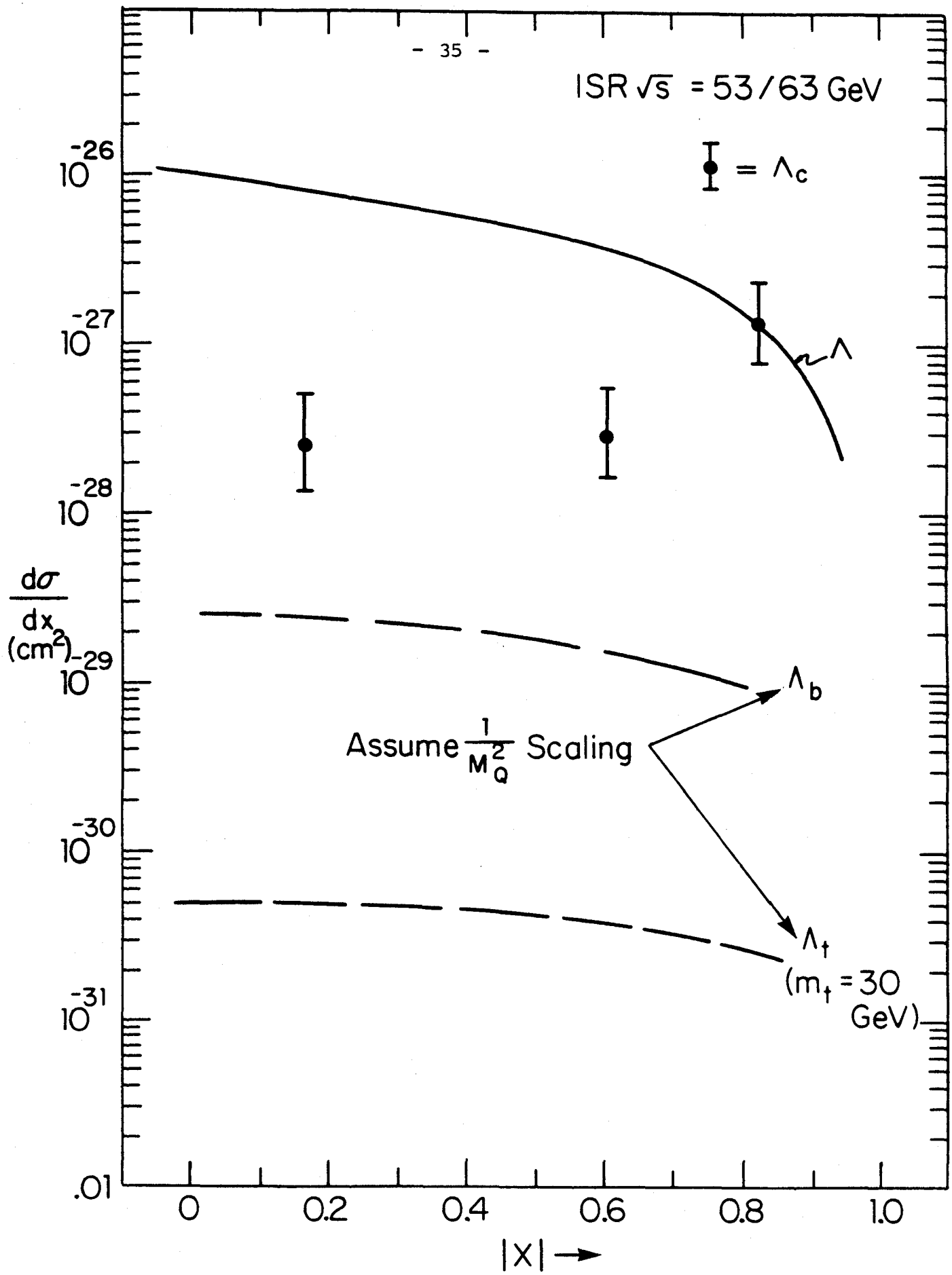
ISR √s = 53/63 GeV
= Λc
Λ
Λb
Assume 1/M_Q^2 Scaling
Λt
(mt = 30 GeV)
dσ/dx (cm²)
10^-26
10^-27
10^-28
10^-29
10^-30
10^-31
.01
0
0.2
0.4
0.6
0.8
1.0
|X| →

FIG. 1.9

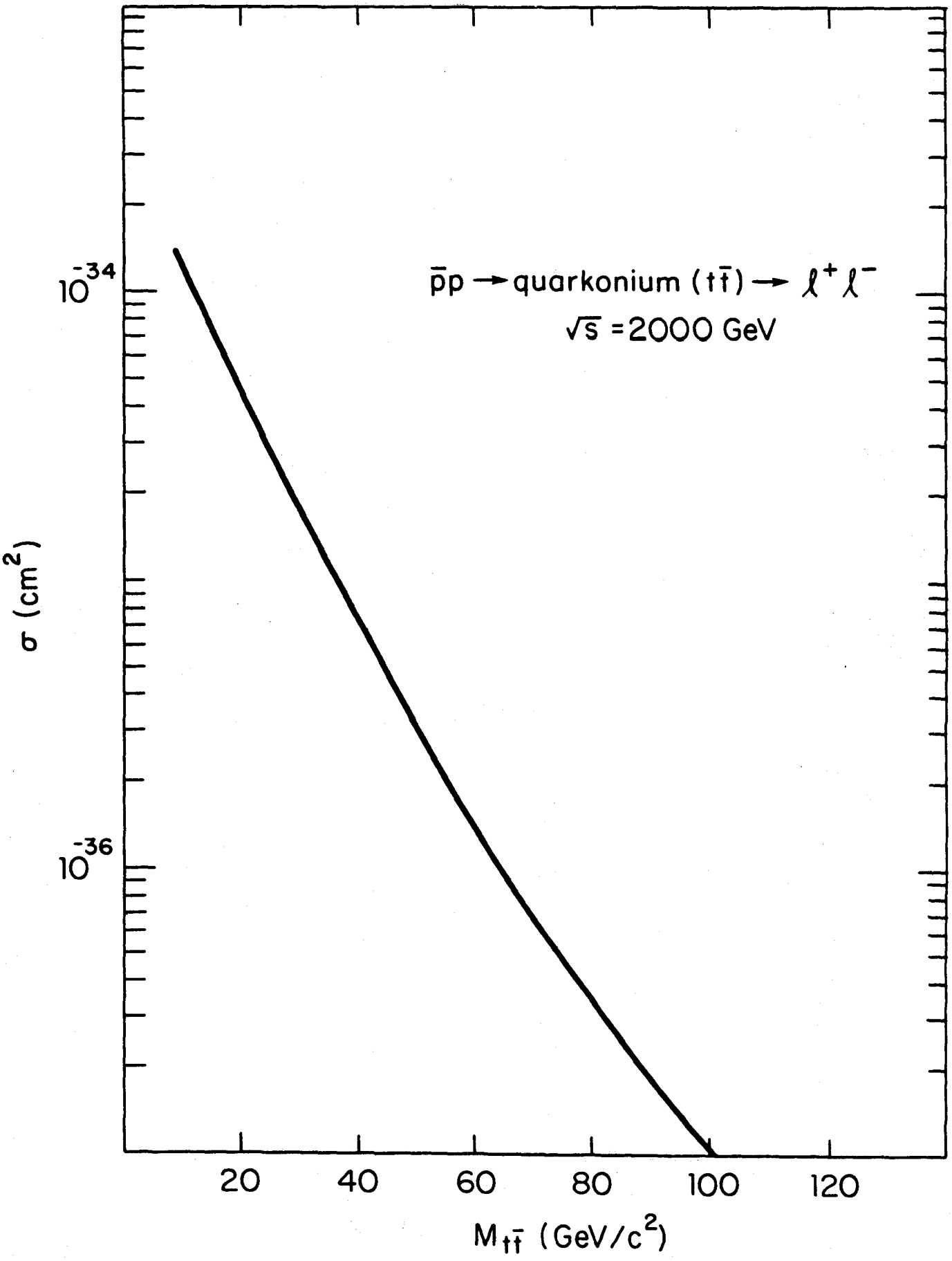
$\bar{p}p \rightarrow$ quarkonium $(t\bar{t}) \rightarrow \ell^+\ell^-$
$\sqrt{s}$ = 2000 GeV
10^{-34}
10^{-36}
σ (cm^2)
20
40
60
80
100
120
$M_{t\bar{t}}$ (GeV/c^2)

FIG. 1.10

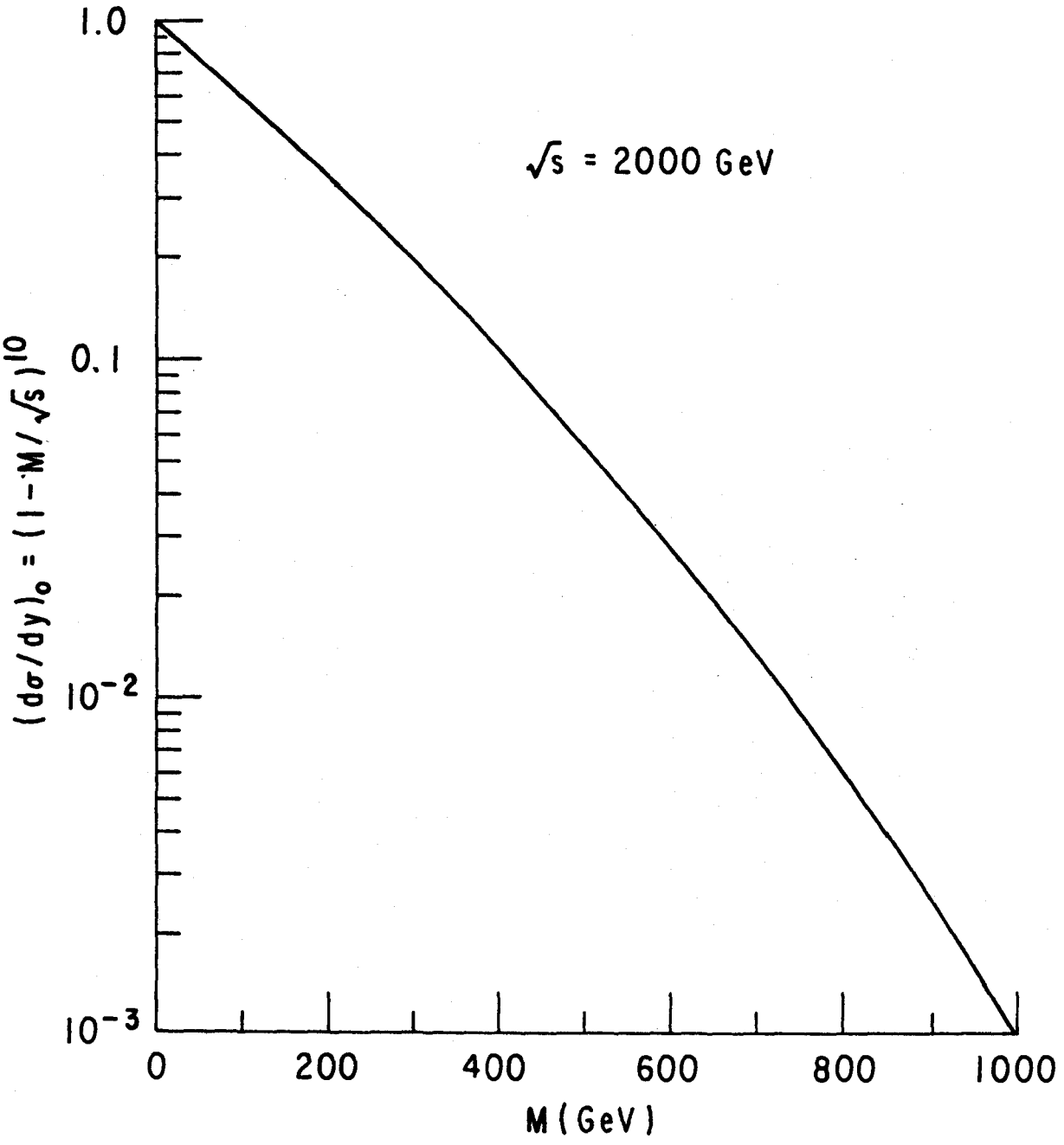
1.0
0.1
10^{-2}
10^{-3}
$(d\sigma/dy)_0 = (1-M/\sqrt{s})^{10}$
$\sqrt{s}$ = 2000 GeV
0
200
400
600
800
1000
M (GeV)

FIG. 1.11

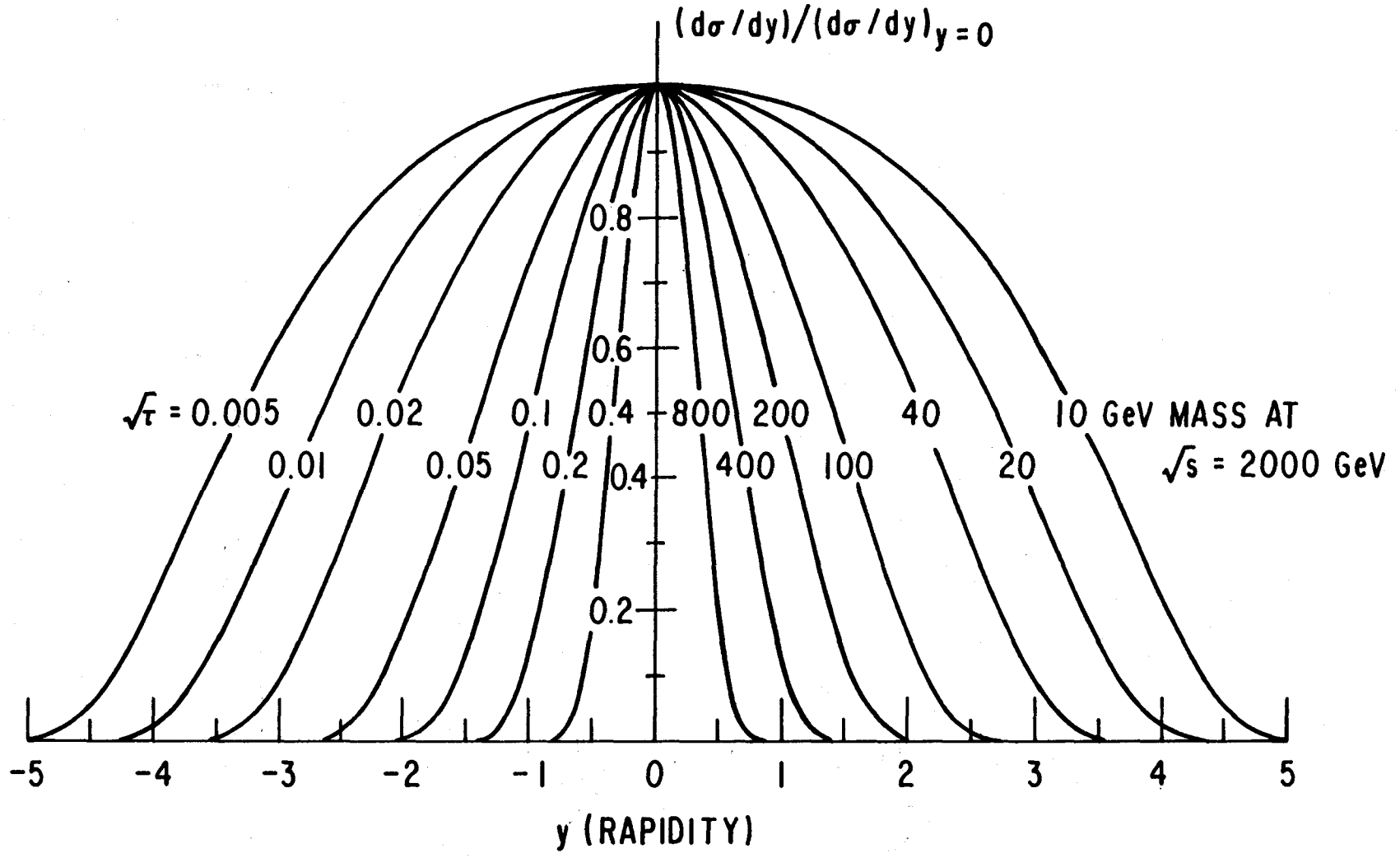
$(d\sigma/dy)/(d\sigma/dy)_{y=0}$
0.8
0.6
0.4
0.2
$\sqrt{\tau}$ = 0.005
0.01
0.02
0.05
0.1
0.2
0.4
800
400
200
100
40
20
10 GeV MASS AT
$\sqrt{s}$ = 2000 GeV
-5
-4
-3
-2
-1
0
1
2
3
4
5
y (RAPIDITY)

FIG. 1.12

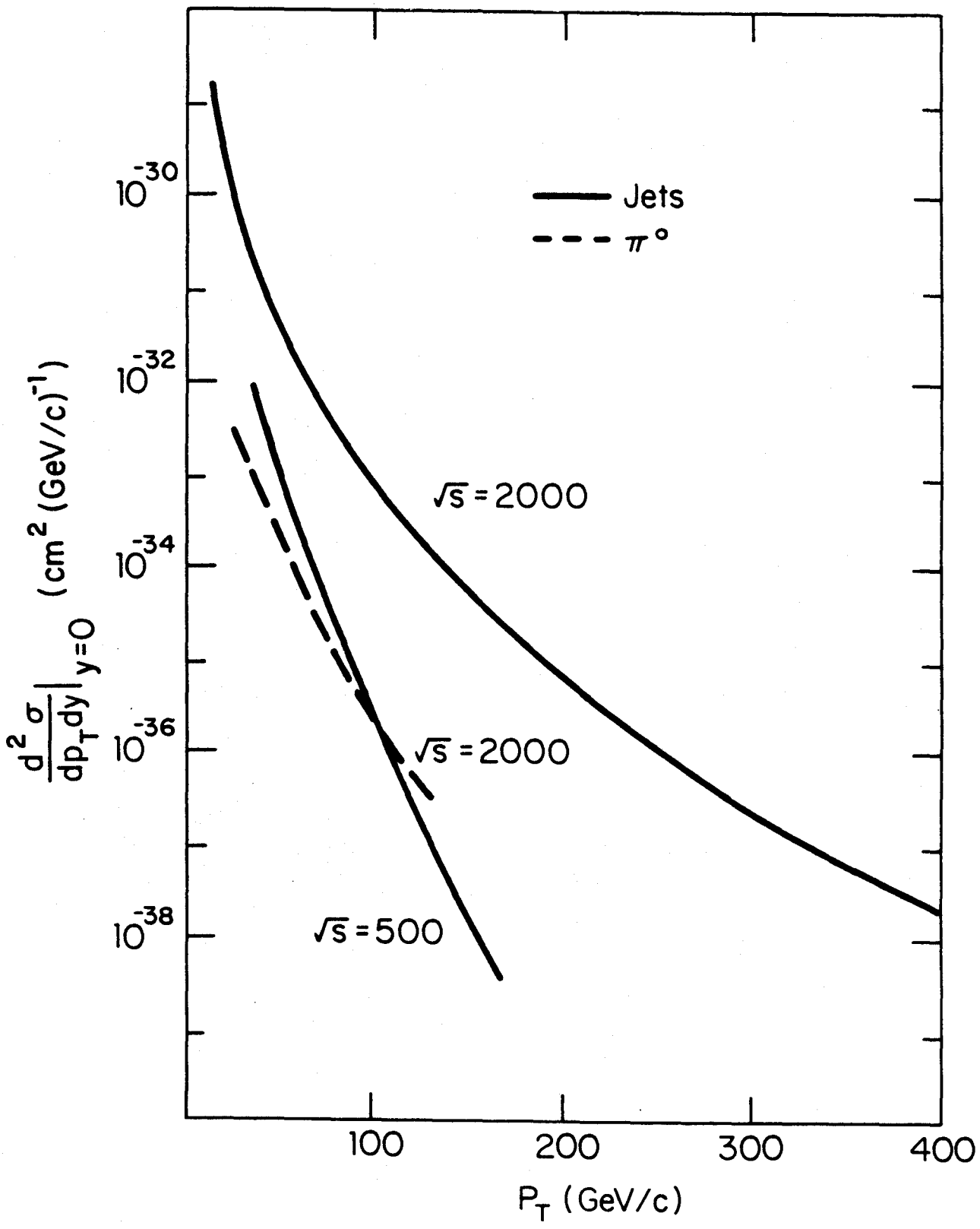
Jets
π°
√s = 2000
√s = 2000
√s = 500
10^{-30}
10^{-32}
10^{-34}
10^{-36}
10^{-38}
$\frac{d^2\sigma}{dp_T dy}\Big|_{y=0}$ (cm² (GeV/c)⁻¹)
100
200
300
400
P_T (GeV/c)

FIG. 1.13

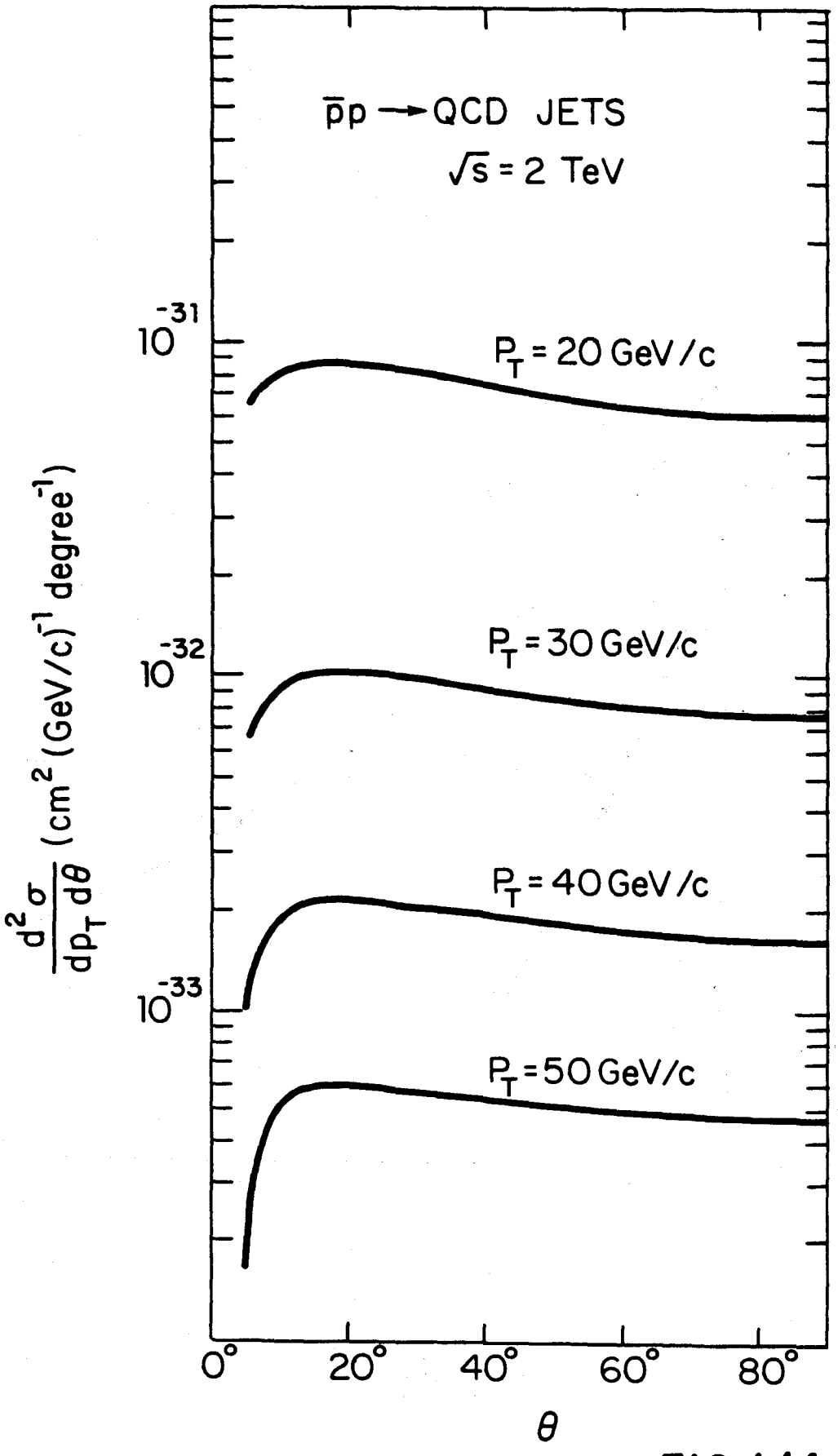
$\bar{p}p \rightarrow$ QCD JETS
$\sqrt{s}$ = 2 TeV
P_T = 20 GeV/c
P_T = 30 GeV/c
P_T = 40 GeV/c
P_T = 50 GeV/c
10^{-31}
10^{-32}
10^{-33}
$\frac{d^2\sigma}{dp_T\, d\theta}$ (cm^2 (GeV/c)$^{-1}$ degree^{-1})
0°
20°
40°
60°
80°
θ

FIG. 1.14

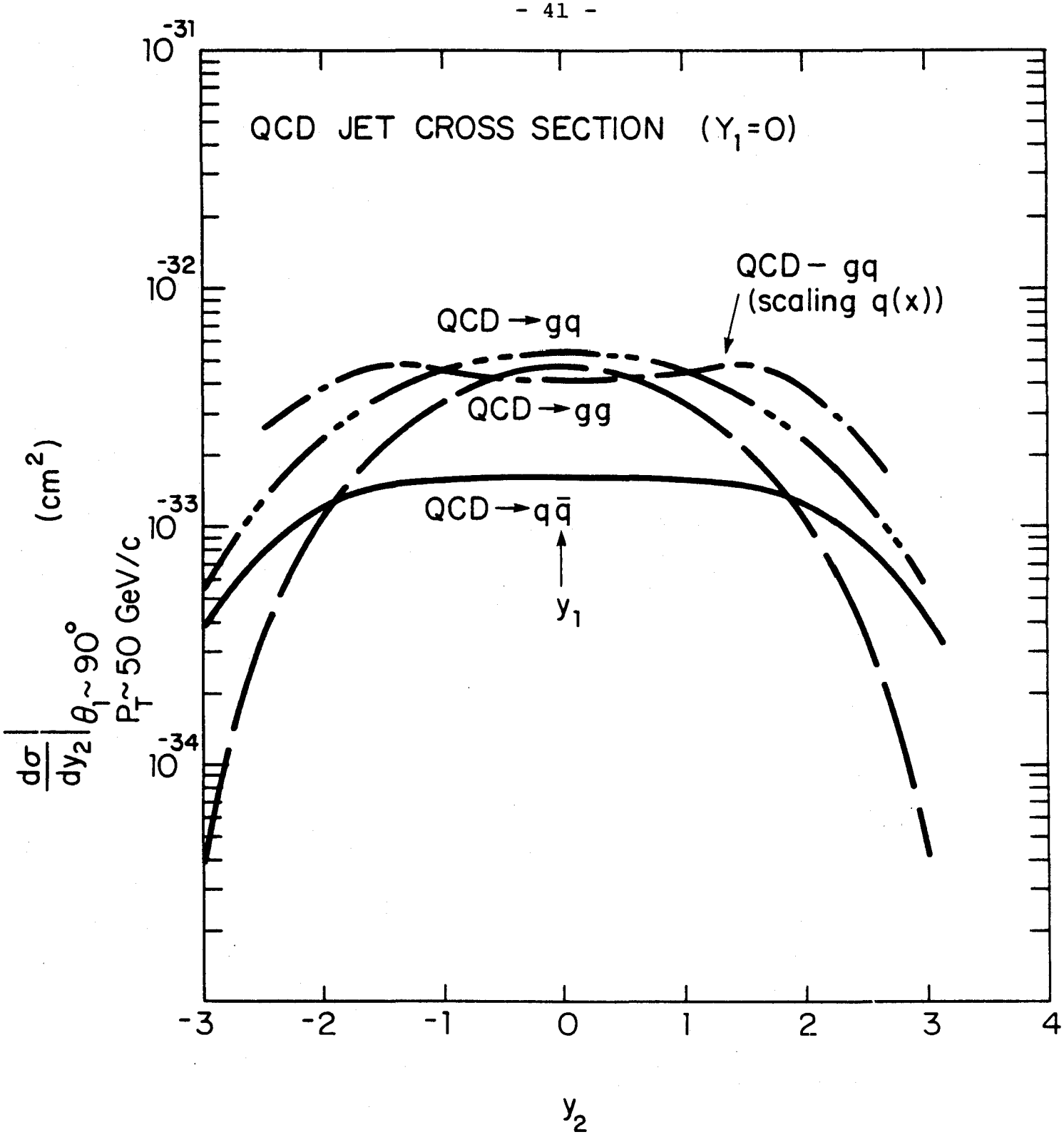
QCD JET CROSS SECTION (Y1=0)
QCD → gq
QCD − gq
(scaling q(x))
QCD → gg
QCD → qq̄
y1
y2
dσ/dy2 |θ1~90° PT~50 GeV/c (cm²)
10^-31
10^-32
10^-33
10^-34
-3
-2
-1
0
1
2
3
4

FIG.1.15

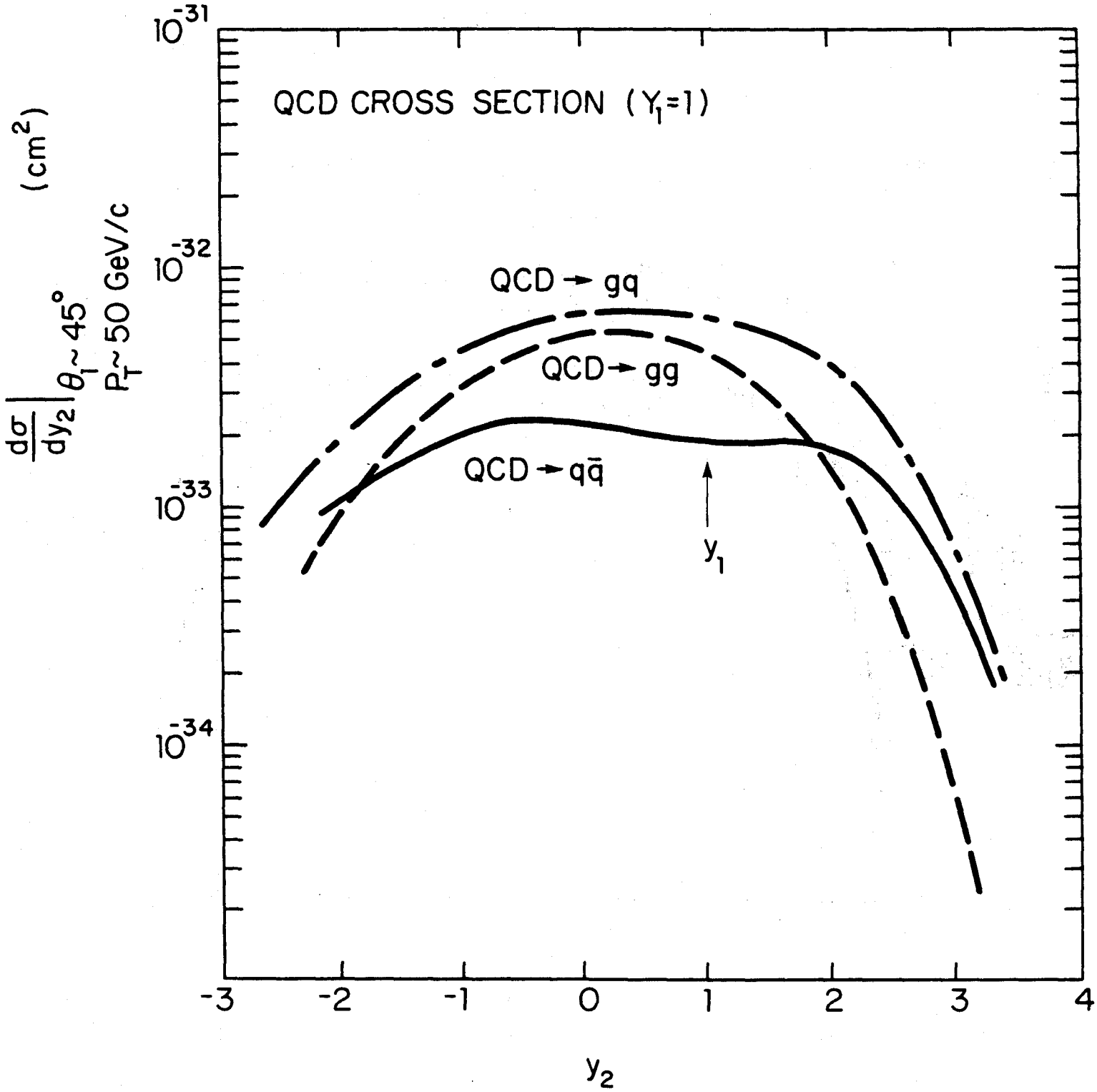
QCD CROSS SECTION (Y_1=1)
$\frac{d\sigma}{dy_2}\Big|_{\theta_1\sim 45^\circ}$ (cm^2)
$P_T \sim 50$ GeV/c
10^{-31}
10^{-32}
10^{-33}
10^{-34}
QCD → gq
QCD → gg
QCD → qq̄
y_1
-3
-2
-1
0
1
2
3
4
y_2

FIG. 1.16

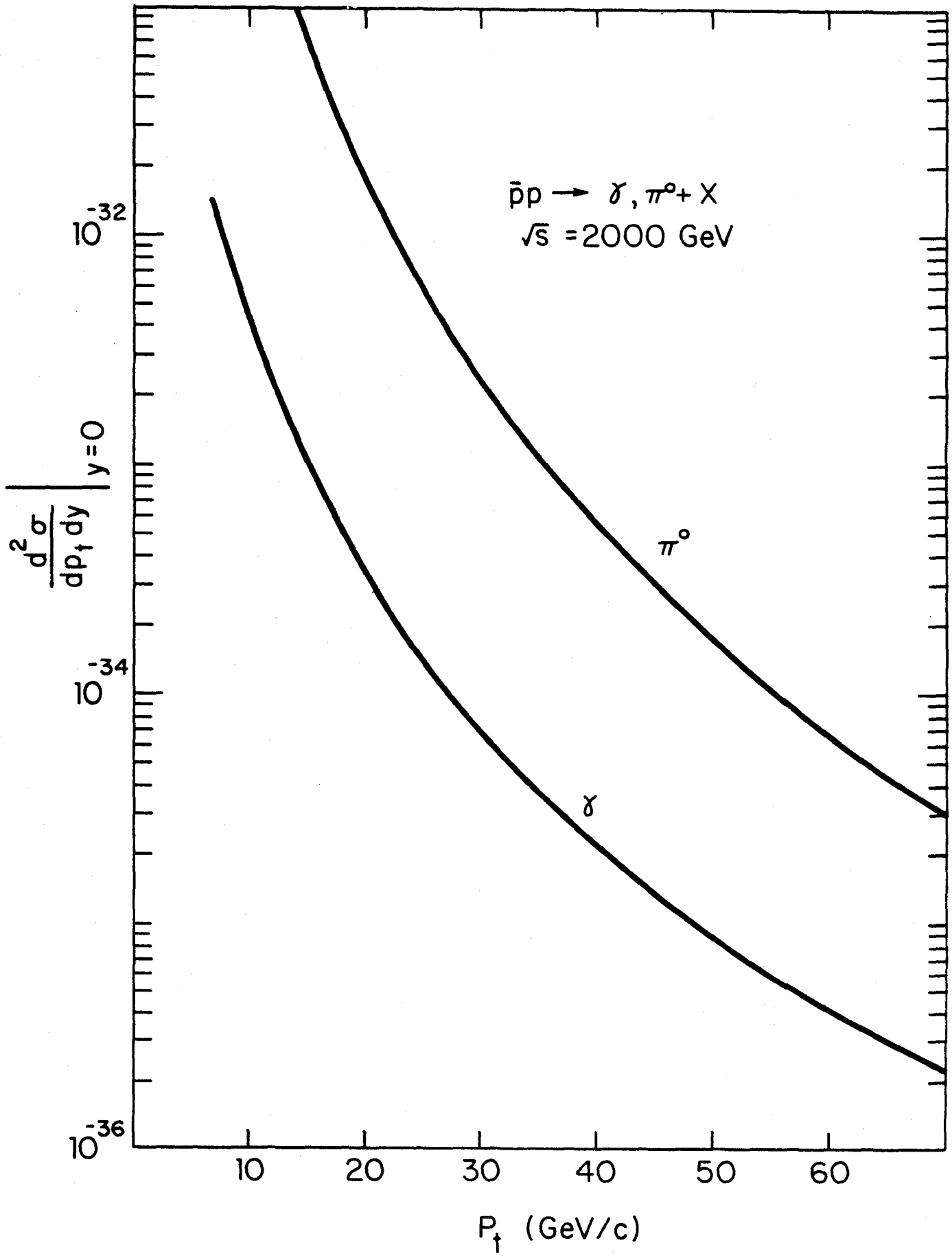
$\bar{p}p \rightarrow \gamma, \pi^0 + X$
$\sqrt{s}$ = 2000 GeV
π^0
γ
$\left.\frac{d^2\sigma}{dp_t\,dy}\right|_{y=0}$
10^{-32}
10^{-34}
10^{-36}
10
20
30
40
50
60
P_t (GeV/c)

FIG. 1.17

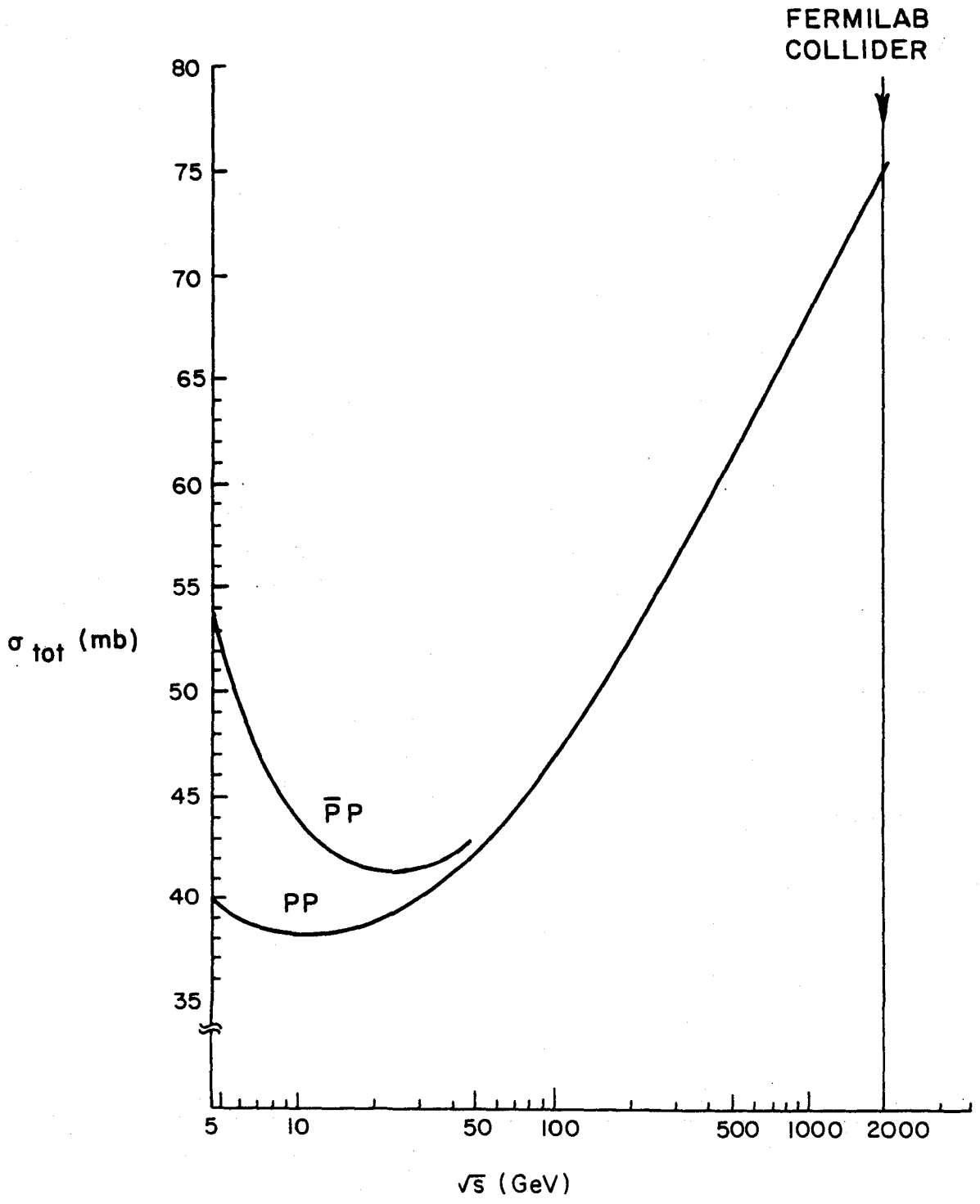
FERMILAB
COLLIDER
80
75
70
65
60
55
50
45
40
35
σ tot (mb)
P̄P
PP
5
10
50
100
500
1000
2000
√s (GeV)

FIG. 1.18

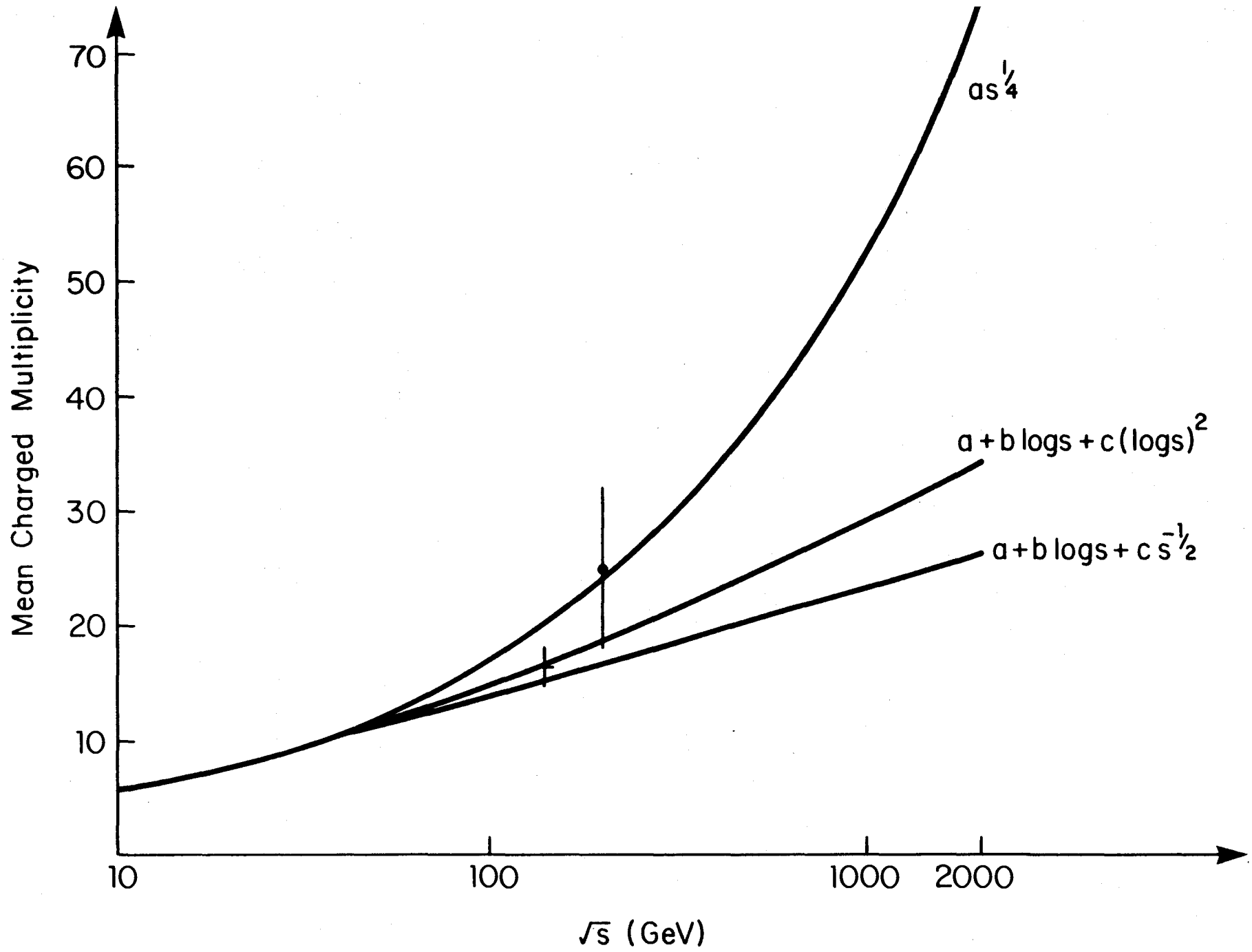
Mean Charged Multiplicity
70
60
50
40
30
20
10
10
100
1000
2000
√s (GeV)
as^1/4
a + b logs + c (logs)^2
a + b logs + c s^-1/2

FIG. 1.19

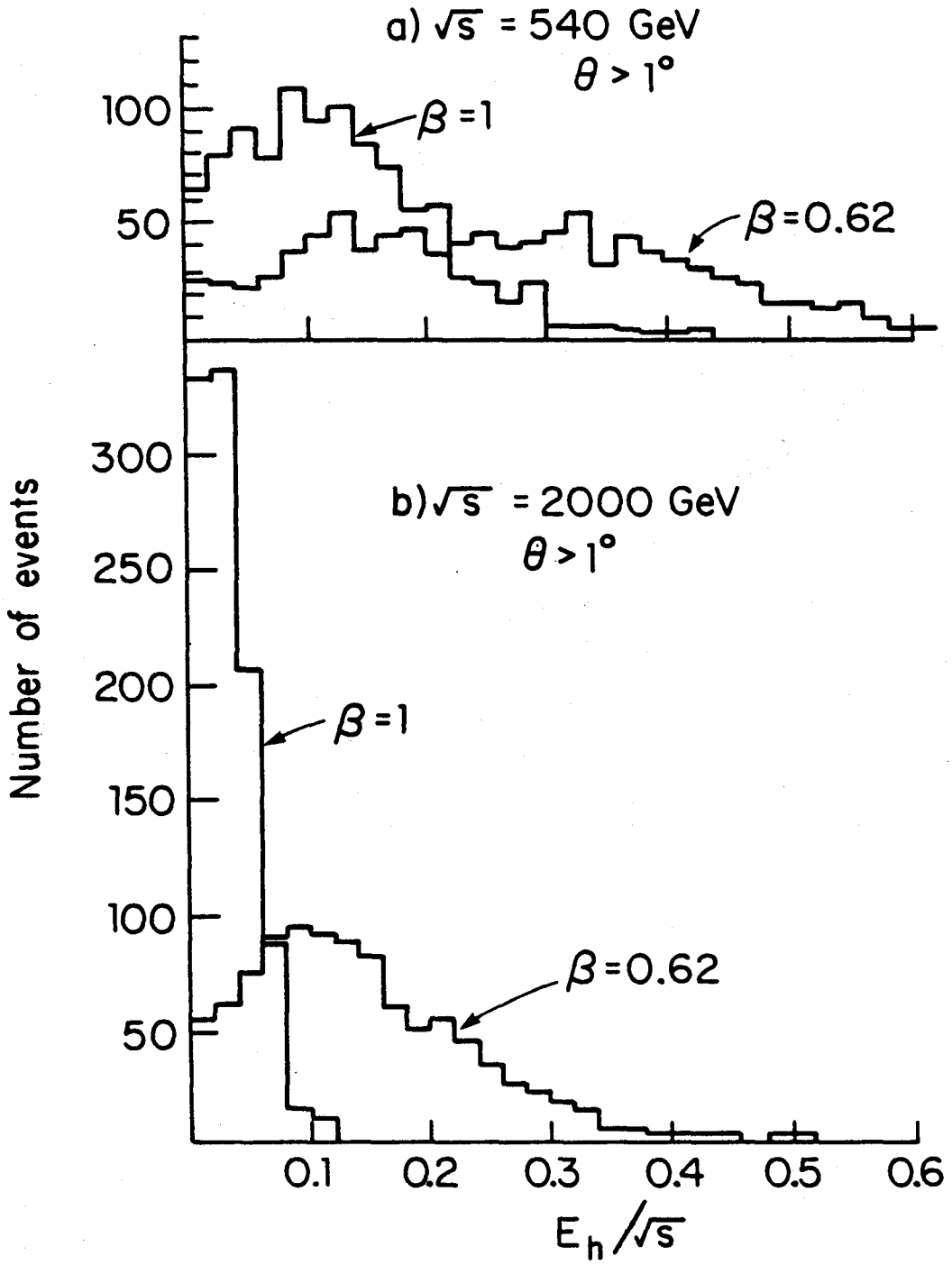
a) √s = 540 GeV
θ > 1°
β = 1
β = 0.62
100
50
b) √s = 2000 GeV
θ > 1°
β = 1
β = 0.62
300
250
200
150
100
50
Number of events
0.1
0.2
0.3
0.4
0.5
0.6
E_h/√s

FIG. 1.20

Chapter 2

OVERVIEW OF THE CDF DETECTOR

Perspective views of the detector are shown in Figs. 2.1 and 2.2. Due to mechanical considerations, the components of this detector are naturally organized into three regions according to their angular coverage with respect to the direction of the proton beam. The central part of the detector covers the angular range $10° < \theta < 170°$. An elevation view is shown in Fig. 2.3, and a beam's eye view in Fig. 2.4. The forward and backward parts of the detector cover the ranges $2° < \theta < 10°$, $170° < \theta < 178°$, respectively. An elevation view of the backward detector and its relationship to the central detector is shown in Fig. 2.5.

After leaving the vacuum chamber, particles produced by $\bar{p}p$ collisions in the angular range covered by the central detector pass in sequence through: a drift chamber system for measuring charged particle momenta in the 1.5 Tesla field of the solenoid magnet, less than one radiation length of material from either the solenoid coil and cryostat or the end plate of the drift chamber, about 20 radiation lengths of highly segmented shower counters, about 5 absorption lengths of highly segmented hadron calorimeters, and tracking chambers for muon identification. Over a restricted angular region of the central detector, the magnet return yoke will provide additional material in the path of particles, and hence, improved muon identification.

Particles produced in the forward or backward direction at angles between about 2° and 10° to the beams pass through holes in the end plugs of the magnet and enter two forward-backward spectrometers. The directions of charged particles are measured by drift chambers in the front part of these spectrometers. The particles then enter a segmented shower counter and hadron calorimeter. In addition, on one end of the apparatus (the backward or $\bar{p}$ direction) two sets of magnetized iron toroids and drift chambers provide momentum analysis for

muons produced in the angular range $150° < \theta < 178°$.

The basic scale and choice of components for the CDF detector are set by our primary physics goals of measuring as completely as possible the interactions of quarks and gluons and of being prepared for completely unexpected phenomena that may arise at the extremely high center-of-mass energy of Tevatron I.

As discussed earlier in this report, from our current understanding of quark, gluon, and lepton interactions we can make rather detailed predictions for some of the physics that will be seen with this apparatus. Because the testing of these predictions is such an important part of our physics program, we have taken them as our strongest guide in designing the detector.

The required angular acceptance follows from the constituent nature of the initial protons and antiprotons. Large Q^2 interactions take place between single constituents of the beam particles; the center of mass frame for these fundamental collisions moves in the laboratory with a velocity distribution characteristic of the motion of the constituents of the initial p and $\bar{p}$ and often has large values either along the proton or along the antiproton direction. The effect of this center of mass motion of the interacting constituents is that produced particles are distributed over a wide range of the rapidity variable $y \simeq \eta \equiv -\ln \tan \theta/2$. Consequently, coverage down to small polar angles is required.

The maximum possible y depends on the mass of the produced particles. Since we want to have large acceptance for particles with mass of the order of 100 GeV as well as for jets with p_T of order of 100 GeV/c, this requirement translates to our design criterion of covering the angular range $2° < \theta < 178°$, which corresponds to ±4 units of rapidity. In addition, complete coverage over this range of ±4 in rapidity is important for multiple jet correlation studies, the detection of missing transverse energy, and the study of diffractive heavy mass production.

The goal of observing the products of the interactions of quarks and gluons, after taking into account the kinematic spread discussed above, sets many of the parameters of the detector. The most important consideration is that these interactions normally manifest themselves as jets of neutral and charged hadrons, accompanied by beam jets. Leptons will also be spread at all angles because of the primary production and decay kinematics. Thus the detector must be able to deal with high multiplicity hadron clusters and also have the ability to distinguish charged leptons from hadrons.

The best available technology for observing a multijet structure in events is sampling calorimetry. In order to separate electrons from hadrons, we use two types of calorimeters, shower counters involving relatively high Z materials, in front of hadron calorimeters employing a much longer radiation length. Both for the purposes of triggering the apparatus and for subsequent jet searches in the data analysis, by far the most desirable way to organize the calorimetry is in terms of non-overlapping, "projective towers". These towers measure the energy flow into a definite region of solid angle. This organization of towers can be thought of as measuring the total transverse energy within a given bin in rapidity and azimuthal angle. This is the natural phase space element for the $\bar{p}p$ reactions we wish to study. The question remains, however, of how many cells are needed and how they should be distributed across the acceptance of the detector.

A natural size for the granularity of the towers can be set by considering the jets likely to be encountered with CDF. The polar angle with respect to the jet axis containing one half of the particles in the jet ($\theta_{1/2}$) is a function of the mean transverse momentum of the particles in the jet (q_t) and the total energy of the jet (E). For a simple model of the jet fragmentation that is uniform in rapidity along the jet axis, $\theta_{1/2}$ is given by $\sqrt{2q_t/E}$. The actual energy dependence and magnitude of $\theta_{1/2}$ will of course be different from this simple

model. Nevertheless, it gives us a good way of estimating a typical size of jets. For example, from experience gained with electron-positron colliding beams we expect q_t to be about .5 GeV/c. For a 30 GeV jet, the median polar angle will be approximately 10° in this model. Thus, if such a jet were produced at 90° within our apparatus, this cone would correspond to a 20° bite in azimuthal angle and a 0.4 unit extension in rapidity. At angles different from θ of 90°, jets with the same p_T will shrink in opening angle, but will still have the same size in Δy and approximately the same size in $\Delta\phi$. In order to resolve the jet clearly, it is advisable to have tower sizes somewhat less than these dimensions. Thus we may take a Δy-$\Delta\phi$ bin size of 0.1 x 5° as the natural granularity for events such as these. Such a granularity covering the entire angular range of the detector results in slightly less than 6,000 towers total. As discussed below, practical considerations of choice of materials, construction techniques, and costs will reduce the total number of towers from this figure, although the actual acceptance of the CDF towers is close to $\Delta y = 0.1$, $\Delta\phi = 5°$.

It seems clear that the best way to arrange these towers is with uniform granularity in rapidity and azimuthal angle over the entire acceptance of the apparatus. This means that ordinary hadronic events will appear uniformly distributed over the towers of the calorimeter system and that jets will be detected in essentially the same number of towers at all angles. Again, practical considerations make it impossible to have exactly uniform acceptance for all of the towers, but the design presented here represents a reasonable practical compromise.

The properties of materials used in the calorimeters will determine the basic scale of the apparatus. In lead based shower counters, the typical transverse shower size is of order of 1 centimeter for electrons and photons. For iron plate sampling calorimeters, the transverse size of the core of the hadronic shower extends over about five centimeters. In order

to exploit the granularity as discussed above it is necessary that the single particle shower sizes do not exceed the transverse size of the towers. This puts a constraint at small angles for towers with a constant rapidity coverage. A rapidity interval $\Delta y = .1$ is reduced to a width of a few centimeters at a distance of about 3 meters (which is a typical radius of our detector) when the polar angle becomes as small as 10°. This is the reason why a 10° hole is cut in the end plug and that smaller angles are covered by the forward-backward calorimeters which are further removed from the interaction point.

In the electromagnetic shower counters, a segmentation finer than provided by the towers is desired in order to measure better the impact position of photons and electrons. This is because in the direct electron search, one needs to reject fake electrons simulated by charged hadrons accompanied by a photon in the same tower. Since covering the entire solid angle with very small pads is too costly, we use PWC's with readout of orthogonal strips.

The central electromagnetic and hadron calorimeters are at larger radii than would be required on the basis of shower size alone. This somewhat larger scale is dictated by the requirements for magnetic analysis in the tracking system. As is well known, the momentum resolution scales as BL^2 and, therefore, it is advantageous to have a relatively large radius tracking system. In addition, the pattern recognition problems in drift chambers are helped enormously by increasing the number of layers and this consideration also argues for a relatively large tracking system.

There are several reasons for choosing to have a magnet in a detector such as this. First of all, the magnetic field offers a complementary measurement of particle momenta to the energy information provided by the hadron and electromagnetic calorimeters. Individual hadrons with p_T less than about 40 GeV/c are more accurately measured by magnetic analysis than by the hadron calorimeter. One can improve the pion rejection of

the electromagnetic shower counters by checking that candidate electrons have matching energy and momentum. The magnet provides the only momentum measurement for muons in the central region. Also, knowledge of the momentum of tracks will assist in the calibration of the calorimeters. Perhaps the strongest reason for insisting on a magnetic field is that it will provide a great deal of information in the event that entirely unexpected phenomena are observed in these very high energy $\bar{p}p$ collisions. Finally, there are the signs of particles and charge asymmetries which can only be determined with a magnet.

Once one has decided to have a magnetic field the choice of orientation of the field is a difficult one. For this experiment we have chosen a solenoid magnet because this field configuration has the maximum efficiency in the study of large p_T events, because of the symmetry properties of this kind of magnet and because of the wide experience gained with solenoid detectors at the electron-positron machines. The choices of a 15 kilogauss magnetic field and 1.5 meter tracking radius were made by considering the largest practical field and tracking volume to provide the best possible momentum resolution. Detectors of this general scale have been built and operated successfully; the extrapolation to a much larger field or tracking volume seems beyond the scope of this project. These parameters should result in a momentum resolution that is quite adequate for tracking the particles of interest to us in this experiment, including even the muons associated with weak boson decays where transverse momenta of order 50 GeV/c are expected.

Considerations of access to sensitive detector components, ease of assembly, costs, and the ability to build the detector in stages with early pieces available for physics at low luminosity have led to the basic mechanical design of CDF. In order to allow for the possibility of a staged detector where calorimetry and tracking are available for the earliest collisions, it is necessary to separate the functions of the calorimeters from the solenoid magnet. To do this we have designed a separated iron return yoke that serves as a basic

structure for the solenoid magnet. The large angle hadron calorimeters, which are mounted on rolling arches, can be removed from the solenoid magnet and its associated return yoke with minimal structural and magnetic interference. Therefore, if it becomes desirable, one will be able to perform a significant first stage non-magnetic experiment employing the large angle calorimeters and the central chambers as basic elements, while the implementation of the magnet proceeds in parallel.

A measurement of the absolute luminosity of the Collider will be important and difficult. While several methods will certainly be tried, our design includes the special feature of high resolution solid state minichambers located in two stations inside the beam pipes downstream along the two beams. Their coverage can be extended enough both at small and at large angles to allow a simultaneous measurement of the forward elastic cross section, the total cross section and the machine luminosity.

Figure Captions

Fig. 2.1 Perspective view of the CDF Detector

Fig. 2.2 Exploded view of the Central Detector

Fig. 2.3 Elevation view of the Central Detector

Fig. 2.4 Beam's eye view of the Central Detector

Fig. 2.5 Elevation view of the Backward ($\bar{p}$ - direction) half of the detector

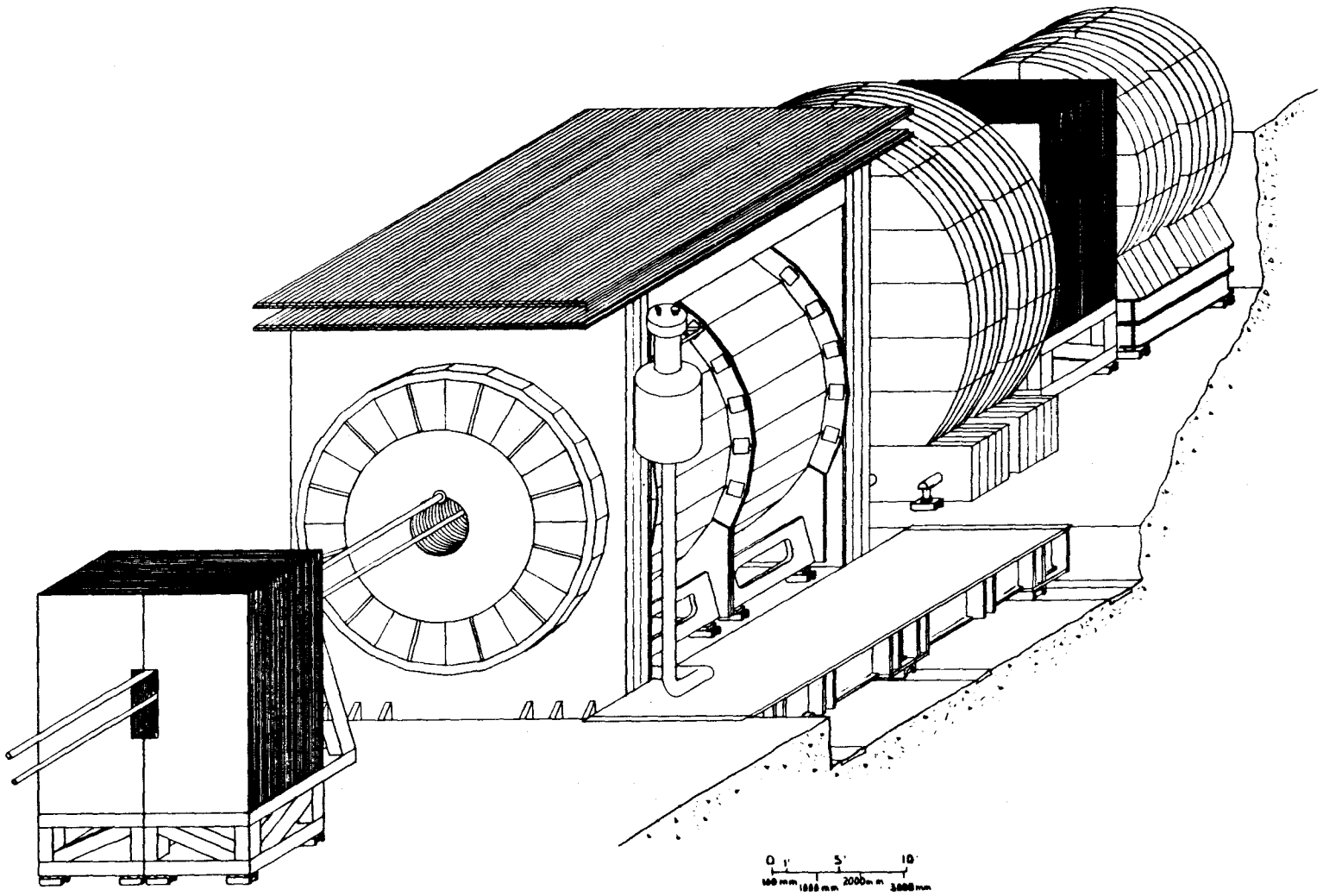

FIG. 2.1

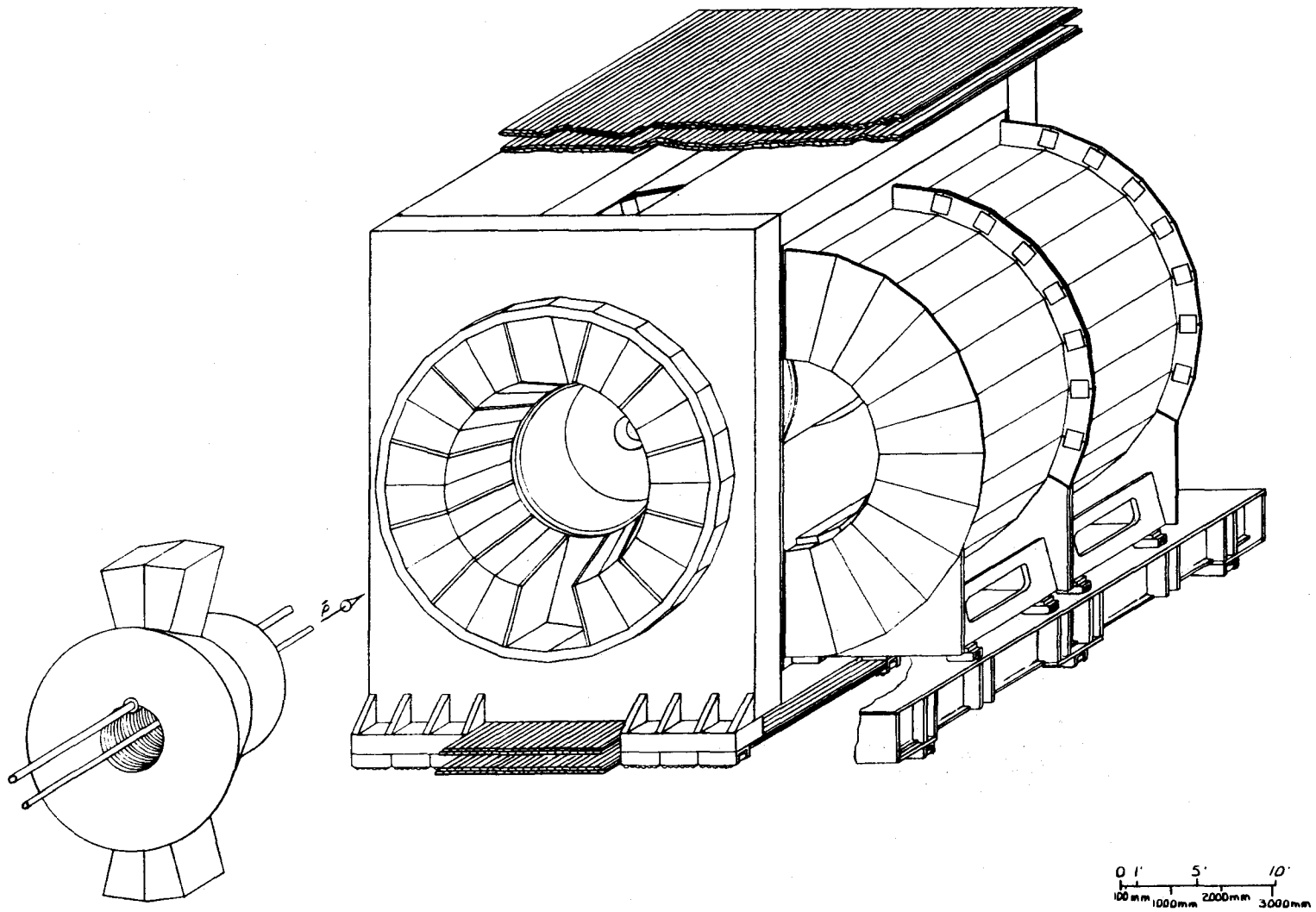

FIG. 2.2

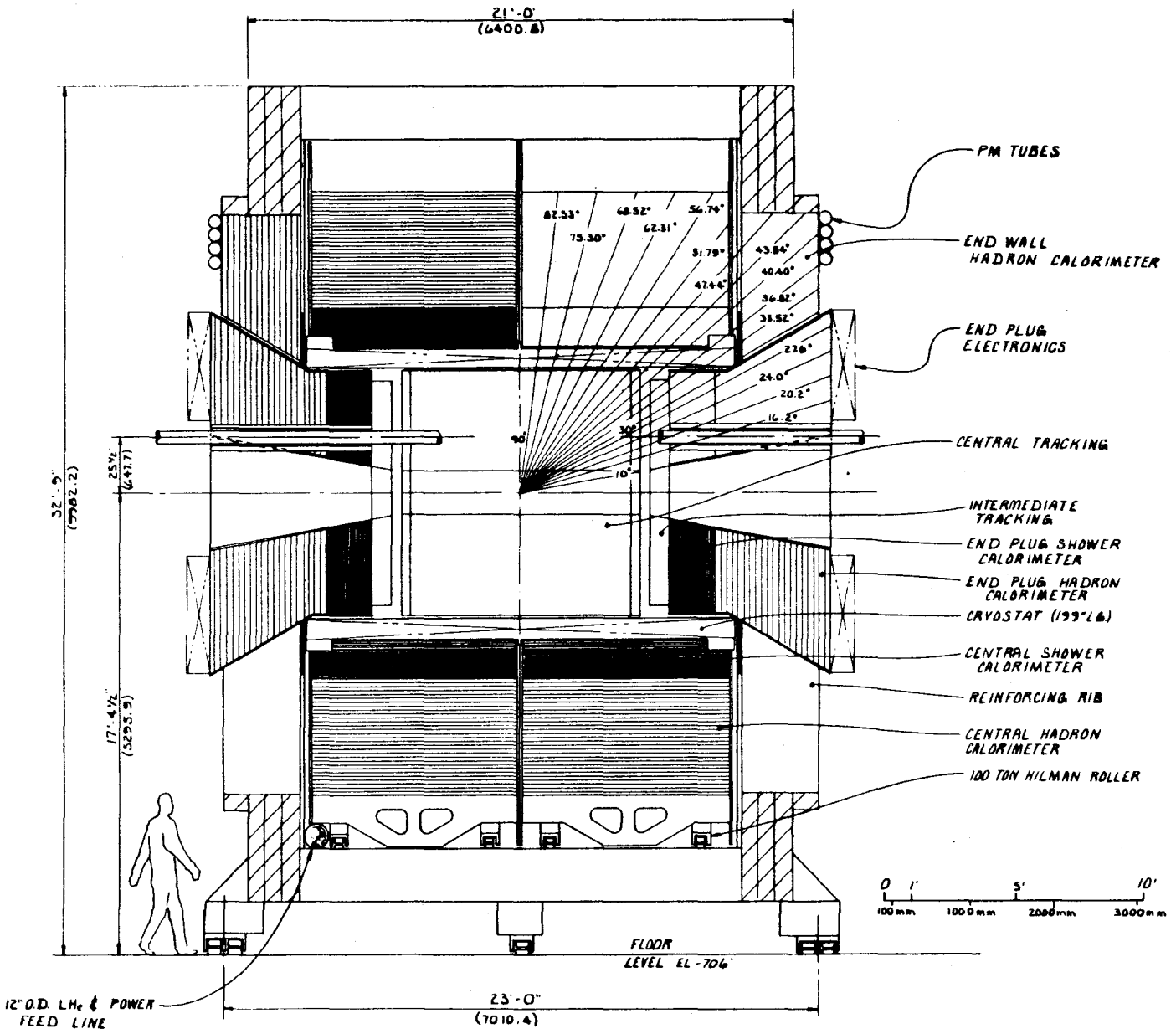
21'-0"
(6400.8)
32'-9"
(9982.2)
25'½"
(7741.7)
17'-4½"
(5295.9)
PM TUBES
END WALL
HADRON CALORIMETER
END PLUG
ELECTRONICS
CENTRAL TRACKING
INTERMEDIATE
TRACKING
END PLUG SHOWER
CALORIMETER
END PLUG HADRON
CALORIMETER
CRYOSTAT (199"Ø)
CENTRAL SHOWER
CALORIMETER
REINFORCING RIB
CENTRAL HADRON
CALORIMETER
100 TON HILMAN ROLLER
82.53°
75.30°
68.52°
62.31°
56.79°
51.79°
47.44°
43.84°
40.40°
36.82°
33.52°
27.6°
24.0°
20.2°
16.2°
90°
30°
10°
0 1' 5' 10'
100 mm 1000 mm 2000 mm 3000 mm
FLOOR
LEVEL EL -706'
12" O.D. LHe & POWER
FEED LINE
23'-0"
(7010.4)

FIG. 2.3

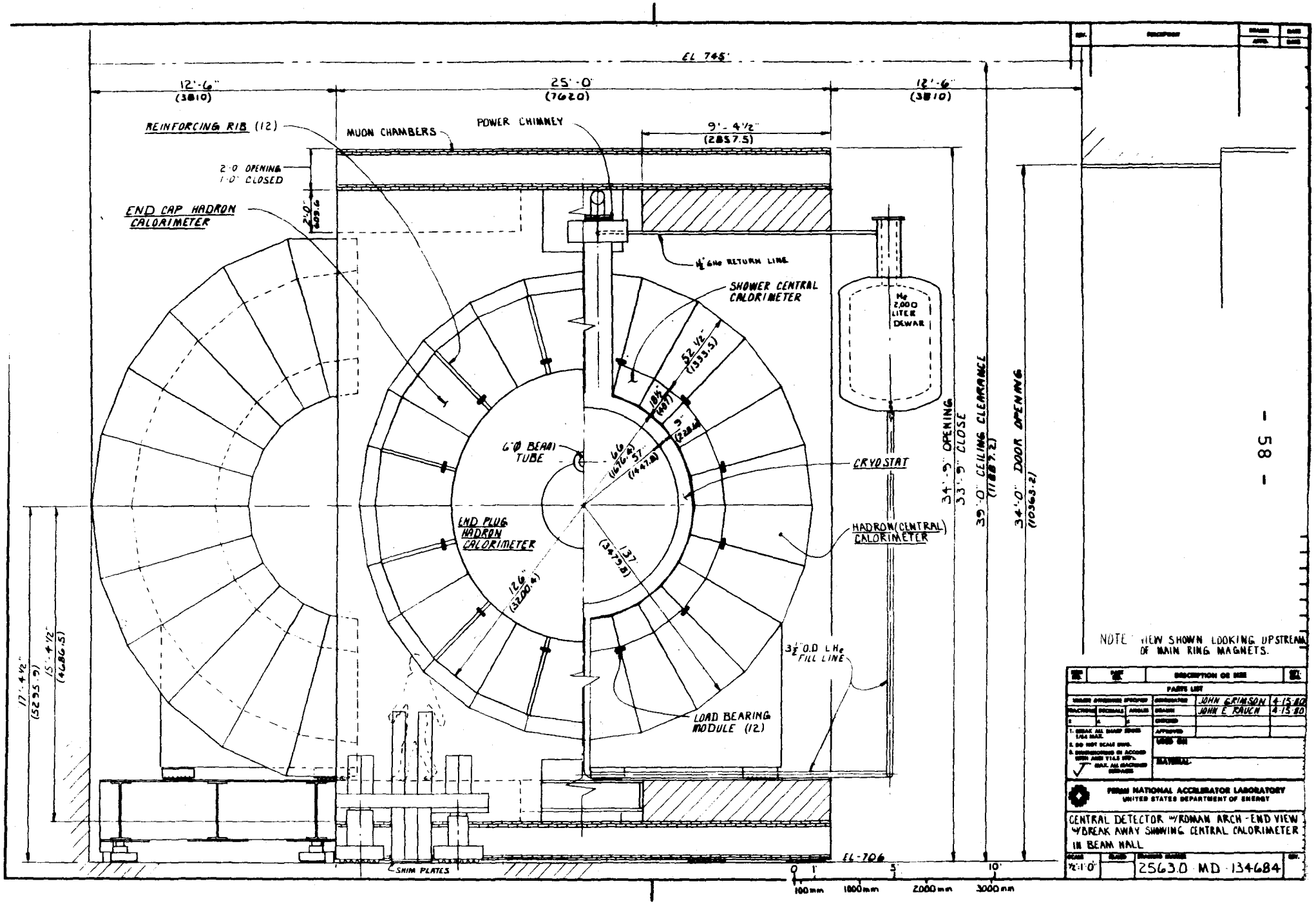
EL 745'
12'-6" (3810)
25'-0" (7620)
12'-6" (3810)
REINFORCING RIB (12)
MUON CHAMBERS
POWER CHIMNEY
9'-4½" (2857.5)
2'-0 OPENING
1'-0" CLOSED
2'-0" (609.6)
END CAP HADRON CALORIMETER
½" GHe RETURN LINE
SHOWER CENTRAL CALORIMETER
He 2,000 LITER DEWAR
52½" (1333.5)
18" (457)
3" (228.6)
6'Ø BEAM TUBE
66 (1676.4)
57" (1447.8)
CRYOSTAT
END PLUG HADRON CALORIMETER
HADRON (CENTRAL) CALORIMETER
137 (3479.8)
126" (3200.4)
3½" O.D LHe FILL LINE
LOAD BEARING MODULE (12)
34'-5" OPENING
33'-9" CLOSE
39'-0" CEILING CLEARANCE (11887.2)
34'-0" DOOR OPENING (10363.2)
17'-4½" (5295.9)
15'-4½" (4686.5)
EL 706
SHIM PLATES
0 1' 5' 10'
100mm 1000mm 2000mm 3000mm
NOTE: VIEW SHOWN LOOKING UPSTREAM OF MAIN RING MAGNETS.
DESCRIPTION OR NOTE
PARTS LIST
JOHN GRIMSON 4-15-80
JOHN E RAUCH 4-15-80
DRAWN
CHECKED
APPROVED
USED ON
MATERIAL
FERMI NATIONAL ACCELERATOR LABORATORY
UNITED STATES DEPARTMENT OF ENERGY
CENTRAL DETECTOR w/ROMAN ARCH - END VIEW w/BREAK AWAY SHOWING CENTRAL CALORIMETER IN BEAM HALL
SCALE ½"=1'-0"
DRAWING NUMBER 2563.0 MD-134684

FIG. 2.4

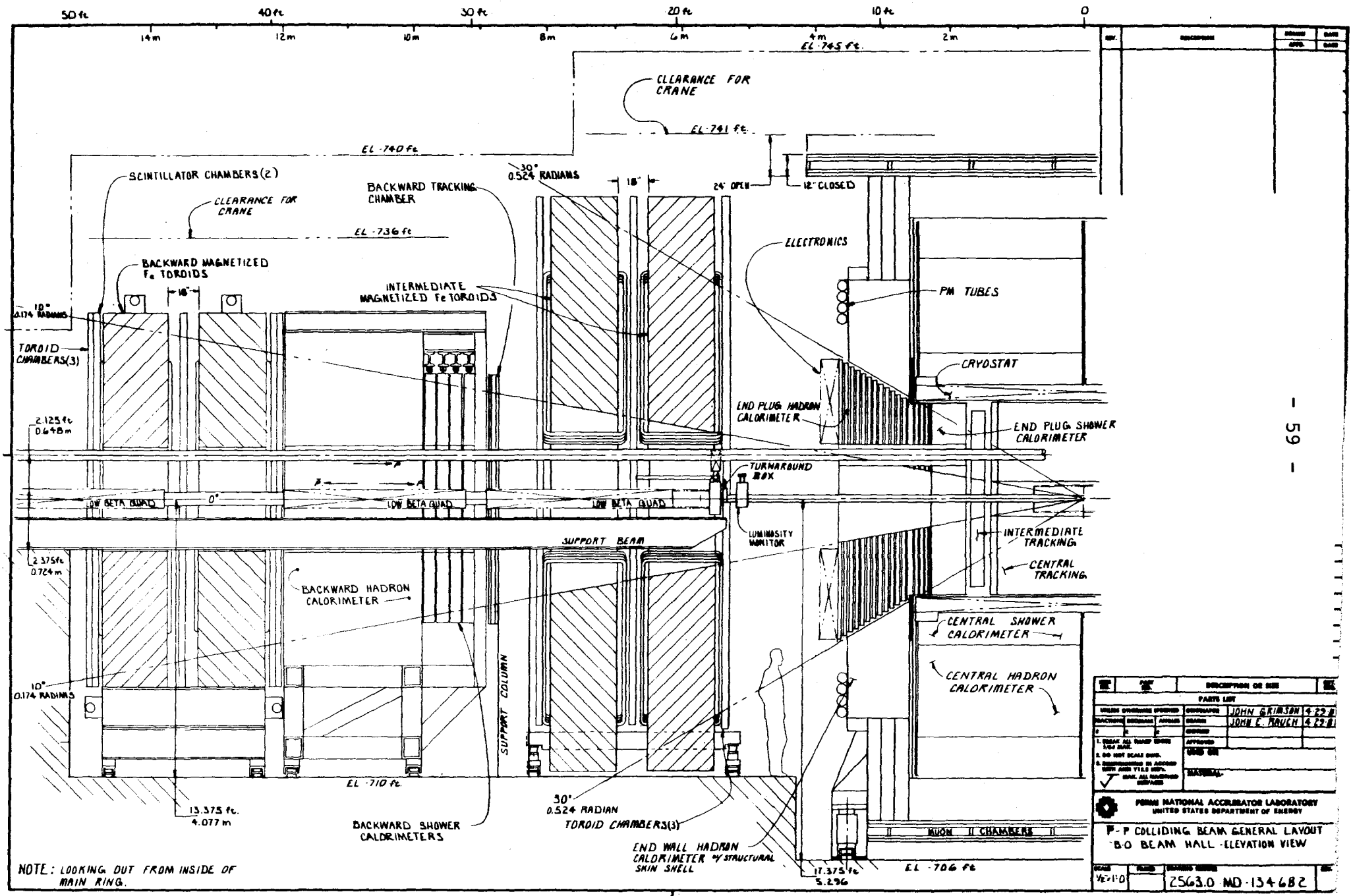
50 ft
40 ft
30 ft
20 ft
10 ft
0
14 m
12 m
10 m
8 m
6 m
4 m
2 m
EL 745 ft.
CLEARANCE FOR CRANE
EL 741 ft.
EL 740 ft
SCINTILLATOR CHAMBERS(2)
CLEARANCE FOR CRANE
EL 736 ft
BACKWARD TRACKING CHAMBER
30° 0.524 RADIANS
18"
24" OPEN
12" CLOSED
ELECTRONICS
PM TUBES
CRYOSTAT
BACKWARD MAGNETIZED Fe TOROIDS
INTERMEDIATE MAGNETIZED Fe TOROIDS
10° 0.174 RADIANS
TOROID CHAMBERS(3)
END PLUG HADRON CALORIMETER
END PLUG SHOWER CALORIMETER
2.125 ft 0.648 m
TURNAROUND BOX
LOW BETA QUAD
0°
LOW BETA QUAD
LOW BETA QUAD
LUMINOSITY MONITOR
SUPPORT BEAM
INTERMEDIATE TRACKING
CENTRAL TRACKING
2.375 ft 0.724 m
BACKWARD HADRON CALORIMETER
CENTRAL SHOWER CALORIMETER
CENTRAL HADRON CALORIMETER
SUPPORT COLUMN
10° 0.174 RADIANS
EL 710 ft.
13.375 ft. 4.077 m
30° 0.524 RADIAN
BACKWARD SHOWER CALORIMETERS
TOROID CHAMBERS(3)
END WALL HADRON CALORIMETER w/ STRUCTURAL SKIN SHELL
MUON II CHAMBERS II
17.375 ft 5.296
EL 706 ft
NOTE: LOOKING OUT FROM INSIDE OF MAIN RING.
FERMI NATIONAL ACCELERATOR LABORATORY
UNITED STATES DEPARTMENT OF ENERGY
P-P COLLIDING BEAM GENERAL LAYOUT
B-0 BEAM HALL - ELEVATION VIEW
JOHN GRIMSON 4-22-81
JOHN E. RAUCH 4-29-81
3/8"=1'-0
2563.0 MD-134682

FIG. 2.5

Chapter 3

CDF SOLENOID MAGNET

The central detector for the Collider Detector Facility employs a large axial magnetic field volume instrumented with multiple layers of cylindrical drift chambers. The purpose of this system is to determine the trajectories, sign of electric charge, and momenta of charged particles produced with polar angles between 10 and 170 degrees. The magnetic field volume required for tracking is approximately 4m long and 3m in diameter. To provide the desired $\Delta p_T/p_T \lesssim 15\%$ at 50 GeV/c using drift chambers with $\sigma \gtrsim 200\mu$, the field inside this volume should be 1.5 Tesla and should be as uniform as is practical to simplify both track finding and the reconstruction of particle trajectories with the drift chambers.

Such a field can be produced by a "cylindrical current sheet" solenoid with a uniform current density of 1.2×10^6 amps/meter surrounded by an iron return yoke as shown in Fig.3.1. For practical coils and return yokes, both electromagnetic and hadronic calorimetry must be located outside the coil of the magnet. This geometry places the additional requirement on the coil that it be "thin" both in physical thickness and in radiation and absorption lengths. This dual requirement of high linear current density and minimal coil thickness can only be satisfied using superconducting technology. A summary of the CDF solenoid design parameters is presented in Table 3.1.

3.1 MAGNET YOKE

The function of the yoke is to provide a flux return path for the central solenoidal field. The magnet yoke also provides the structural support for most of the modules of the central detector. An isometric view of the bare yoke is shown in Fig. 3.2. It is constructed of distressed steel plates approximately 8 in. thick, cut to size, machined on appropriate surfaces, and welded into pieces weighing approximately 50 tons each. The basic structure is that of two end walls and four return legs.

The two end walls are used as the structural support for the superconducting coil-cryostat package and the calorimeter modules between 10° and 50° with respect to the beam. The edges are distressed steel plates. Extending in from the edges are 12 reinforcing ribs of 2 in. thick steel welded to a 2 in. thick stainless back plate that serves as support for the cryostat and for the conical end plug.

The four return legs are solid steel simply connecting the end walls. The two lower return legs act as the supporting structure for the four arches that carry the central calorimetry. The elevation of the upper surface of these lower return legs is set at 710 ft.,the same as the predominate floor level in both the collision hall and assembly area. This allows the arches to be rolled out onto the floor in the assembly area or onto the transporter carts for servicing as shown in Fig. 2.2.

The entire yoke will be assembled in the assembly area with the help of the 50 ton crane. When the end wall and end plug calorimetry is in place, the yoke, coil, and cryostat can be tested and mapped independent of the central calorimetry.

The annular region between 30° and 50° is covered by 24 end wall hadron calorimeter modules mounted between the 12 ribs of the end wall as shown in Fig. 3.3. The details of these modules are discussed in Section 4.5. The annular region between 10° and 30° is covered by the end plug hadron calorimeter discussed in Section 4.6. Both of these hadron

calorimeters are used in the flux return path for the central solenoidal field. Since the axial forces on these calorimeters are large (approximately 640 tons total on each end), the calorimeters are fabricated from 2 in. thick steel plates. The conical end plug rests on the 12 radial reinforcing ribs of the end wall. The axial compressive force will be carried through these ribs to the central calorimetry modules which will act as beams. When these central calorimetry modules are not in place (as in testing the coil), this function will be supplied by a set of separate beams.

Another function of the magnet yoke is to provide the support structure to roll the entire central detector between the assembly area and the collision hall. The actual rolling mechanism is provided by six 600 ton Hilman rollers.

Access to all phototubes is from the outside of each of the central and end wall calorimetry modules. The end plug calorimetry electronics is mounted on the end wall of the end plug itself. The only parts of the central detector that must move for service access are the central arches to service the central EM position chambers and the end plugs that must move to provide access to service the central and intermediate tracking chambers. Fig. 3.4 shows the end plug extended for access.

3.2 SUPERCONDUCTING COIL AND CRYOSTAT

Three different types of superconducting magnet coils seem possible for the CDF solenoid and the engineering consequences of each are currently being explored.

The first type is adiabatically stabilized. This type of coil relies upon the heat capacity and high thermal conductivity of a high purity aluminum stabilizer to absorb and dissipate transient heat pulses in the conductor so that the superconductor remains below its critical temperature. Such heat pulses can be generated by conductor motion, cracking epoxy or other similar releases of mechanical energy. If the total energy release is sufficiently large, the conductor will quench. The coil is protected against this eventuality by insuring that the "quench wave" velocity is sufficiently high that the energy deposited in the coil is widely distributed and thus can be absorbed without damage to the coil. A preliminary design of the CDF solenoid based upon this type of coil is published in a Fermilab technical memo TM-826 (ref. 3.1). Examples of other large solenoids of this type include those for CELLO, TPC, and CLEO. A 1m diameter test coil of this type has been fabricated and tested at Hitachi Ltd., Japan. A description of this coil and test results are given in Appendix III.

The second type of coil we are investigating is a pool boiling cryostable design. In this scheme the conductor is kept in intimate contact with a bath of helium at 4.2°K and atmospheric pressure. The conductor is designed to have sufficient cooling surface and stabilizer (both aluminum and copper seem feasible) such that the heat transfer through the surface of the conductor exceeds the ohmic heating. Thus the normal zone collapses and the coil recovers without quenching. Operating currents between 5000 and 15000 amps appear to be possible.

The third type of coil is a cryostable coil using forced flow, super-critical helium for refrigeration. In this type of coil, the conductor is also designed so that a normal zone if

created rapidly collapses and the coil does not quench. Cooling is provided by helium circulating in a tube attached to the conductor with helium circulating at pressures above the critical point, so that phase transitions in the helium are prohibited. This design favors operating currents of 15,000 to 20,000 amps.

Some of the electrical properties of the solenoid are summarized in Table 3.2 and a magnetic field map, calculated with the program TRIM for the CDF solenoid in its iron yoke is shown in Fig. 3.5. Results from this program have been used to calculate the magnetic forces on the coil. The coil is in an unstable equilibrium both axially and radially with an axial magnetic spring constant of 50 T/in. and a radial spring constant of $\lesssim$ 30 T/in. These forces will be carried by a system of fiberglass/epoxy compression members located at each end of the coil and bearing upon a structural aluminum ring at each end of the coil package. Detailed engineering design and thermal analysis of this support scheme is in progress. Both the large stored magnetic energy and rapid charging rate present other engineering problems that are under consideration.

References

3.1 Conceptual Design of a large, thin coil superconducting solenoid magnet for colliding beam experiments at Fermilab, D. Cline et al., TM-826, October 25, 1978.

Table 3.1

CDF Solenoid Design Parameters

Outside radius	66"
Length:	200"
Coil/Cryostat Thickness:	
a) Physical thickness:	9" (design goal)
b) # radiation lengths:	$\lesssim$ 1.5
c) # absorption lengths:	$\lesssim$0.2
Central Field:	15 kG
Desired field uniformity:	±1%
Stored Energy:	30 x 10^6 J
Axial magnetic decentering force:	50 T/in.
Radial magnetic decentering force:	$\lesssim$ 30 T/in.
Desired Charge Time:	$\lesssim$ 20 minutes

Table 3.2

Electrical Properties of CDF Coil

(Independent of coil type)

Stored Energy $E = \int_{\text{volume}} B^2 \, dV = 30 \times 10^6$ Joules

(1) $L = 2E/I^2$

(2) Discharge time constant $\tau = L/R$

R = dump resistor $= \frac{V_{max}}{I_{max}}$

for $V_{max} = 200$ volts $\Rightarrow$

I	L(H)	τ(sec)	# Turns
1000	60	300	6600
2000	15	150	3300
5000	2.4	60	1320
10000	0.6	30	660
15000	0.27	20	440
20000	0.15	15	330

(3) Power Supply

Must be capable of charging coil in $\sim$ 10 minutes

$$\langle \text{power} \rangle = \frac{30 \times 10^6 \text{ J}}{600 \text{ sec}} = 50 \text{ kW}$$

$$E = 1/2 \, LI^2$$

$$p = \frac{dE}{dt} = LI \frac{dI}{dt} \text{ for linear charge } \frac{dI}{dt} = \frac{I_{MAX}}{600}$$

$$P_{MAX} = \frac{LI^2_{max}}{600} = \frac{2E_{max}}{600} = 100 \text{ KW}$$

Figure Captions

Fig. 3.1 Layout of solenoid, steel return yoke and other components of the central detector.

Fig. 3.2 Isometric view of the bare yoke.

Fig. 3.3 End wall hadron calorimeters installed between ribs.

Fig. 3.4 End plug of central detector moved back for access to the tracking system

Fig. 3.5 Magnetic field map for the solenoid as calculated by the two-dimensional program TRIM. The density of the field lines in this plot is proportional to BR, where R is the radius, and not B. The field inside the solenoid (0<R<60 inches) is uniform.

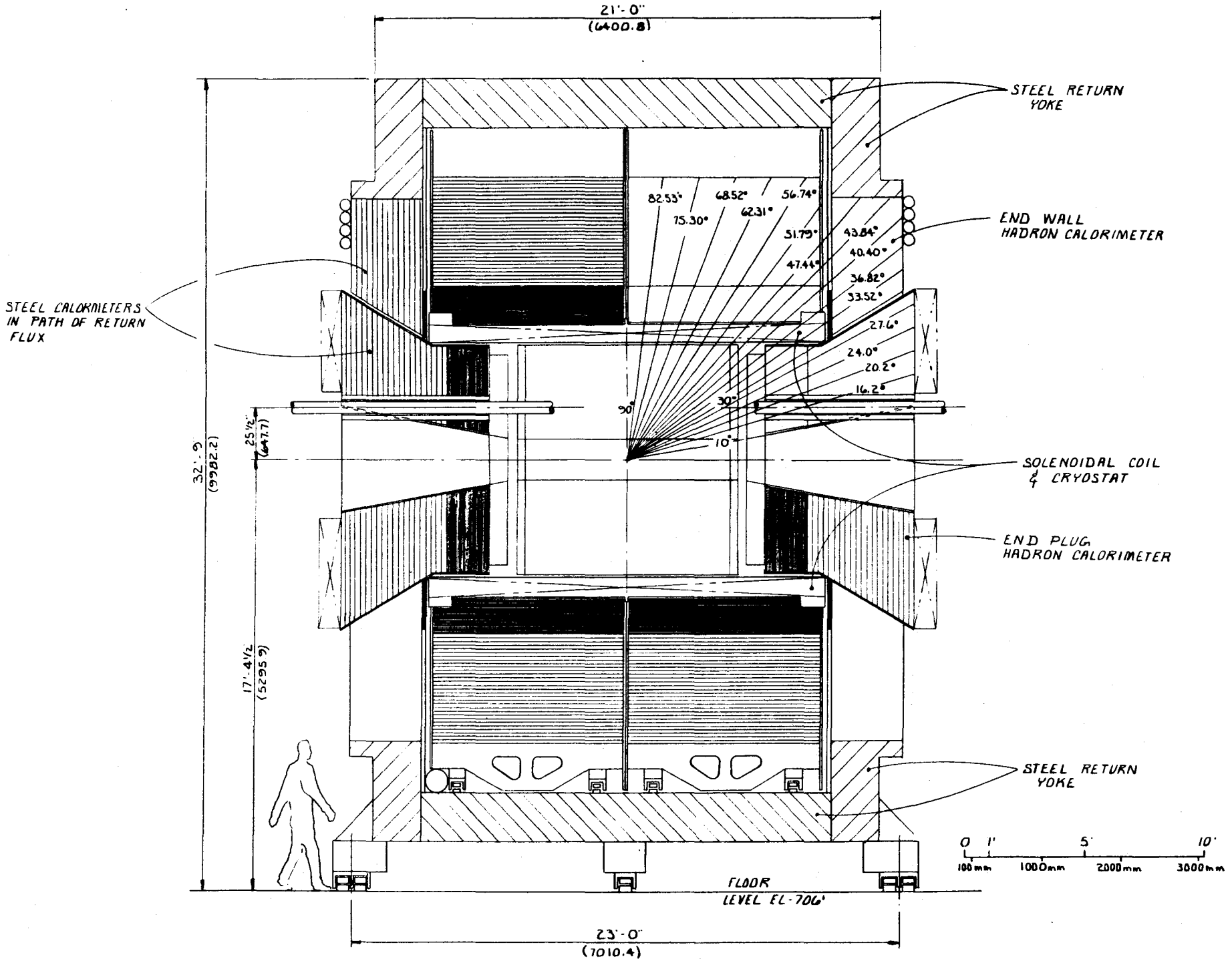
21'-0"
(6400.8)
STEEL RETURN YOKE
END WALL HADRON CALORIMETER
STEEL CALORIMETERS IN PATH OF RETURN FLUX
SOLENOIDAL COIL & CRYOSTAT
END PLUG HADRON CALORIMETER
STEEL RETURN YOKE
FLOOR LEVEL EL-706'
23'-0"
(7010.4)
32'-9
(9982.2)
17'-4½
(5295.9)
25½"
(647.7)
82.53°
75.30°
68.52°
62.31°
56.74°
51.79°
47.44°
43.84°
40.40°
36.82°
33.52°
27.6°
24.0°
20.2°
16.2°
90°
30°
10°
0 1' 5' 10'
100mm 1000mm 2000mm 3000mm

FIG. 3.1

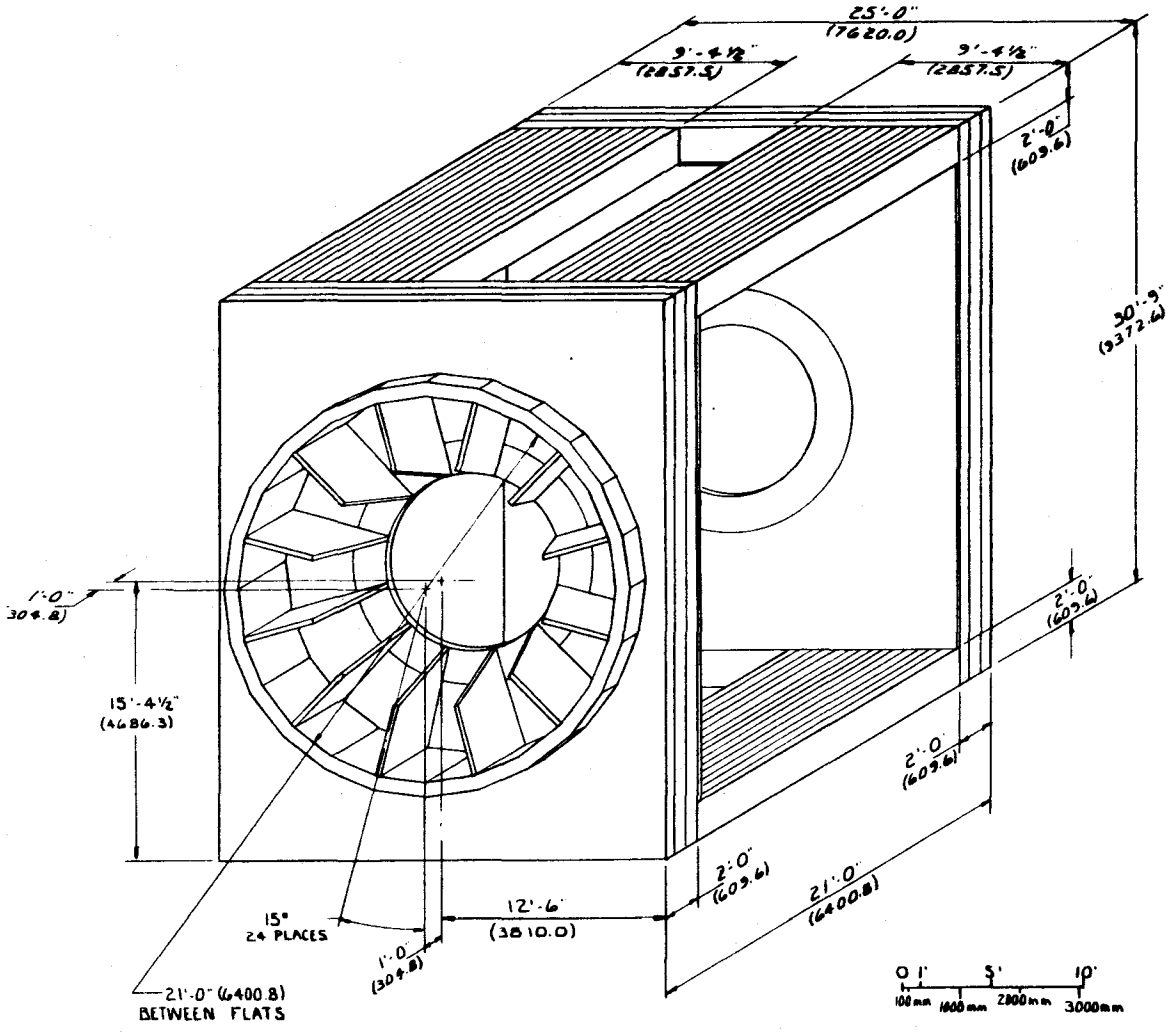
25'-0"
(7620.0)
9'-4½"
(2857.5)
9'-4½"
(2857.5)
2'-0"
(609.6)
30'-9"
(9372.6)
1'-0"
(304.8)
15'-4½"
(4686.3)
2'-0"
(609.6)
2'-0"
(609.6)
2'-0"
(609.6)
21'-0"
(6400.8)
12'-6"
(3810.0)
15°
24 PLACES
1'-0"
(304.8)
21'-0" (6400.8)
BETWEEN FLATS
0 1' 5' 10'
100mm 1000mm 2000mm 3000mm

FIG. 3.2

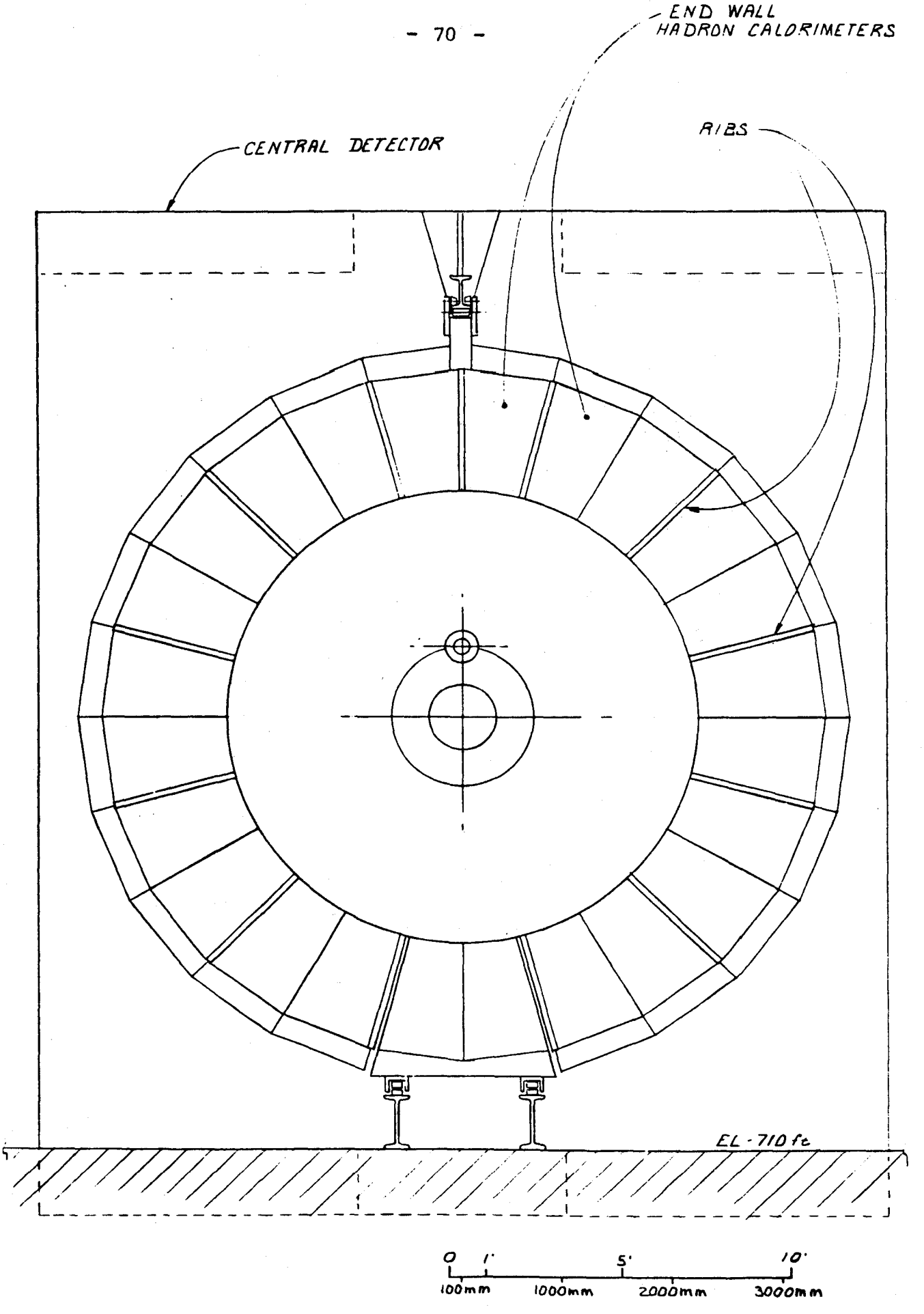
END WALL
HADRON CALORIMETERS
RIBS
CENTRAL DETECTOR
EL - 710 ft
0
1'
5'
10'
100mm
1000mm
2000mm
3000mm

FIG. 3.3

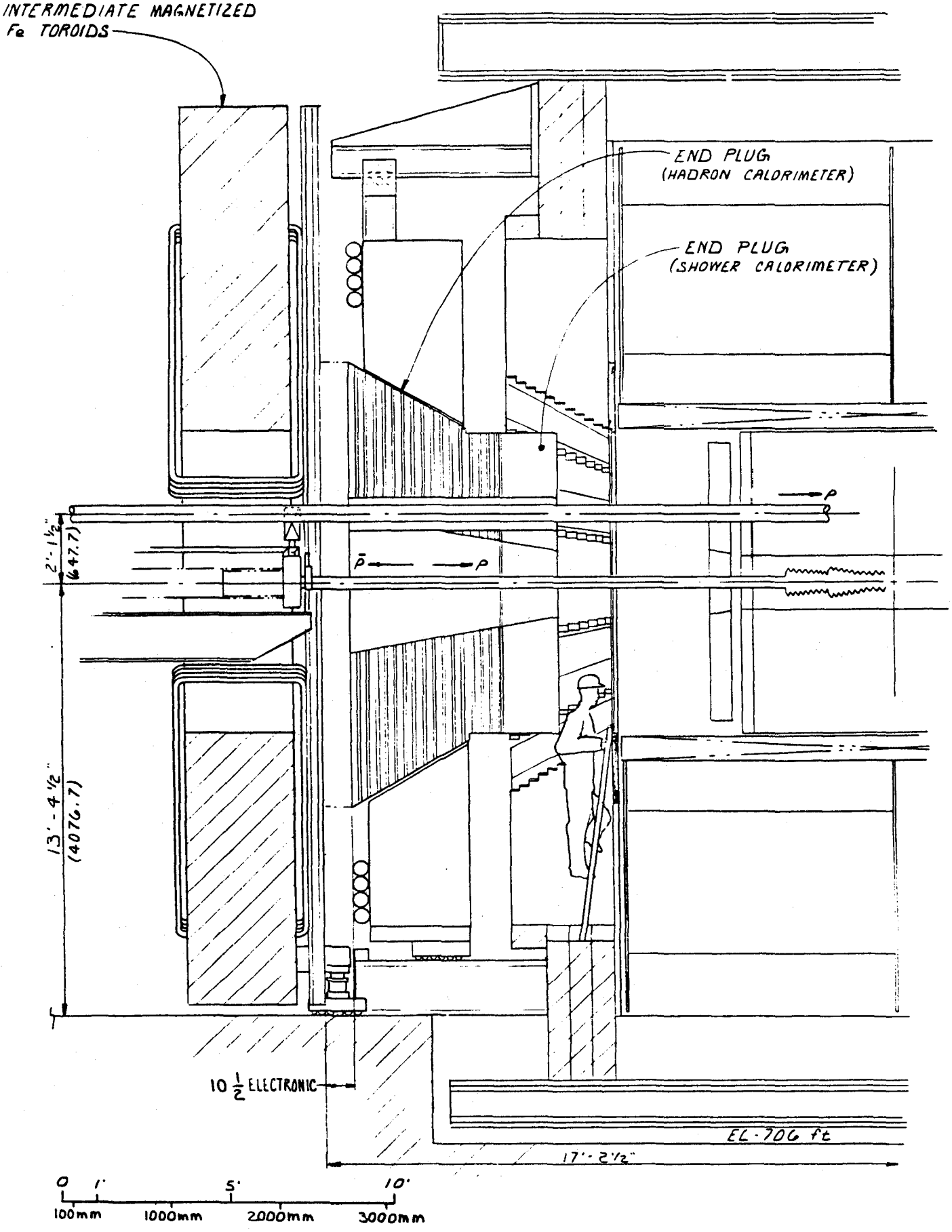
INTERMEDIATE MAGNETIZED
Fe TOROIDS
END PLUG
(HADRON CALORIMETER)
END PLUG
(SHOWER CALORIMETER)
p
p̄
p
2'-1½"
(647.7)
13'-4½"
(4076.7)
10 ½ ELECTRONIC
EL-706 ft
17'-2½"
0
1'
5'
10'
100mm
1000mm
2000mm
3000mm

FIG. 3.4

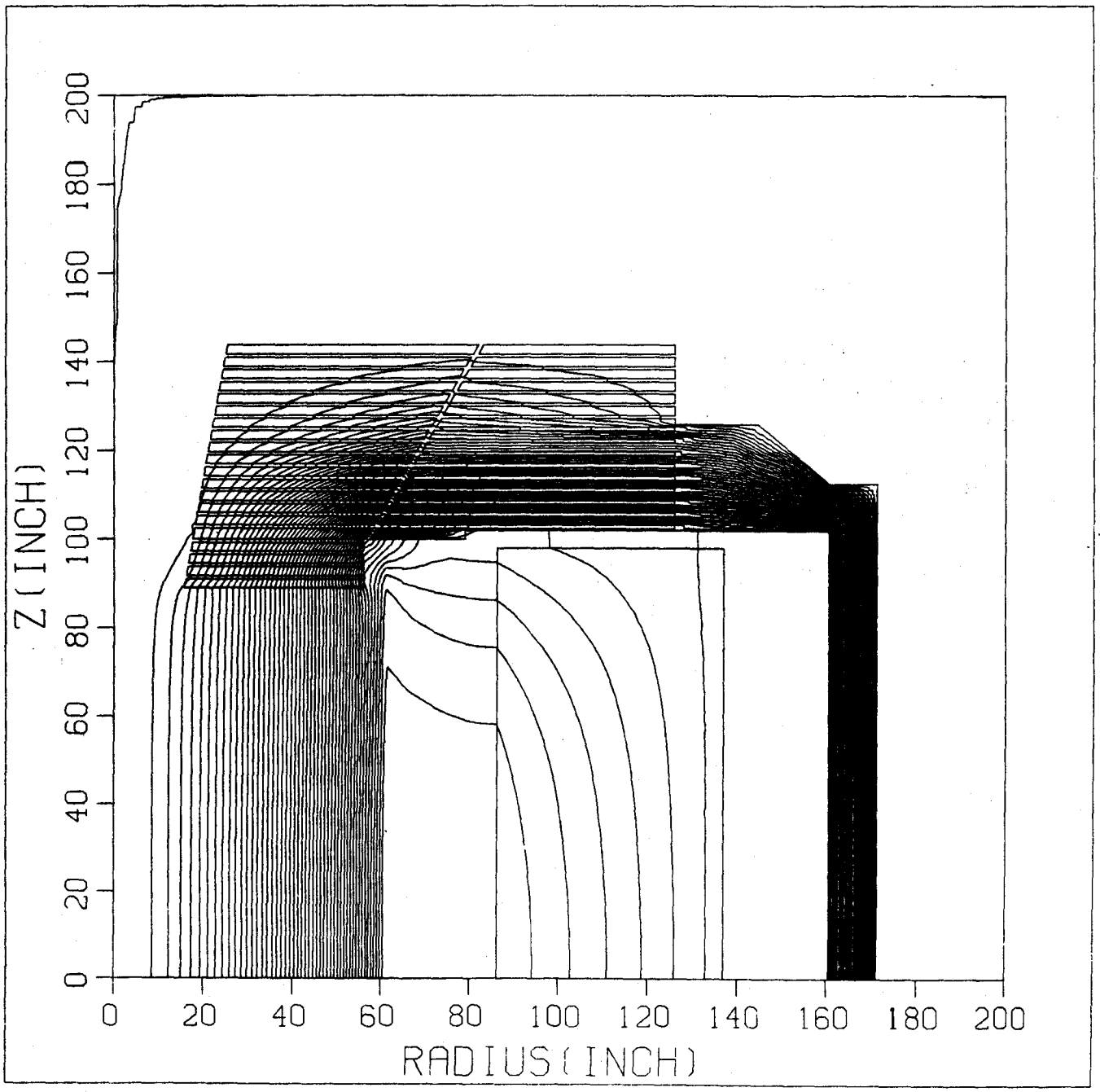

FIG. 3.5

Chapter 4

CALORIMETRY

One of the fundamental design goals for the detector has been that it should provide particle detection and energy measurement via calorimeters over virtually the full solid angle ($2° < \theta < 178°$). The resolution (σ/E) of most calorimeters varies with energy as $1/\sqrt{E}$, so calorimeters should perform better at collider energies than at lower energy machines.

The calorimeters have a "front" part of electromagnetic shower counters followed by a "back" part of hadron calorimeters. This arrangement assures the detection via energy measurement of both charged and neutral hadrons, γ-rays, and electrons ($e\pm$). Only the energy of muons and neutrinos is not measured by calorimetry. Energetic muons, for instance, leave only about 1.5 GeV equivalent in the calorimeters, independent of the muon energy.

The calorimetry is arranged in "towers". The approximate tower size is dictated by the requirement that quark and gluon jets should spread over several towers in the detector as discussed before. The chosen segmentation is shown in Fig. 4.1. This geometry is, of course, particularly well suited for event vertices at the midpoint of the interaction region, but even particles emerging up to ±45 cm from this point along the beam axis will cross into at most two adjacent towers.

The actual arrangement of calorimeters, dictated largely by mechanical considerations, is shown in Fig. 4.2. The corresponding angular and rapidity coverage of the various calorimeter systems is indicated in Fig. 4.1

Two basic detector techniques are used in the calorimeter system, multiwire gas-filled chambers with cathode pad readout and scintillator-wave shifter readout with photomultipliers. Wire chambers are used in calorimeter modules that cover the

angular region below $\theta = 36^{o}$ (the forward shower counters, forward hadron calorimeters, end plug shower counters, and end plug hadron calorimeters). The ease of matching the desired granularity with cathode pads, lack of complicated light pipes, and expectations of better calibration techniques argue for wire chamber systems in this small-angle region where particle energies and densities are the highest, and where there are complicated mechanical problems involving the beam line and end of the solenoid.

Mechanical problems are somewhat eased in the angular region $30° \lesssim \theta \lesssim 150°$, and the average particle energies are lower. The central shower counter, central hadron calorimeter, and end wall hadron calorimeter are therefore built with scintillator-BBQ wave shifter-photomultiplier readout for which the energy resolution can be made to be superior to gas chamber systems.

The central shower counters and hadron calorimeters are arranged in the form of a barrel with 24 modules in azimuth and 2 sets of modules along the beam axis for a total of 48 modules. This choice was taken to keep the total weight of each module below 20 tons for ease in handling while minimizing the total number of distinct modules and the attendant dead regions due to edge effects. Each module is further divided into towers giving a granularity of $\Delta\phi = 15^{o}$, $\Delta\eta = 0.11$. This somewhat coarser $\Delta\phi$ acceptance (compared to 5^{0} at smaller angles) is partially offset by the fact that two photomultipliers, one on either side in the ϕ direction, read out each tower and provide interpolation information within the tower. To match the barrel system, the end wall hadron calorimeters also have a $\Delta\phi$ acceptance of 15^{o}.

The 48 central calorimeter modules are mounted into four arches of 12 modules each for ease of moving and staging the detector.

4.1 THE CENTRAL ELECTROMAGNETIC SHOWER COUNTERS

General Description

The central calorimeter modules are wrapped around the outside of the solenoid in a 24-fold configuration. Their location is shown in Fig. 4.2. The 5-m length along the beam is split in two, giving a total of 48 modules covering the angular range $36^{o}<\theta<144^{o}$. The parameters of the shower detector are listed in Table 4.1. Within each of the shower counter modules there are 10 lead-scintillator towers with projective geometry arranged such that the four sides of each tower point back to the interaction region. These towers match those of the hadron calorimeter. Each tower is read out by two BBQ wave-shifter sheets, one at each end, connected through acrylic light pipes to 2-inch diameter phototubes located outside the hadron calorimeter for easy access. Sketches of one module are shown in Figs. 4.3, 4.4

The lead-scintillator towers are composed of 33 layers, each having 1/8-inch of lead and 1/4-inch of plexinonpop, $0.6X_{o}$/layer, for a total of $20X_{o}$. For mechanical strength the lead sheets are clad with 15 mils of aluminum on each side. Plexinonpop with 11% naphthalene doping was chosen for its low cost, radiation resistance, and resistance to crazing. The wave-shifter is 1/8-inch thick, 90 mg/ℓ BBQ in acrylic; ultraviolet absorbing material is added to eliminate "hot spots" caused by showers making Cerenkov light in the wave-shifter bar.

Two layers of wire proportional tube strip chambers (CDF-39,63) are embedded in the scintillator, the first at $2.6X_{o}$ depth (including the magnet coil) and the second near shower maximum at $6.2X_{o}$. Initially only the chamber near shower maximum will be instrumented. The chambers are mechanically similar to those of the MAC calorimeter (ref. 4.1) and are made by placing wires in U-shaped channels formed in a plate of extruded aluminum; this is then covered with a G10 board having strips at 90^{o} to the wire direction. The resulting cells are

8 x 8 mm^2. Each chamber is divided into 0.5 x 1.2 m^2 logical regions. Within this area the hits are measured by wires and orthogonal strips. The wires are ganged together in pairs to give bins 1.6 cm wide. The strip spacing is also 1.6 cm in the half of the module near 90^o. In the other half the strip width is enlarged to 1.9 cm since the projected width is reduced by $\sin\theta$. The wires are connected to high voltage in groups of six so that if a wire should break, only a fraction of a given wire chamber need be shut off.

Performance

The engineering design of the central shower counters has been developed after extensive tests of first-generation prototypes. A final prototype of full size has been built, providing us with experience on fabrication techniques and costs. The beam tests of this prototype have given good results, as explained below. A summary of the performance is given in Table 4.1.

Scintillator Energy Resolution

Energy resolution of lead-scintillator sandwiches has been measured by several groups; the compilation of Stone et al.(ref. 4.2) shows that for 1/4-inch plastic scintillator sampling with good photoelectron statistics a typical resolution is

$$\sigma/E = 15\% \sqrt{t/E}$$

where E is the energy of the electron in GeV and t is the lead thickness in radiation lengths. This resolution is dominated by sampling fluctuations, has no contribution from photoelectron statistics, and at our value of $t = 0.6X_o$ gives $\sigma/E = 12\%/\sqrt{E}$.

Geometry and cost preclude direct viewing of our cells, so we use the elegant wave-shifter technique(ref.4.3-4.5) to collect and concentrate the light from a large area. Unfortunately, this method does result in considerable loss of light and the statistical spread in the number of photoelectrons can become important. To resolve the question of actual light collection possible given the somewhat restrictive geometry and long light pipes in CDF, a prototype module was tested. As shown by Fig. 4.5 the first beam tests of the module(CDF-90) gave an energy resolution of

$$\sigma/E = 14\%/\sqrt{E}$$

for cell number 1c (nearest 90^{o}). Examination of the resolution from each phototube separately, and of the difference between the two phototubes, gave 142 photoelectrons/GeV, very close to the number estimated from tests in the laboratory.(CDF-67) Further improvements in the light pipes seem possible and will be studied in the laboratory. On the other hand, there will be a factor of ~1.5 loss in light in going from the polystyrene of the prototype module to the less expensive plexinonpop that we plan to use in the final modules. We estimate that near 90^{o} the present design will yield

$$N_{p.e.} = (120 \pm 20)/GeV,$$

$$\sigma/E = 15\%/\sqrt{E}$$

The effect of attenuation in the polystyrene was measured in the prototype module by sweeping the beam across one of the towers and taking the ratio of the two phototube pulse-heights as a function of beam position. This method gave an attenuation length of 44 cm, the same as measured directly in the lab on a piece of polystyrene with a β-ray source.

Leakage from the back of the shower counters was examined using test data, a sample of which is shown in Fig. 4.6 (CDF27,29). At $20X_{o}$,~1% of a 30-GeV electron shower will leak out the back with fluctuations of typically half this value. For γ showers, which develop more slowly (CDF-36), the leakage

fluctuation is expected to be 1.4 times larger. The leakage fluctuations are well under the nominal resolution of $\sigma/E = 15\%/\sqrt{E} = 2.7\%$ at E = 30 GeV.

Position Resolution

While electrons will be accurately located with the central tracking package, the shower counters must be used to find γ-ray positions. Coarse information is available from the scintillators:

$$\sigma_\theta \tilde{} 25 \text{ cm}/\sqrt{12} = \pm 7 \text{ cm},$$

$$\sigma_\phi = \pm\lambda/\sqrt{N_{p.e.}} = \pm 70\text{cm}/\sqrt{120E} = \pm 7\text{cm}/\sqrt{E}.$$

where λ is the attenuation length for plexinonpop.

The wire chambers with ~1.6 cm bin size will provide an accurate position measurement. Some preliminary results from the beam tests of the prototype module are shown in Fig. 4.7. No position information on the beam particles was available when these data were taken, so we have compared the positions measured in the first chamber (which was instrumented in this test) with those in the second. The strip resolution was measured to be $\sigma \curvearrowright 2.7$ mm, while the wire resolution, σ = 5mm, is considerably worse.

The matching of wire and strip coordinates will use the close correlation of pulse heights in the two views. The test results in Fig. 4.8 show that the wire and strip pulse heights for 40 GeV electrons track one another to within ±4%. This may deteriorate somewhat in a large system, so we have assumed ±8% in Table 4.1. A coarse energy measurement is also available with this chamber. The average pulse height scales linearly with energy in the range measured (10-40 GeV). A pulse height spectrum for the strip chamber with 40 GeV electrons is shown in Fig. 4.9. The rms width of this distribution is 21%.

An example of the use of the strip chambers is π° detection. The minimum opening angle for $\pi^0 \to \gamma\gamma$ decay is

$$\theta_{min} = 2m_\pi/E_\pi$$

and the minimum separation, S_{min}, between the γ-rays at the location of the strip chamber at $6X_o$ is

$$S_{min} \sim 50cm/E_T$$

For E_T up to 10 GeV, the minimum separation is then greater than 5cm, and two separate showers should be detectable. In this region, detection of single γ-rays can therefore be attempted. This same separation allows η° identification up to $E_T \simeq 40$ GeV.

Hadron Rejection

The shower counter is a powerful identifier of electrons. Hadron rejection will be achieved by cuts on various pieces of information:

1. Energy deposited in the shower counter compared to that measured by the magnetic curvature, $E/p \simeq 1$.

2. Early development of the shower, i.e. large signals in the wire chambers.

3. Relatively well collimated showers in the wire chambers.

4. Little energy remaining in the shower to penetrate the hadron calorimeter.

Using E/p and the pulse height in a proportional chamber, Singer (CDF-25) obtained the results shown in Fig. 4.10 for test data with momentum spread $\Delta P/p \sim 1\%$; even without cuts 3 and 4 he obtained rejections of a few thousand for 30 GeV pions. In CDF this will be degraded by $\pi^\pm$ interactions in the solenoid coil and by the finite momentum resolution in the solenoid. A very preliminary analysis of the data from the full-scale prototype with a simulated coil in front of the shower counter finds a rejection of 10^3 at 30 GeV.

Calibration

The calibration of the 960 phototubes of the scintillator cells to the desired (1 or 2)% systematic level will require considerable effort.

Short term drifts of electronics and phototubes will be tracked with a light-flasher system under computer control. A light source will supply several modules with light transmitted to each lightpipe of both electromagnetic and hadron calorimeters by fiber optics. Such a light-flasher system is being installed on the prototype module. The same light source will also be viewed by "standard" phototubes to allow an absolute cross-calibration against a radioactive source. Remote-controlled neutral density filters will be used to monitor the linearity of the system.

Absolute calibration will take place in a test beam. This calibration is direct and simple because showers are totally contained in a single cell. With two phototubes per cell, crosschecks are available at all times.

Long term changes (in the scintillator light output for instance) are harder to monitor. A uniform degradation in all modules is probably best discovered and corrected for by means of renewed absolute calibration in a test beam. Other changes may well be discovered and corrected for during data taking, since many cross checks are available. Examples of such checks are:

1. Uniformity of pulse height spectra in ϕ and η.

2. Pulse heights from cosmic rays and mimimum ionizing particles. This requires a large dynamic range.

3. Use of reconstructed events to compare E and p for electrons from γ-ray conversion.

4. Reconstruction of π° and η° mass peaks.

Experience with other large systems of this type (ref. 4.6) shows that systematics can be controlled to the $\pm$(1-2)% level.

Table 4.1

Parameters of the Central Shower Counters

Modules	
Number required (N_ϕ x N_z = 24 x 2)	48
Length	2.5 m
Width	0.45 to 0.56 m
Depth	0.42 m
Weight/module	2.0 metric tons
Scintillator Cells	
Total number (10/module)	480
Length ($\Delta\phi$ = 15°)	45 to 56 cm
Width ($\Delta\theta \simeq 6°$; $\Delta y \simeq 0.11$ units of rapidity)	23 to 28 cm
Total depth (at normal incidence)	0.42 m $20X_o$ $1.1^o\Lambda_{abs}$
Layers	
Number	33
Lead/layer	1/8 inch
Scintillator/layer	1/4 inch
Radiation lengths/layer	$0.6X_o$
Scintillator type	plexinonpop (11% naphthalene)
total in 48 modules	1750 m^2 = 13 metric tons
Wave shifter readout	BBQ doped UVA acrylic
Number of 2-inch phototubes (2/cell)	960
Wire Chambers	
Number/module	2 (1 instrumented)
Depth (including coil) of chambers at normal incidence	$6.2X_o$ (and $2.6X_o$)
Area of each chamber (wires cut at center and read out each end)	0.5 x 2.5 m^2 physical 0.5 x 1.2 m^2 logical

Table 4.1 continued

Wire spacing (ganged in pairs)	0.8 cm
Strip spacing (wider at 35^{o} end)	1.6 to 1.9 cm
Gap height	0.8 cm
Total number of channels in wire chambers	8976
Angular Coverage	
ϕ	0 to 360^{o}
θ	36^{o} to 144^{o}
η (pseudorapidity)	-1.1 to 1.1
Scintillator	
Number of photoelectrons	120/GeV
σ_E/E	$\pm 15\%\sqrt{E}$
Limit at very high energy	$\pm$(1 or 2)%
σ_y(ϕ direction)	± 7 cm/$\sqrt{E}$
σ_z(beam direction)	± 7 cm
Strip Chambers	
σ/E (at $6X_o$) 5 GeV	$\pm 42\%$
40 GeV	$\pm 22\%$
σ_y (wires measuring ϕ)	± 5 mm
σ_z (strips measuring θ)	± 3 mm
Minimum separation for 2γ identification	~5 cm
Correlation of strip/wire pulse heights	$\pm 8\%$
Hybrid System	
Hadron rejection at 30 GeV	$\gtrsim 10^3$

4.2 END PLUG ELECTROMAGNETIC SHOWER COUNTERS

General Description

The two end-plug electromagnetic shower counters cover the regions between 10° and approximately 37° with respect to the beam axis. Their location is shown in Fig. 4.2. They are inside the magnetic field volume of the 3 meter diameter superconducting solenoid. Each plug forms a cylindrical disk, about 50 cm thick with a 3 m diameter, and with a 10° conical hole through the middle. The plugs provide full depth coverage (21 radiation lengths) between 10° and 30° and decreasing thickness up to θ = 37°.

The segmentation is given by $\Delta\phi$ = 5°, $\Delta\eta$ = 0.1, and the energy loss sampling is done with proportional wire chambers sandwiched between the 4 mm thick lead plates. The tower geometry is defined by the pattern of "pads" cut in the layers of printed circuit board which act as cathodes for the wire chambers. The shower energy is measured by adding in depth the signals induced on these cathode pads.

At the smallest angles, for 10° < θ < 21°, these pads are quite small, ranging from about 3.4 cm x 4.0 cm to about 6 cm x 7 cm. The core of a high energy electromagnetic shower is slightly smaller than this size, so that this fine segmentation is useful. The shower tails will spread into several neighbor cells, making possible an excellent position determination for the showers by weighting the pad positions with the energy. The expected resolution is $\sigma_x \curvearrowdown \sigma_y \curvearrowdown$ 3 mm for isolated showers. Consequently, no finer (strip) segmentation is needed in this region.

At the larger angles, 21° < θ < 37° , where the pad size is typically $\curvearrowdown$ 10 cm x 10 cm, a better position measurement via cathode strips is needed. The arrangement of θ and ϕ measuring strips is shown pictorially in Fig. 4.11.

The number of readout channels is summarized in Table 4.2.

Longitudinal Segmentation

There will be two longitudinal readouts of the pads, the first integrating over the front 4 radiation lengths (5 chambers), the second over the remaining 17 radiation lengths. The total depth of 21 radiation lengths is set by a requirement of 98 percent containment for 50 GeV/c p_T electrons. The sum signal from the two sections measures the total electromagnetic energy in a tower, while the requirement of a large pulse height in the first section, i.e. early shower development, improves the charged pion rejection.

A chamber with θ-strips on one cathode and ϕ strips on the other is located at a depth of 6 radiation lengths. According to beam test results with the central electromagnetic shower counter, the pulse height correlation between the signals on such orthogonal strips is within ±4 percent. This very good correlation is useful in resolving ambiguities when there are multiple hits in the chamber.

Construction Method

The chambers are built from graphite-loaded plastic tubes. The cathode pads which define the towers are on G-10 sheets glued to the outside of the tubes. Positive pulses are induced on the pads through the resistive walls.

This construction gives good tolerances on the gap thickness, provides easy solder connections to the pads, and is very rigid.

The base plastic substrates so far tested are ACS (polymer substrate blend of acryl nitril-chlorinated polyethyrene -styrene) and high impact polystyrene. Very fine graphite grains ($\sim$ 30 micron) are mixed in the above substrate to provide conductivity. So far, a gap width tolerance of 250 μm has been achieved for the multitube sheet. We believe that about 100μ tolerance can be achieved in the near future. At about 100 kΩ/square, where we plan to operate, quoted nonuniformities of the resistivity do not affect the performance.

The cross sectional view of the chamber structure for the final calorimeter is shown in Fig. 4.12. The pads/strips are read out from the back of the G-10 sheets via plated-through holes. The wires are supported by molded plastic plugs glued on both ends of each tube.

The shape of the plastic plug is shown in Fig. 4.13. It has a shallow groove in the middle to determine the wire position precisely. 50 μm gold plated tungsten wires are placed on the groove and wound once around a copper tube 1.5 mm in diameter. After applying an appropriate wire tension, the wires are soldered onto the copper tubing. High voltage is fed to the wire through a blocking resistor directly soldered to the wire supporting copper tubing. With this scheme, the deadspace is less than 1.5 cm including the space for a gas manifold. Each individual plane is made gas tight and will be checked prior to the installation.

In the front view, the chamber is trimmed into a half moon shape as shown in Fig. 4.14. The maximum tube length is 110 cm.

While constructing a prototype using this technique, we have observed that the constructed assembly of plastic tubes and 1 mm thick G-10 sheets has the required rigidity and flatness.

The arrangement of pads and strips is shown in Figs. 4.15 - 4.17.

Expected Performance

In order to measure the performance we built and tested a prototype module. The resistive plastic tube chambers were made close to the final specification described above, except that in the test module the plastic tubes were individually extruded and then glued together between the two G-10 boards. The resistivity is lower by a factor of 5 than the optimum 100 kΩ/square, and the tube walls are thicker, 1.6mm, causing reduced sampling efficiency. The cathode pads are typically 3 x 6 cm^2 and the radial and azimuthal strips give a segmentation 5 times finer than the pads.

The longitudinal shower development is shown in Fig. 4.18, a typical pulse height distribution for 30 GeV electrons in Fig. 4.19, and the energy resolution in Fig. 4.20.

The energy resolution is $\sigma/E = 29\%/\sqrt{E}$ with 4 mm lead plates, and the position resolution measured with the pads is $\sigma_x = \sigma_y \lesssim$ 3 mm at 10 GeV and 1.6mm at 40 GeV. The position resolution from the single layer of strip chamber was σ = 4.5mm and 3.0mm respectively at 10 and 40 GeV. These results are all preliminary.

Mechanical Structure and Assembly Procedure

The whole weight of the system of 7 metric tons for one end cap is supported by the 2 in. thick re-entrant steel plate which is the first plate of the end plug hadron calorimeter. The exploded view in Fig. 4.21 illustrates the mechanical structure. There are 24-one inch thick stainless steel tie rods around the outer circumference, and the same number of 1/2 in. steel tie rods around the inner 10° hole of the plate. The G-10 sheets for the pads and strips are extended outwards and inwards with holes to fit these tie rods. The lead sheets have such holes too, and the chamber and the lead sheets will be stacked one on top of the other. The lead sheets will be 6.5 percent Calcium loaded lead alloy (SJM610) which has a factor of 2 larger ultimate tensile strength and 4 times smaller elongation than 6 percent Antimony alloy. A 1/2 in. thick stainless steel cover plate reinforced with 3/4 in.high radial and circular ribs is placed upon the top and is tightened by screws on the rods. After all the high voltage and signal cables and the gas tubings are connected, the side cylindrical wall made of 1/2 in. thick stainless steel plate will be bolted onto the cover plate and the bottom steel plate from the side.

Since the intrinsic energy resolution is expected to be about 2% or less at 200 GeV (E_T = 50 GeV at 15°), it is desirable to suppress systematic errors below this level. Therefore it is of prime importance to maintain good mechanical tolerances of the chambers.

Chamber Plane Test Prior to the Installation

Each chamber plane will be tested for gain uniformity over the entire surface prior to the installation. The chamber is mounted on an automatic, computer controlled scanning table which moves a Cd^{109} source over the surface of the chamber plane and the pulse height distribution at every spot is accumulated for the pads/strips and the wires. At least three high voltage points are taken to calibrate the chamber and to assure the expected dynamic range. Those chambers which exceed a tolerance on the gain of about ±4% will be rejected at this stage.

Absolute Calibration of the Assembled Calorimeter

After assembly of the calorimeter, it will be transported to the test beam for absolute calibration. The calibration will be done at the center of each tower by aligning the tower axis to the beam. Using an automatically movable mounting table, it is not unreasonable to assume that all 1728 towers in both plugs could be calibrated. A small fraction of these towers will be examined in more detail by varying the energy and the high voltage.

The simultaneous accumulation of the minimum ionizing particle signal gives an additional calibration point although the signal is small (about 350 MeV equivalent) and the minimum ionizing particle signal only reflects the overall gain of all the penetrated chambers while the electromagnetic shower is mainly measured by the chambers around the shower maximum.

Monitoring in the Course of the Experiment

Two Cd^{109} sources will be imbedded in each of five chamber planes, one in the shortest tube which is closest to the gas inlet and the other in the longest tube which is close to the outlet. Thus the overall performance of the chamber will be regularly monitored and any deterioration of the gas or nonuniform circulation will be detected. Cd^{109} sources are also used on two monitoring proportional tubes connected in series to the main gas

tubing, one at the inlet to the calorimeter and the other at the outlet from the calorimeter on each of the plugs.

Pressure, composition, and temperature will also be monitored carefully.

One possible solution is to control the gas pressure and the composition simultaneously by employing an accurate gas mixing system fed with pure Argon and ethane gas. Once the nominal absolute pressure is reached the container will be isolated. In the recent M-5 beam test on the prototype calorimeter with conductive plastic tubes, no shift of the 40 GeV electron signal was observed within an accuracy of ±0.3% within an 8- hour shift. Throughout the run the container was kept closed after the initial gas filling at 1 PSI above atmospheric pressure and the beam rate of up to 2×10^4 particles/burst was taken at the same spot on the calorimeter. Such a closed gas system is also the practice recommended by the MAC collaboration.

Temperature sensors will be distributed around the outer and the inner circumferences of the calorimeter.

Electronics Monitoring

The chamber high voltage will be monitored. The individual pad response is tested by pulsing the anode wires through the common high voltage bus lines by a calibrated pulser. This gives a relative check of the wire/pad response and will be useful in trouble shooting. The individual amplifier channel is calibrated by a pulser connected to each amplifier input.

Checks

In the angular region above 20° in θ, a consistency check is possible on a statistical basis by comparing the measured energy deposit in the calorimeter with the momentum measured in the tracking chamber. The regular accumulation of spectra provides a relative gain monitoring among the 72 towers of the same polar angle.

Minimum ionizing particle signals accumulated with triggers from other parts of the detector could be used as an absolute calibration source. In order to distinguish the signal better from the noise, the high voltage can be raised in the calibration runs.

Table 4.2

Parameters of the End Plug Electromagnetic Shower Counters

Modules	
Number of modules	2
Angular coverage for one module	$10° \leq \theta \leq 37°$
Instrumented coverage	$1.1 \leq \eta \leq 2.3$ or $11° \leq \theta \leq 37°$
Radius of cylindrical plug	140 cm
Depth along axis	53 cm
Weight per module	7 metric tons
Lead Chamber Sandwich	
Lead thickness	4 mm
Total chamber thickness	11.5 mm
Number of layers	30
Total thickness	21 X_o
Pad Readout	
Pad Size	$\Delta\eta = 0.1$, $\Delta\phi = 5°$
Physical pad size ranges from	3.4 x 4 cm^2 to 11 x 16 cm^2
Number of pads per end plug	72 (N_ϕ) x 12 (N_η) = 864
Number of longitudinal segments	2
Pad Readout channels per end plug	1728
η, ϕ Strip Chamber	
Number per module	1
Location (depth)	6 X_o
Angular coverage	$1.1 < \eta < 1.7$ or $21° < \theta < 37°$
η-strip size $\Delta\eta = 0.02$, covering $\Delta\phi = 30°$	
ϕ-strip size $\Delta\phi = 1°$, covering $1.1 < \eta < 1.7$	
Number of η strips	12 x 30 = 360
Number of ϕ strips	360
Number of strips per end plug	720
Total number of signals for 2 end plugs	4896
Expected energy resolution	$\sigma/E \backsim 29\%/\sqrt{E}$
Expected position resolution	$\sigma_\eta \backsim \sigma_\phi \backsim 3$ mm (at 40 GeV)
Expected hadron rejection	$\gtrsim 10^2$

4.3 FORWARD-BACKWARD ELECTROMAGNETIC SHOWER COUNTERS

These shower counters, placed about 8.5 m upstream-downstream from the center of the detector, cover the angular range $2° < \theta < 10°$ and $170° < \theta < 178°$. The location of the backward shower counter is shown in Fig. 4.22. They are similar in size to the end plug shower counters. Gas proportional chambers are used to measure shower energy and position, using cathode pad readout. The segmentation of the readout, shown in Figure 4.23, corresponds to $\Delta y = 0.1$, $\Delta\phi = 5°$. The calorimeter contains 23 radiation lengths of lead, distributed in 40 1/8" plates. In the first 4 radiation lengths, fine grain position measurement is provided by a crossed pattern of strips, in the y and ϕ directions, covering the region $5°<\theta<10°$. The localization corresponds to $\Delta y = .02$, $\Delta\phi = 1°$. A summary of the parameters of the calorimeter is given in Table 4.3.

Construction Method

The calorimeter is constructed of 4 modules of ten layers each, as shown in Figure 4.24. The lead plates are laminated to G-10 panels for rigidity. Cathode readout is accomplished using etched sheets of copper-clad mylar. The chamber planes and lead sheet laminates are assembled onto a common jig plate, and sealed as a single gas volume.

Pending prototype tests later this year, we plan to run the chambers in limited avalanche mode. The large current pulse in this mode minimizes problems from distributed capacitance, and eliminates the need for local preamplifiers.

Expected Perfomance

The performance is expected to be close to that of the endplug shower counters since the construction is similar (See Section 4.2).

Table 4.3

Parameters of the Forward-Backward Electromagnetic Shower Counters

For One Side

Angular Coverage	$2.3 \leq \eta \leq 4.0$, $2° \leq \theta \leq 11°$
Physical Size	3.5 x 3.5 x 1.0 m
Total weight	20 tons
Lead-Chamber Sandwich	
Lead thickness	1/8 in.
Total chamber thickness	15 mm
Number of layers	40
Total thickness	23 X_o
Pad Readout	
Pad size	$\Delta\eta = 0.1$, $\Delta\phi = 5°$
Physical pad size ranges from	$\sim$ 3 x 3 cm to $\sim$ 13 x 15 cm
Number of pads	72 (N_ϕ) x 17 (N_η) = 1224
Number of longitudinal segments	2
Pad readout channels	2448
η, ϕ Strip Chamber	
Location (depth)	4 X_o
Coverage	$2.3 < \eta < 3.1$, $5° < \theta < 11°$
η strip size $\Delta\eta = 0.02$, covering $\Delta\phi = 30°$	
ϕ strip size = 1°, covering $2.3 < \eta < 3.1$	
Number of η strips	40 x 12 = 480
Number of ϕ strips	360
Strip readout channels	840
Total number of signals for 2 sides	6576
Expected energy resolution	$\sigma/E \sim 25 - 30\%/\sqrt{E}$
Expected position resolution	$\sigma_\eta \sim \sigma_\phi \sim 3$ mm
Expected hadron rejection	$\gtrsim 10^2$

4.4 CENTRAL HADRON CALORIMETRY

General Description

The central hadron calorimeter is a barrel shaped array of 48 modules. Its location is shown in Fig. 4.2. Each module (see Fig. 4.25) consists of 34 1"-thick steel plates with 5/8" gaps containing 1 cm thick scintillator. The modules are subdivided into 8 towers corresponding to fixed increments in Z at any radius. They match the barrel shower counter segmentation. The axial dimension is 98" and the average width (in ϕ) is approximately 27". The total weight of a module is approximately 13 tons. The modules are arranged into two adjacent barrels of calorimetry, covering approximately 45° to 135° in polar angle (θ). The complete azimuthal range in each barrel is covered by 24 modules.

The light collection scheme is shown in Fig. 4.26. It involves BBQ strips (5mm x 10mm, 150 mg/liter) placed along the constant θ sides of the rectangular scintillators, as shown in Fig. 4.27. The BBQ strips join smoothly onto (5mm x 10mm) lucite (UVA plexi 232) light pipes (fingers) that terminate at the phototube. Two phototubes collect the light at opposite ends of each tower in ϕ. The comparison of the signals gives a measure of the ϕ position of the shower. The fingers from alternate layers alternate in θ position to average out any θ dependence. In a given tower, the light output of the 33 scintillator-BBQ- finger combinations decreases with depth (radius) in the calorimeter because the scintillator size grows. We have equalized the total light output of all 33 layers to better than 10% (as measured) by adjusting the length of the 33 plexiglass fingers correspondingly.

The energy resolution is determined by the sampling thickness, the light collection efficiency, and shower containment. The one inch sampling is chosen to give the minimum practical sampling thickness and consequently the best energy resolution for iron calorimeters. For shower confinement one has approximately 95 cm equivalent of iron at 90° in θ if one includes the E.M. calorimeter. This corresponds to approximately 5.6

absorption lengths, and means that on the average 96% of the energy of showers induced by 50 GeV/c pions will be contained. At 45° the sampling thickness increases to 1.4" and the total thickness to nearly 8 absorption lengths. The leakage varies logarithmically with the incident particle energy.

Performance

A full sized hadron module and a matching electromagnetic calorimeter were built and tested in a beam. A pulse height spectrum of 30 GeV π's is shown in Fig. 4.28.

The energy resolution for the hadron calorimeter (σ/E) at 90° is 5.5% + 62%/$\sqrt{E}$ (see Fig. 4.29) as measured in the momentum range from 15 to 50 GeV/c. The measured resolution for electrons is σ/E = 0.5% + 27%/$\sqrt{E}$ in agreement with expectation:

$$\sigma/E = \left((\sigma/E)^2_{\text{sampling}} + (\sigma/E)^2_{\text{photoelectron statistics}} \right)^{1/2}$$
$$= \left((16.9\%\sqrt{t/X_{o\ \text{iron}}})^2 + (1/\sqrt{n_{\text{photoelectron}}})^2 \right)^{1/2}$$
$$= \left((16.9\%\sqrt{2.54/1.76})^2 + (1/\sqrt{30})^2 \right)^{1/2}$$
$$= 27.3\%.$$

The light collection is excellent giving a clean muon signal with ~36 photoelectrons per muon. The cosmic ray muon signal will be valuable in maintaining long term stability of our calibration. The pulse height for electrons is 1.17 times higher than for hadrons of the same energy. Hadrons give ~26 photoelectrons per GeV. The energy response was linear over the full range within our systematics (~2%). For hadrons there is no high energy tail above that of a Gaussian distribution. A small low energy tail, corresponding to 4% average longitudinal leakage, is observed. The energy resolution of the combined electromagnetic and hadron calorimeter is shown in Fig. 4.30. The uniformity of response is shown in Figs. 4.31 and 4.32.

The shower location between the phototubes (ϕ direction) was measured with a standard deviation σ of 5.4 cm for 30 GeV hadrons (see Fig. 4.32). This corresponds to a ϕ resolution of σ ~20 milliradians.

The time resolution for traversing muons has been measured. The standard deviation is σ = 1.2 nsec.

Calibration

The calibration system built to check the hadron calorimeter photomultiplier stability has been described in the section on the central electromagnetic shower counters.

Table 4.4

Parameters of the Central Hadron Calorimeter

Modules	
Number of modules (N_ϕ x N_η = 24 x 2)	48
Length	2.5 m
Width (in ϕ-direction)	0.56 to 0.91 m
Depth (in radial direction)	1.33 m
Weight per module	13 tons
Scintillator Cells	
Total number (8/module)	384
Length ($\Delta\phi$ = 15°)	0.56 to 0.91 m
Width ($\Delta\eta \sim 0.11$)	0.28 to 0.45 m
Total depth (hadron calorimeter alone)	0.86 m Fe $5\ \lambda_{abs}$
Layers	
Number	34
Steel thickness	2.5 cm
Scintillator thickness	1 cm
Scintillator type	UV acrylic with 8% Naphthalene 1% BPBD, and 0.01% POPOP
Total in modules	2600 m² = 31 metric tons
Wave shifters	BBQ doped UVA acrylic
Number of phototubes (2 - inch)	768
Angular coverage	$-1 < \eta < 1$, $40° < \theta < 140°$
Light yield	26 photoelectrons/GeV
σ_y (ϕ-direction)	5.4 cm (30 GeV)
Energy resolution	$\sigma/E \simeq 5.5\% + 62\%/\sqrt{E}$

4.5 THE END WALL HADRON CALORIMETERS

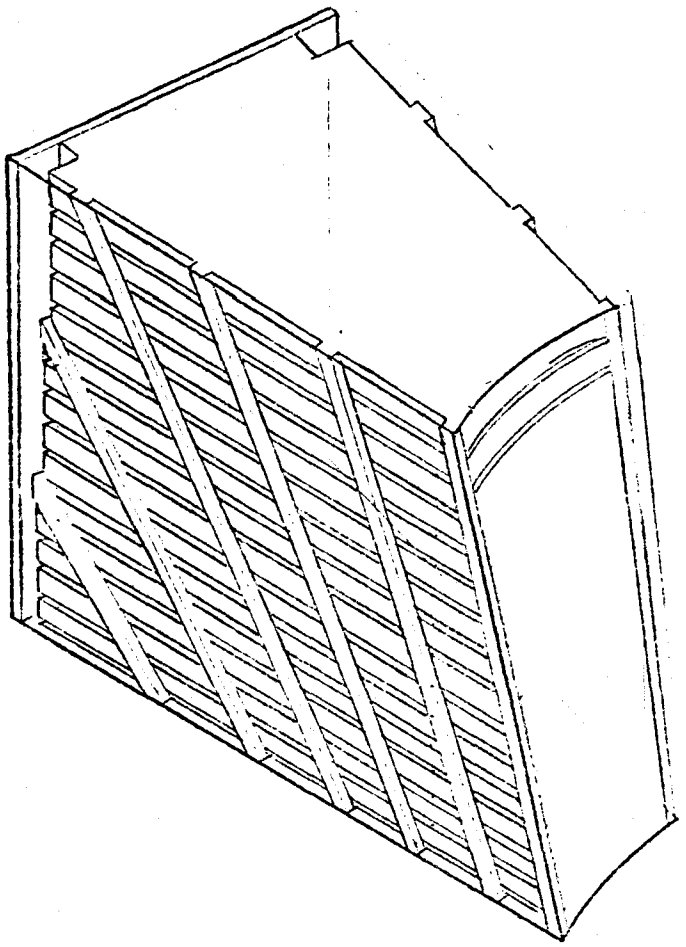

General Description

These calorimeters are mounted between the twelve ribs of the end wall. Their location in the central detector is shown in Fig. 4.2. The angular ranges covered by these modules are $30° < \theta < 50°$ and $130° \lesssim \theta < 150°$. There are 24 modules in each wall, matching the modularity of the central calorimeters. The construction is such that the tower structure smoothly joins and extends the structure of the barrel calorimetry, even in this difficult "corner". This has been achieved with the same system of scintillator-wave shifter-light guide readout that is employed in the central hadron calorimeters. The tower arrangement in the

module is shown in Fig. 4.33, and the light readout in Fig.4.27. The sampling thickness is 2 in. of steel. The reasons for this choice are that the flux return are through these modules, which argues for thicker steel plates than the 1 in. used in the barrel region, that thicker plates give greater compactness, and that the higher energies of secondaries in this angular region allow a coarser segmentation. Further details of the layout can be found in Appendix VI.

Expected Performance

The expected performance of a single module can be judged from the test results of the central calorimeter module prototype since the readout system is similar. Therefore, we expect an energy resolution $\sigma/E \simeq 6\% + 77\%/\sqrt{E}$ (Fig. 4.30) and a position resolution $\sigma \sim 6$cm (30 GeV).

In the experiment, hadrons emitted at angles θ between 40° and 50° pass through part of the central hadron calorimeter before entering the end wall calorimeters (see Fig. 4.2). The minimum amount of iron encountered by hadrons occurs at $\theta = 40°$, and amounts to 30 inches or $\sim$4 interaction lengths. At this angle the coil, cryostat, and electromagnetic shower counter represent an additional 1.5 interaction lengths. There is a possible degradation of performance in this region because of the awkward geometry. Some help may be derived from the fact that we have managed to preserve the tower structure even in this region and that the hadron shower is actually sampled and read out in two longitudinal segments. This provides more information aout the shower development than elsewhere in the hadron calorimeters.

Calibration

The calibration system is the same as that used for the central hadron calorimeters.

Table 4.5

Parameters of the End Wall Hadron Calorimeters

Modules	
Number of modules (N_ϕ x N_η = 24 x 2)	48
Approximate dimensions	0.8 x 1.0 x 1.1 m^3
Weight per module	6 tons
Scintillator Cells	
Total number (6/module)	288
Length ($\Delta\phi$ = 15°)	0.35 to 0.78 m
Width ($\Delta\eta \sim 0.1$)	0.25 to 0.40 m
Total depth (hadron calorimeter only)	0.75 m Fe 4.4 Λ_{abs}
Layers	
Number	15
Steel thickness	5 cm
Scintillator thickness	1 cm
Scintillator type	UV acrylic with 8% Naphthalene, 1% BPBD, and 0.01% POPOP
Total in 48 modules	660 m^2 = 8 tons
Wave shifters	BBQ doped UVA acrylic
Number of phototubes	576
Angular coverage	$0.8 < \eta < 1.3$, $30° < \theta < 50°$
Expected energy resolution	$\sigma/E \simeq 6\% + 77\%/\sqrt{E}$
Light yield	15 photoelectrons/GeV
σ_y (ϕ-direction)	$\sim$ 6 cm (30 GeV)

4.6 END PLUG HADRON CALORIMETER

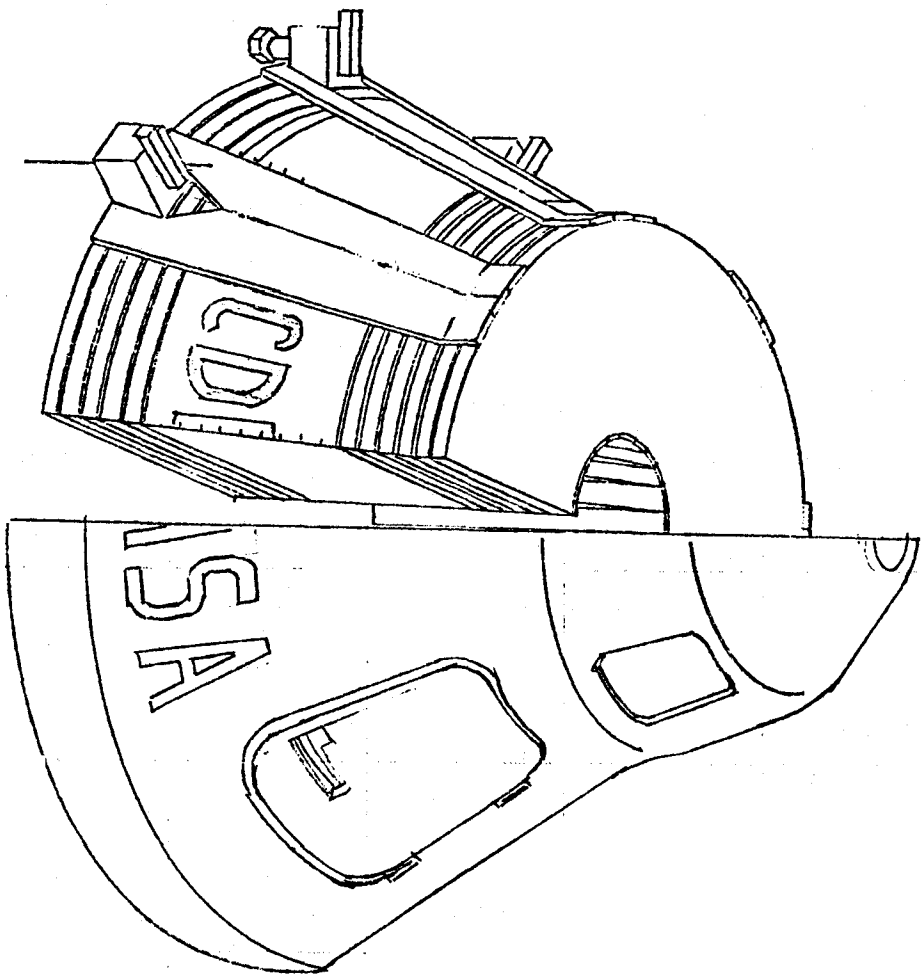

General Description

The end plugs cover the intermediate angular region from 10° to 30° to the beams and the corresponding pseudorapidity range of 1.3 to 2.4. Their location within the central detector is shown in Fig. 4.2. This region is typically populated by hadrons of relatively high energy and high spatial density. The physics is best matched by coverage that is essentially constant in rapidity, but extending this concept to smaller angles requires either spatially small towers or a more distant detector. The economics favor smaller towers closer to the interaction region, up to the

point where overlapping showers negate the advantages of segmentation. We believe that these requirements can best be met by instrumenting the end plug hadron calorimeter with gas-multiplication wire planes using cathode plane readout. The 2 inch steel plates of the end plugs will be instrumented with pad proportional chambers in the 3/4" air gaps between the steel plates. The 2" steel plates of these calorimeters are in the flux return path of the solenoid. The total force on each end plug is approximately 640 tons (!).

Construction Details

A conical end plug, built from 2" steel plates, is sketched in Fig. 4.34. The wire chambers are designed with a high degree of modularity. Each detector plane is divided into 12 (30°) sectors in azimuth. Each sector is an independent chamber with its own gas volume. The principal readout consists of pads etched into standard printed circuit board forming one cathode plane. The pad signals are taken out through plated-through holes and printed lines. The other cathode is formed from aluminum jig plate which provides mechanical stiffness but is not read out. The wires run azimuthally and are all ganged together within a sector by soldering to a copper-clad G-10 strip. The wire plane is read out as a single signal per sector in order to monitor the chamber gains. The 1 cm gas gap is maintained by "I beam" supports parallel to the wires and spaced every 10 cm. The gas enclosure is completed by thin extruded aluminum side walls and aluminum end plates. The end plates provide gas and high voltage penetration. Corresponding pads from each layer are wired together to form towers. This wiring is accomplished with twisted pairs arranged in a flat ribbon cable mass-terminated to connectors which mate with the PC cathode plane. For the application to the small angle hadron calorimeters we favor conventional proportional chambers with cathode pads over the use of plastic tubes as employed in the shower counters at these angles. The conventional chambers may be cheaper, and the problem

of gain variations due to mechanical tolerances on the gap spacing is less important (sampling fluctuations are much larger in the hadronic calorimeter).

The towers have a projective geometry - i.e. they form a truncated pyramid with the intersection region as the apex. This geometry is especially important in a hadron calorimeter since the large fluctuations in the depth of the starting point of the shower would otherwise result in fluctuations in the reconstructed transverse position and the spatial resolution would directly suffer. The finite size of the luminous region causes some smearing of the projective geometry, but is not a limitation. Realizing a projective geometry does require the additional complication of different pad sizes for each layer.

The high degree of modularity in the end cap calorimeter design should result in a number of advantages. A single module is small enough that prototypes can be built and tested quickly so the design can be optimized and then replicated. Each module can be constructed from "off-the-shelf" components and can be handled by one or two people without special jigs. Moreover, the detector construction is decoupled from the heavy steel work and each module can be tested and certified as it is built, rather than waiting until the entire detector is assembled. If problems develop during a run a single module can be disconnected without compromising the detector performance. During a shutdown, the affected module can be easily removed and replaced.

Expected Performance

The following properties are expectations based on scaling published data and on admittedly crude computer simulations of shower development. The proposed device has not yet been tested in a beam.

Energy Resolution

The energy resolution is determined principally by the shower sampling statistics in the 2" steel plates. Substantial data is available on iron-scintillator calorimeters, and one can reliably predict that the sampling statistics yield an RMS width, $\sigma/E \simeq (.82 \pm .05)\ E(\text{GeV})^{-1/2}$. This resolution will be degraded by the choice of wire chambers as the active medium. Gaseous devices suffer additional fluctuations in the ionization (Landau) losses, track length variations for oblique tracks, and gas gain variations due to mechanical tolerances. We believe that these effects will result in a total RMS width, $\sigma/E \simeq 1.05\ E\ (\text{GeV})^{-1/2}$.

There is some evidence that the resolution can be improved by operating the gas gain in a highly saturated mode so that one is less sensitive to ionization fluctuations. Preliminary tests on a "limited streamer" mode are encouraging and will be pursued. This mode has the additional advantages of permitting the use of thick, strong signal wires and providing large signals that require no pre-amplification.

Spatial Resolution

The resolution for locating a single, isolated shower is shown in Fig. 4.35. Reconstruction of jets will be more complicated and algorithm-dependent, but the precision on the measurement of the first and second moments of the jet energy distribution will be limited by the energy resolution rather than the angular resolution. The extremely good spatial resolution that results from small towers and the "hot core" shape of individual showers will be most useful in developing topological signatures for dense, multi-jet events.

Table 4.6

Parameters of the End Plug Hadron Calorimeters

Modules	
Number	2
Shape	Truncated cones with cylindrical extension
Total height	1.39 m
Maximum diameter	4.25 m
Minimum diameter	2.8 m
Weight per module	75 tons
Layers	
Number	20
Steel thickness	5 cm
Air gap between steel plates	1.9 cm (3/4 in.)
Total thickness (hadron calorimeter only)	1 m Fe ($\sim 6\ \lambda_{abs}$)
Chamber thickness	1.3 cm (1/2 in.)
Pad Readout	
Angular coverage	$1.3 < \eta < 2.4$, $10° < \theta < 30°$
Tower size	$\Delta\eta = 0.1$, $\Delta\phi = 5°$
Physical pad size	from 4.4 x 5.2 cm² to 11 x 15 cm²
Number of pads per end plug	(N_ϕ x N_η = 72 x 11) 792
Total number of pad channels (2 end plugs)	1584
Total number of anode readout channels	480
Expected energy resolution	$\sigma/E \sim 105\%/\sqrt{E}$
Expected position resolution	$\sigma_x = \sigma_y \simeq$ 1-1.5 cm

4.7 FORWARD-BACKWARD HADRON CALORIMETER

General Description

The location of the backward hadron calorimeter, about 10 m upstream from the interaction point, is shown in Fig. 4.22. The forward calorimeter is placed symmetrically on the other side of the central detector. These calorimeters cover the angular ranges $2° < \theta < 10°$ and $170° < \theta < 178°$. The hadron energy in this region of phase space is typically large. Proportional chambers with cathode pad readout represent a good match to the detector requirements in this region. The pad segmentation is $\Delta\eta = 0.1$, $\Delta\phi = 5°$. A summary of the parameters of these calorimeters is given in Table 4.7.

Construction Method

The calorimeters consist of alternating layers of 2 inch steel plates and pad chambers, 28 layers total, corresponding to 8 absorption lengths. The calorimeters are split into two parts, one on each side of the beam pipes. The pad chambers are constructed from extruded resistive plastic panels, containing (1.5x2) cm^2 rectangular tubes. The chambers may be operated in the limited streamer mode. The plastic panels have a surface resistance between 10 and 100kΩ/square, which provides the DC cathode for chamber operation. A foil of copper-clad Mylar is laminated to one face of each chamber. The copper layer will be etched to form a pattern of pads, as shown in Figure 4.36. Each pad will be accessed from the chamber edge by printed readout lines, see Figures 4.36, 4.37. The pad size and position in successive layers will be arranged to form towers which aim to the event vertex.

Expected Performance

For practical purposes, these calorimeters should have the same properties as the end plug hadron calorimeters (see Section 4.6).

Table 4.7

Parameters of the Forward-Backward Hadron Calorimeters

One Side

Modules	
Number	2
Approximate dimensions	4.8 x 4.8 x 2.1 m^3
Total weight, one side	250 tons
Layers	
Number	28
Steel thickness	5 cm
Total steel thickness	140 cm = 8.3 Λ_{abs}
Air gap between steel plates	2.5 cm
Total thickness	2.1 m
Chamber thickness	2.5 cm
Pad Readout	
Angular coverage	$2.3 < \eta < 4.0$, $2° < \theta < 11°$
Tower size	$\Delta\eta = 0.1$, $\Delta\phi = 5°$
Physical pad size	from $\sim$ 3 x 3 cm^2 to $\sim$ 14 x 16 cm^2
Number of pads per side	(N_ϕ x N_η = 72 x 17) 1224
Total number of pad channels (2 sides)	2448
Expected energy resolution σ/E	$\simeq 105\%/\sqrt{E}$
Expected position resolution	$\sigma_x = \sigma_y \simeq$ 1-1.5 cm

References

4.1 R. L. Anderson et al., IEEE Trans. Nucl. Sci. NS-25, 340 (1978).

4.2 S. L. Stone et al. Nucl. Instr. Meth. 151, 387 (1978).

4.3 R.L. Garwin, Rev. Sci. Instr. 31, 1010 (1960); G. Keil, J. App. Phy. 40, 3544 (1969); Nucl. Instr. and Meth. 83, 145 (1970) and 87, 111 (1979).

4.4 W. Selove, CERN Report NP72-22 (1972); W. Selove et al., Nucl. Instr. and Meth. 161, 233 (1979).

4.5 W. B. Atwood et al., SLAC-TN-76-7 (1976); B. Barish et al., IEEE Trans. on Nucl. Sc. NS-25, 532 (1978).

4.6 J. A. Appel et al., Nucl. Instr. and Meth. 127, 495 (1975).

FIGURE CAPTIONS

Fig. 4.1 Calorimetry segmentation in η-ϕ space showing the coverage of the subsystems. A) The dashed lines indicate the area inside which on the average 80% of the energy of p_T = 50 GeV/c jets is found for jets at θ = 15°, 30°, and 60°. Field-Feynman jets with an internal transverse momentum of 0.7 GeV/c were used. The physical shower spread in the calorimeter materials widens the area, as indicated by the full lines. B) Energy deposition in GeV in towers for a random 50 GeV/c jet.

Fig. 4.2 Arrangement of calorimeters in the detector.

Fig. 4.3 Perspective view of one central calorimeter module. The shower counter (a lead-scintillator sandwich) and its associated sheets of wave shifters, light guides and photomultipliers are shown.

Fig. 4.4 Cross sections of the central electromagnetic shower counters.

Fig. 4.5 Energy resolution σ/E for the prototype shower counter plotted versus $E^{-1/2}$. A better fit can be obtained if the form $A + BE^{-1/2}$ is used.

Fig. 4.6 Longitudinal energy leakage of showers initiated by electrons. Also shown is the integral distribution of events for energy penetration beyond 18.8 X_o from 30 GeV incident energy.

Fig. 4.7 Position information from the two strip chamber layers in the central electromagnetic shower counters.

Fig. 4.8 Ratio of strip to wire pulse heights (renormalized) in strip chamber at 6 X_o for 40 GeV electrons.

Fig. 4.9 Pulse height distribution in strip chamber at 6 X_o for 40 GeV electrons.

Fig. 4.10 Probability of pions being misidentified as electrons, for 5% and 10% losses of electrons, as a function of the depth at which the cut on early shower development is made, for 10 and 30 GeV particles. The beam momentum is accurately known, $\frac{\Delta p}{p} \sim 1\%$. The detector samples at 6 X_o (when $\theta = 90°$).

Fig. 4.11 Illustration of the tower geometry in the end cap shower counters. θ and ϕ strips are also shown.

Fig. 4.12 Cross section of one pad chamber built with conductive plastic tubes.

Fig. 4.13 Detail showing a molded plastic plug and the wire positioning mechanism.

Fig. 4.14 Shape of a multitube plastic sheet when trimmed to fit into an end plug.

Fig. 4.15 Pad arrangement in the end plug shower counters.

Fig. 4.16 ϕ-measuring strips in the end plug shower counters. Only the strips in the region $1.14 < \eta < 1.7$ are read out.

Fig. 4.17 θ-measuring strips in the end plug shower counters. Only the strips in the region $1.14 < \eta < 1.7$ are read out.

Fig. 4.18 Longitudinal shower development for pions and electrons in the end plug shower counter prototype, as measured by the anode signals.

Fig. 4.19 Pulse height spectrum for 30 GeV electrons in the end plug shower counter prototype with 4 mm lead thickness.

Fig. 4.20 Energy resolution of the end plug shower counters versus electron energy.

Fig. 4.21 Mechanical structure of the end plug shower counters.

Fig. 4.22 The backward ($\bar{p}$-direction) spectrometer.

Fig. 4.23 Segmentation of the forward (or backward) spectrometer. An attentive reader will notice that the number of channels seems too large, but it should be understood that this drawing was made in Texas.

Fig. 4.24 A module of the forward (backward) shower counter.

Fig. 4.25 Iron skeleton of a calorimeter module.

Fig. 4.26 Hadron calorimeter light pipe arrangement.

Fig. 4.27 Two scintillators in a tower are shown with their BBQ readout.

Fig. 4.28 The M5 30 GeV negative particle beam spectrum as measured by the hadron calorimeter only.

Fig. 4.29 The measured energy resolution of the central hadron calorimeter both for hadrons and electrons between 15 and 46 GeV. The measured resolution for electrons is $\sigma/E \simeq 0.5\% + 27\%/\sqrt{E}$ in agreement with expectation. The hadron energy resolution is well approximated by $\sigma/E = 5.5\% + 62\%/\sqrt{E}$.

Fig. 4.30 (a) points (.) represent, at different hadron energies, the energy resolution of the hadron calorimeter alone. Crosses (x) represent the measured energy resolution of the calorimeter when only each second iron layer is instrumented with scintillator (2" iron sampling). This resolution is approximately $6\% + 77\%/\sqrt{E}$. Plusses (+) indicate the resolution of the hadron and elecromagnetic calorimeters together with 1" iron sampling.
(b) Plusses (+) show the resolution of the combined hadron and electromagnetic calorimeter, when the requirement is made that hadrons interact in the electromagnetic calorimeter. Circles (o) represent the energy resolution measured by the CDHS collaboration at CERN with a similar calorimeter (A. Abramowitz et al., NIM 180 (1981) pp. 429). In that experiment 7 modules are summed longitudinally, each module consisting of five 60 x 60 cm^2 sheets of 1" thick iron, each followed by a .5 cm scintillator (the five scintillators are read directly by a single photomultiplier). Their iron thickness corresponds to that of our module, and the requirement is made that hadron showers start in the first of the seven modules.

Fig. 4.31 (a) Pulse height of the hadron calorimeter only as measured moving the 30 GeV π^- beam from one tower to the adjacent one. 0" is the boundary between the two towers, which end respectively at -11.5" and 11.5".

(b) Energy resolution as a function of the same beam displacements. Tower two is scintillator instrumented only at each second iron layer (2" sampling) while Tower 1 corresponds to 1" iron sampling thickness.

Fig. 4.32 (b) Pulse height in a single tower for different impact positions between the two photomultipliers. The R photomultiplier is at 10". 1/2 (L+R) represents the average pulse height of the photomultipliers on both sides. When the light is attenuated in the BBQ-scintillator system as $R(x) = I\ e^{-(x-D)/\lambda}$ and $L(x) = I\ e^{-(x+D)/\lambda}$ (where 2D is the tower length in the ϕ direction), then $\sqrt{LR} = I$ is an x (or ϕ) independent measurement of the total pulse height. On the other hand (Fig.a) 1/2 $\ell n\ R/L$ measures the x position in fractions of the attenuation length λ of the light in the scintillator-BBQ system. λ is determined to be 108 cm in one of our towers.

Fig. 4.33 An end wall hadron calorimeter module. The definition of towers and the layout of light guides and phototubes is shown.

Fig. 4.34 A conical end plug.

Fig. 4.35 Position resolution for hadronic showers as a function of the calorimeter cell size. Both data and Monte Carlo simulation results are shown.

Fig. 4.36 Detail of hadron calorimeter chamber.

Fig. 4.37 Assembly drawing of single chamber panel.

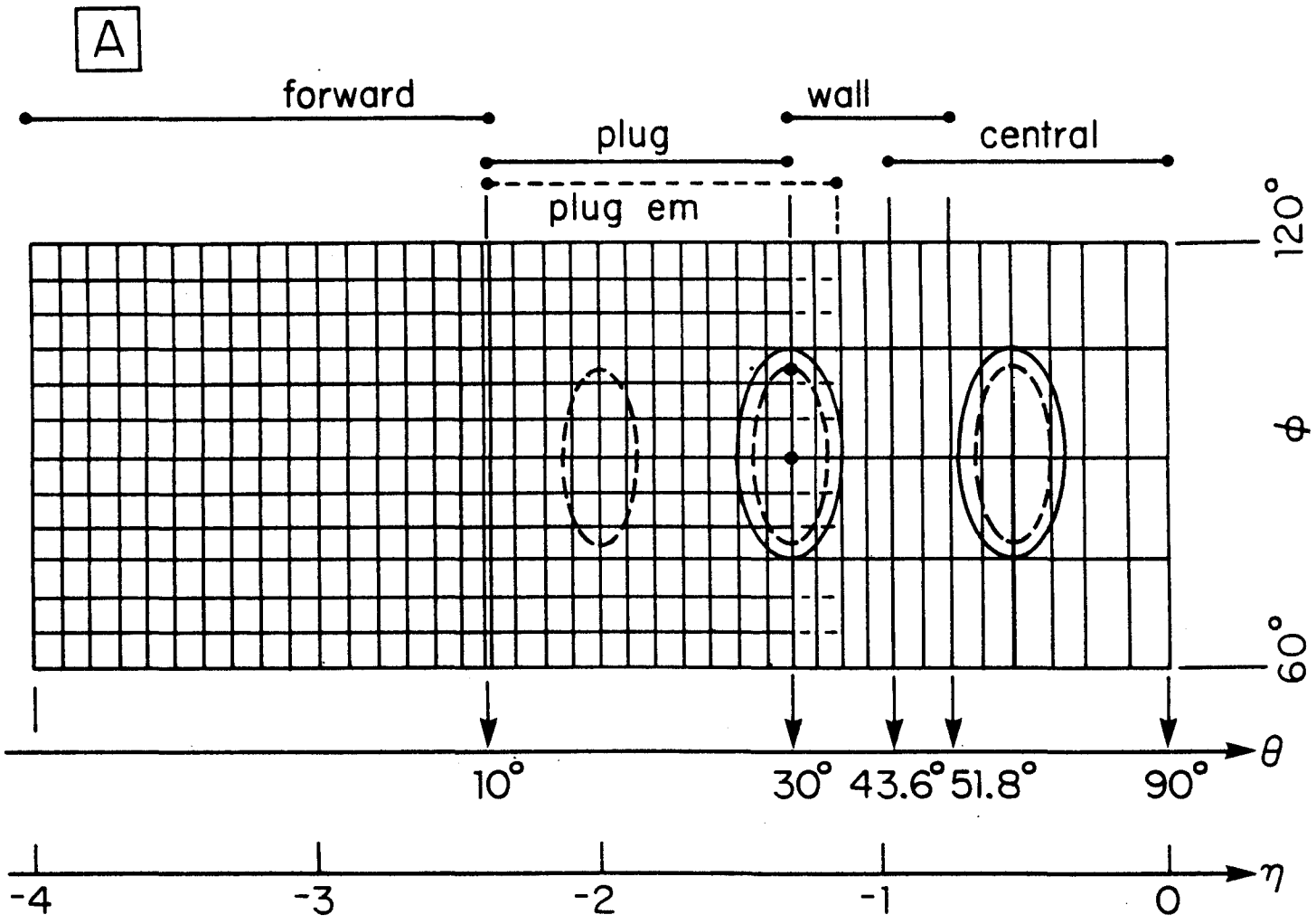
A
forward
plug
wall
central
plug em
120°
60°
φ
θ
10°
30°
43.6°
51.8°
90°
η
-4
-3
-2
-1
0

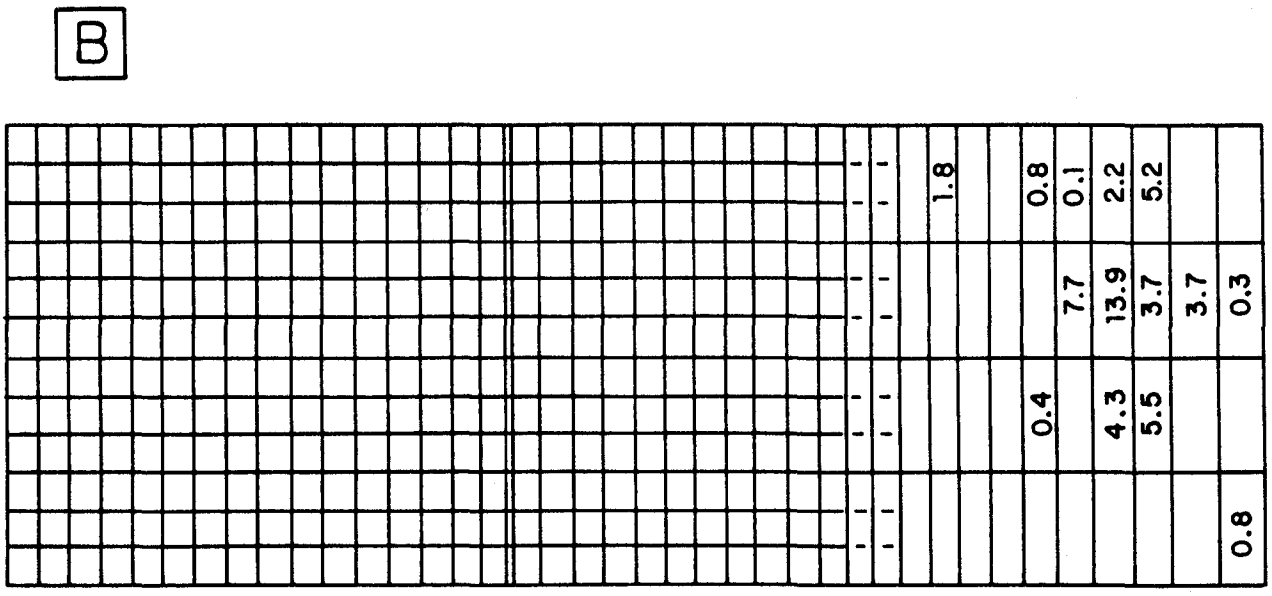
B
1.8
0.8
0.1
2.2
5.2
7.7
13.9
3.7
3.7
0.3
0.4
4.3
5.5
0.8

FIG. 4.1

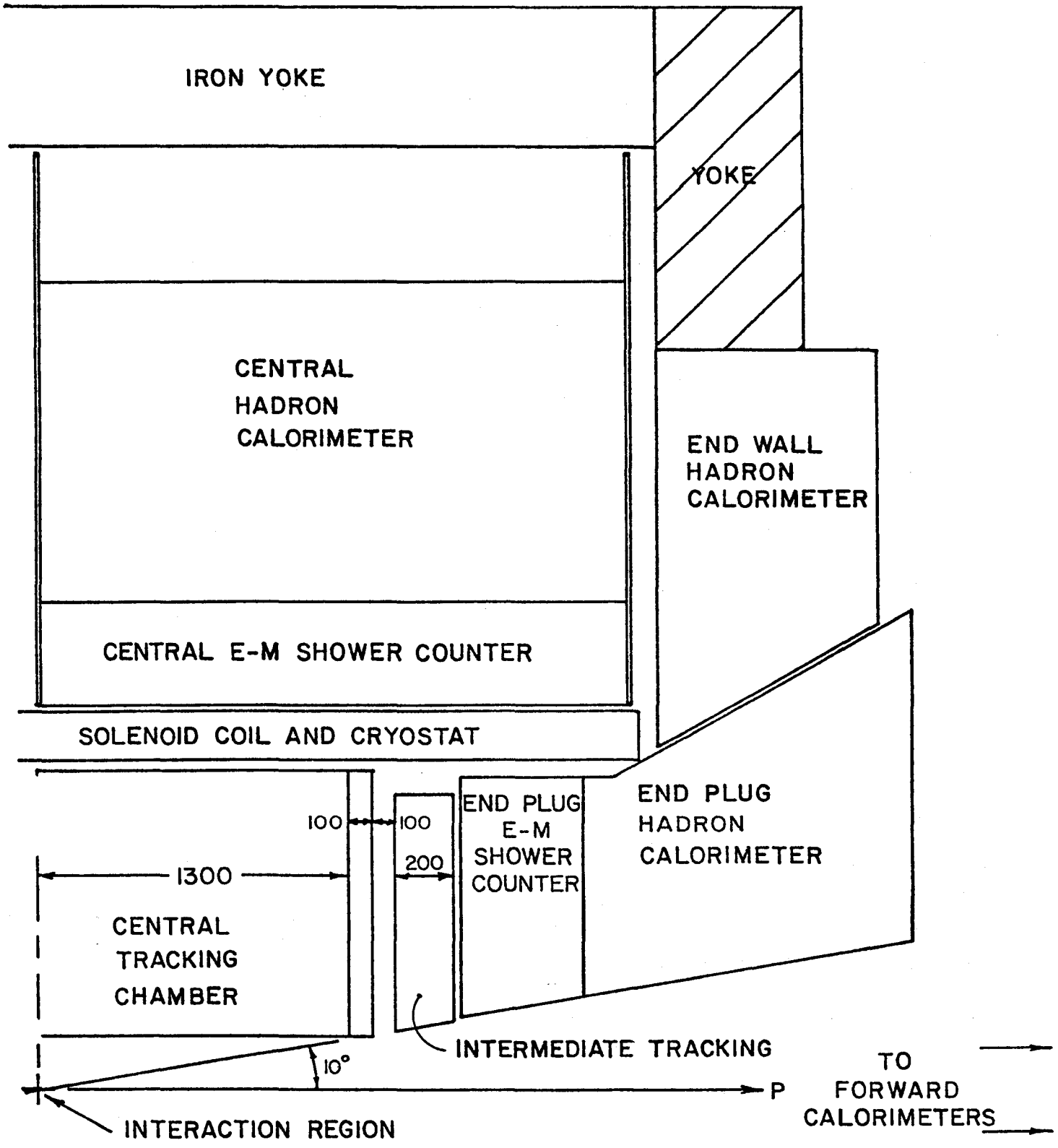
IRON YOKE
YOKE
CENTRAL
HADRON
CALORIMETER
END WALL
HADRON
CALORIMETER
CENTRAL E-M SHOWER COUNTER
SOLENOID COIL AND CRYOSTAT
100
100
200
1300
END PLUG
E-M
SHOWER
COUNTER
END PLUG
HADRON
CALORIMETER
CENTRAL
TRACKING
CHAMBER
INTERMEDIATE TRACKING
10°
P
TO
FORWARD
CALORIMETERS
INTERACTION REGION

FIG. 4.2

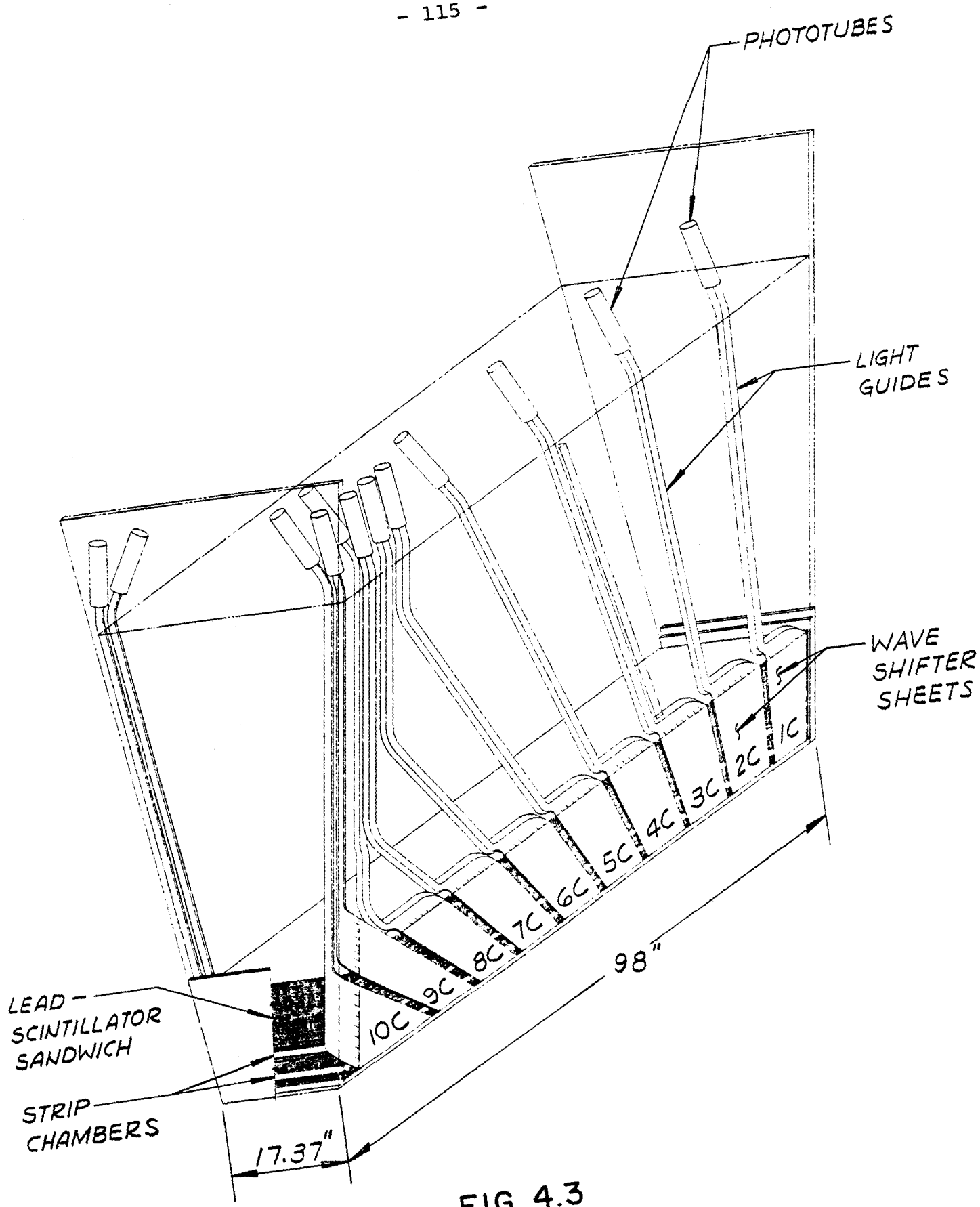
PHOTOTUBES
LIGHT GUIDES
WAVE SHIFTER SHEETS
1C
2C
3C
4C
5C
6C
7C
8C
9C
10C
98"
LEAD - SCINTILLATOR SANDWICH
STRIP CHAMBERS
17.37"

FIG. 4.3

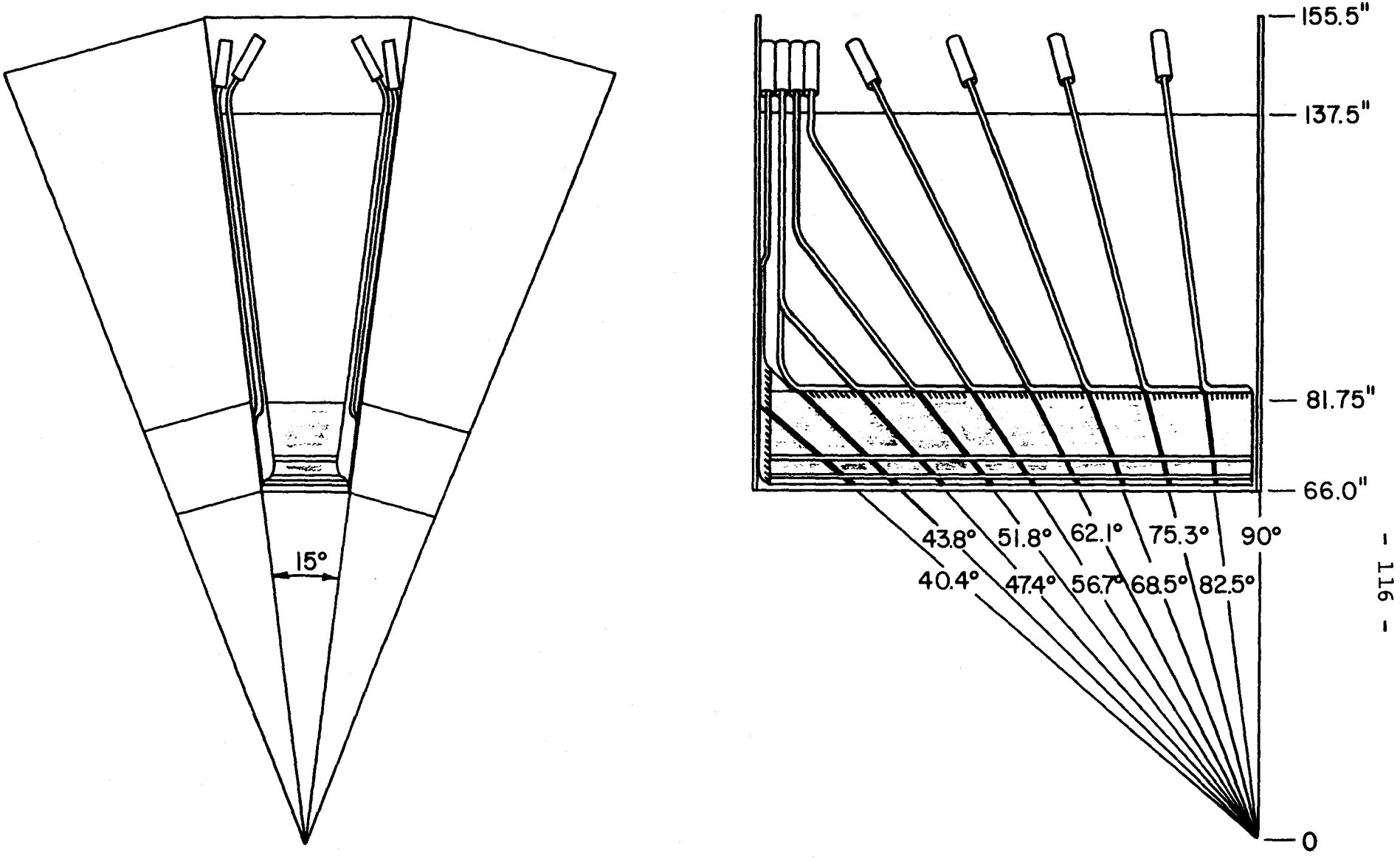

FIG. 4.4

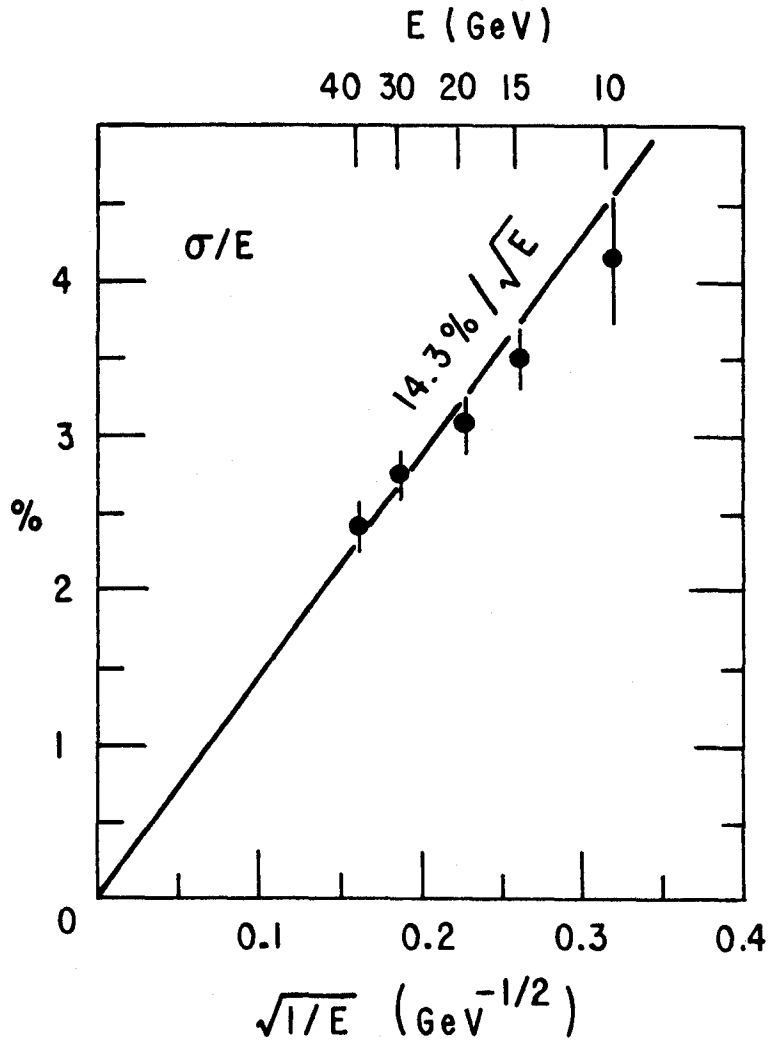

FIG. 4.5

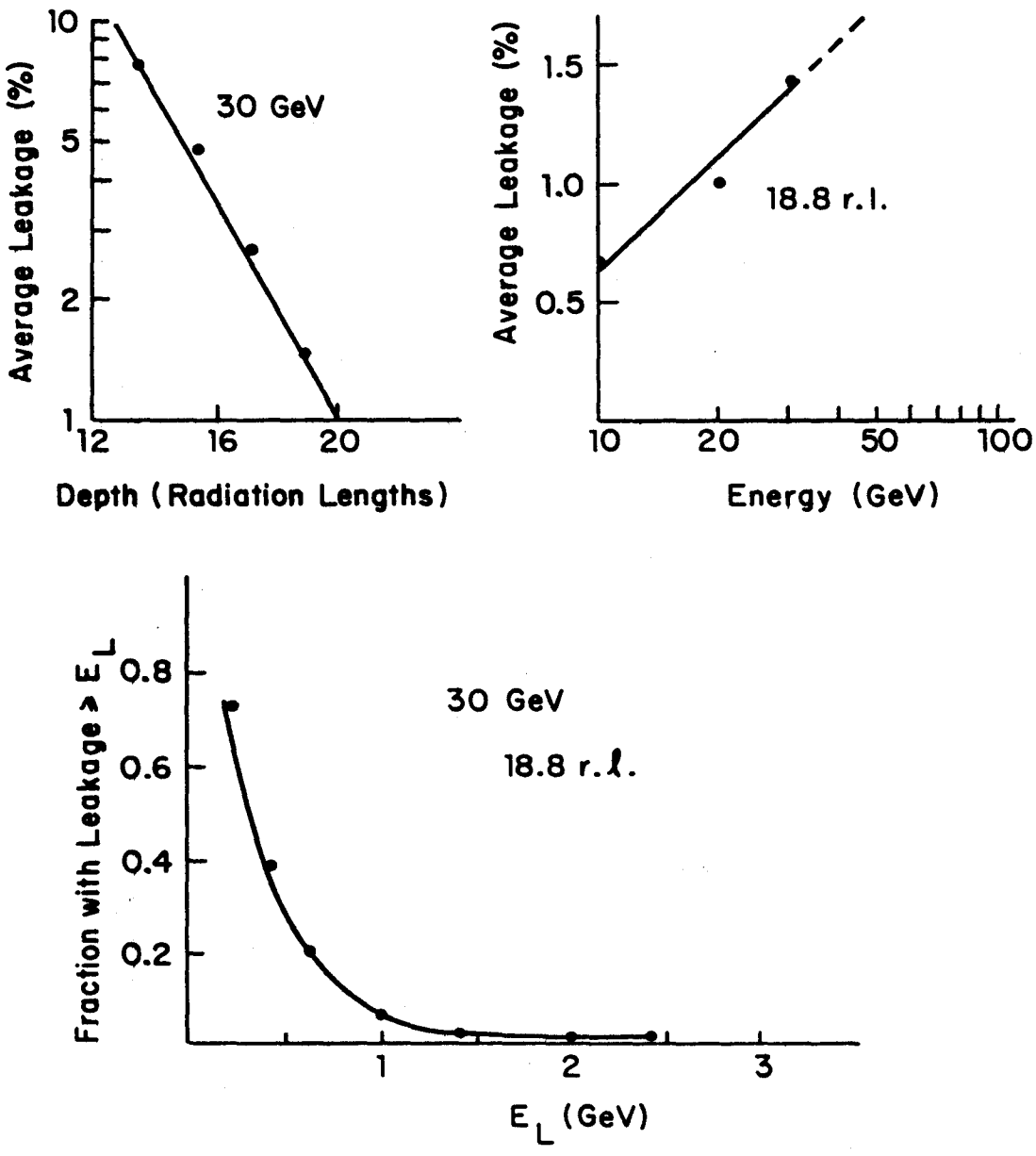
Average Leakage (%)
10
5
2
1
30 GeV
12
16
20
Depth (Radiation Lengths)
Average Leakage (%)
1.5
1.0
0.5
18.8 r.l.
10
20
50
100
Energy (GeV)
Fraction with Leakage ≥ E_L
0.8
0.6
0.4
0.2
30 GeV
18.8 r.l.
1
2
3
E_L (GeV)

FIG. 4.6

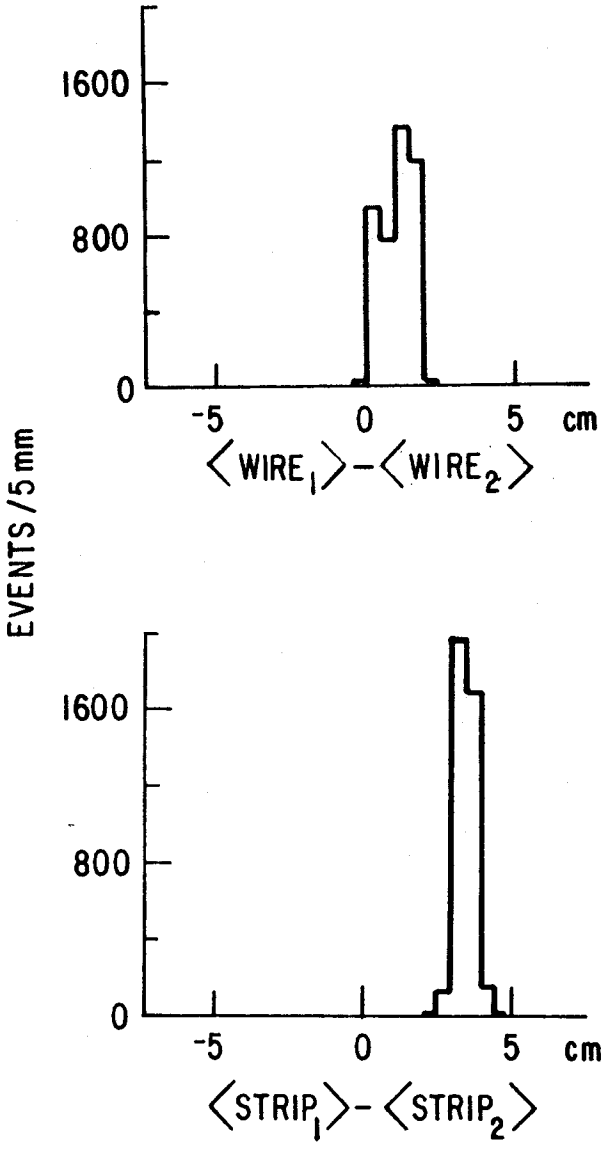

FIG. 4.7

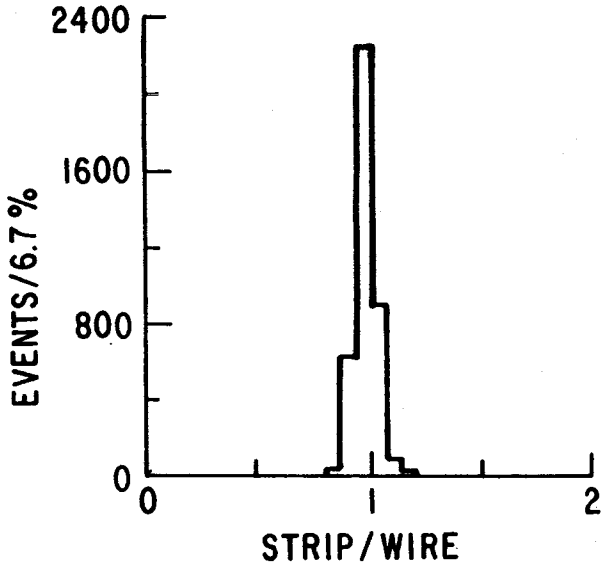

FIG. 4.8

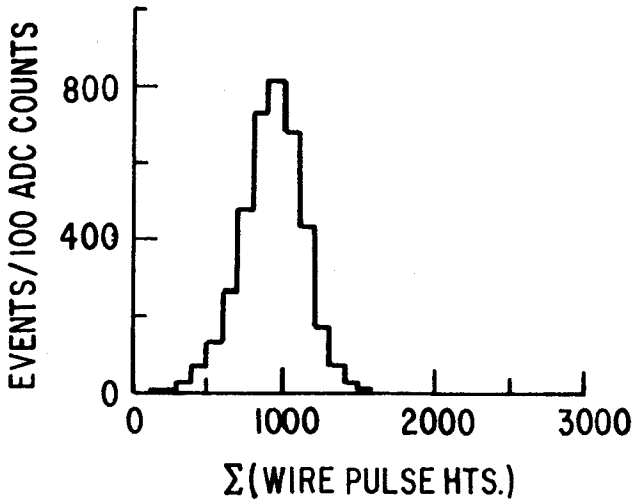

FIG. 4.9

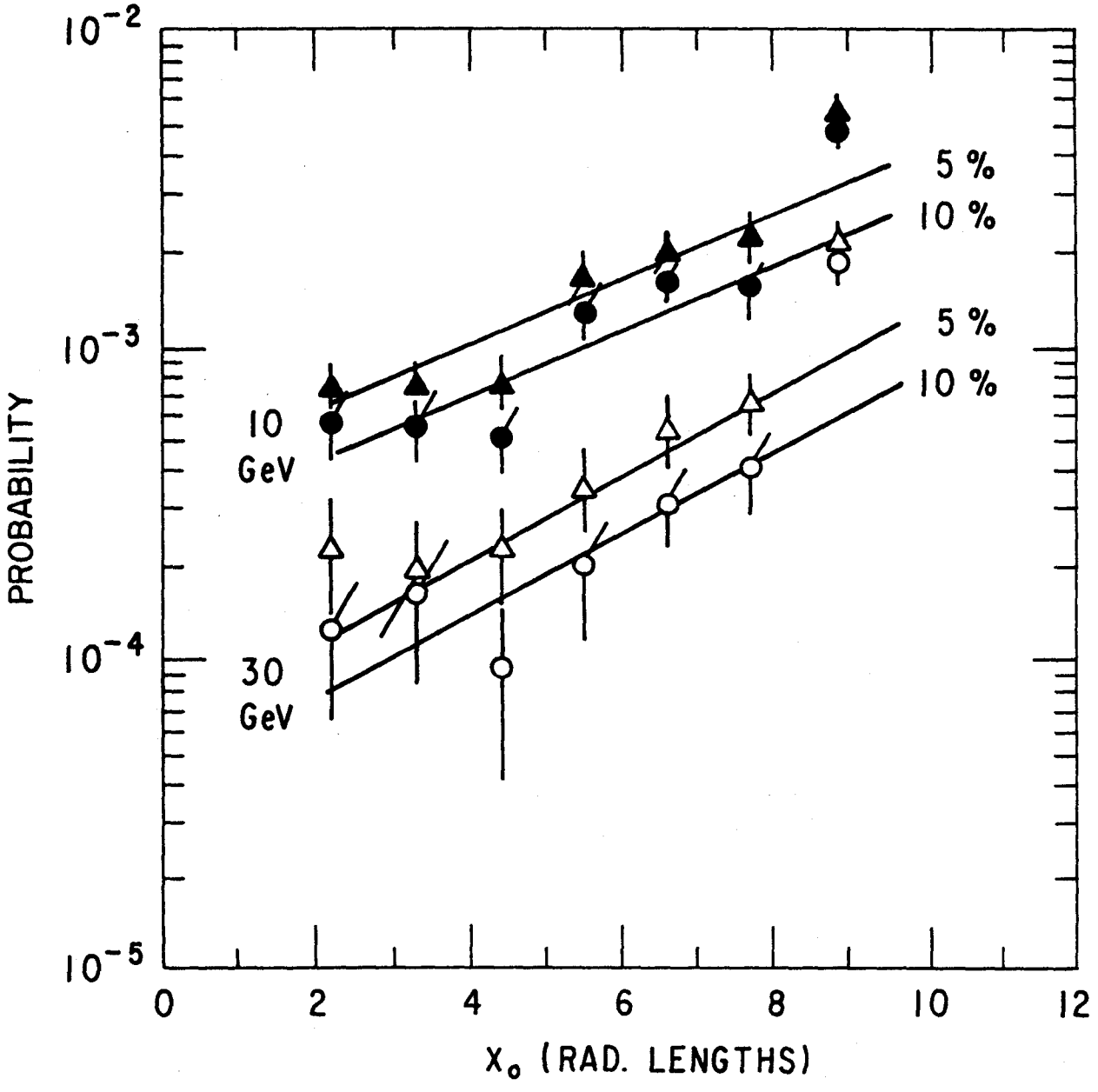
10^{-2}
10^{-3}
10^{-4}
10^{-5}
PROBABILITY
10 GeV
30 GeV
5 %
10 %
5 %
10 %
0
2
4
6
8
10
12
X_0 (RAD. LENGTHS)

FIG. 4.10

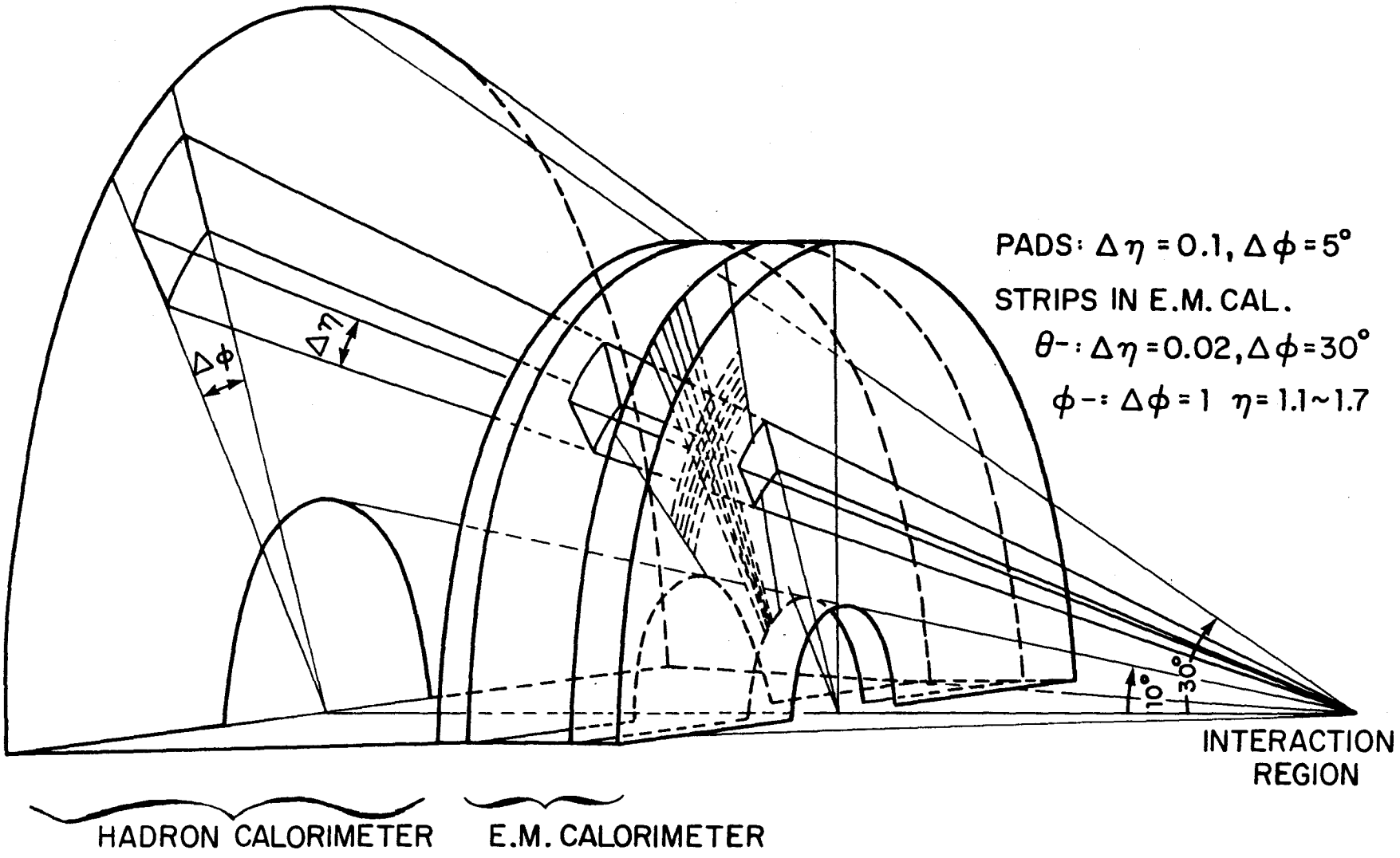
PADS: Δη = 0.1, Δφ = 5°
STRIPS IN E.M. CAL.
θ-: Δη = 0.02, Δφ = 30°
φ-: Δφ = 1 η = 1.1~1.7
Δφ
Δη
10°
30°
INTERACTION REGION
HADRON CALORIMETER
E.M. CALORIMETER

FIG. 4.11

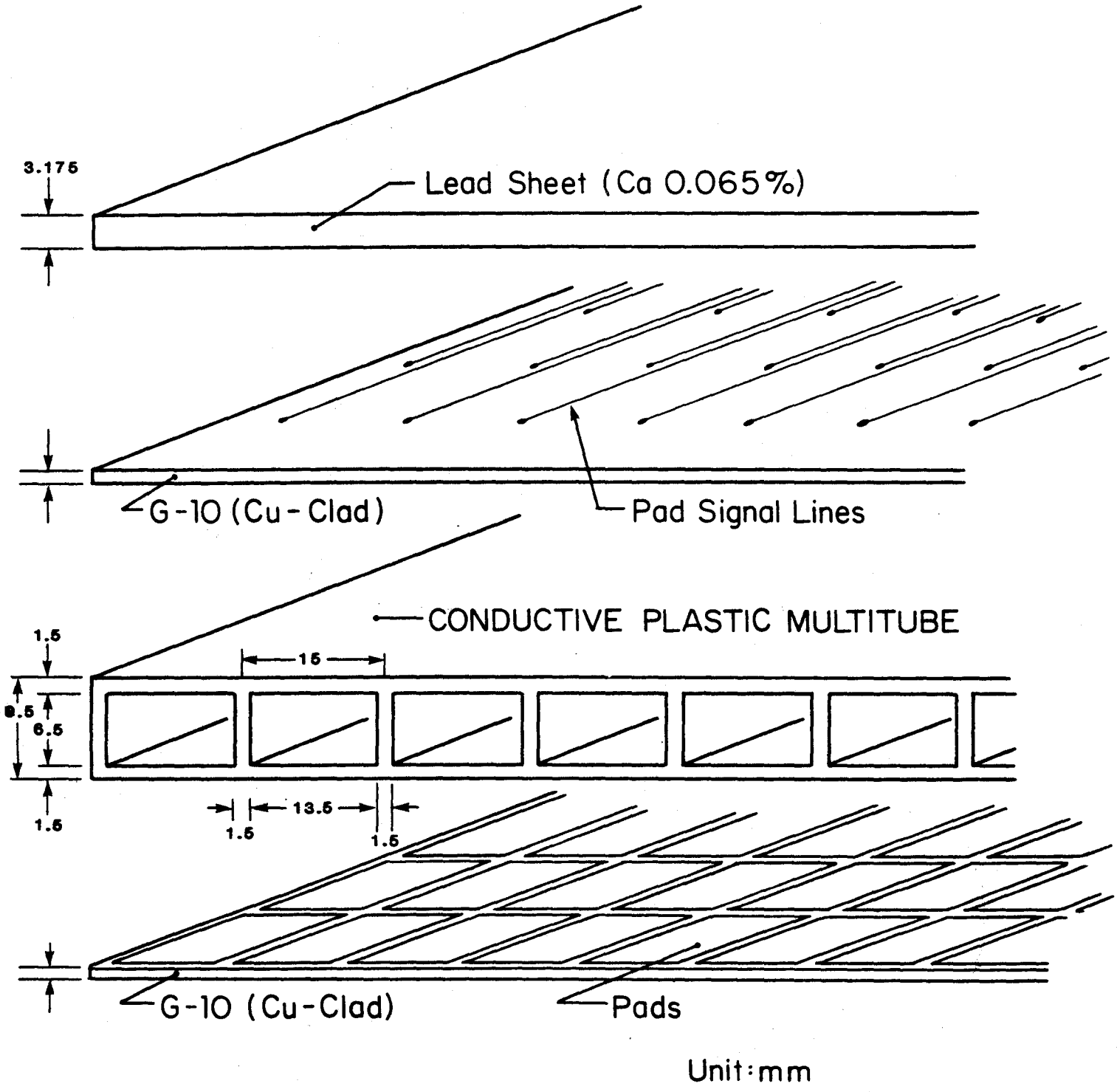
3.175
Lead Sheet (Ca 0.065%)
G-10 (Cu-Clad)
Pad Signal Lines
CONDUCTIVE PLASTIC MULTITUBE
1.5
15
8.5
6.5
1.5
13.5
1.5
1.5
G-10 (Cu-Clad)
Pads
Unit: mm

FIG. 4.12

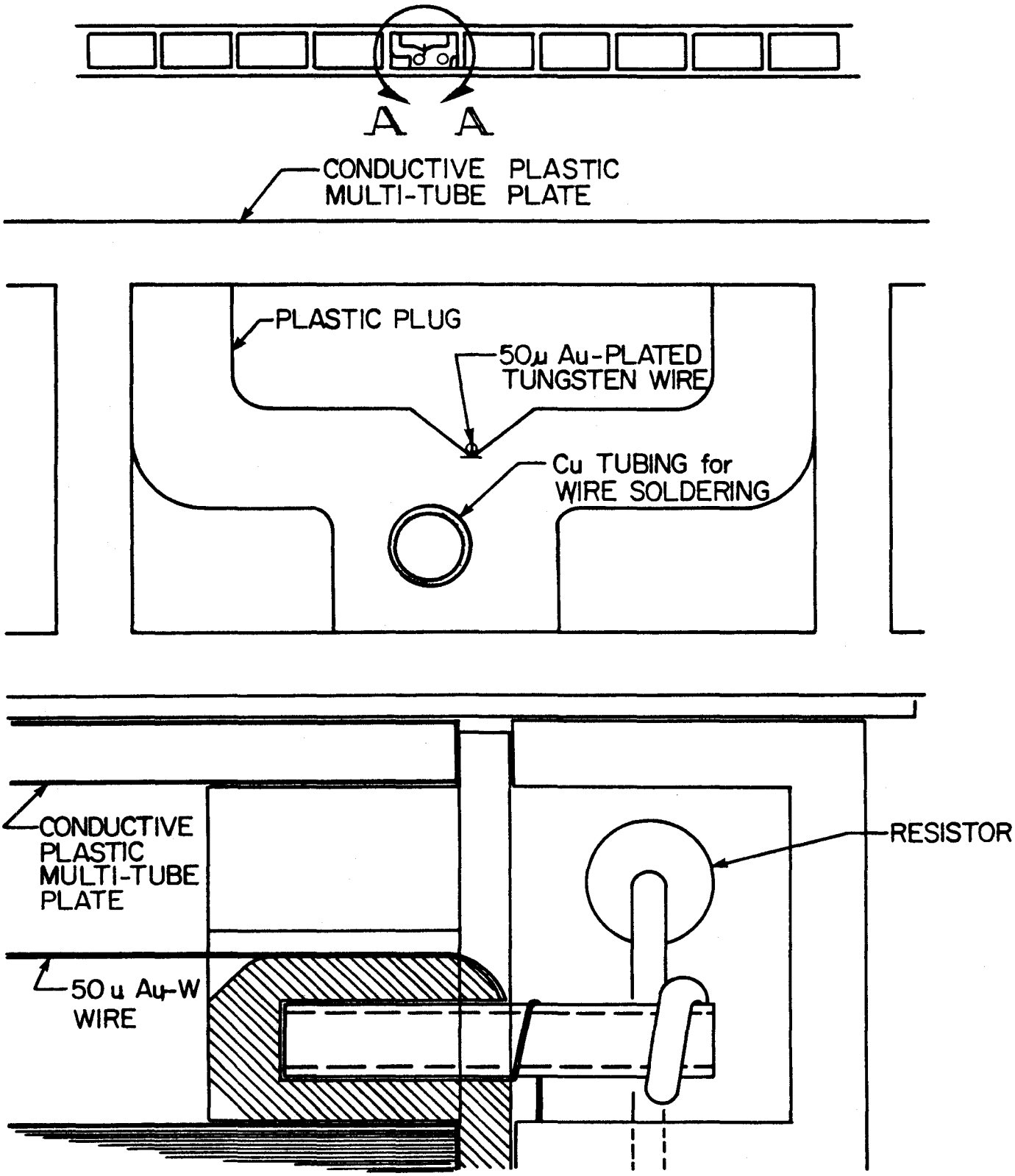

SECTION A-A

FIG. 4.13

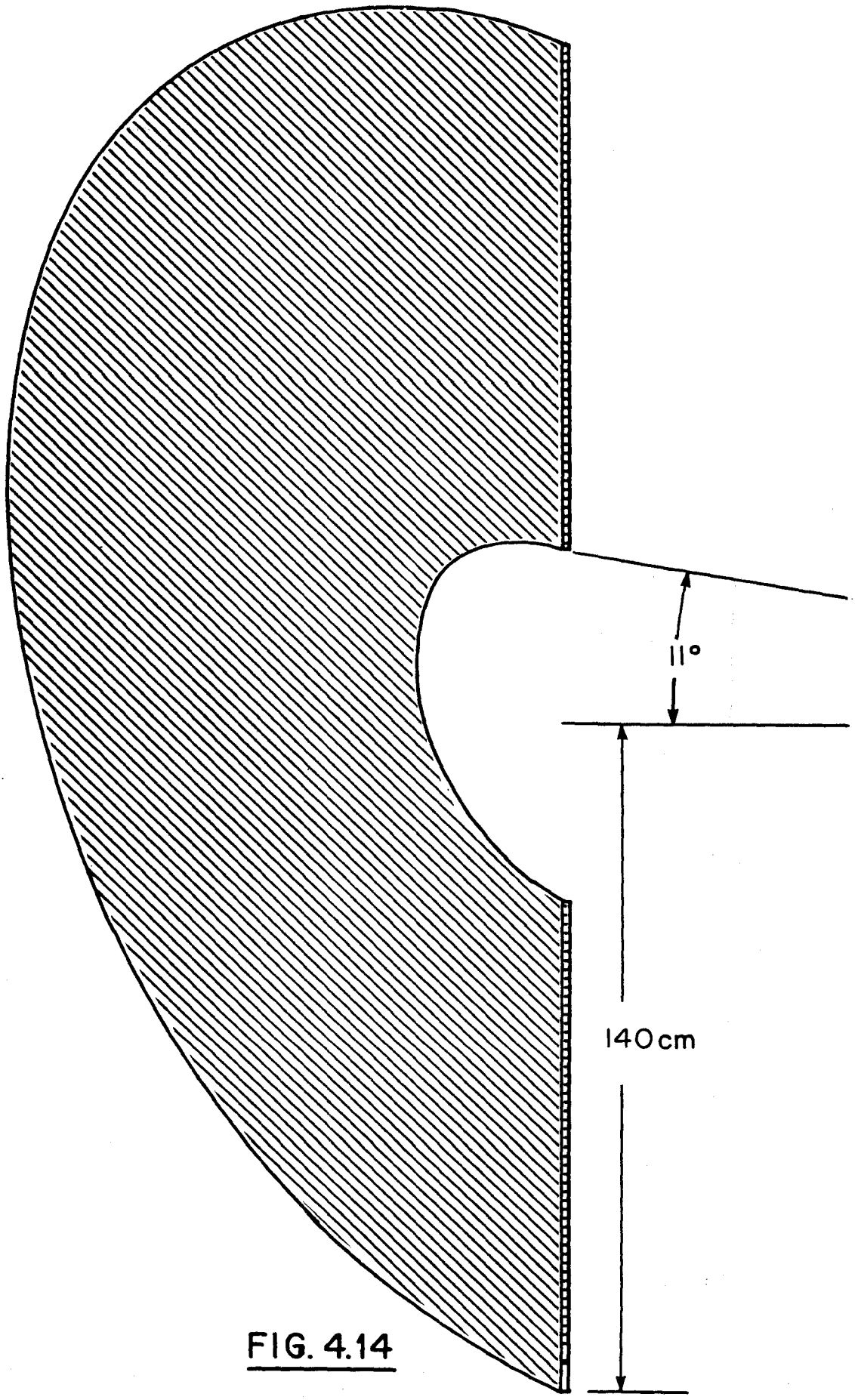

FIG. 4.14

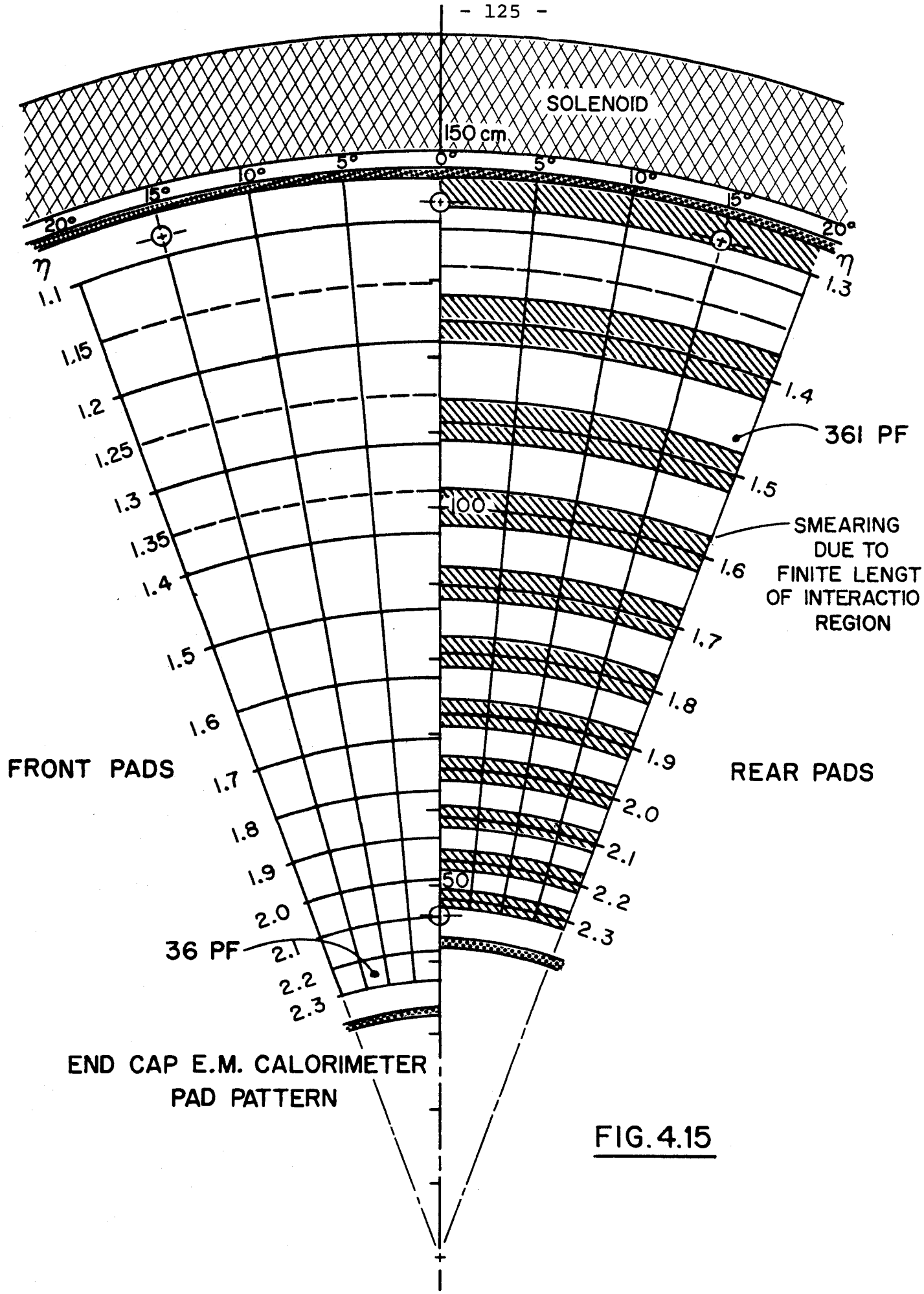
SOLENOID
150 cm
0°
5°
10°
15°
20°
η
1.1
1.15
1.2
1.25
1.3
1.35
1.4
1.5
1.6
1.7
1.8
1.9
2.0
2.1
2.2
2.3
1.3
1.4
1.5
1.6
1.7
1.8
1.9
2.0
2.1
2.2
2.3
100
50
361 PF
36 PF
SMEARING DUE TO FINITE LENGT OF INTERACTIO REGION
FRONT PADS
REAR PADS
END CAP E.M. CALORIMETER PAD PATTERN

FIG. 4.15

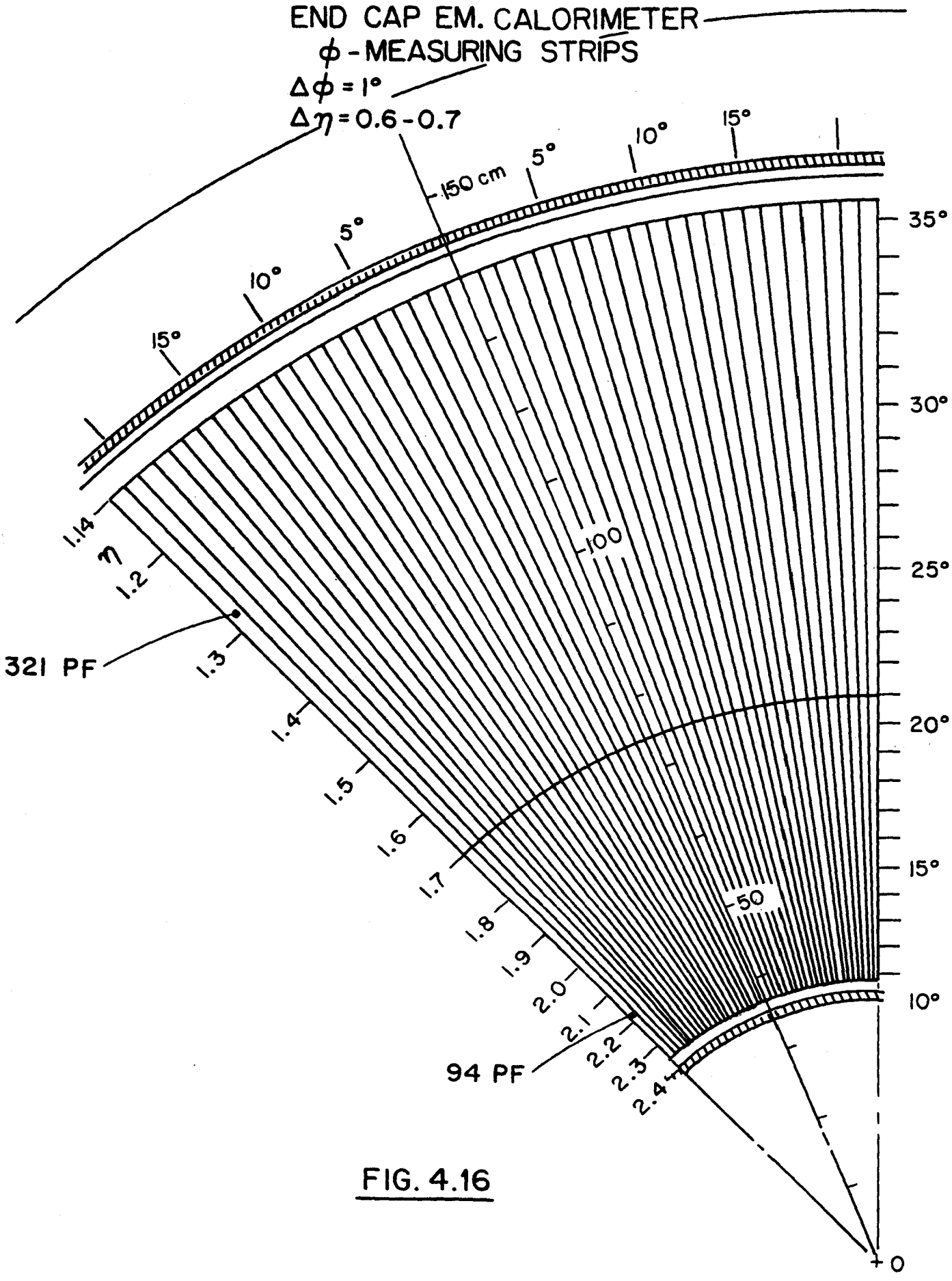
END CAP EM. CALORIMETER
φ - MEASURING STRIPS
Δφ = 1°
Δη = 0.6 - 0.7
150 cm
5°
10°
15°
5°
10°
15°
35°
30°
25°
20°
15°
10°
0
100
50
η
1.14
1.2
1.3
1.4
1.5
1.6
1.7
1.8
1.9
2.0
2.1
2.2
2.3
2.4
321 PF
94 PF

FIG. 4.16

END CAP EM. CALORIMETER
θ- MEASURING STRIPS

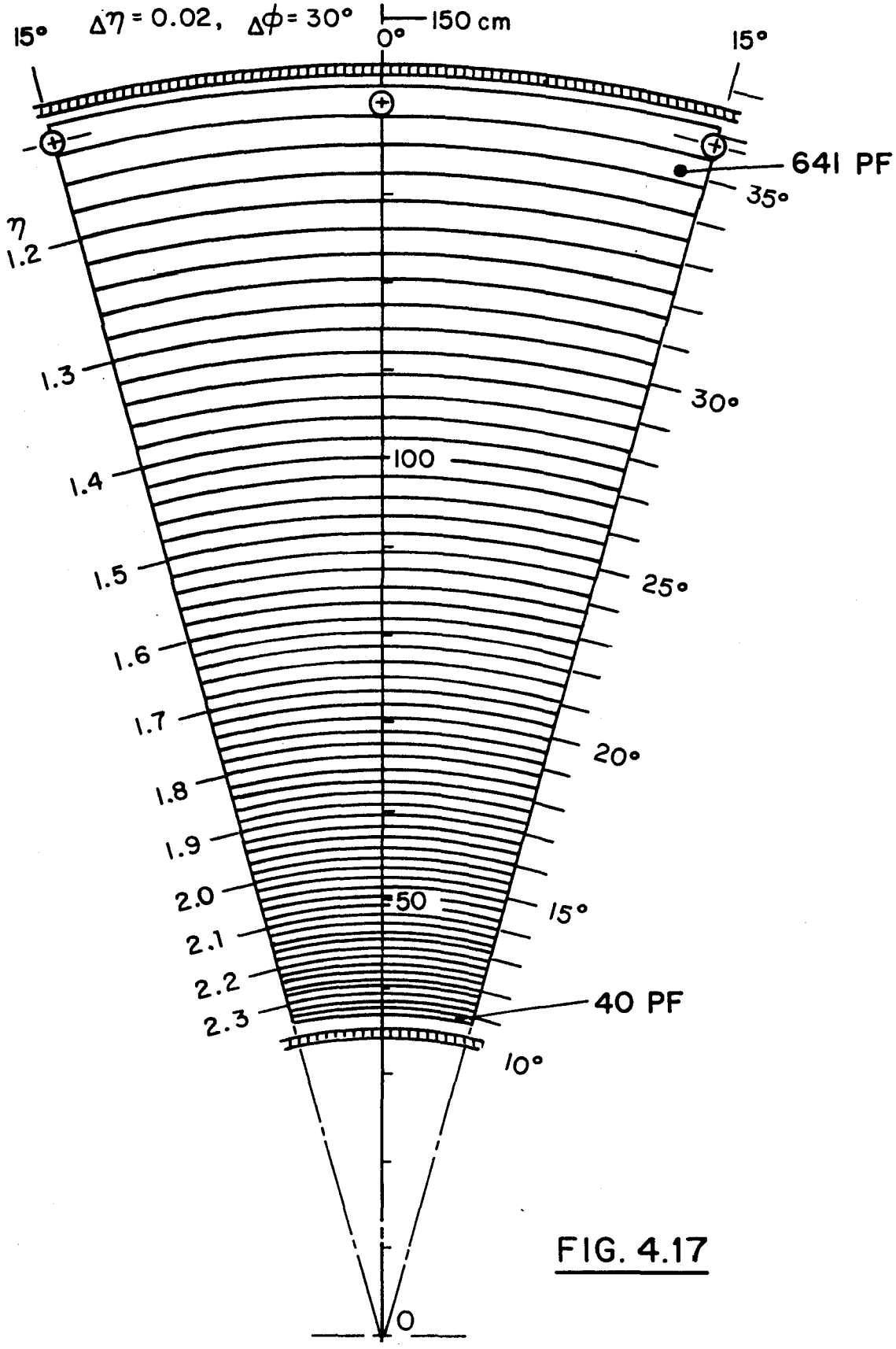

FIG. 4.17

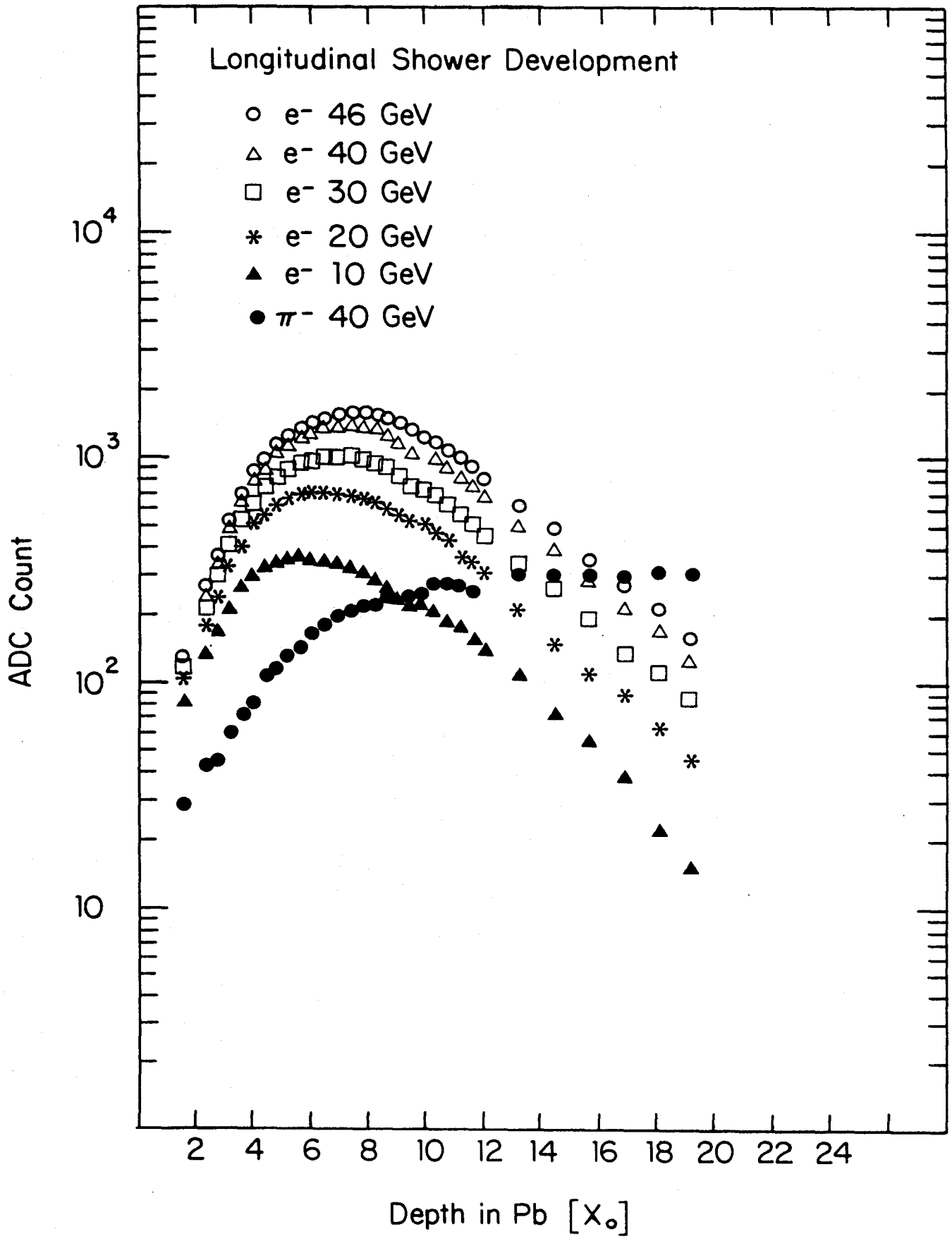
Longitudinal Shower Development
e⁻ 46 GeV
e⁻ 40 GeV
e⁻ 30 GeV
e⁻ 20 GeV
e⁻ 10 GeV
π⁻ 40 GeV
ADC Count
10⁴
10³
10²
10
2
4
6
8
10
12
14
16
18
20
22
24
Depth in Pb [X₀]

FIG. 4.18

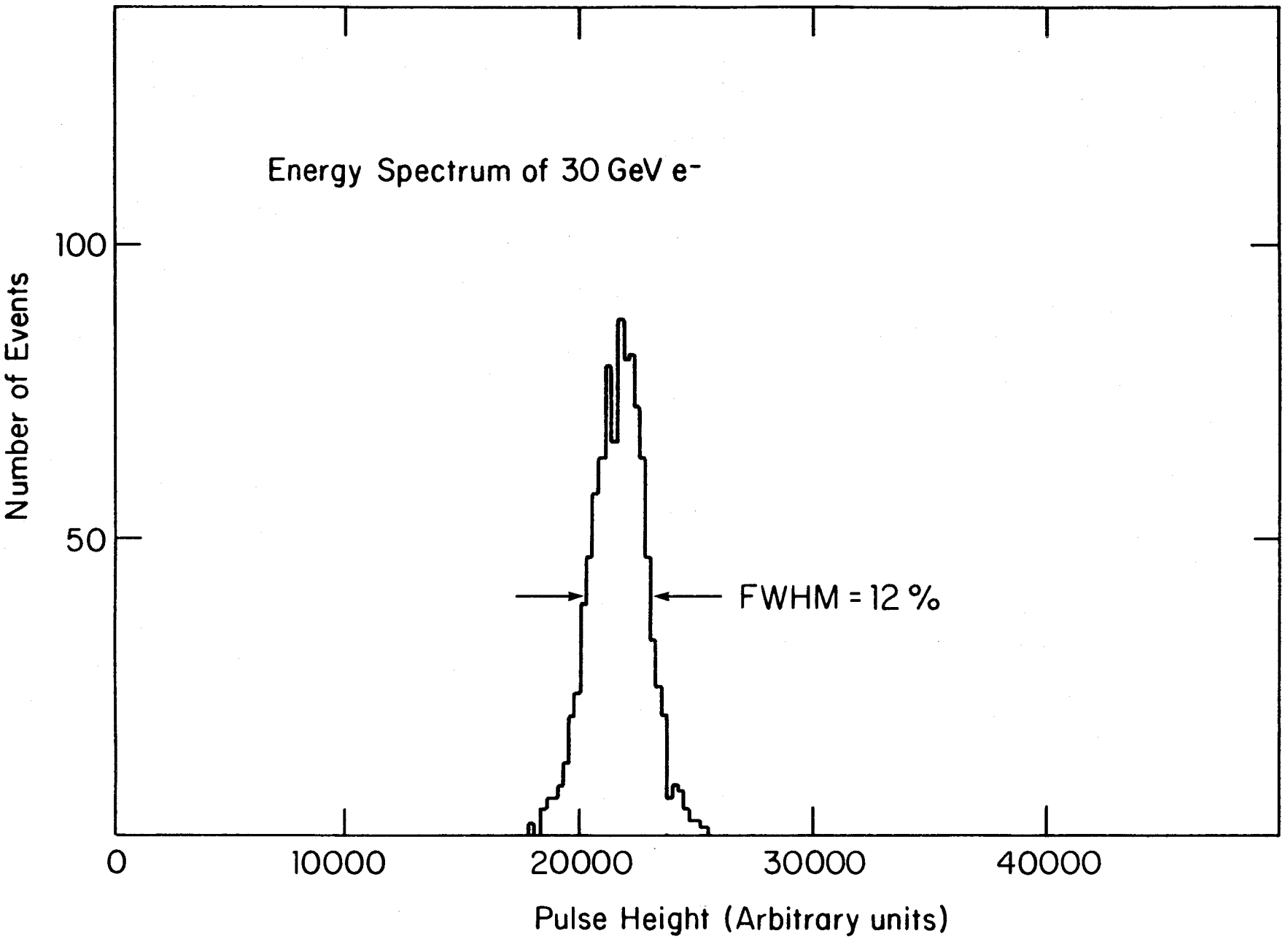
Energy Spectrum of 30 GeV e⁻
Number of Events
100
50
FWHM = 12 %
0
10000
20000
30000
40000
Pulse Height (Arbitrary units)

FIG. 4.19

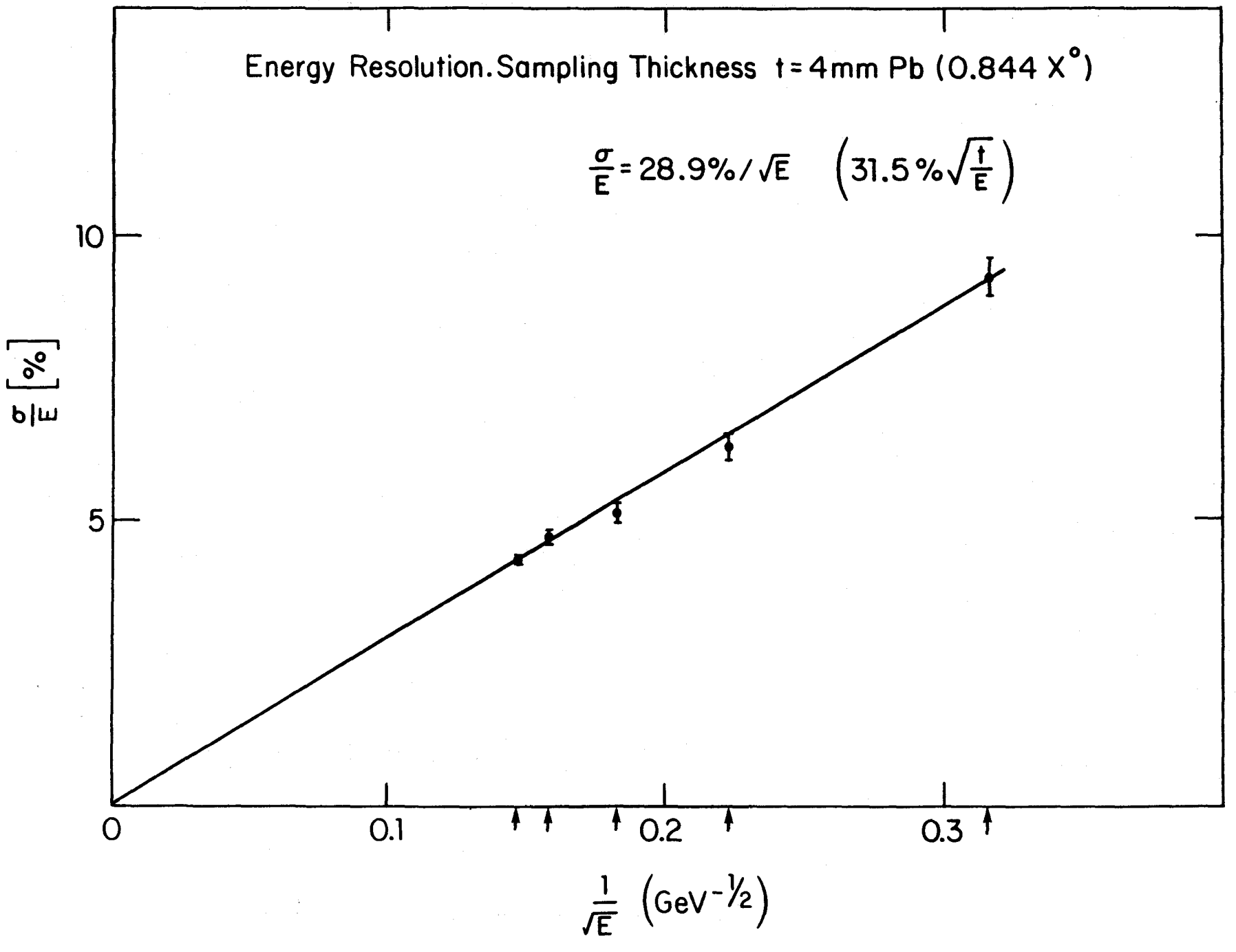
Energy Resolution. Sampling Thickness t = 4mm Pb (0.844 X°)
$\frac{\sigma}{E} = 28.9\%/\sqrt{E}$ $\left(31.5\%\sqrt{\frac{t}{E}}\right)$
10
5
$\frac{\sigma}{E}$ [%]
0
0.1
0.2
0.3
$\frac{1}{\sqrt{E}}$ (GeV$^{-1/2}$)

FIG. 4.20

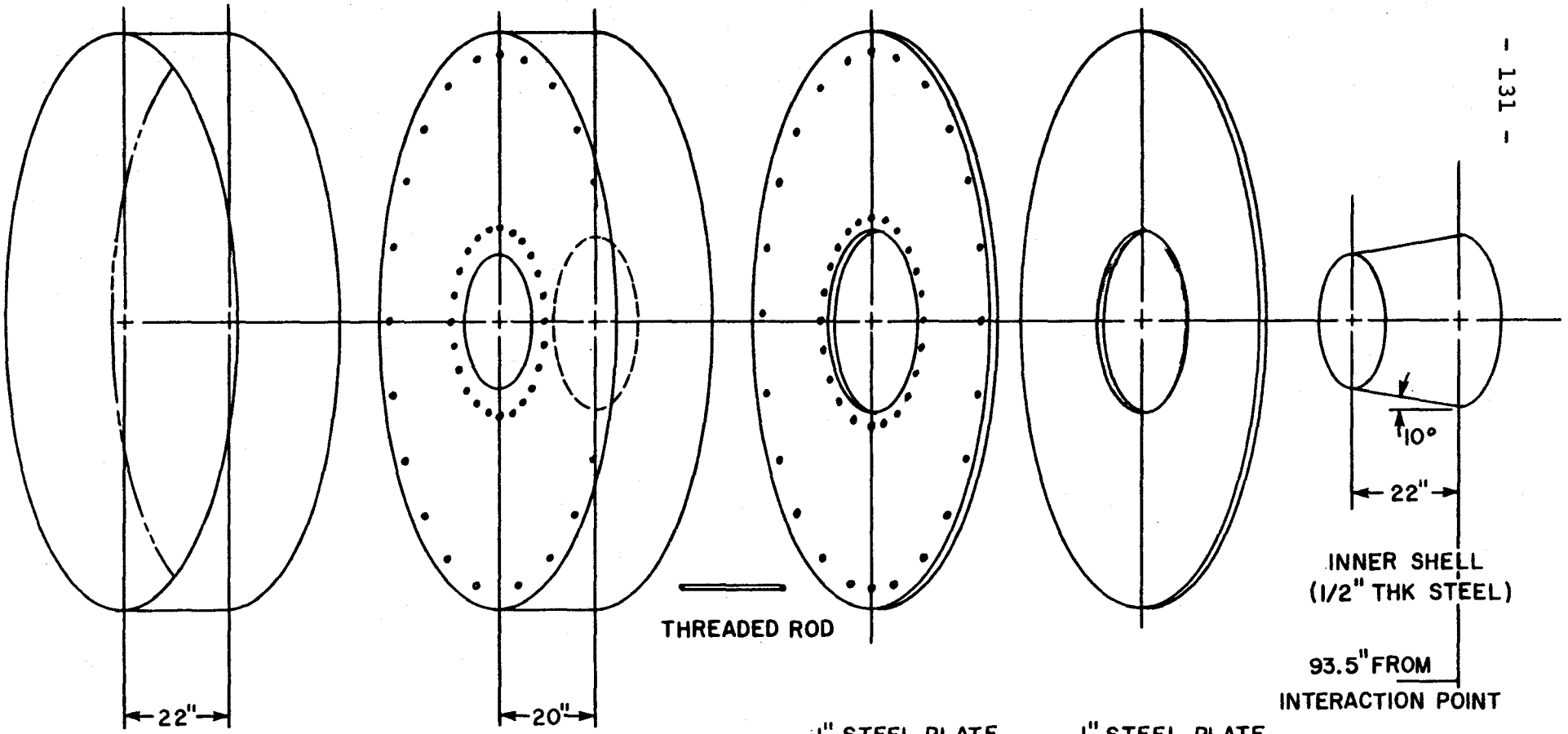
22"
20"
THREADED ROD
1" STEEL PLATE
1" STEEL PLATE
10°
22"
INNER SHELL
(1/2" THK STEEL)
93.5" FROM
INTERACTION POINT
OUTER SHELL
(1/2" THK STEEL)

FIG. 4.21

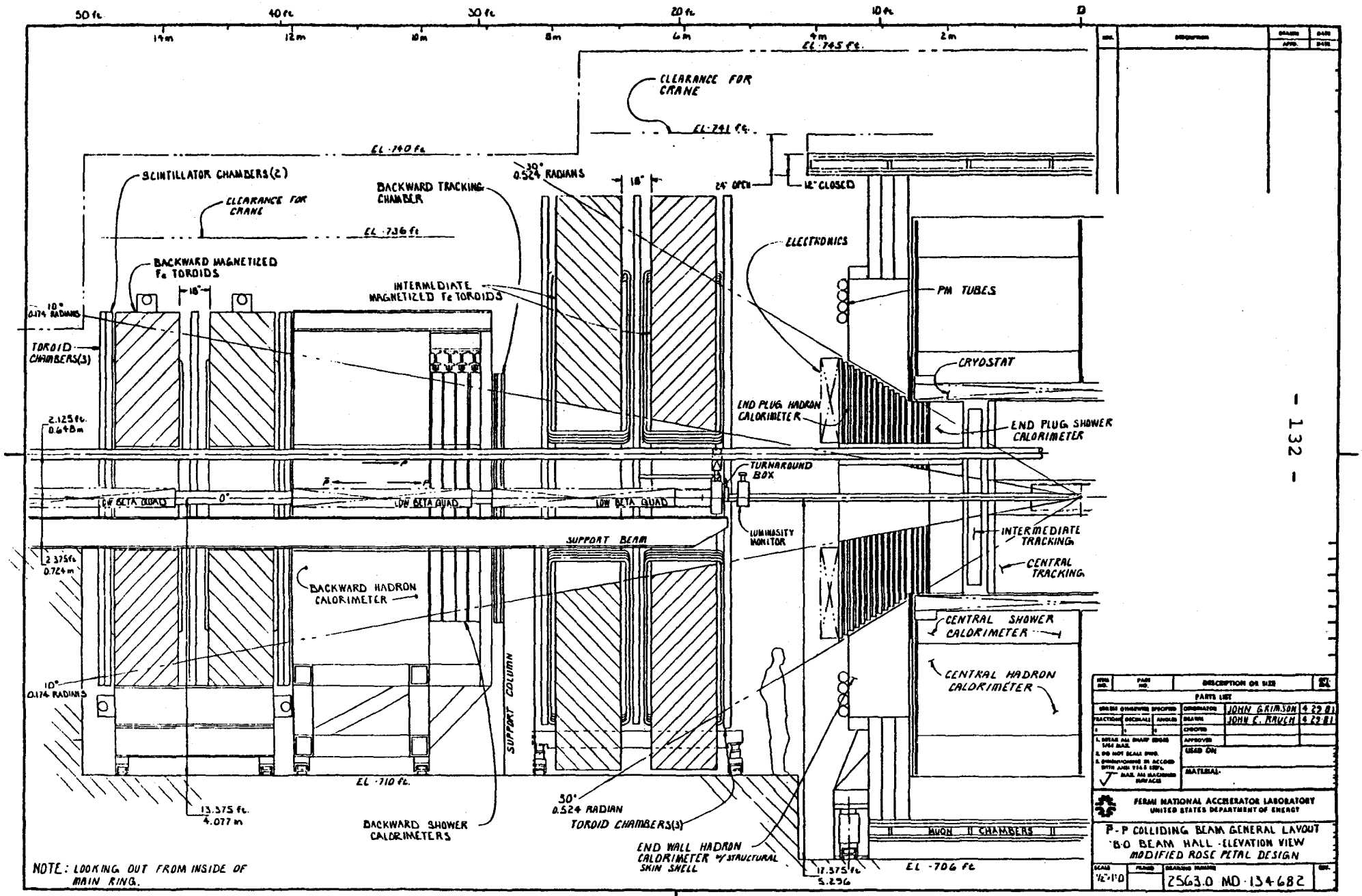
50 ft
40 ft
30 ft
20 ft
10 ft
0
14m
12m
10m
8m
6m
4m
2m
EL 745 ft.
CLEARANCE FOR CRANE
EL 741 ft.
EL 740 ft.
SCINTILLATOR CHAMBERS(2)
CLEARANCE FOR CRANE
EL 736 ft
BACKWARD TRACKING CHAMBER
30° 0.524 RADIANS
18"
24" OPEN
12" CLOSED
ELECTRONICS
PM TUBES
CRYOSTAT
BACKWARD MAGNETIZED Fe TOROIDS
INTERMEDIATE MAGNETIZED Fe TOROIDS
10° 0.174 RADIANS
TOROID CHAMBERS(3)
2.125 ft. 0.648m
END PLUG HADRON CALORIMETER
END PLUG SHOWER CALORIMETER
TURNAROUND BOX
LOW BETA QUAD
LOW BETA QUAD
LOW BETA QUAD
LUMINOSITY MONITOR
SUPPORT BEAM
INTERMEDIATE TRACKING
CENTRAL TRACKING
2.375 ft. 0.724 m
BACKWARD HADRON CALORIMETER
CENTRAL SHOWER CALORIMETER
CENTRAL HADRON CALORIMETER
10° 0.174 RADIANS
SUPPORT COLUMN
EL 710 ft.
13.375 ft. 4.077 m
BACKWARD SHOWER CALORIMETERS
30° 0.524 RADIAN
TOROID CHAMBERS(3)
END WALL HADRON CALORIMETER w/STRUCTURAL SKIN SHELL
MUON II CHAMBERS II
17.375 ft. 5.296
EL 706 ft
NOTE: LOOKING OUT FROM INSIDE OF MAIN RING.
PARTS LIST
DESCRIPTION OR SIZE
JOHN GRIMSON 4 29 81
JOHN E. RAUCH 4 29 81
DRAWN
CHECKED
APPROVED
USED ON
MATERIAL
FERMI NATIONAL ACCELERATOR LABORATORY
UNITED STATES DEPARTMENT OF ENERGY
P-P COLLIDING BEAM GENERAL LAYOUT
B-0 BEAM HALL - ELEVATION VIEW
MODIFIED ROSE PETAL DESIGN
SCALE 1/2"=1'0
2563.0 MD-134682

FIG. 4.22

FORWARD SPECTROMETER SEGMENTATION

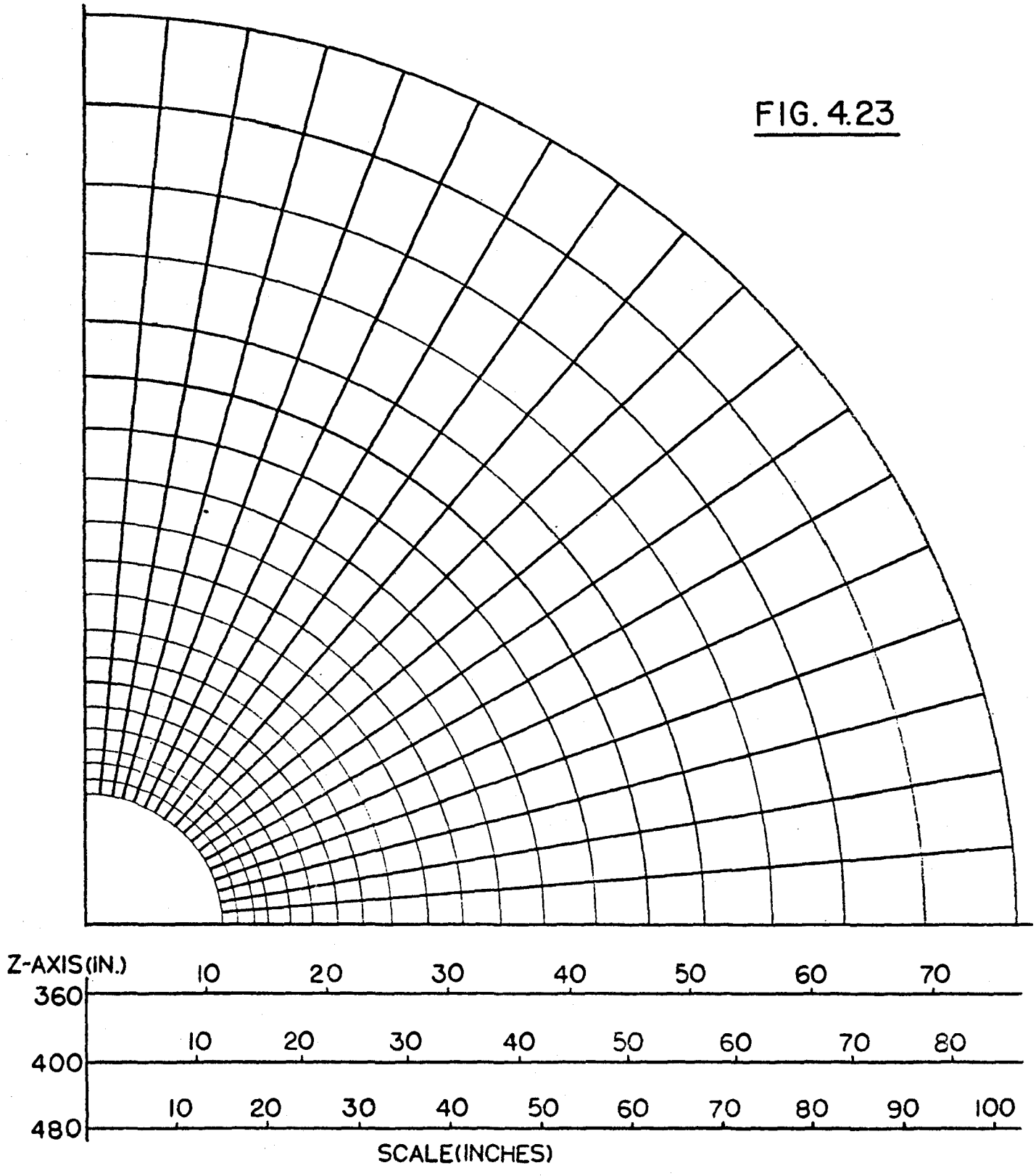

FIG. 4.23

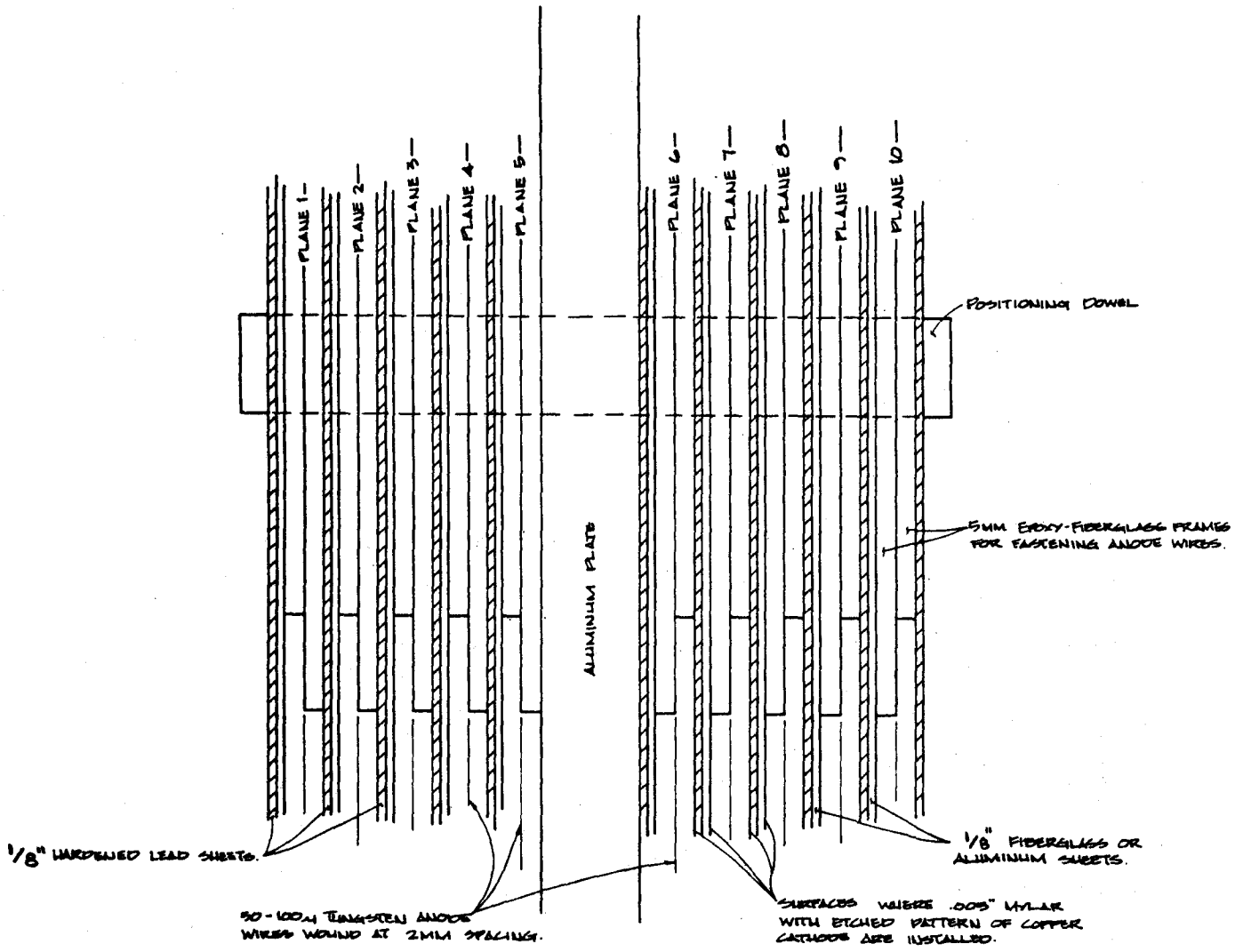

CROSS SECTION
THROUGH
A SINGLE SHOWER CALORIMETER MODULE

FIG. 4.24

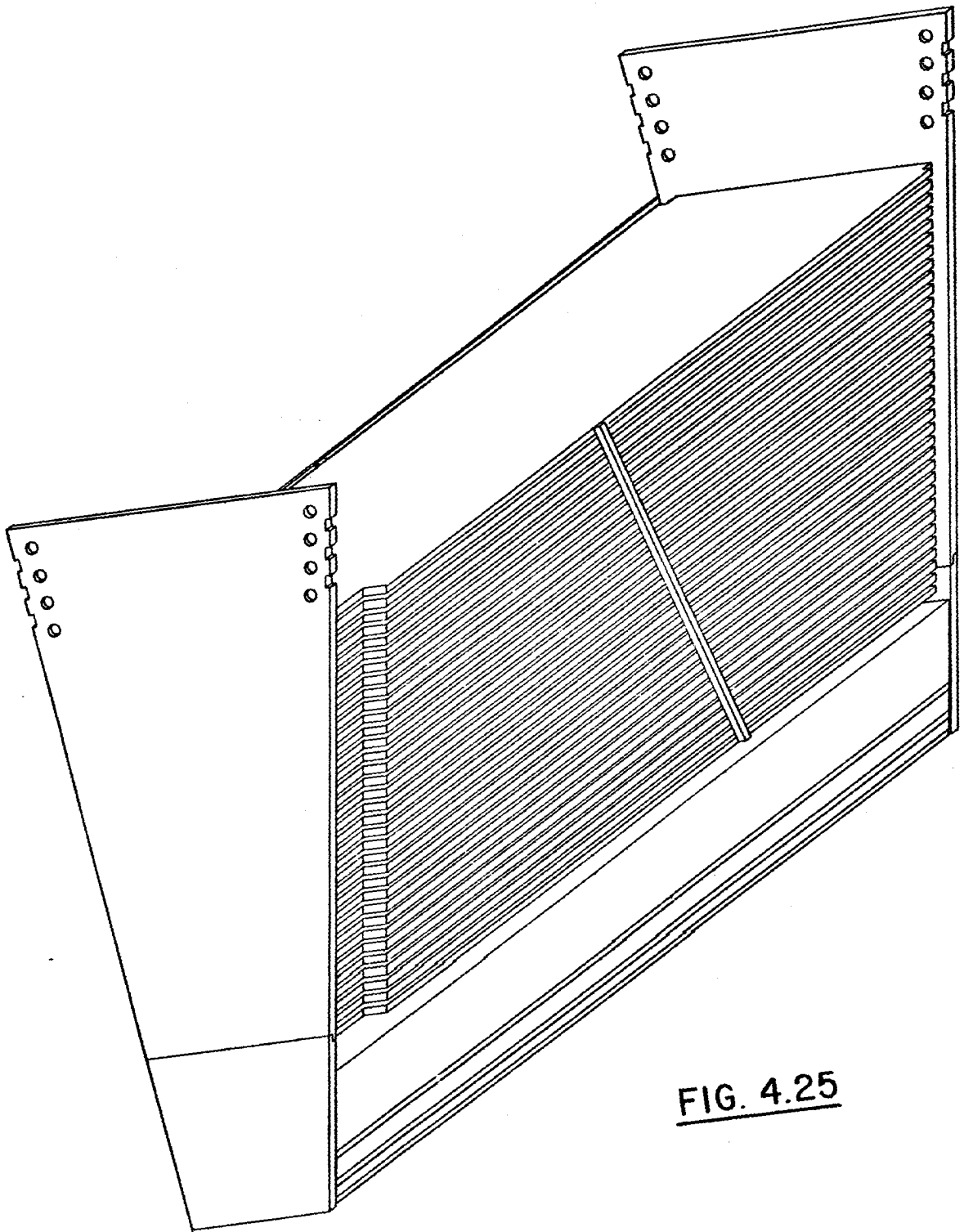

FIG. 4.25

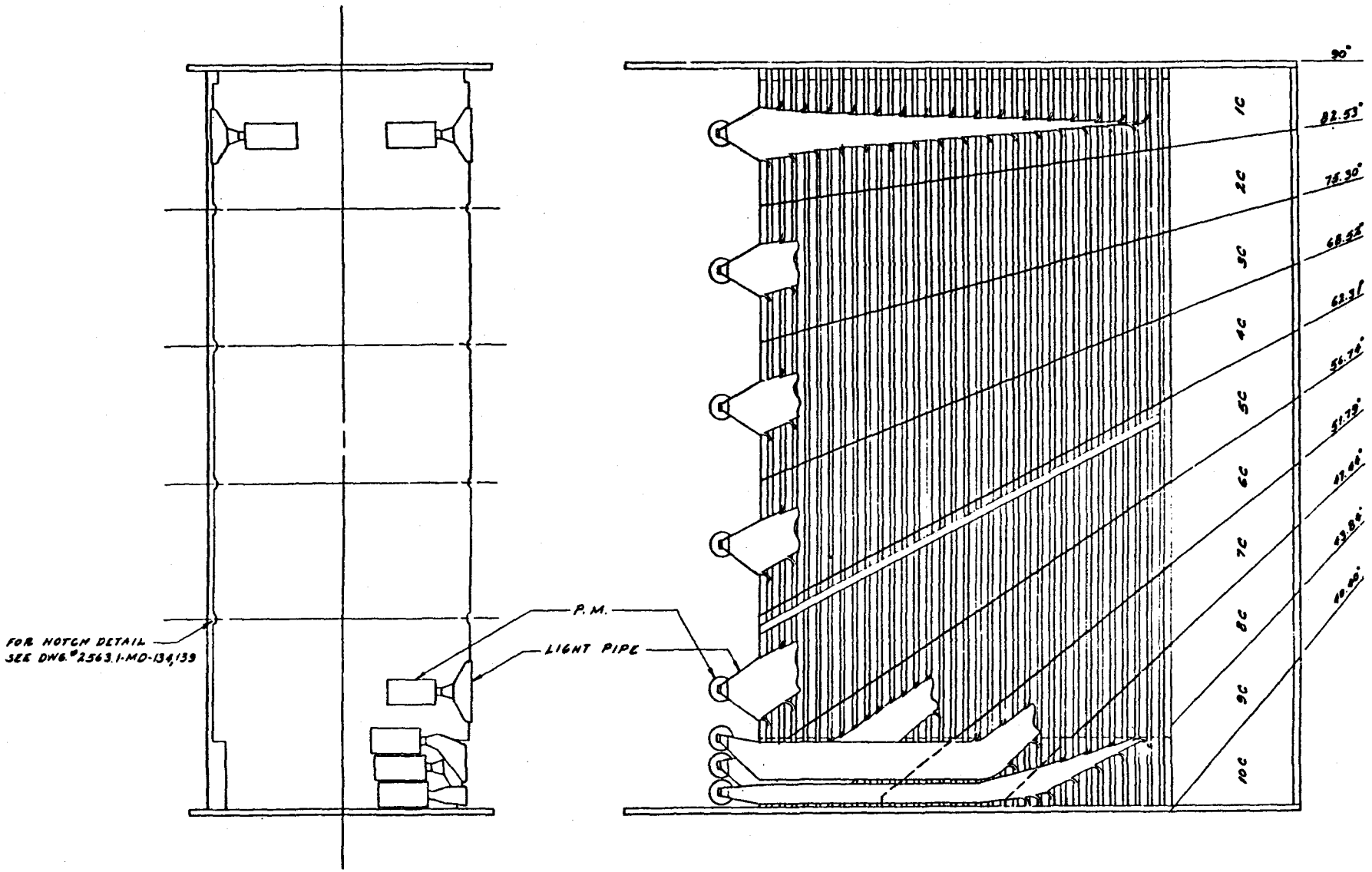
FOR NOTCH DETAIL
SEE DWG. # 2563.1-MD-134,139
P. M.
LIGHT PIPE
TOP VIEW
FRONT VIEW
90°
82.53°
75.30°
68.52°
62.31°
56.74°
51.72°
47.26°
43.36°
40.00°
1C
2C
3C
4C
5C
6C
7C
8C
9C
10C

FIG. 4.26

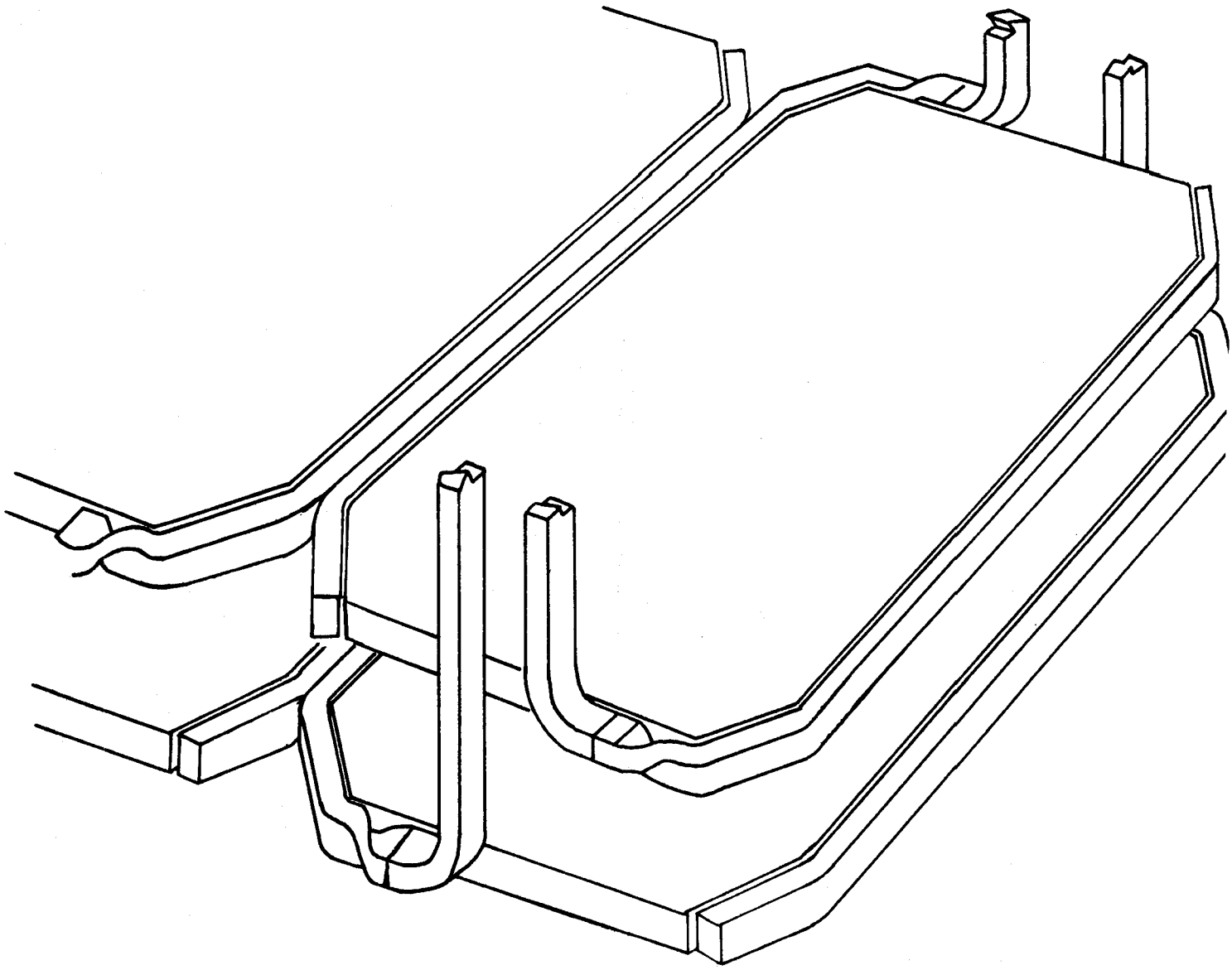

FIG. 4.27

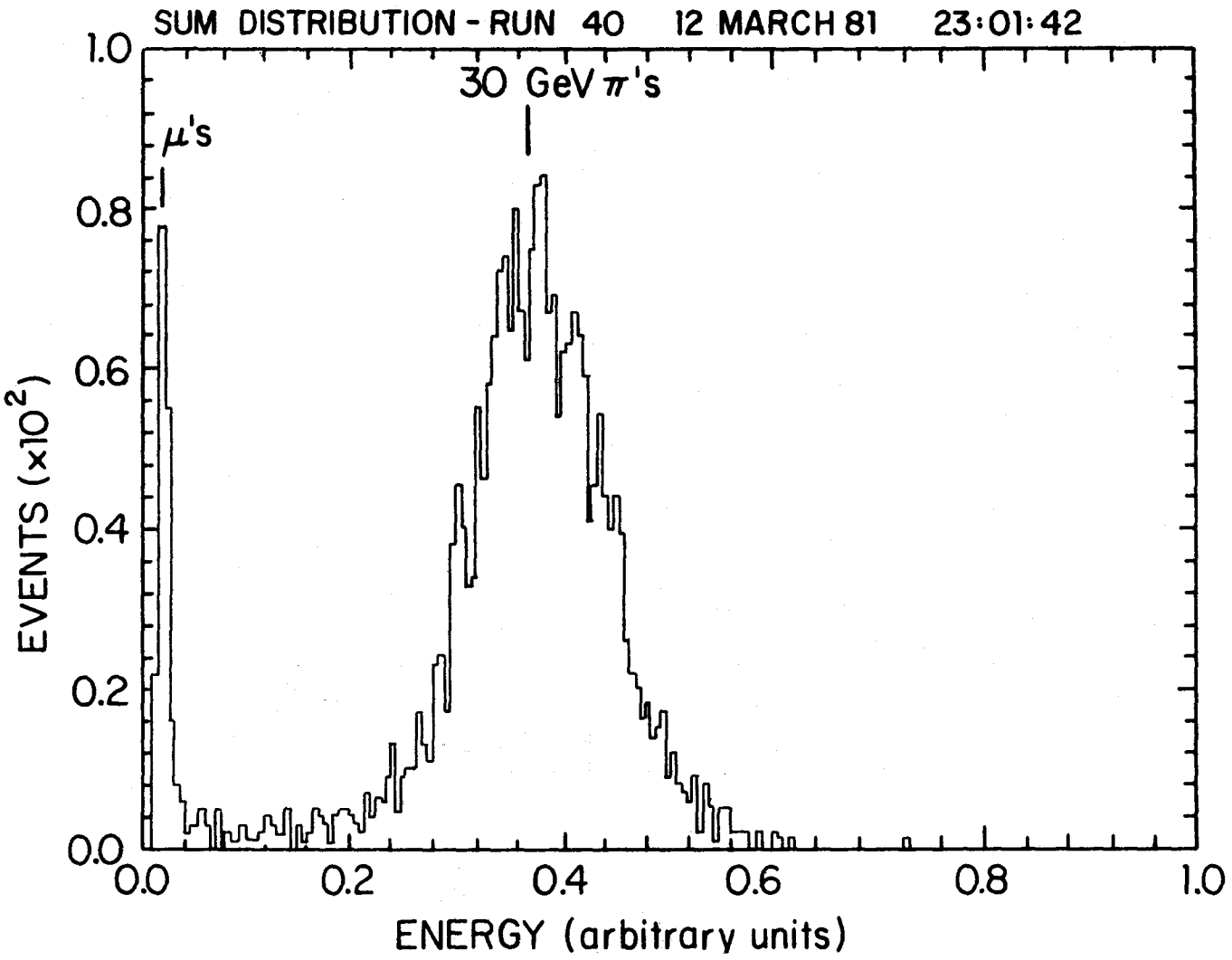
SUM DISTRIBUTION - RUN 40 12 MARCH 81 23:01:42
30 GeV π's
μ's
EVENTS (x10²)
ENERGY (arbitrary units)
0.0
0.2
0.4
0.6
0.8
1.0

FIG. 4.28

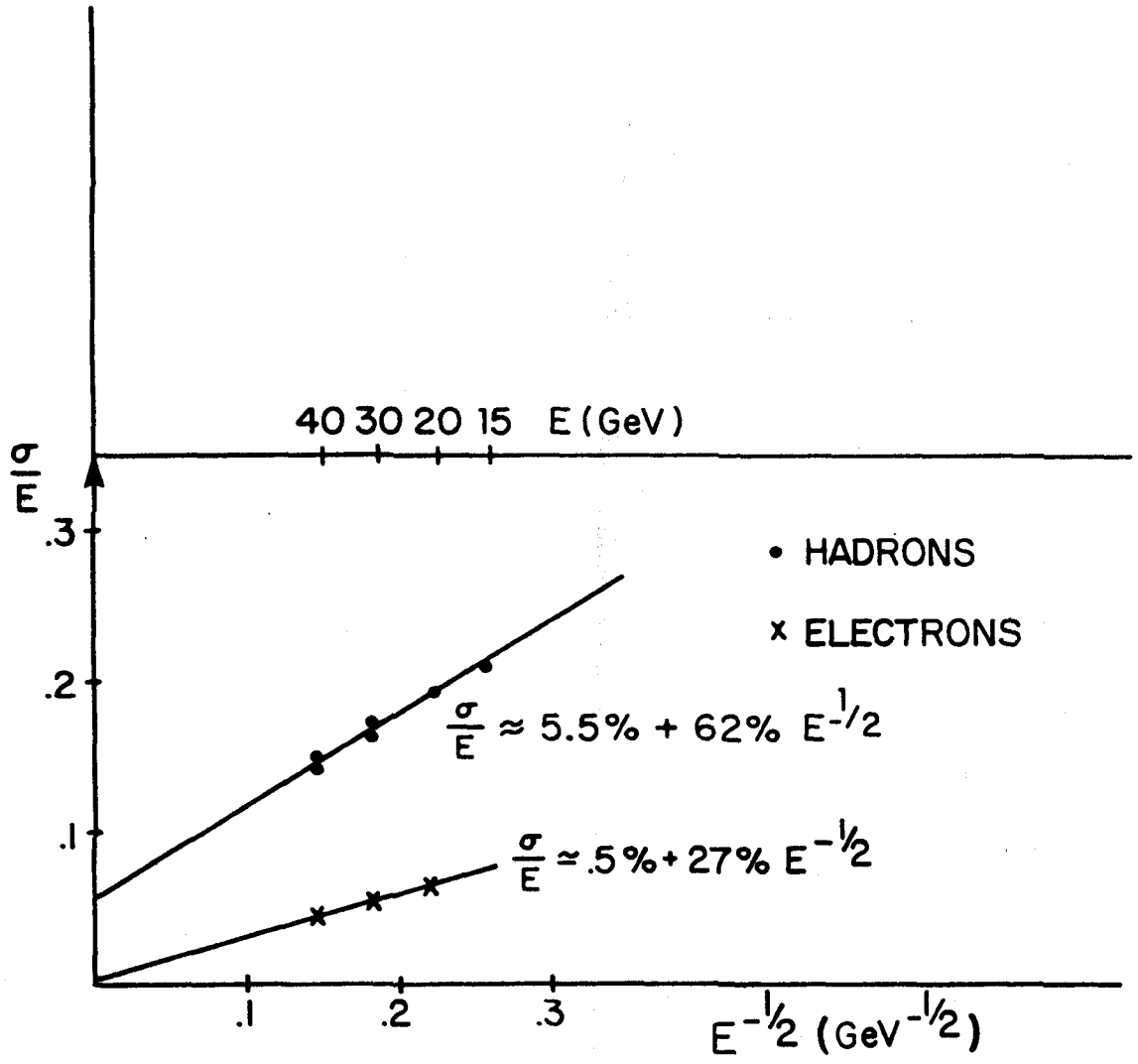
40 30 20 15 E (GeV)
σ/E
.3
.2
.1
• HADRONS
x ELECTRONS
σ/E ≈ 5.5% + 62% E^-1/2
σ/E ≈ .5% + 27% E^-1/2
.1
.2
.3
E^-1/2 (GeV^-1/2)

FIG. 4.29

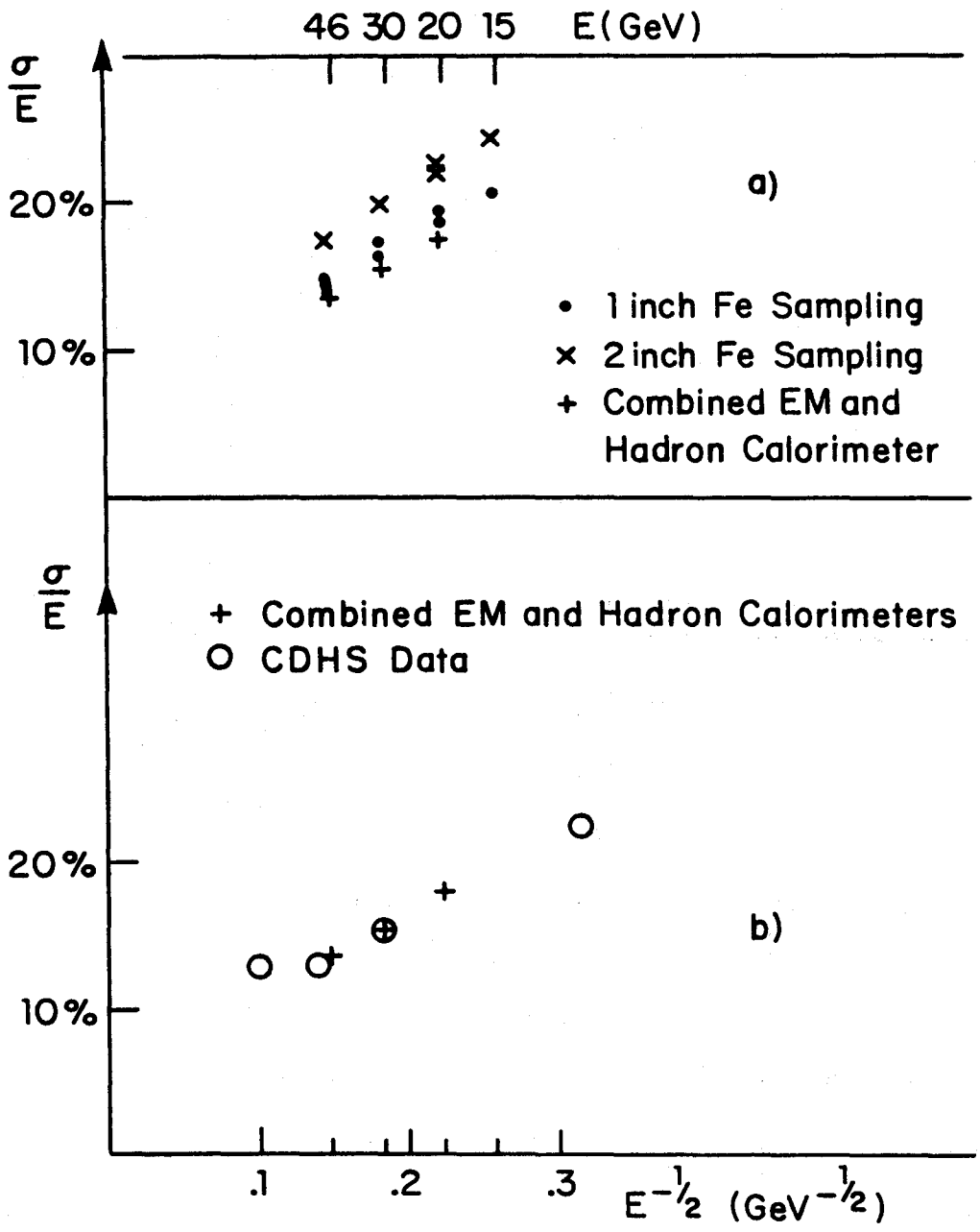
46 30 20 15 E(GeV)
σ/E
20%
10%
a)
• 1 inch Fe Sampling
× 2 inch Fe Sampling
+ Combined EM and Hadron Calorimeter
σ/E
+ Combined EM and Hadron Calorimeters
O CDHS Data
20%
10%
b)
.1
.2
.3
E^-1/2 (GeV^-1/2)

FIG. 4.30

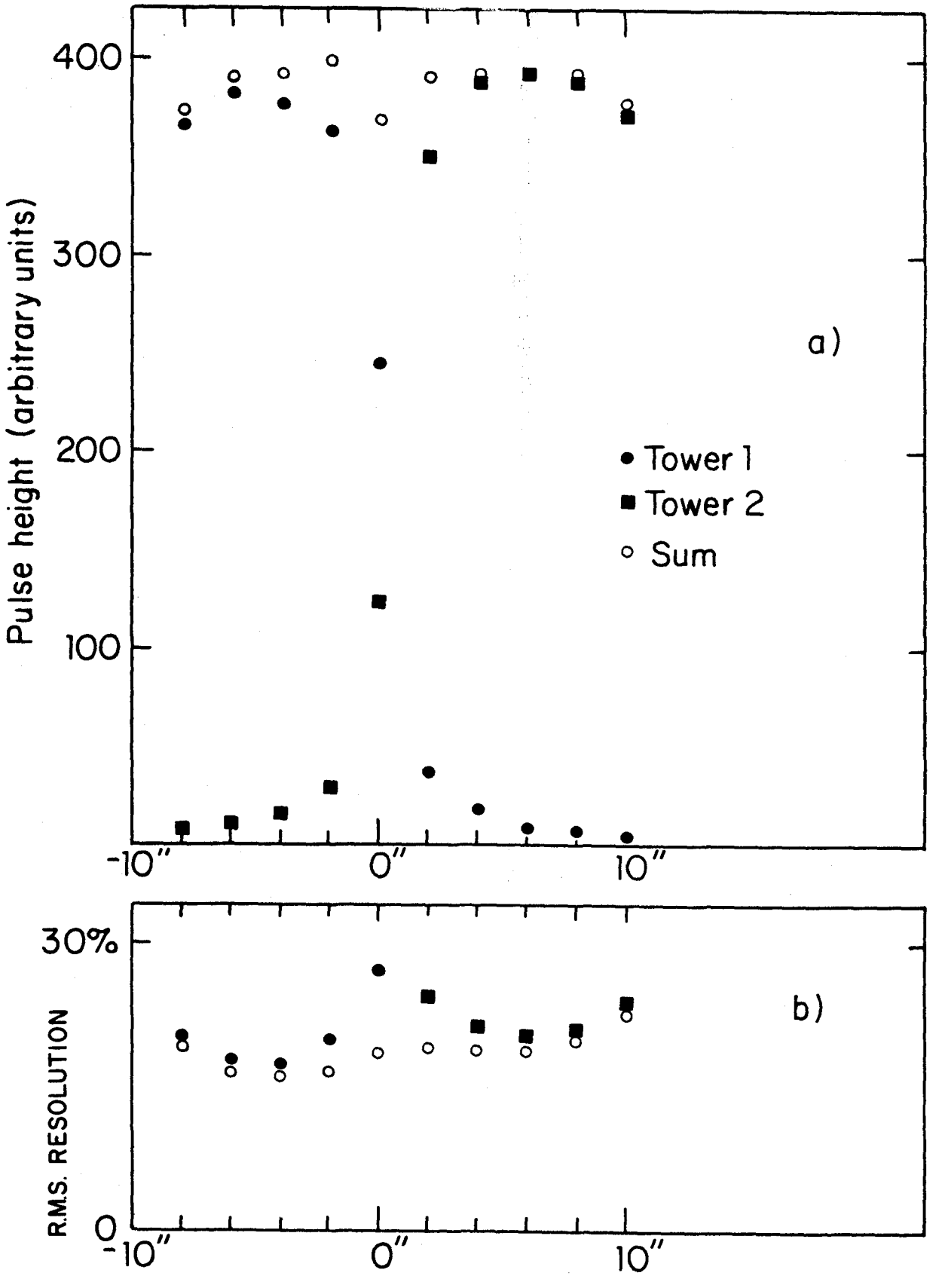
400
300
200
100
Pulse height (arbitrary units)
a)
• Tower 1
■ Tower 2
○ Sum
-10"
0"
10"
30%
0
R.M.S. RESOLUTION
b)
-10"
0"
10"

FIG. 4.31

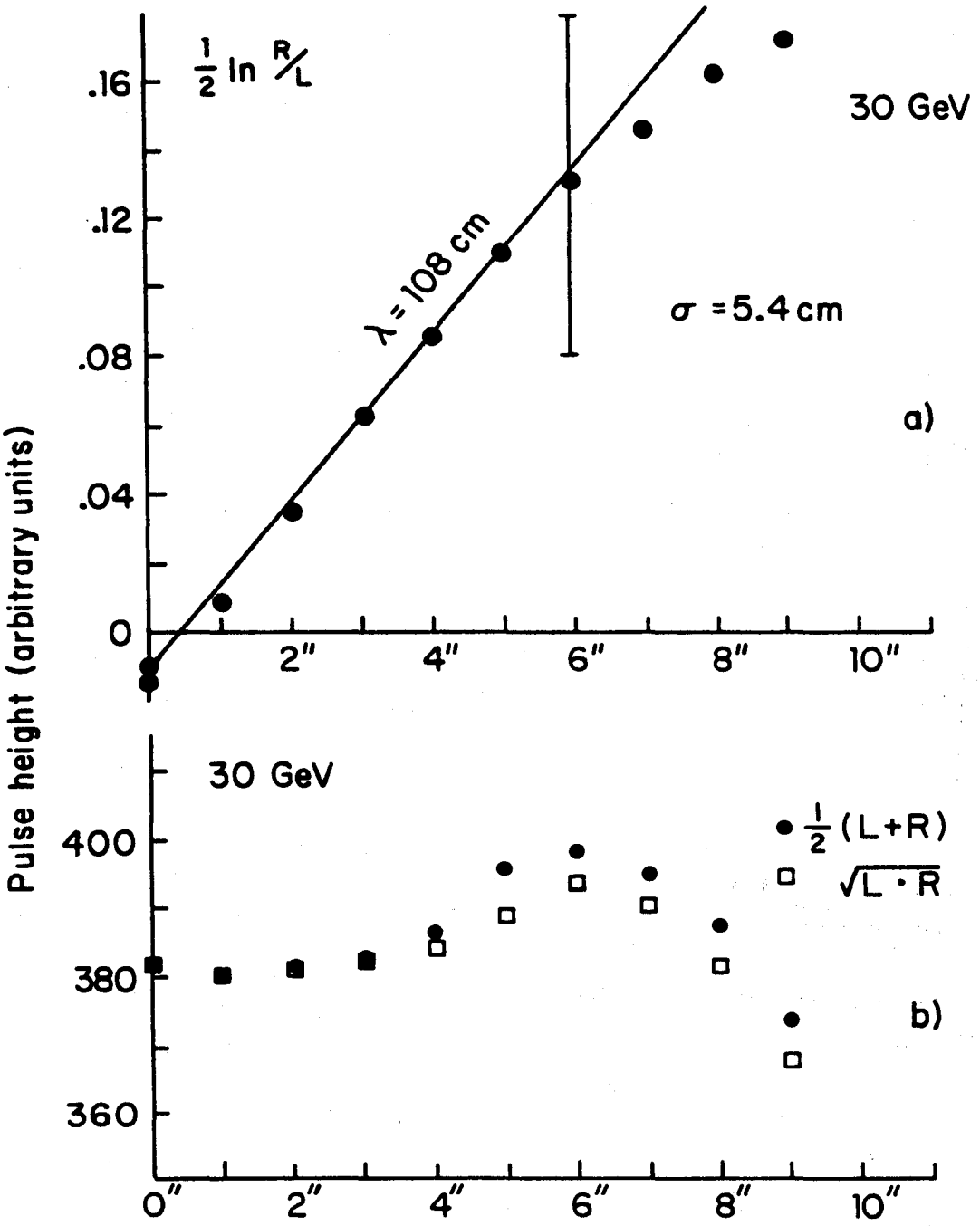
Pulse height (arbitrary units)
$\frac{1}{2}\ln R/L$
.16
.12
.08
.04
0
$\lambda = 108$ cm
$\sigma = 5.4$ cm
30 GeV
a)
2"
4"
6"
8"
10"
30 GeV
400
380
360
$\frac{1}{2}(L+R)$
$\sqrt{L \cdot R}$
b)
0"
2"
4"
6"
8"
10"

FIG. 4.32

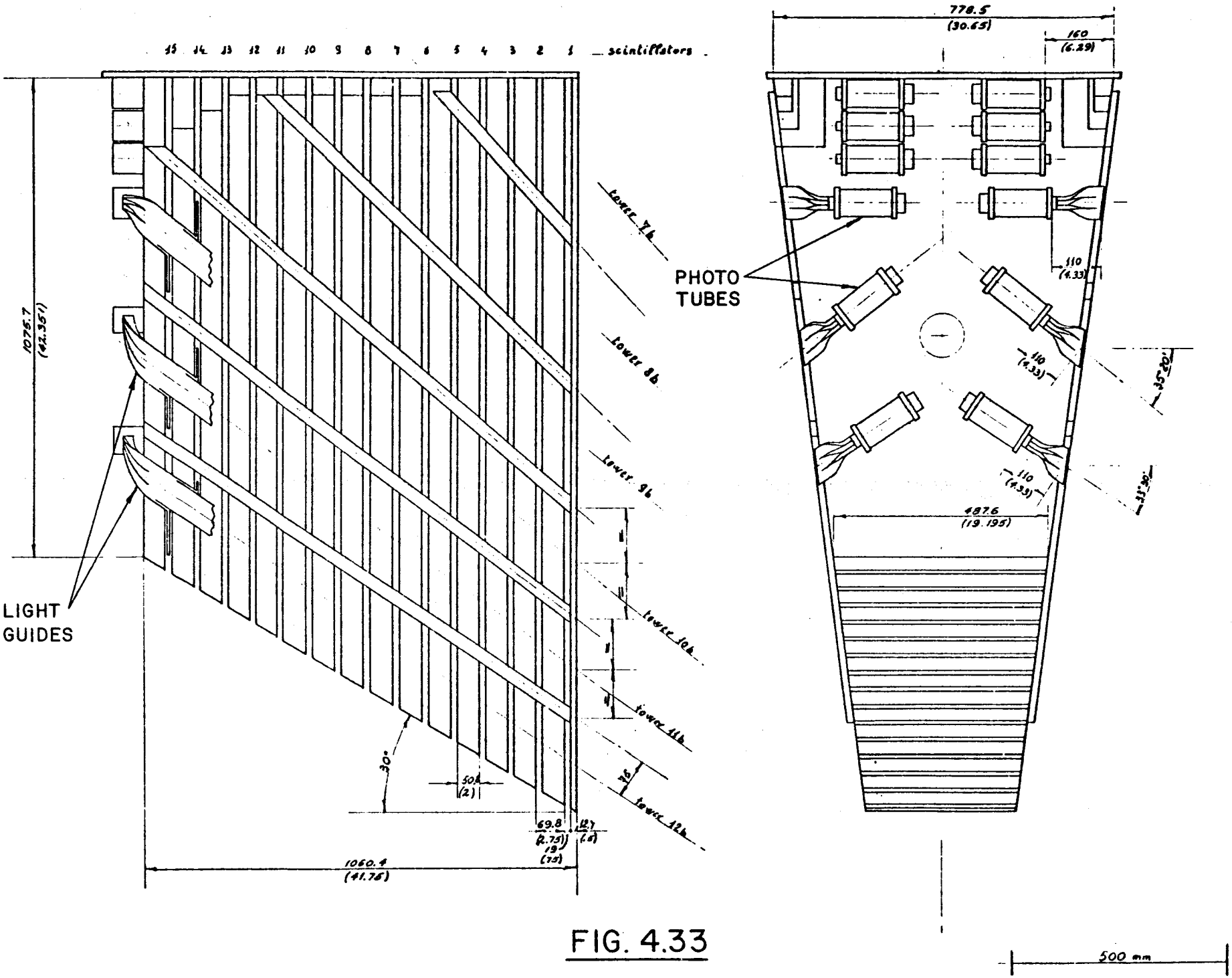
15 14 13 12 11 10 9 8 7 6 5 4 3 2 1 scintillators
1075.7
(42.351)
tower 7b
tower 8b
tower 9b
tower 10b
tower 11b
tower 12b
LIGHT
GUIDES
30°
50.8
(2)
69.8
(2.75)
19
(.75)
12.7
(.5)
1060.4
(41.76)
778.5
(30.65)
160
(6.29)
PHOTO
TUBES
110
(4.33)
35°20'
31°30'
487.6
(19.195)
500 mm

FIG. 4.33

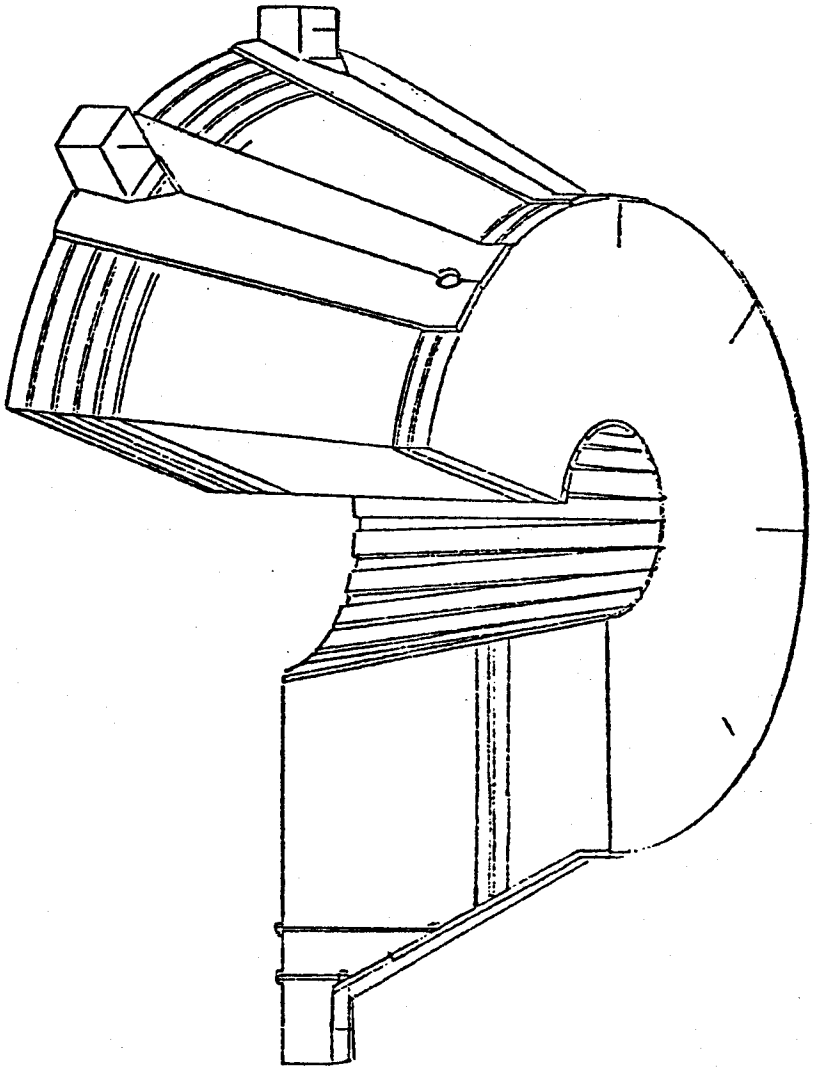

FIG. 4.34

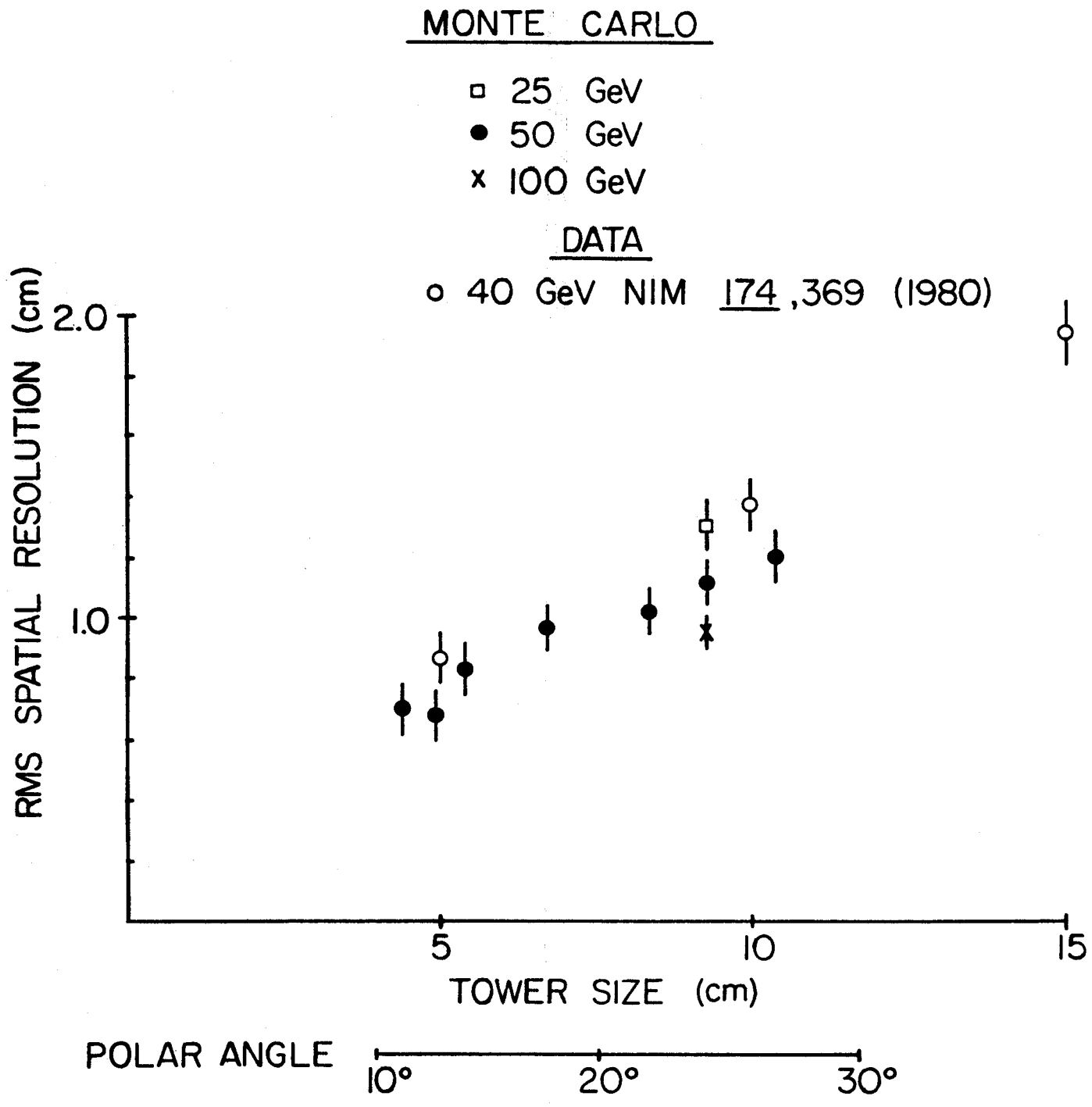
MONTE CARLO
25 GeV
50 GeV
100 GeV
DATA
40 GeV NIM 174,369 (1980)
RMS SPATIAL RESOLUTION (cm)
2.0
1.0
5
10
15
TOWER SIZE (cm)
POLAR ANGLE
10°
20°
30°

FIG. 4.35

Detail of

Hadron Calorimeter Chamber

Scale: 1 : 1

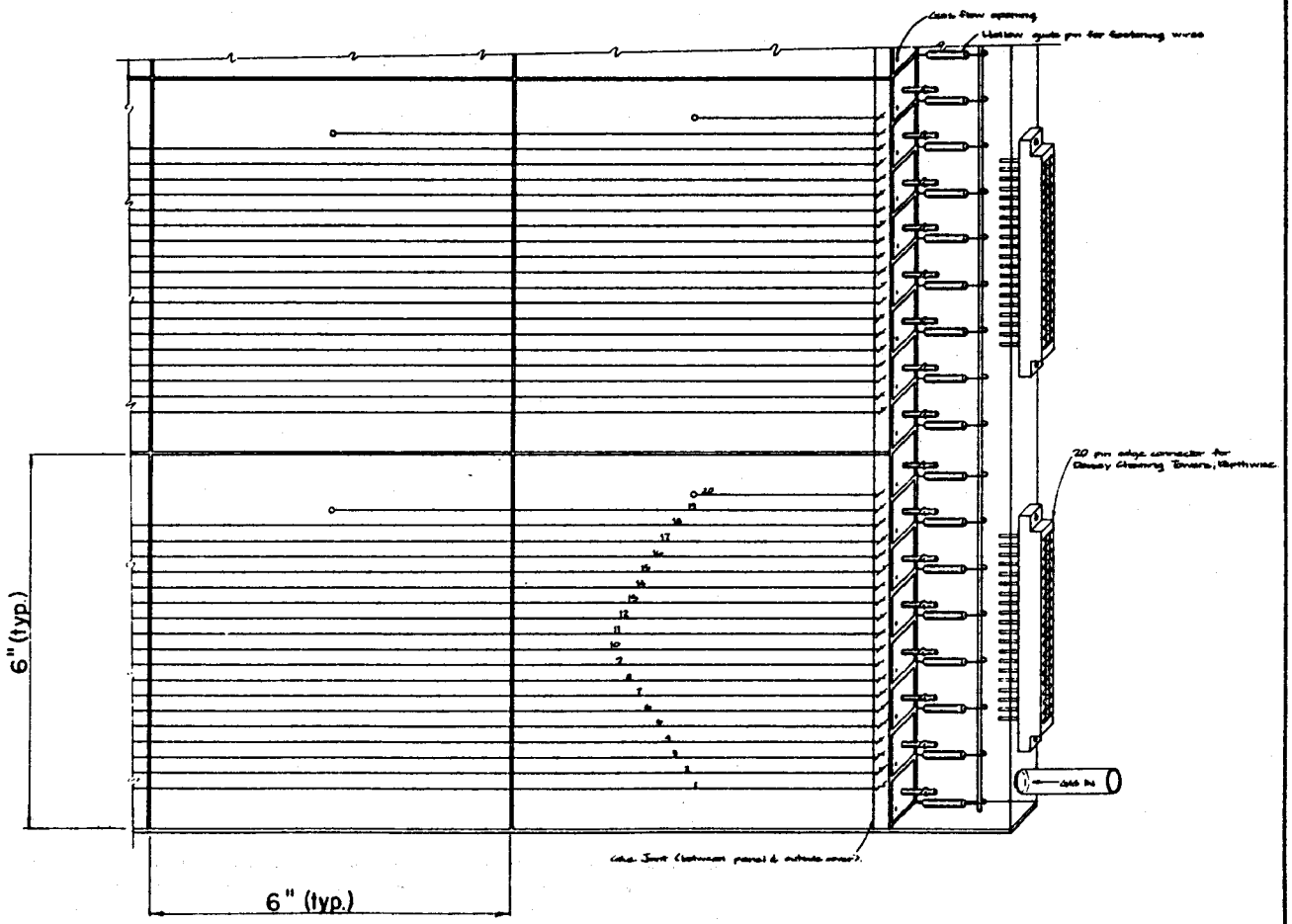

FIG. 4.36

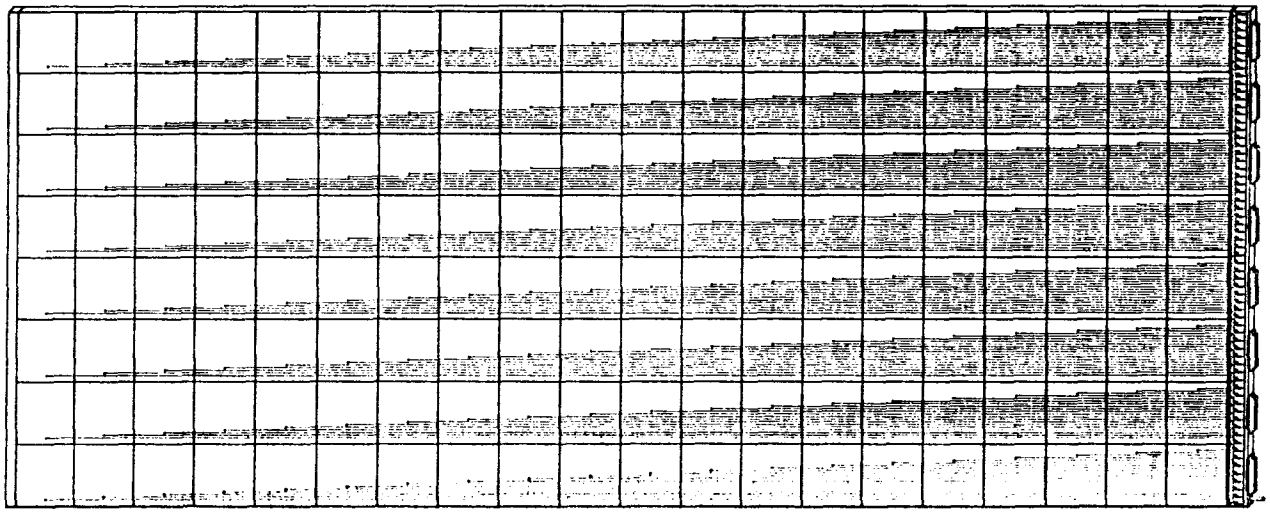

FIG. 4.37

Assembly Drawing of

Single Chamber Panel

Scale 2"=1'-0"

Chapter 5

TRACKING

5.1 THE CENTRAL AND INTERMEDIATE TRACKING SYSTEMS

The magnetic analysis provided by the central and intermediate tracking systems supplements the calorimetry by providing an independent measurement of the directions and momenta of charged particles. It is complementary to the calorimetry as it will have good resolution at low momentum where the performance of the calorimetry is poor. Furthermore, it permits detailed studies of the fragmentation of jets, which are seen with poor spatial resolution by the calorimeters. The main functions of the central tracking are:

1. To measure the momentum and direction of isolated charged particles with the best possible resolution.

2. To measure the momenta and directions of particles in tightly collimated jets and to provide position information for the calorimetry.

3. To measure the charge of leptons over the widest possible angular range and to improve the separation between electrons and pions by providing a consistency check between the momentum of a particle and the energy deposited in the electromagnetic shower counters.

The system we propose has two major components: a central tracking chamber covering the angular region $35°<\theta<145°$ and two endcap tracking chambers for the intermediate region between 10^{o} and 35^{o} (170^{o} to 145^{o}); the small angle region from 0^{o} to 10^{o} is discussed in section 5.2. Figure 5.1 shows the location

of the central tracking chamber and the two intermediate tracking chambers. The active length of the central tracking chamber is 2600 mm and each intermediate tracking chamber extends another 200 mm in the longitudinal direction. The 100 mm gap between the two chambers is reserved for preamplifiers and electrical and mechanical connections to the central tracking chamber.

The Central Tracking Chamber

In designing the central tracking chamber we have taken into account the experiences of similar solenoidal detectors at PEP, PETRA and CESR (Ref. 5.1-5.4). To gain experience in track reconstruction, we have used the CLEO track finding program to reconstruct Field-Feynman jets in a simulated central tracking chamber with a CLEO-like design. The results of these studies can be found in Appendix V. Although the performance of this chamber was satisfactory at low momentum, jets with high transverse momentum (70 GeV/c) were poorly reconstructed. The momentum resolution of single leptons resulting from W-decay was also disappointing as a large fraction of tracks were reconstructed with momenta significantly higher than that which the nominal momentum resolution of the chamber would predict. The defects of this system were caused by two factors:

1. Mixing of hits belonging to very close tracks and the loss of hits resulting from overlapping tracks.

2. The left-right ambiguity is not properly resolved.

Guided by this experience, we concluded that a better tracking system would be one where the right-left ambiguity is locally resolved by the introduction of half-cell staggered double planes. Monte Carlo studies (see Appendix V) indicated that the momentum resolution is significantly improved in this

scheme. In particular the long tails towards high momenta are absent.

The design of the central tracking chamber consists of a large open volume drift chamber with a total of 30 wire planes. The overall dimensions of the chamber are shown in Figures 5.2 and 5.3 and the relevant parameters are listed in Table 5.1. The cell size in the central tracking chamber has been kept small (15.7 mm) to reduce the number of multiple hits in a single cell. A small cell will also help to minimize systematic errors arising from uncertainties in the drift-distance vs time relationship due to the strong magnetic field. The 30 planes are divided into 22 planes of axial wires and 8 planes of small-angle stereo wires.

We have departed from the standard geometry by pairing the 22 axial planes into eleven half-cell staggered double planes. There are four major advantages to the half-cell staggered scheme:

1. One malady commmon to most cylindrical tracking chambers is the inability to resolve the right-left ambiguity for tracks passing very close to the individual sense wires. This effect is reduced in the current geometry as a track passing close to an axial wire in one plane will be far from the adjacent sense wire in the companion plane.

2. By examining the sum of drift times from two adjacent cells we will be able in an unambiguous way to determine whether one or more particles traversed a single cell. Although the sum of the two drift times (T1+T2) is not a constant, it is a well defined function of T1 and T2 that can be used in the pattern recognition. The measured drift times can be pre-processed before the pattern recognition to isolate adjacent wires consistent with a single particle passing between them, thereby reducing the

combinatorial background in the track finding routines.

3. Half cell staggering will provide a powerful method of calibrating the drift-time relationship. Using cells where only a single particle was present, we can use a constraint on the total drift distance to determine the drift-time relationship in a self-consistent manner.

4. The effective granularity of the chamber is increased by a factor of two in the half-cell staggered scheme. We can use this fact at the trigger level to help identify stiff tracks in the detector. In this respect we have an advantage over a chamber with half the cell size, as we can also apply loose cuts on the drift sum.

The remaining 8 planes of the central tracking system have been designated as small-angle stereo planes (SAS) and will provide the best measurement of the longitudinal position of a particle. The stereo angle (ξ) is ± 3.4 degrees, corresponding to ± 5 cells. The surface generated by these wires is a hyperboloid of revolution and hence the radial distance between the SAS wires and the axial wires is not a constant. For our case, the maximum change in the radial gap between the axial and stereo wires is 8.5 mm at R=360 mm and is negligible at larger radii.

The speed of the pattern recognition can be increased if the z position of the track is approximately known. For this reason we plan to implement 4 planes of wires with charge division electronics. We expect to achieve a resolution of 1% of the total wire length or about .01 * 2600 mm= 26 mm.

The detailed geometry of the sense wires is shown in Figure 5.4. The cell for the axial wires is an open hexagon, so that every sense wire is separated from its neighbors by at least one field wire. This will minimize the electrostatic

deflection of the sense wires as well as reduce cross talk between neighboring cells. Each wire in the chamber will be held by an injection molded feed-thru whose location is determined by a hole in the end wall of the chamber drilled by a numerically controlled machine. The location of the wires should be accurate to 40 microns. The diameter of the sense wires is 50 microns and the field wires are 150 microns in diameter. In Figure 5.5 we plot the electric field and in Figure 5.6 we show the magnitude of the E-field in the plane of the wires. For the SAS planes we have chosen an open cell geometry with 3 field wires separating each pair of sense wires, as shown in Figure 5.4. In total there are approximately 7400 axial wires and 2700 SAS wires.

Spatial Resolution

Both chambers will operate with an A-C_2H_6 (50%-50%) atmosphere. Figure 5.11 shows the drift velocity for various mixtures of A-C_2H_6 as a function of the applied electric field. Comparing with Figures 5.6 and 5.10, we conclude that the chamber will operate in a region where the drift velocity is saturated. In Table 5.3 we summarize our understanding of the relative magnitude of systematic errors for the central tracking chamber. The dominant error comes from the intrinsic resolution due to the diffusion of the electron swarm in the gas and the precision with which the space-time relationship can be measured in the magnetic field. We see no fundamental limitation to obtaining a resolution of 125 microns averaged over all cells in the chamber. Both the mechanical design and the electronics will be designed with this goal.

The Intermediate Tracking System

We describe here the radial wire drift chambers (Ref. 5.5) designed to cover the intermediate tracking region between 10 and 35 degrees as was shown in Figure 5.1. In this

configuration, the radial wires provide good azimuthal position information (ie. momentum resolution), good multi-track and high rate capability, and a smooth connection with the tracks in the central tracking chamber.

Each end cap will contain 120 wedge shaped drift chamber cells; each cell possessing 12 sense wires. The minimum drift spacing is 7.5 mm at a radius of 300 mm from the beam and increases linearly to a maximum of 32 mm at a radius of 1300 mm. Thus the length of each sense wire is 1000 mm. Figure 5.7 shows the end and side views of one drift chamber gap. The negative potential applied to thin resistive film (graphite) is increased with the gap width to provide a uniform electric field along the entire length of the wire. Every other sense wire is staggered by 500 microns in order to remove the right-left ambiguity.

Mechanically, the chamber will be constructed from two aluminum rings joined by a circular back plate (Figure 5.8). As in the case of the central tracking chamber, the sense and field wires are held by feed-thru's located by precision drilled holes in the aluminum rings. The cathode films separating adjacent cells are similarly held in tension between the two rings. High voltage is supplied to the cathode planes via a printed circuit board that also serves as a a gas seal and the inside cover of the chamber. Figure 5.9 is a cross-section through an assembled chamber.

The sense wires of each cell exert a total force of 0.6 kg of tension on the frame. The critical tension required for electrostatic stability is 20 grams. A value of fifty grams of tension is taken for a safety factor of 2.5.

Large electric fields can be achieved with this chamber configuration, and the electric field lines are very parallel at the midplane of the chamber as shown in Figure 5.10. The relation between the electric field, the magnetic field, and the electron path is given by $v_M = k\ E \sin\theta\ /B$ where v_M is the magnetic drift velocity, k ($k \simeq 1.0$) is a factor which comes from averaging the electron drift times over a Maxwellian

distribution and θ is the angle between the electron drift direction and the electric field. A resolution in azimuth of 200 microns or better should be possible. Using typical values for the drift velocity (v_M = 5 x 10^4 m/sec), the magnetic field (B = 1.5 T) and the electric field (E = 2 x 10^3 V/cm), we obtain a drift angle (θ) of 30 degrees. For this electric field, the drift velocity should be completely saturated over the entire cell.

The coordinate along the sense wire can be determined using charge division. Note that we can run this chamber at high gain, thereby reducing errors due to time slewing and noise. As in the case of the cylindrical tracking chamber, we anticipate a spatial resolution of 1% of the wire length or about 10 mm. Providing one half the wires with charge division electronics should be adequate for pattern recognition and resolution in the radial direction. A prototype consisting of three cells is currently under construction and will be tested shortly.

5.2 FORWARD-BACKWARD TRACKING

INITIAL DESIGN OF TRACKING CHAMBERS

Since we anticipate a large, but relatively unknown, flux at small angles, it is important that the small angle (2° - 10°) tracking chambers be designed so as to minimize the information lost by overloaded wires near the beam. The basic design of the chambers will be drift chambers where the ionization drifts in the radial direction. The sense wire spacing is 2 cm and includes a cathode pad readout. The basic unit will be an equilateral triangle with a radius of approximately 3 1/2 ft., the diameter of the hole in the first toroid (Fig. 5.12). We plan to offset the wires in an adjacent plane by 1 cm to resolve the drift chamber ambiguity. We estimate each chamber contains 100 wires/triangle or 600 channels/chamber.

The cathode plane contains pads which localize the hit to approximately 0.4 units of rapidity. This requires 4 rows of pads, covering from 2.4 to 4.0 in rapidity. For azimuthal coverage we plan to cover every 3.75° for small angles (first 2 rows) and 1.875° for the 2 rows furthest from the beam pipe, which requires 96 pads/triangle or 576 pads/chamber.

To resolve the inherent x-y ambiguity (r-θ in our case) we propose to rotate the second chamber by 30° which gives stereo reconstruction. The second chamber would be the same size as the first, see Fig. 5.13.

The third chamber would be somewhat larger although otherwise similar to the first plane, with 900 wires and 5 rows of pads (768 pads in all). The total electronics list is:

2100 channels of TDC	(drift chamber wires)
1920 channels of ADC	(cathode pads)

References

5.1 B. Davies White, et. al, NIM, 160, 227 (1978).

5.2 H. Boerner, et. al., NIM, 176, 176 (1980).

5.3 W. DeBohr, et. al., NIM, 156, 249 (1978) and W. DeBohr, et. al., NIM, 176, 176 (1980).

5.4 K. Berkelman, "Suitability of Open Grid Cylindrical Drift Chambers for Charged Particle Tracking at 100 GeV Energies", Cornell Preprint CZF 81-5 (March 1981).

5.5 M. Atac, "Radial Wire Chambers for CDF", CDF note 53, (May 1980).

Table 5.1

CENTRAL TRACKING CHAMBER

Number of Planes:	19
(Axial planes counted one per double plane)	
Number of axial wire double planes:	11
Number of SAS planes:	8
Innermost Radius*:	R_o = 300 mm
Radii*:	$R_n = R_o + (n-1)60$ mm
Number of Wires per Plane:	$M_n = 120 + (n-1)24$
Cell size*:	15.708 mm
Total number of axial wires:	7392
Total number of SAS Wires:	2688
Total number of sense wires:	10080
Stereo angle:	$3.43° \leq \lvert\xi\rvert \leq 3.45°$
Maximum change of radius of SAS wires:	8.5 mm

Wire Configuration

ZZ U ZZ V ZZ U ZZ V ZZ ZZ ZZ U ZZ V ZZ U ZZ V ZZ

*For axial double planes, the value given is the average of the two layers.

Table 5.2

RADIAL WIRE CHAMBER PARAMETERS

Minimum Drift Space:	7.85 mm
Maximum Drift Space:	34 mm
Maximum Drift Length at 1.5 T:	39 mm
Maximum Drift Time:	.980 micro sec
σ_ϕ	200 microns
σ_r	10 mm
Number of Wires per Endcap:	1440
Number of Charge Division Readouts/end:	720
Total Number of TDC Channels:	2880
Total Number of ADC Channels:	2880

Table 5.3

SYSTEMATIC ERRORS

		σ (microns)
I.	Mechanical	
	Wire placement	40
	Gravitational sag (corrected to 10%)	20
	Electrostatic	40
		60
II.	Timing Uncertainties	
	Start time (.5 nsec)	25
	TOF (.1 nsec)	5
	Signal propagation (.1 nsec)	5
	TAC calibration 1 nsec/$\sqrt{12}$	14
	TAC resolution 1 nsec/$\sqrt{12}$	14
		32
III.	Parameters	
	High voltage (1 V)	$\curvearrowleft$
	Temperature (2° C)	15
	Pressure (0.1 atm)	10
	Time slewing 4 nsec/$\sqrt{12}$	58
	Gas composition (1% variations)	30
		67
IV.	Drift Time	
	Intrinsic	60
	Space time	50
		78

Total system resolution $\curvearrowleft$ 125 μ.

Figure Captions

Fig. 5.1 Relative positioning of the central tracking system showing the relationship of the central tracking chamber to the intermediate tracking chambers.

Fig. 5.2 Quarter end section of the central tracking chamber.

Fig. 5.3 Elevation view of the central Tracking chamber.

Fig. 5.4 Detail of the central tracking chamber showing the drift cell structure.

Fig. 5.5 Shape of the electric field for one of the hexagonal cells in the central tracking chamber.

Fig. 5.6 Magnitude of the electric field in the plane of the sense wires for a hexagonal cell.

Fig. 5.7 Side and end view of a radial wire drift chamber cell.

Fig. 5.8 Perspective view of the radial wire chambers.

Fig. 5.9 Cross section through the intermediate tracking chamber.

Fig. 5.10 Schematic diagram showing the relationship between the electric field, magnetic field and drift angle for the intermediate tracking chamber.

Fig. 5.11 Drift velocity vs. E field for A-C_2H_6 (from Ref. 5.1).

Fig. 5.12 Pad (cathode) arrangement showing radial (rapidity) segmentation ($\Delta\eta \simeq 0.4$) and azimuthal segmentation ($\Delta\phi = 1.875°$ and $3.75°$).

Fig. 5.13 Drift wire (anode) configuration for the backward detector tracking chambers showing 0° and 30° (stereo) rotation.

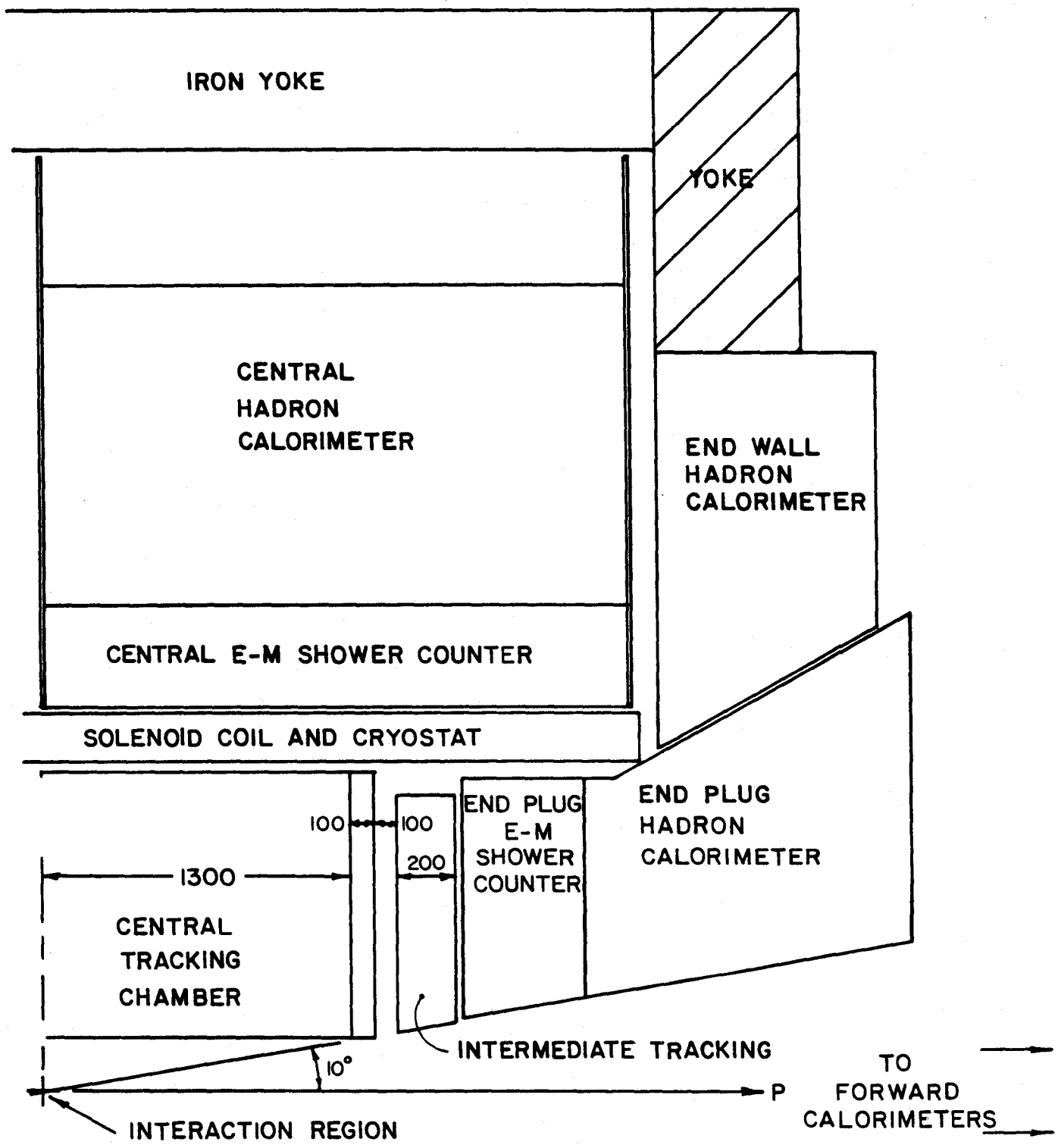
IRON YOKE
YOKE
CENTRAL
HADRON
CALORIMETER
END WALL
HADRON
CALORIMETER
CENTRAL E-M SHOWER COUNTER
SOLENOID COIL AND CRYOSTAT
100
100
200
1300
END PLUG
E-M
SHOWER
COUNTER
END PLUG
HADRON
CALORIMETER
CENTRAL
TRACKING
CHAMBER
INTERMEDIATE TRACKING
10°
P
TO
FORWARD
CALORIMETERS
INTERACTION REGION

FIG. 5.1

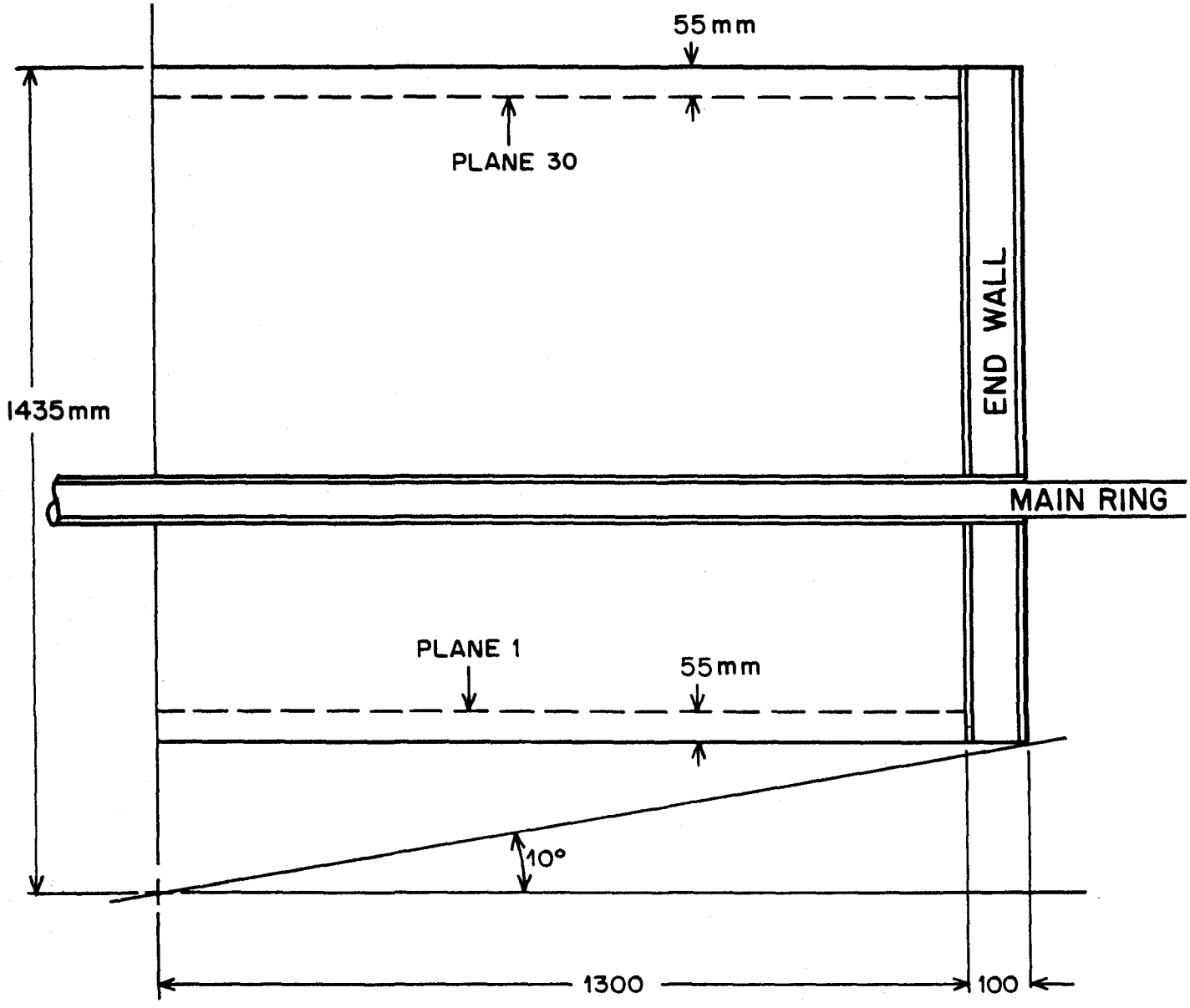
55mm
PLANE 30
END WALL
1435mm
MAIN RING
PLANE 1
55mm
10°
1300
100

FIG. 5.2

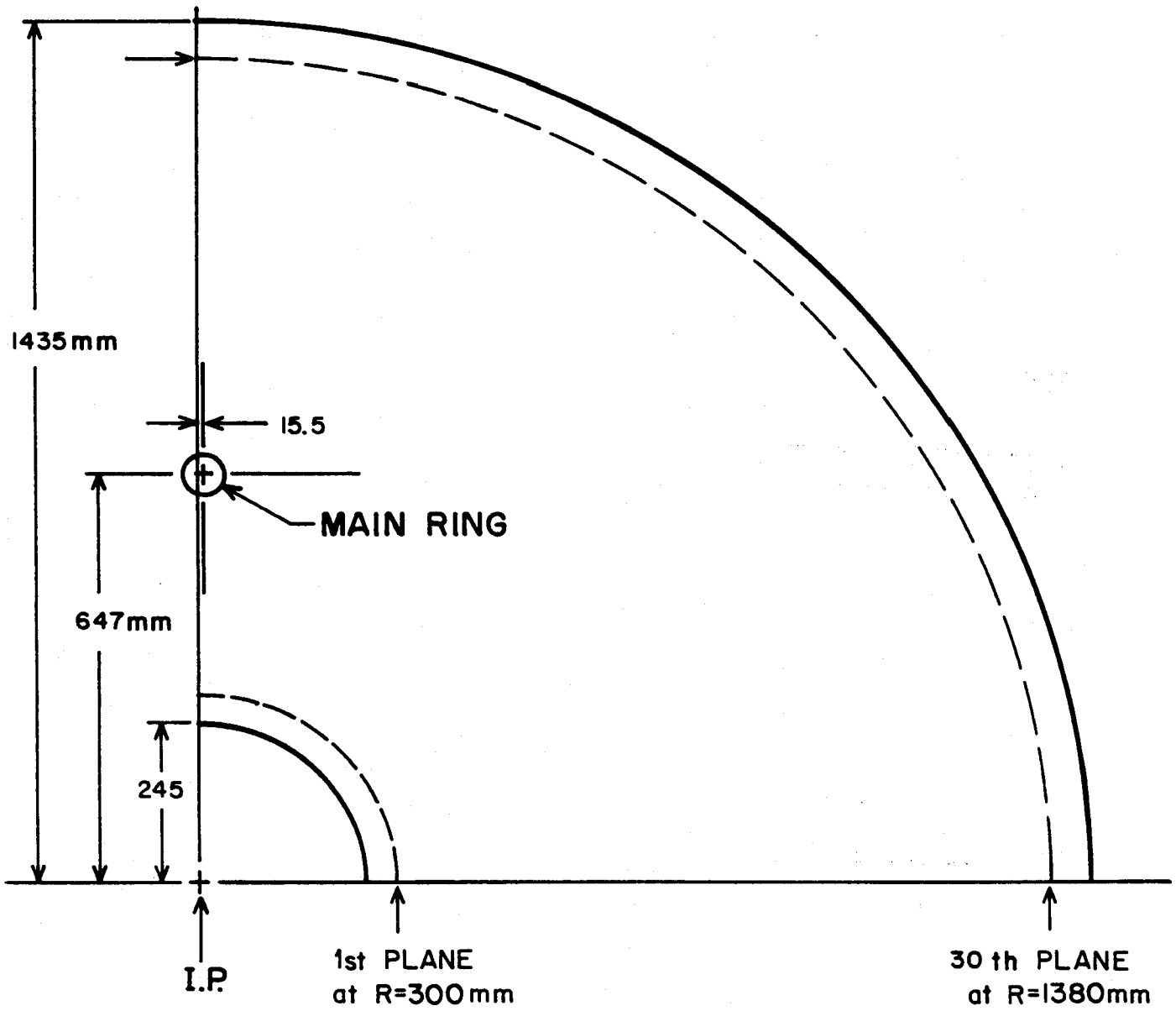
1435mm
15.5
MAIN RING
647mm
245
I.P
1st PLANE
at R=300mm
30 th PLANE
at R=1380mm

FIG. 5.3

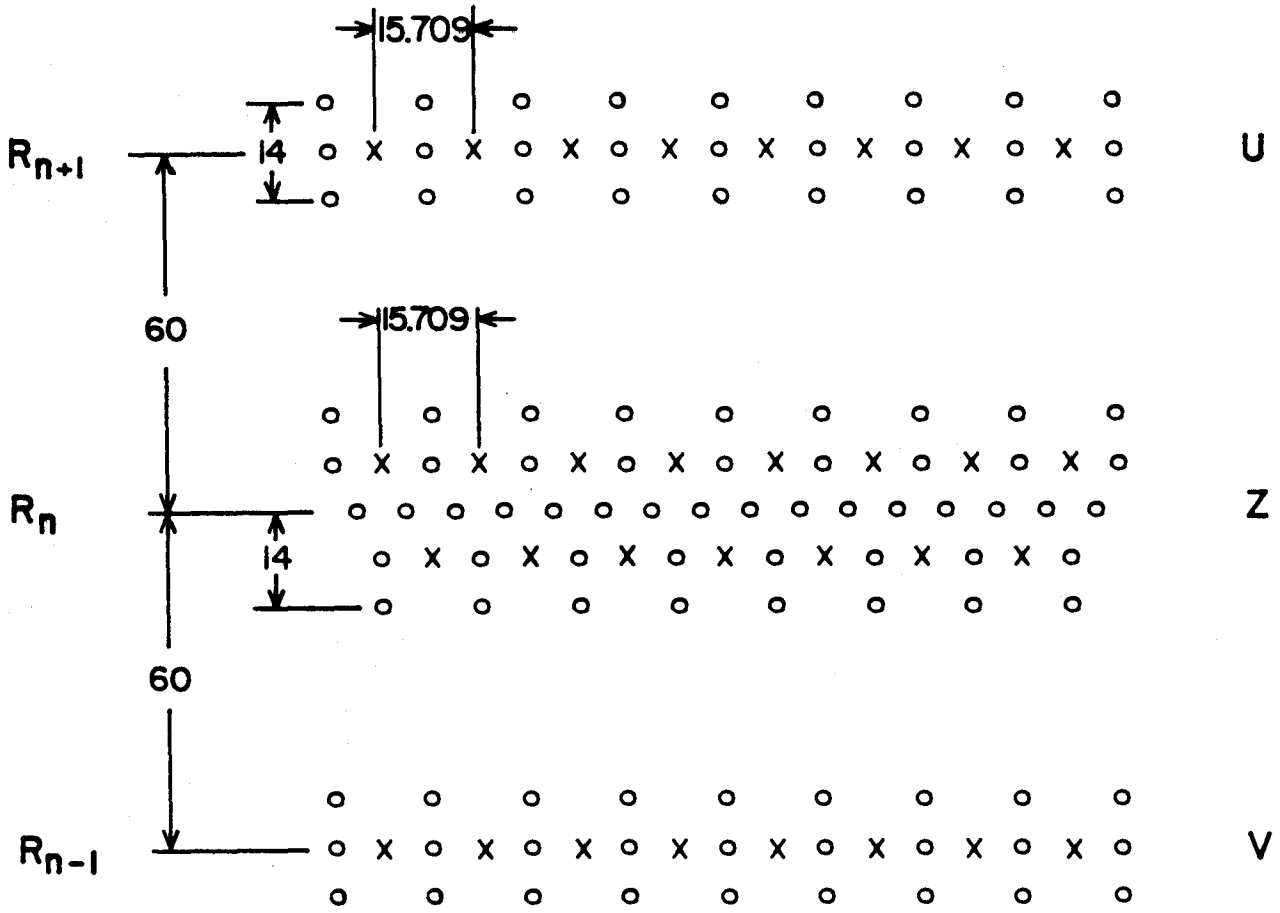

X – SENSE WIRE
o – FIELD WIRE

FIG. 5.4

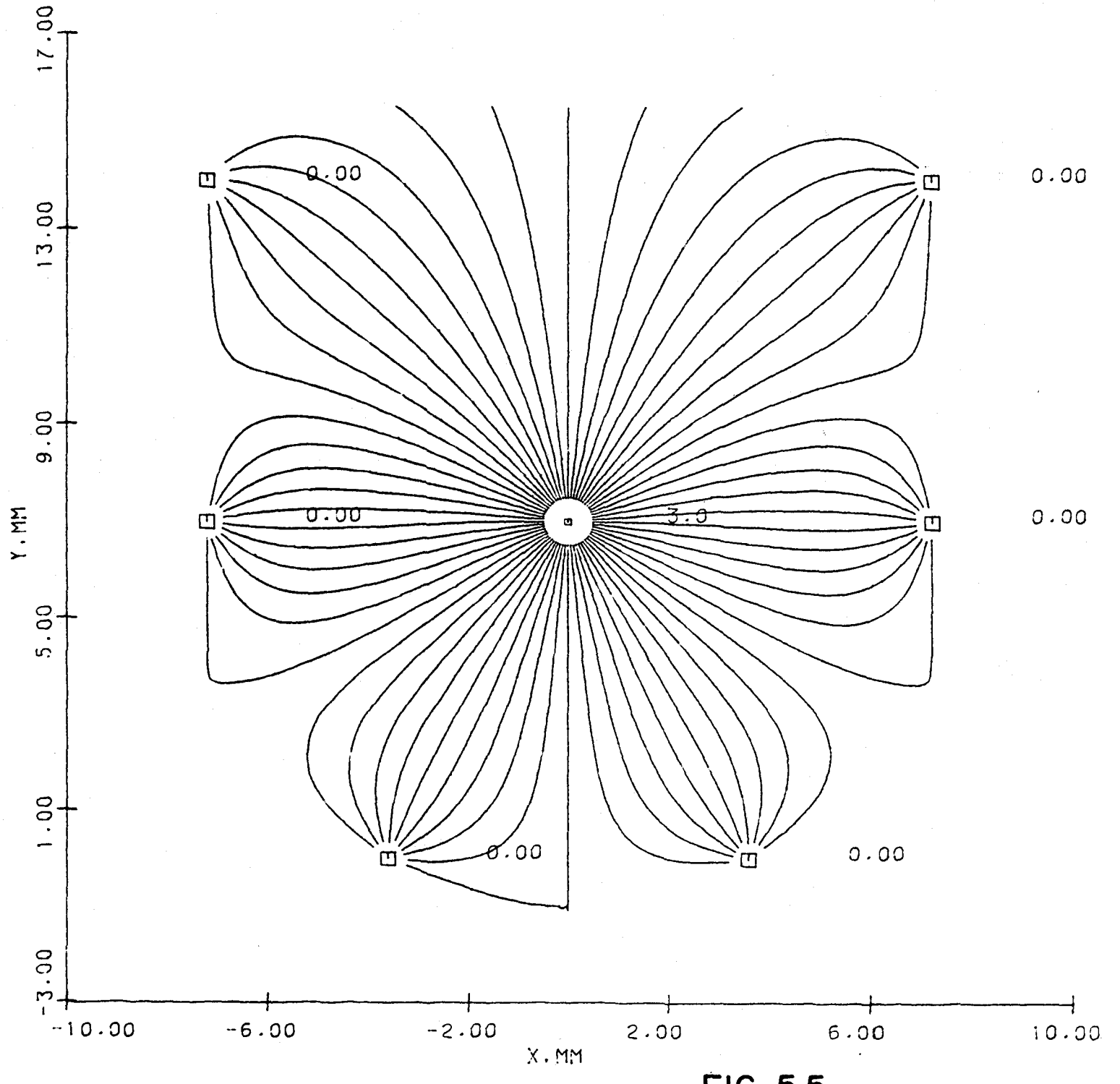
17.00
13.00
9.00
5.00
1.00
-3.00
Y.MM
0.00
0.00
0.00
3.0
0.00
0.00
0.00
-10.00
-6.00
-2.00
2.00
6.00
10.00
X.MM

FIG. 5.5

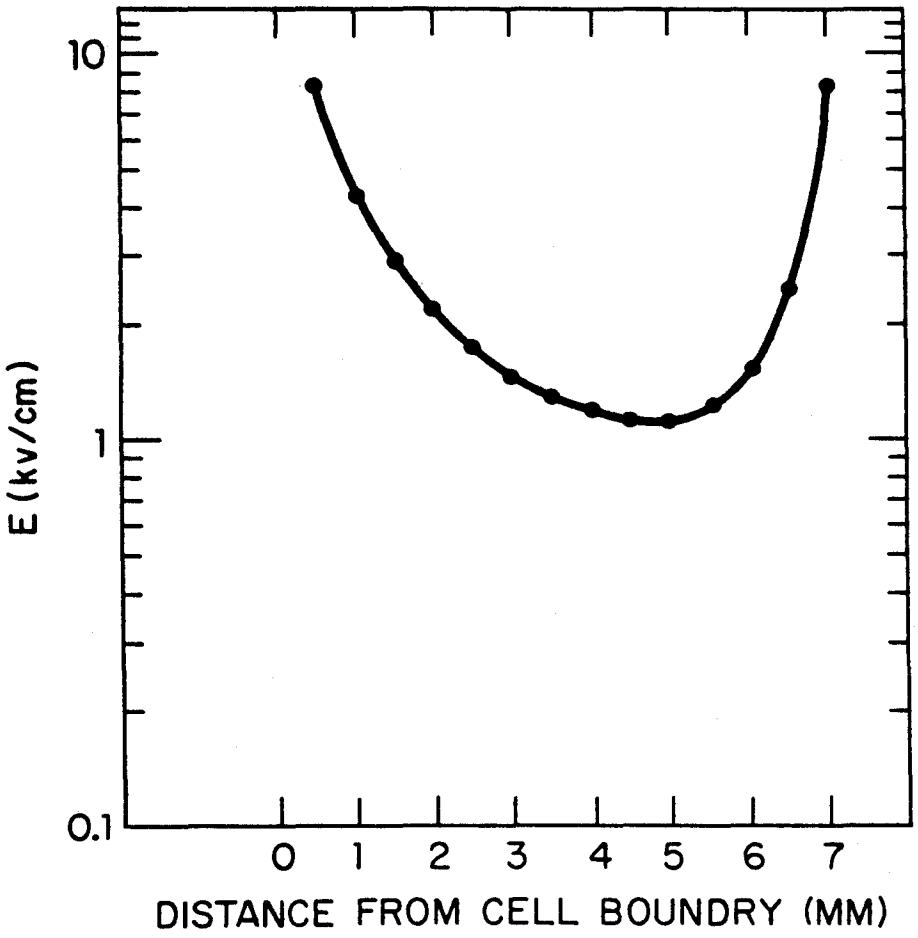

FIG. 5.6

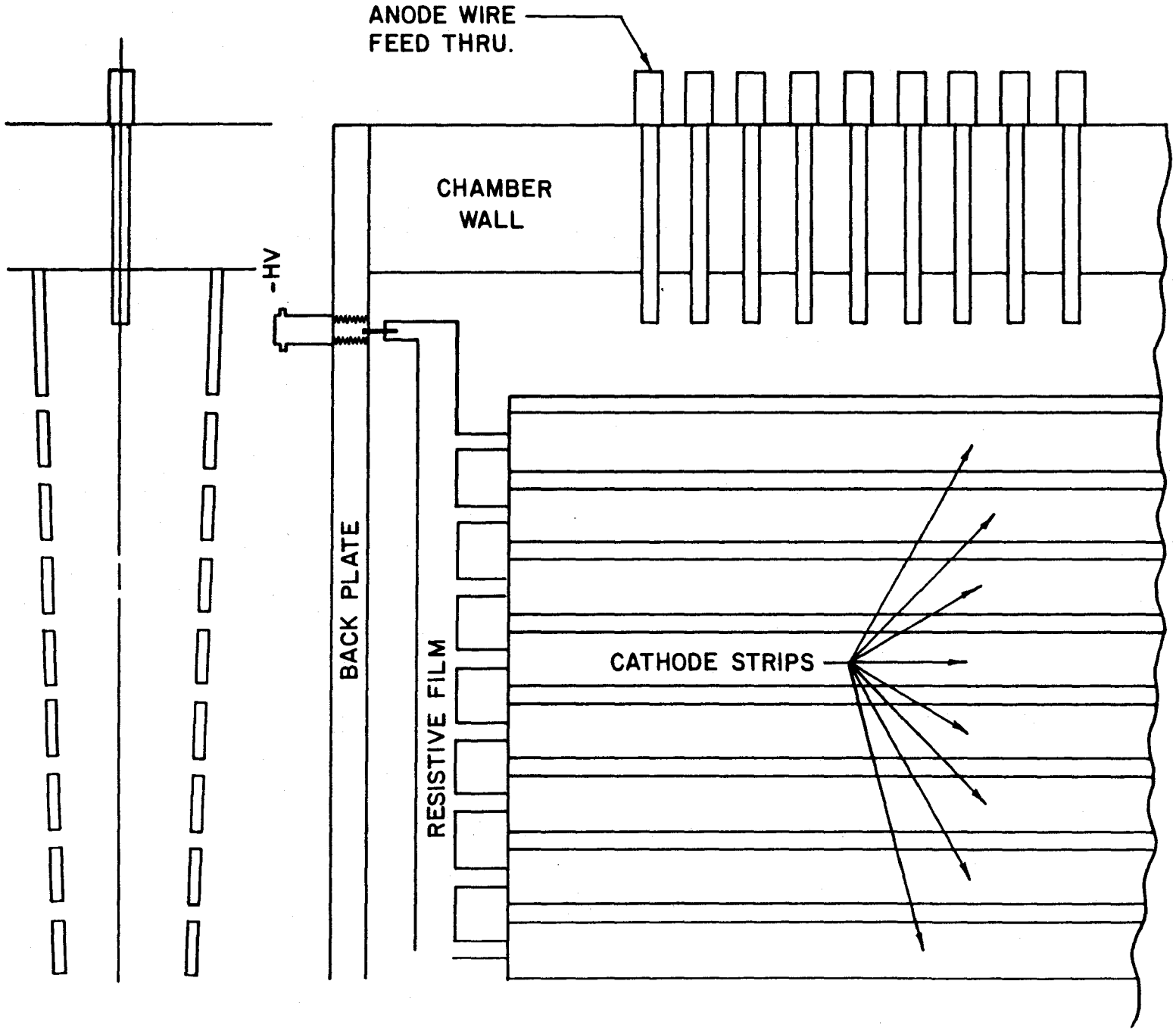
ANODE WIRE
FEED THRU.
CHAMBER
WALL
-HV
BACK PLATE
RESISTIVE FILM
CATHODE STRIPS

FIG. 5.7

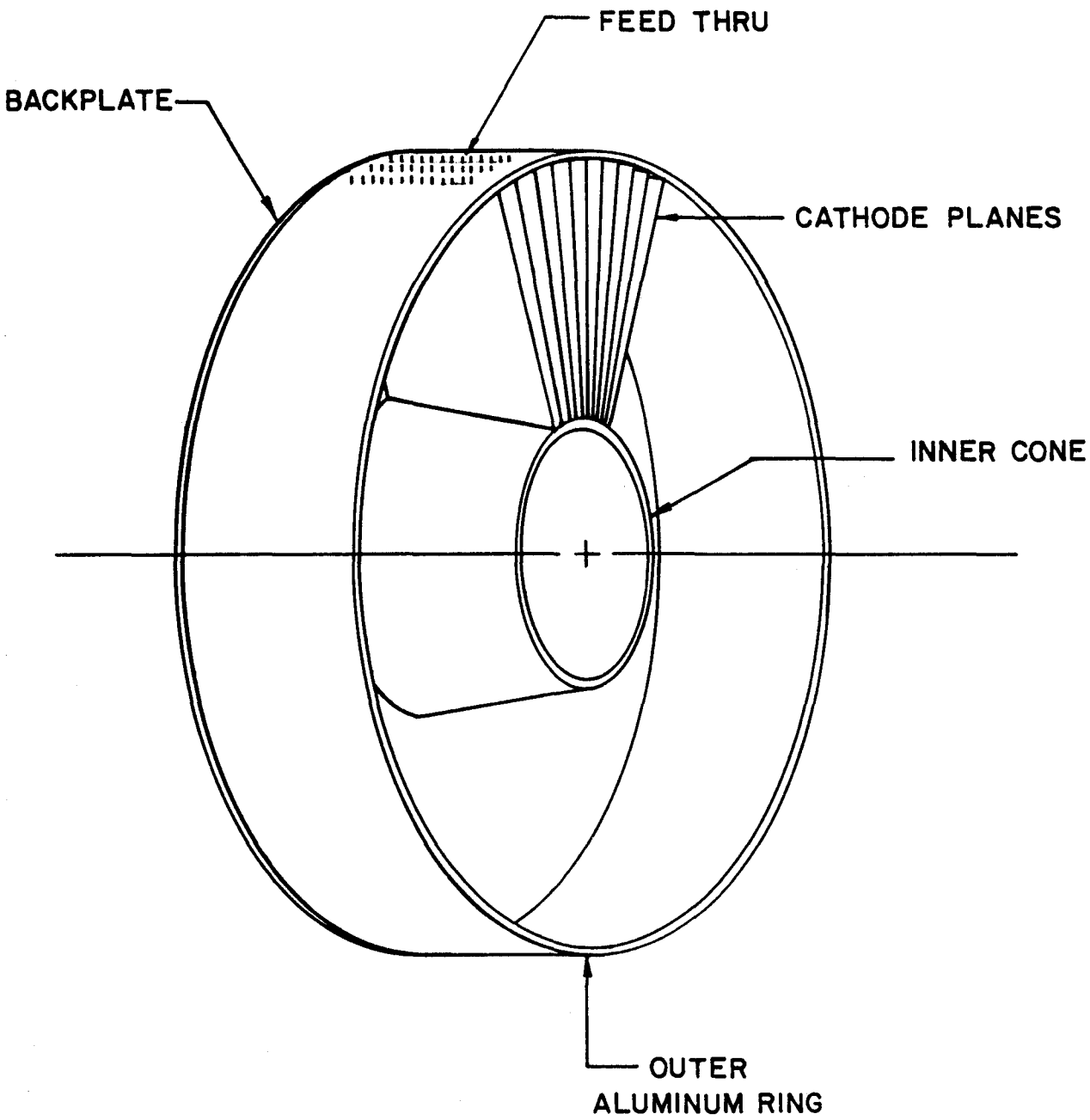
FEED THRU
BACKPLATE
CATHODE PLANES
INNER CONE
OUTER
ALUMINUM RING

FIG. 5.8

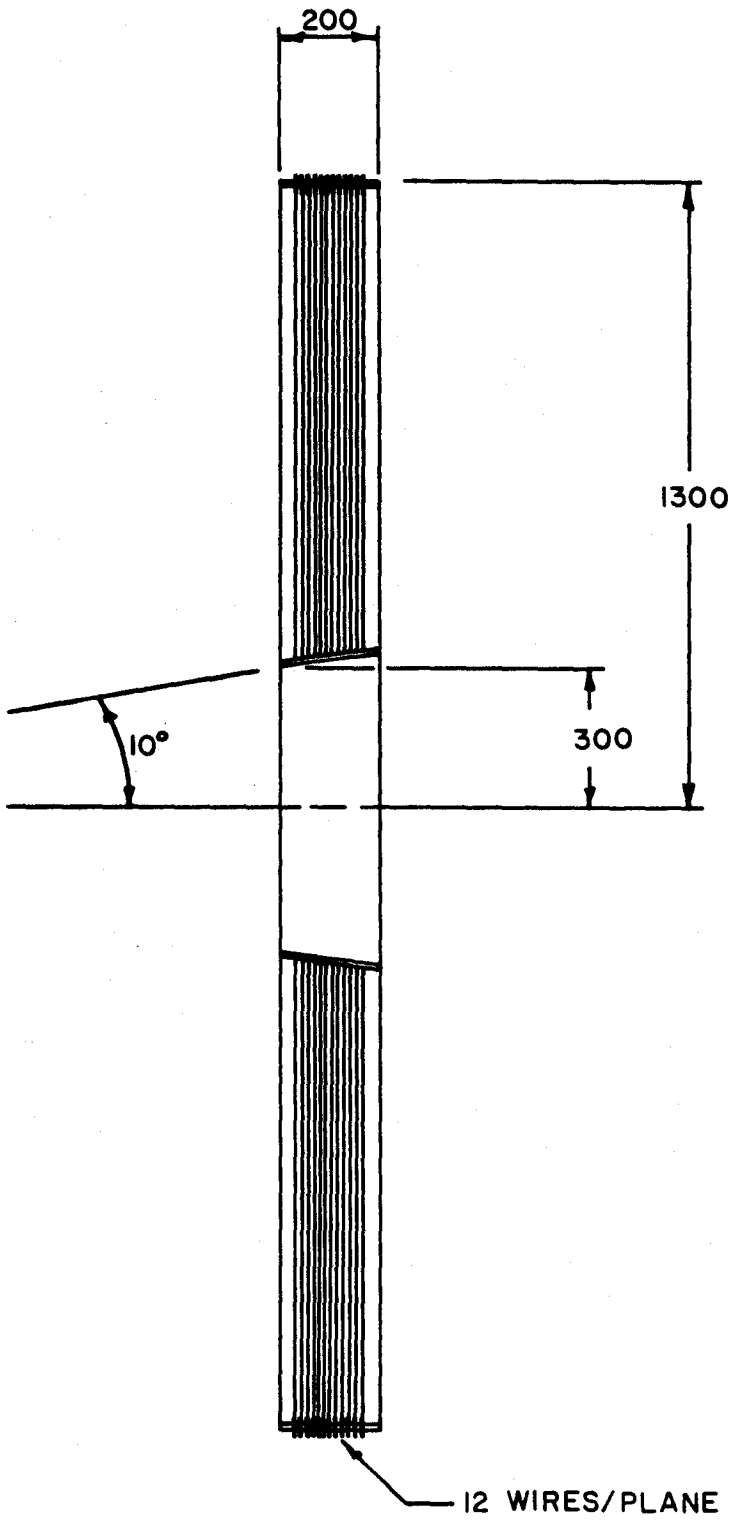

FIG. 5.9

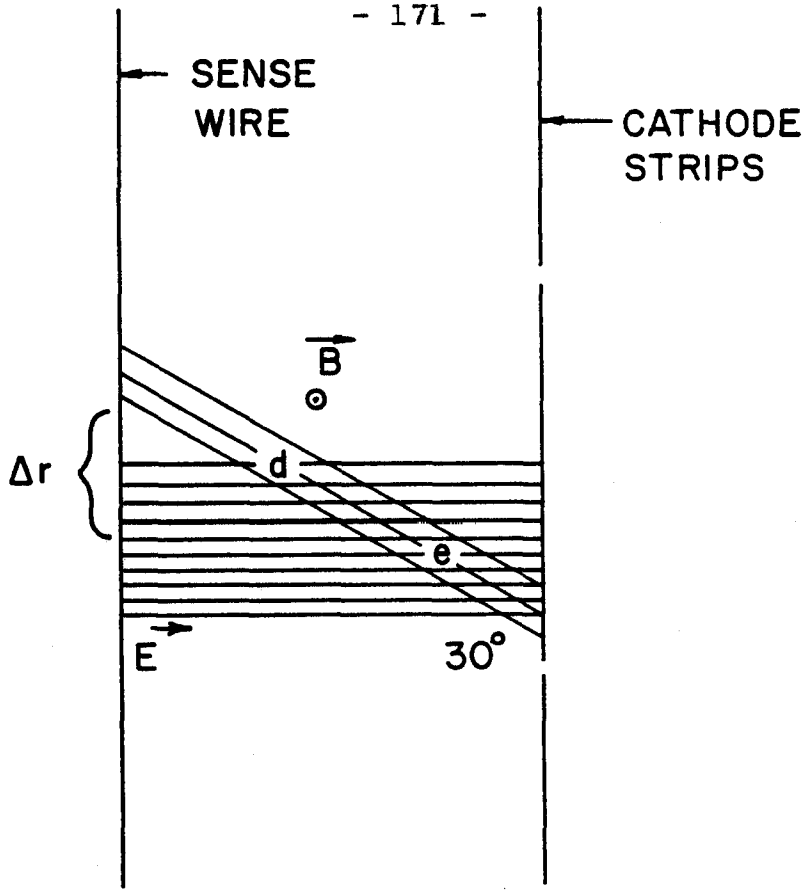

FIG. 5.10

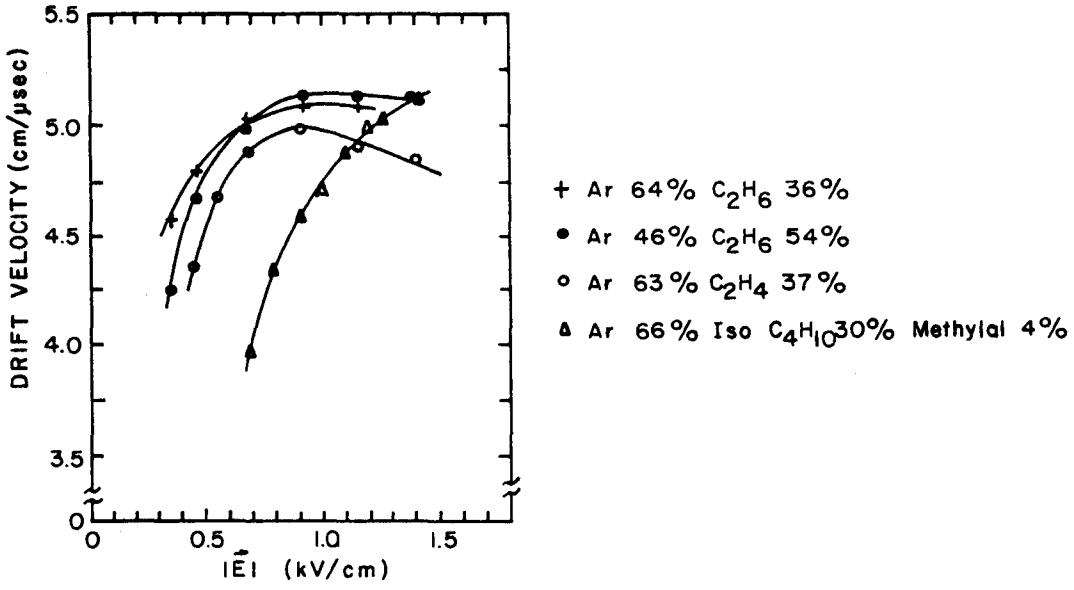

FIG. 5.11

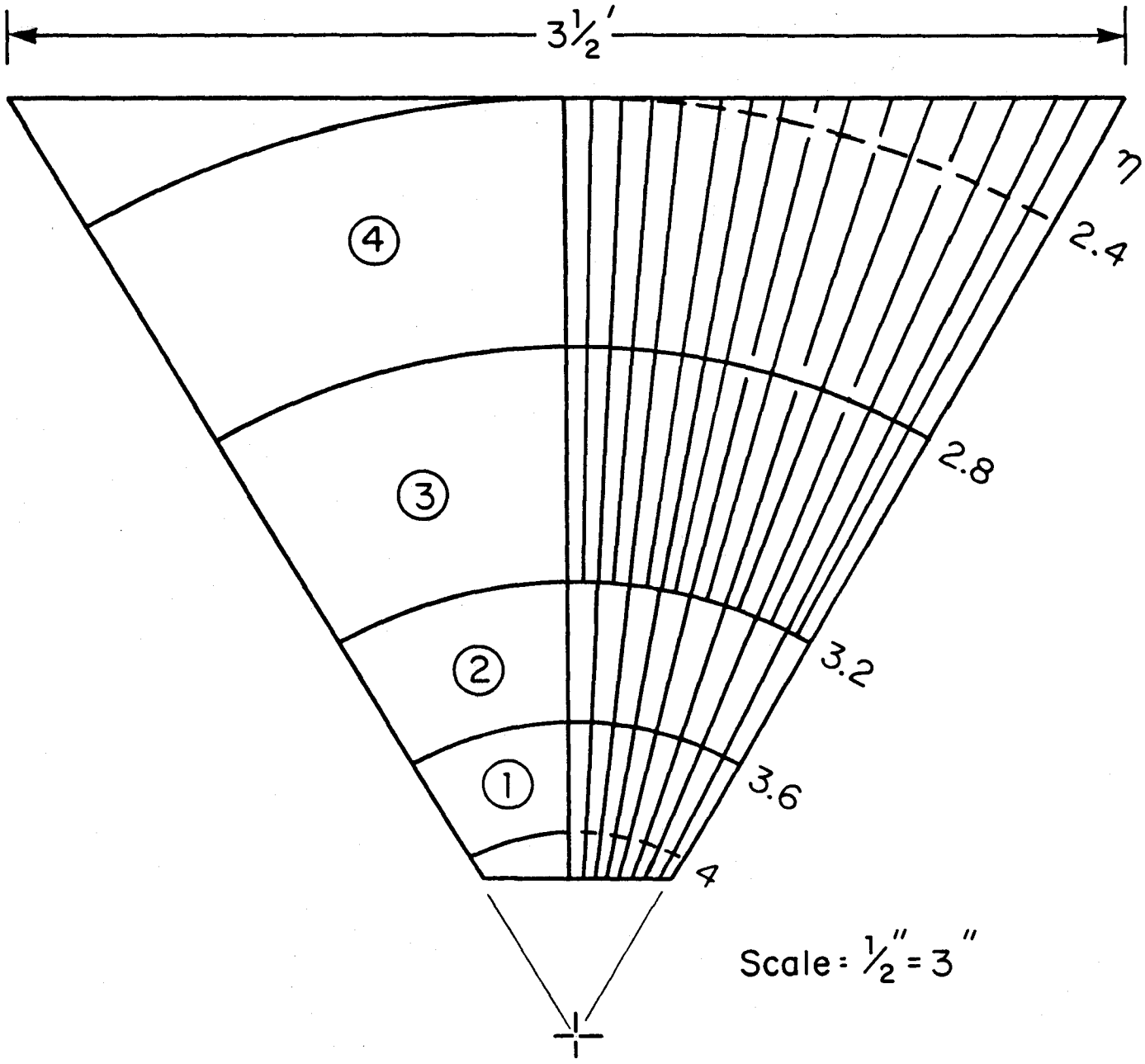

FIG. 5.12

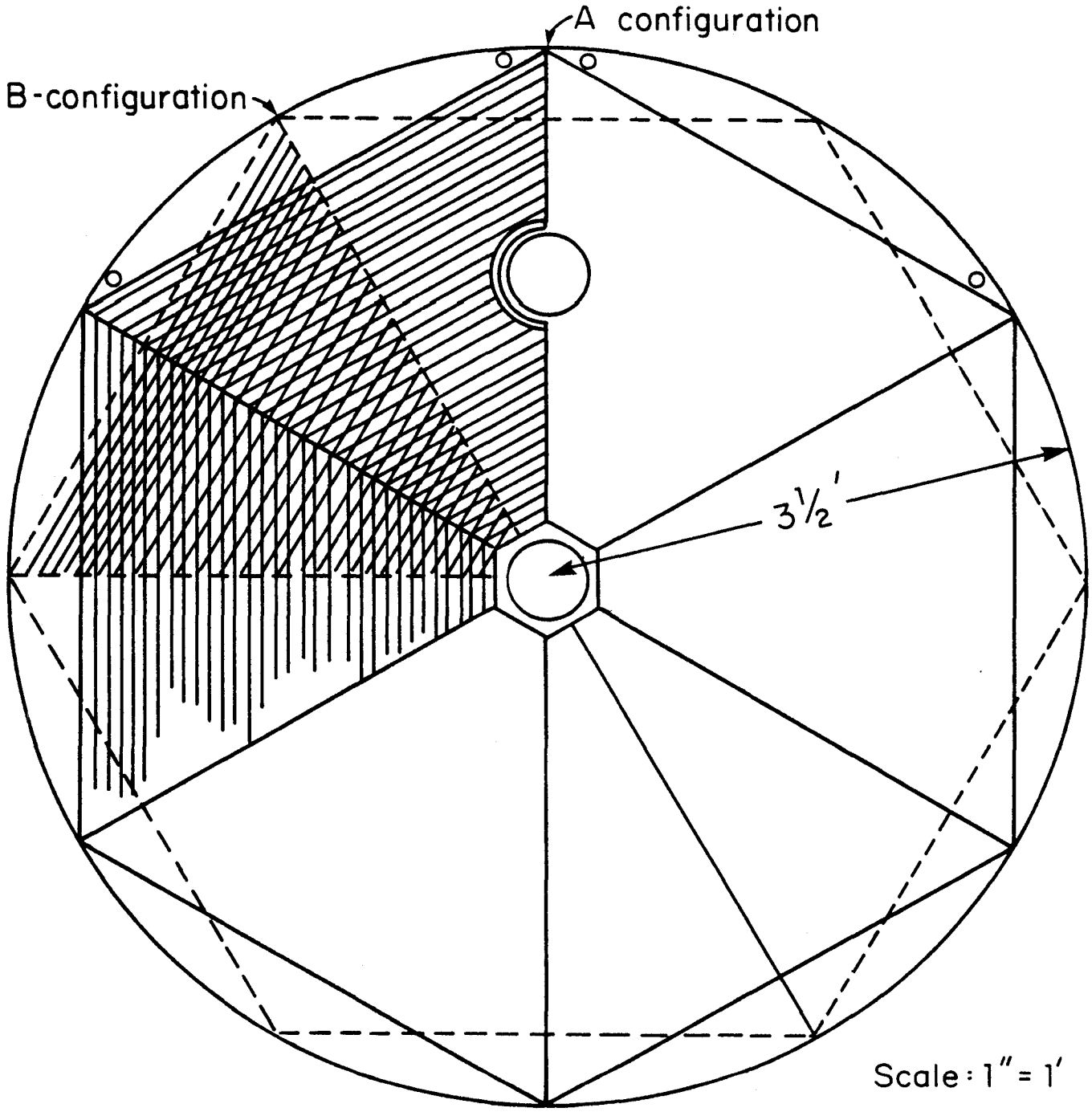

FIG. 5.13

Chapter 6

MUON DETECTION

6.1 TOROID MAGNET MUON SYSTEM

General Description

The backward region, in the direction of the $\bar{p}$ circulating beam, will be instrumented to trigger on single muons and measure their momenta. Two sets of magnetized solid iron toroids will be used for this purpose, each set consisting of two 1 m thick iron rings driven to 1.8 T magnetic field and interleaved with drift chambers. The upstream set will be 8.8 m in diameter with a tapered 10° half-angle hole centered on the Saver beam pipe. The near face of the iron will be about 4.6 m from the center of the pp collision (the I.P.). Each of these toroids will weigh 534 tons, and the set will detect muons between 10° and 30° to the circulating $\bar{p}$ beam. A downstream set 5.5 m in diameter, with a 1.5 m diameter hole, will be located 11.6 m from the IP and will detect muons between 5° and 10°. Each of these toroids will weigh 212 tons.

The Toroid Muon Trigger

The trigger is based on a straight track which travels undeflected from the IP through the 2 m of toroid iron to the back chamber plane. Each toroid pair will be instrumented with three drift chamber assemblies, one in front, one between the two, and one in back, labeled A, B and C respectively. A drift chamber assembly will have two sets of drift cells, one offset to eliminate the ambiguity due to the other. The anode wires will form a pattern of regular 48 sided polygons centered on the doubler beam line and increasing linearly in circumference as the distance from the beam increases. The azimuthal

coordinate will be obtained by cathode read-out pads 2° wide in ϕ, divided in three separate parts radially to decrease accidental problems. The drift cell size will vary with radius to achieve a constant p_T trigger threshold, as described below. The maximum drift distance will be 1.75 cm, corresponding to a drift time of 350 nsec. A schematic view of a 5.5 m toroid chamber is shown in Fig. 6.1. Only one 60° sector of 7.5° cells is shown in detail. The wire spacing will be much smaller than indicated on the drawing. Electrically the signal wires will be hooked together in 60° arcs. Alternate chamber arcs will be offset by 10 cm along the beam line to facilitate access.

The deflection of a muon at the back chamber relative to infinite momentum is given by

$$\varepsilon = \frac{108}{p_\mu} \text{ , where } p_\mu \text{ is in GeV/c and } \varepsilon \text{ is in centimeters.}$$

The multiple scattering is given by $\Delta_{rms} = \frac{18.2}{p_\mu}$ in the same units, or $\frac{\Delta_{rms}}{\varepsilon}=0.17$, independent of muon momentum. At a fixed radial distance from the beam R, a given width δR, corresponds to a transverse momentum threshold. Thus a sequence of rings whose thickness increases linearly with radius will give a fixed p_T threshold. For example, at plane C of the back toroid set, $p_T \geq 10$ GeV/c is assured by spacing the drift chamber pick up wires 0.3" apart at the inner radius of 38" and increasing the spacing gradually (every 20 cells) until the largest separation of 0.75" is reached at 100" radius. There will be a total of 126 drift cells in the trigger plane of this chamber. Dividing into six sectors in ϕ gives 756 trigger elements. The A and B planes will have the same number of trigger elements, resulting in a $p_T \geq 10$ GeV/c threshold trigger from an "OR" of 756 triple coincidence circuits. All told the back chambers will have 2904 TDC channels for the drift wires and 1620 ADC channels to measure pulse height on the 2° azimuth cathode strips. The upstream toroid chambers have the same number of pads, and 3360 TDC channels, giving a grand total of 3240 ADC and 6264 TDC channels. The required resolution in the

electronics is fairly modest, since the muons are travelling through iron (1 mm σ is probably adequate), and only about four bits are needed per ADC channel. It is not clear whether these units should be specially made for this application.

Backgrounds for Triggering

Table 6.1 illustrates the calculation of the trigger backgrounds. Hadronic punch-through is discussed in Table 6.1A, where it is shown that the rates in the A chambers are due predominantly to this effect, but punch-through contributes essentially zero rate in the C chambers because of the extra 2 m of iron. Slow pions (E_π must be at least 3 GeV for the daughter muon to penetrate all the iron) which decay in flight give the dominant fraction of the C chamber counting rates. Because of the trigger pattern granularity (500 cells per plane were used in the estimates) the accidental trigger rates, even with a one μsec gate, are negligible. Two pions can decay in flight and fake a high p_T muon trigger, as discussed in Table 6.1B, but again this rate is not high, because one pion has to have $p_T > 2$ GeV/c to give the correct A·B pattern. High transverse momentum pions which decay and give a real single muon are the major trigger background source. Since $p_T > 10$ GeV/c is required, this rate depends entirely on the model used to calculate high p_T pion yields. The one used here assumes p_T^{-4} at $p_T \geq 5$ GeV/c, and leads to substantial high p_T yields. The background trigger rate is about 0.5 events/sec.

Signals

Table 6.2 gives the best estimates for prompt muon rates from physically interesting processes. There is a great deal of uncertainty in all the numbers, because of the extrapolation in energy from the ISR for the Drell-Yan muon pairs and charm production on the one hand, and because the weak intermediate bosons $W^\pm$, Z° have yet to be observed on the other. The

predicted total signal rate is 2.5×10^{-3}/sec, or a signal-to-noise ratio of 1/200. The D-Y and Z° muon pairs contribute about 15% to this total inclusive prompt muon signal, and have the great advantage of another muon somewhere in the CDF apparatus, which will improve the signal to noise dramatically for these events. The Z° has the added advantage of a fixed invariant mass. The $W^{\pm}$ signal has to be extracted by looking for events where transverse momentum carried away by the neutrino is missing on the side opposite the detected muon. The charm or other flavor decays with prompt high p_T muons will be difficult in general to separate from π-μ decays in flight. Characteristics of the individual events such as extra visible leptons or reconstructed accompanying charmed particles which decay non-leptonically or other details of the event topology will have to be used. If new particles with the top quark quantum number are produced with $\sigma \simeq 1$ μb, then leptonic yields from these decays may compete favorably with other sources. The reason for this is that the $p_T \gtrsim 10$ GeV/c threshold requirement can be satisfied by decay kinematics rather than by the hadronic production mechanism.

TABLE 6.1

Background Rates

50,000 Interactions/sec

A. Pion hadronic punch-through

θ	Δy	π's per int	Iron Thickness to Chambers (feet)			π Punch thru per $\bar{p}p$ int.			Counting Rate A
			A	B	C	A	B	C	
5°-10°	0.7	1.4	3.7'	7.2'	10.7'	0.2	6×10^{-4}	10^{-6}	10^4/sec
10°-30°	1.2	2.4	3.0'	6.5'	10.0'	0.13	3×10^{-4}	7×10^{-7}	7×10^3/sec

B. $\pi\to\mu$ Decay in Flight ($E_\pi \geq 3$ GeV)

Two muons fake a single high p_T event. One must have $p_T \geq 2$ GeV/c to satisfy the A·B coincidence pattern. A low energy $\pi\to\mu$ decay then happens to hit the correct C counter to give A·B·C

θ	decay distance	$\pi\to\mu$ per int.	counting rate at C	counting rate A·B	A·B·C μ trigger
5°-10°	30'	0.08	4×10^3/sec	60/sec	10^{-2}/sec
10°-30°	10'	0.05	2.5×10^3/sec	60/sec	10^{-2}/sec

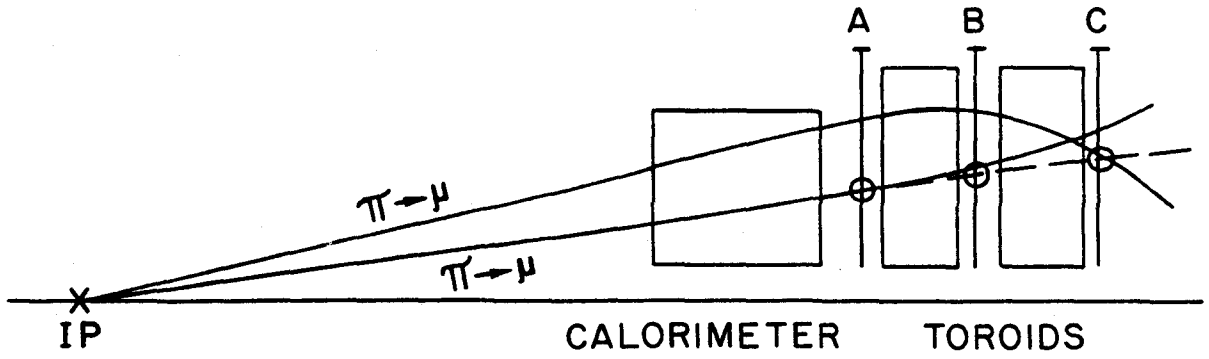

Background from two $\pi\to\mu$ decays in flight

Table 6.1 (continued)

C. Single p_T > 10 GeV/c $\pi \to \mu$ decay in flight using $1/p_T^4$ law for high p_T hadrons

θ	$\pi \to \mu$ p_T > 10 GeV/c
5°-10°	0.36/sec
10°-30°	0.18/sec

Table 6.2

Inclusive Muon Rates (p_T > 10 GeV)

10^{30} Luminosity, 5°-30° angle

Source	Rate
Drell-Yan	0.1×10^{-3}/sec
$W^{\pm} \to \mu^{\pm}$	0.3×10^{-3}/sec
$Z^{\circ} \to \mu^{+}\mu^{-}$	0.1×10^{-3}/sec
Charm and Other Flavors	2.0×10^{-3}/sec
Total	2.5×10^{-3}/sec

6.2 CENTRAL MUON SYSTEM

General Considerations

At large angles ($30° < \theta < 150°$), muons are momentum analyzed in the solenoid. A high p_T muon ($p_T > 10$ GeV/c, say) leaves only a small fraction of its energy in the calorimeter tower that it traverses. The resultant mismatch between a high momentum in the tracking system and a small energy deposition in the calorimeters is a useful signature for a high p_T muon. An additional tracking system for muon detection external to the hadron calorimeters improves the muon identification further. It also serves as an important element in a high p_T muon trigger.

The general features of such a system are clear: The position and direction of the muon should be measured outside the calorimeters with sufficient accuracy to allow extrapolation to the inner tracking system and the vertex. The required accuracy is actually modest because the multiple scattering in the calorimeters is large. We describe here a design with drift tubes based on aluminum extrusions similar to those built by Aachen for the UA1 collider experiment at CERN. The placement of planes of drift tubes above and below the central detector can be seen in Fig. 2.2. For clarity, the side walls are not shown in this figure. This system of drift tubes covers the angular range $50° < \theta < 130°$. In the angular ranges $30° < \theta < 50°$ and $130° < \theta < 150°$ coverage with external muon chambers is also possible, but more complicated.

The total area of drift tubes is very large, and the space required is substantial. For these reasons, we do not consider the design final. However, the considerations of triggering and background rejection given below have some general validity and would probably apply even to a muon detector with a different placement of the external chambers.

Preliminary Design

We visualize the central detector as a rectangular solid with H = 369 in., W = 300 in., and L = 287.5 in. (along the beam). Assuming coverage of the barrel by a rectangular array of drift tubes 27 ft. (2 x 13.5 ft.) long, with the outer layer about 16 in. from the detector, we arrive at the schematic outline shown in Fig. 6.2. In this diagram we also give the value of θ, the polar angle, for various points at the ends of the barrel detector. The large size of the barrel is misleading since the (average) coverage in rapidity is only $y = \pm 0.74$, and in θ to 51° (129°).

The UA1 drift tube is shown in Fig. 6.3. It is approximately 2 in. x 6 in., and would have a maximum drift distance (time) of 7.5 cm (1.5 μsec) for 40% Argon/60% Ethane. For an assumed 12 bunches and 21 μsec revolution, the crossings are separated by 1.75 μsec. With muon tubes of one half the size of the UA1 tubes, the maximum drift time (750 nsec) is sufficiently short that muon triggering between bunch crossings can be achieved. Two layers of drift tubes with wires parallel to the solenoid axis are required to measure the muon direction outside the barrel calorimeters. In order to eliminate dead spaces and to resolve left-right ambiguities, each "measurement" should be made with a double layer of (offset) drift tubes. Such an arrangement is sketched in Fig. 6.4. The barrel requires four layers of 480 (3 in. wide, 162 in. long) drift tubes. This arrangement is repeated twice down the length of the barrel for a total of 3840 tubes. The drift wires will be equipped with charge division readout so that the Z-coordinate can be measured.

Hadron-Muon Discrimination, Background, and Trigger Rate

These matters are considered in painful detail in CDF-57 and CDF-68 and are discussed in Chapter 8 of this report. We refer the interested (or skeptical) reader to these sources for more detailed information. We will confine ourselves here to summaries and general comments.

The first remark to be made is that the hadron rejection is really quite modest. Two phenomena contribute: pion and kaon decay in flight, and hadron penetration of the central calorimeter without interaction. The rejection ratio depends on p_T but is of the order of one in a few hundred as is shown in Table 6.3.

Cosmic rays are a potentially overwhelming source of trigger background since the rate in the detector is about 10^4/sec. We use the good time resolution ($\sigma_t \lesssim 1.2$ nsec) of the hadron calorimeters to reduce this rate. A 15 nsec gate on the hadron calorimeter selected by a coincidence in a set of external muon chambers will, for instance, reduce the rate to about 100/sec. The requirement that the track point to the interaction region (both in impact parameter and z) will reduce the trigger rate further, to less than 1/sec. Ultimately the timing information from the muon drift tubes and more accurate tracking and matching of the tracks with those in the central tracking chamber will reduce this source of background triggers to a negligible amount.

The dominant source of muons emerging from the outer surface of the central calorimeter is due to pions with p_T of about 1 to 2 GeV/c which decay in flight. The rates are readily calculated to be 40 to 50 per second at a luminosity of 10^{30}; much too high. As the pion spectrum falls very rapidly with p_T, we plan to implement a p_T cut by requiring that the emerging track point to the interaction region (impact parameter cut). This will be accomplished by requiring a time coincidence between two layers of drift tubes (e.g. wires a and c or wires b and d in Fig. 6.4). The trigger rate will be reduced to 2 to 4 per second by this method. Higher level trigger decisions can be made to reduce this even further.

Table 6.3

Approximate Hadron Rejection Ratios

P_T(GeV/c)	Decay + Penetration	= Total
10	$(6.6 + 1.6) \times 10^{-3} = 8.2 \times 10^{-3}$	= 1/120
20	$(3.3 + 1.6) \times 10^{-3} = 4.9 \times 10^{-3}$	= 1/200
30	$(2.2 + 1.6) \times 10^{-3} = 3.8 \times 10^{-3}$	= 1/260
50	$(1.3 + 1.6) \times 10^{-3} = 2.9 \times 10^{-3}$	= 1/350

Figure Captions

Fig. 6.1 Drift chamber plane arrangement for the back toroid C plane. The eight 7.5° pieces in the upper right 60° sector are shown separately. The anode drift wires are chords between the radii, forming families of similar 48 sided polygons. Each sector has 126 drift cells, plus another 126 ambiguity resolving cells offset by half a cell thickness.

Fig. 6.2 Representation of the central detector surface as a rectangular solid on which drift tubes are mounted. Allowance has been made for 16" depth for muon tubes. Angles shown are representative polar angles at the end of the region covered by the barrel tubes, except for $\theta = 30°$ which gives upper limit of coverage by forward detector.

Fig. 6.3 From Nucl. Instr. Meth. 176, 217 (1980). See also the UA1 proposal CERN/SPSC/78.06.

Fig. 6.4 Arrangement of offset drift tubes on the barrel.

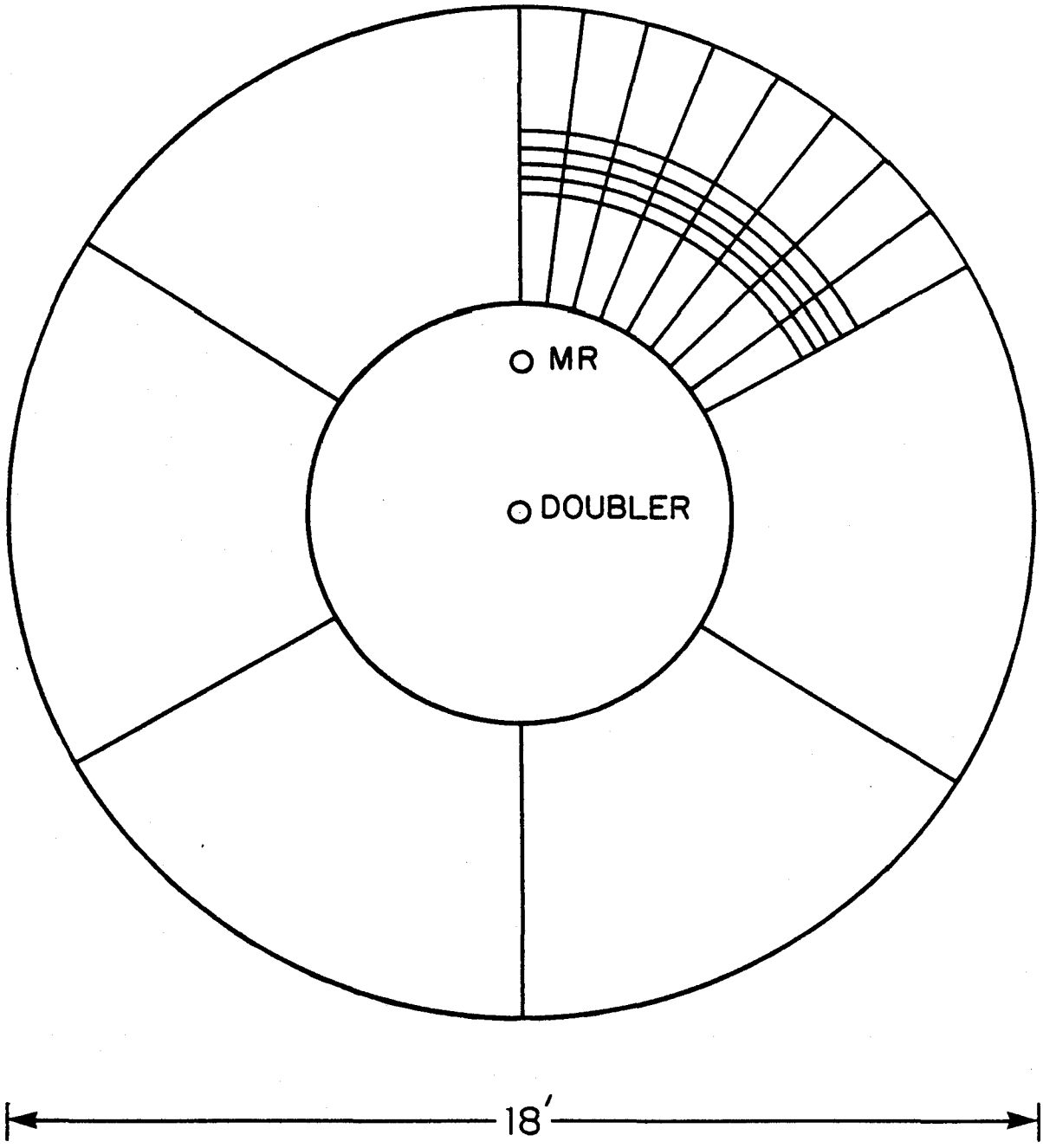

FIG. 6.1

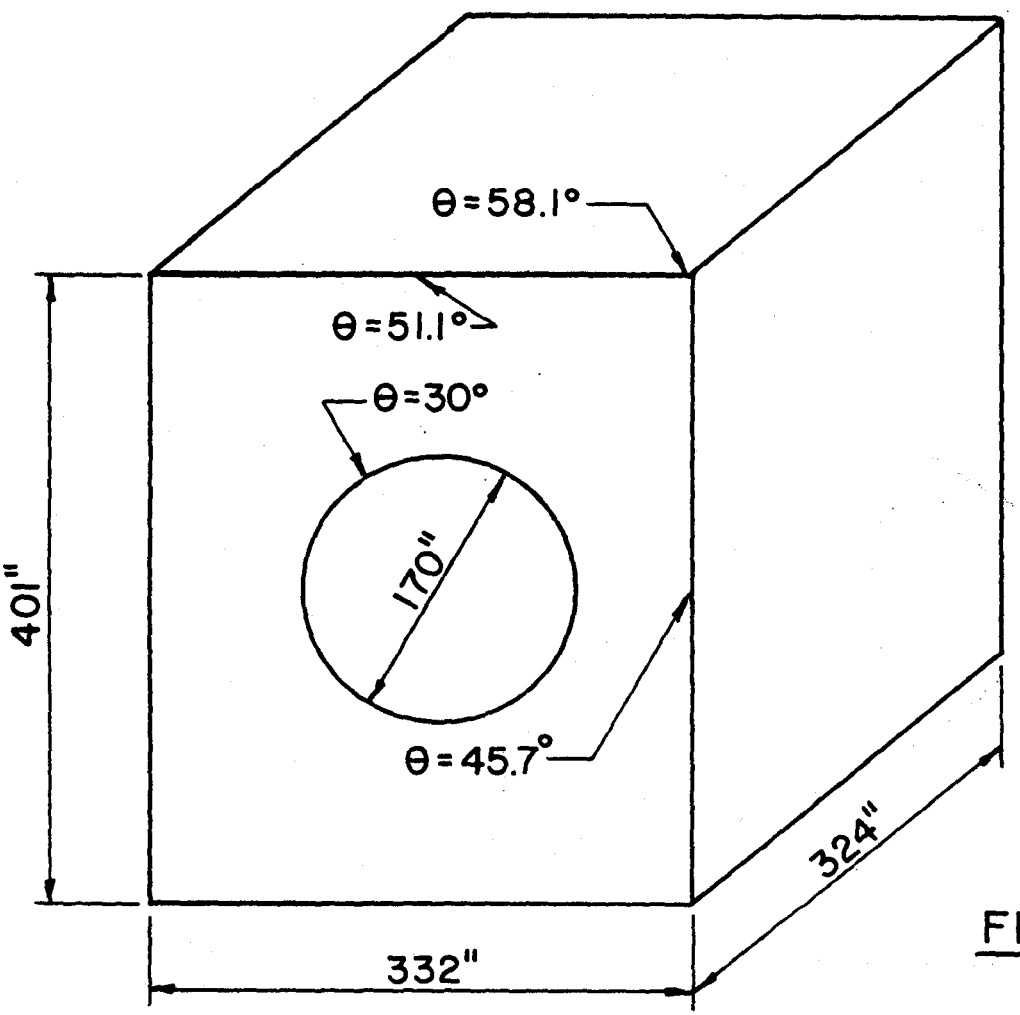

FIG. 6.2

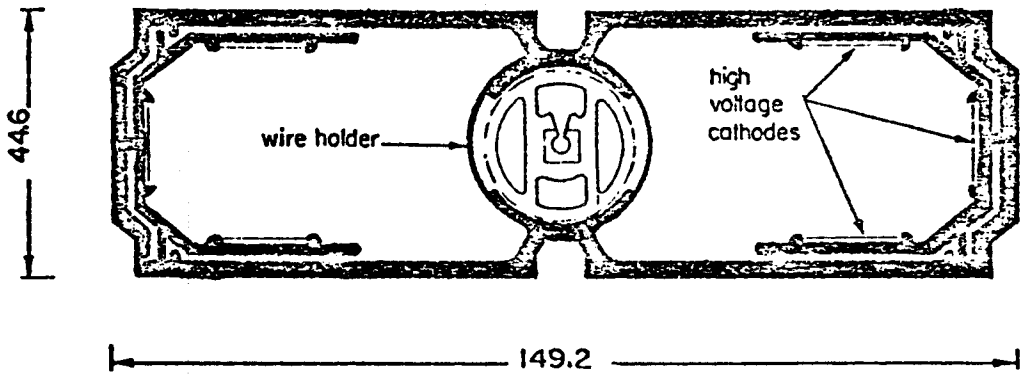

Cross-section of the extruded aluminium profile. Inserted are the PVC-U-profiles with the copper electrodes and the wire holder fixed in the center of the collimating electrode.

FIG. 6.3

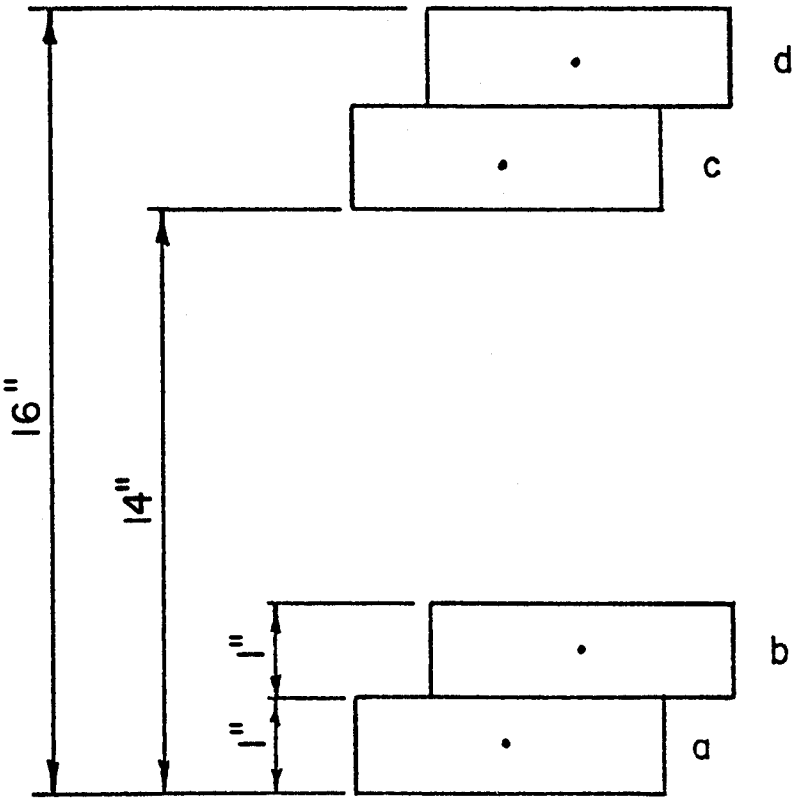

FIG. 6.4

Chapter 7

PHYSICS WITH DETECTORS INSIDE THE BEAM PIPE

We discuss in this chapter a number of different physics goals that we can pursue by inserting mini-detectors inside the beam pipe, both at small and at large angles. These goals span a wide field, covering measurements of luminosity, elastic scattering, total cross-section, and searches for quarks and for heavy flavours and leptons. However, all these problems are attacked employing the same new technology of mini-silicon-detectors operating under vacuum. This is why they are dealt with together in this chapter.

7.1 LUMINOSITY MEASUREMENT

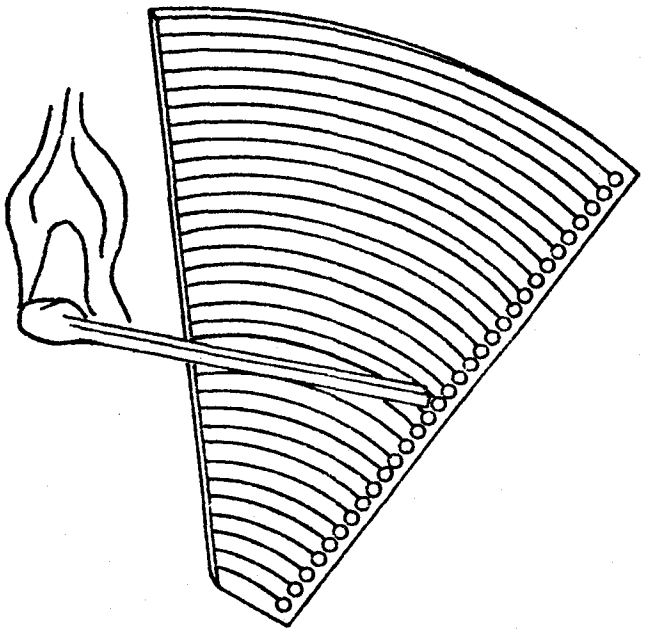

For head-on collisions of two bunches containing n_1 and n_2 particles the machine luminosity is given by

$$L = f\, n_1\, n_2\, \frac{1}{A}$$

where f is the rotation frequency, and A represents the effective area of the bunch-bunch overlap - $n_{1,2}$ can be directly obtained by measuring the circulating currents.

In terms of $i_{1,2}(x,y)$, the transverse beam profiles, the factor $\frac{1}{A}$ is given by

$$\frac{1}{A} = \frac{\int i_1(x,y)\, i_2(x,y)\, dxdy}{\int i_1(x,y)\, dxdy \int i_2(x,y)\, dxdy} \qquad (1)$$

$i_{1,2}(x,y)$ is defined such that $\int i_{1,2}(x,y)dxdy$ is proportional to the beam currents.

One can consider several methods to measure L. Some of them would be essentially the same as those employed at the CERN ISR, others have been implemented or considered at the CERN collider.

1) The extended Van der Meer method (ref. 7.1).

The beams would have to be moved relative to each other horizontally and vertically by known amounts, and the beam-beam event rate $R_m(x,y)$ measured at the various positions in a suitable monitor. The ratio of the maximum rate to the x,y integrated rate gives the constant $\frac{1}{A}$:

$$\frac{1}{A} = \frac{R_M(0,0)}{\int R_M(x,y)\, dxdy}$$

In order to apply this method one would need long electrostatic x and y - deflecting H.T plates, (ref. 7.2) and the engineering problems involved in integrating them inside the superconducting dipoles may be very hard. Therefore, although this method looks very attractive and has given excellent results at the ISR, one cannot rely on it for the time being.

2) Direct measurement of $i_{1,2}(x,y)$.

This can be done exploiting beam-gas interactions (ref. 7.3). Once $i_{1,2}(x,y)$ are known, one can compute $\frac{1}{A}$ using formula (1). One will try to apply this method using the beam-gas background accepted during the experiment. However, if the vacuum is as good as expected, the rate is likely to be low. Also, the accuracy in the reconstructed transverse vertex position of the events is expected to be $\gtrsim 100\ \mu$, which is of the same order as the vertical beam width in normal high luminosity runs. One would therefore need to apply this method to special low luminosity runs with artificially blown-up beams, and a suitable beam-gas trigger. Given the complications of the method, it can only be useful to provide checks on other luminosity measurements.

3) Measurements of beam profile by the flying wire technique.

In this method (ref. 7.4) thin solid wires are swept through each beam fast enough not to deteriorate it. By detecting the rate of beam-wire interactions with a suitable monitor, one can measure $i_{1,2}(x)$, $i_{1,2}(y)$. Under the assumption $i_{1,2}(x,y) = i_{1,2}(x)\,i_{1,2}(y)$ one can derive $\frac{1}{A}$. Since the wires have to be thin relative to the beam width, their speed of traversal is in practice forced to be very high to avoid melting the wire after a few traversals. Therefore the accuracy of the method is likely to suffer from statistical limitations. This method, which in any case involves considerable technological difficulties and cannot be applied very near the

intersection point, will be tested in the near future at the CERN collider and its potentialities will then be better understood.

4) Simultaneous measurement of the elastic differential cross-section and of the total rate.

It has been shown at the ISR that accurate luminosity and total cross-section measurements can be obtained with this method (ref. 7.5). As the two measurements are related by the optical theorem, they determine both σ_T and L via simple equations. We show in the following how the same method can be applied in the conditions of the Fermilab collider. If R_t is the total interaction rate and R_{el} is the elastic rate:

$$L = \frac{1}{16\pi\hbar^2} \frac{R_t^2}{(dR_{el}/dt)_{t=0}}$$

$$\sigma_T = \frac{R_t}{L} \qquad \frac{d\sigma}{dt} = \frac{1}{L} \frac{d R_{el}}{dt}$$

In practice, the quality of the measurement will depend on how well one can extrapolate $\frac{d\sigma}{dt}$ to t=0, and on how well one can measure the total interaction rate including the highly inelastic events. The first condition requires covering the smallest possible angles, the second one requires covering relatively larger angles. However, at the extremely high energies of the Fermilab collider a large fraction of the products of the inelastic collisions will be collimated to very small angles. We discuss in the following how this should allow us to reach extremely high detection efficiencies for both elastic and inelastic interactions using detector telescopes located inside the beam pipe, left and right of the intersection region. Elastic events will be indicated by two collinear tracks. Single diffractive events will have one track on one side and two or more tracks on the other side, pointing

to a common origin. Highly inelastic events will have several tracks on both sides. The longitudinal position of the event vertex will be reconstructed with a precision of the order of a few centimeters, thus providing a powerful rejection factor against background. The total event rate will be obtained by extrapolating the detector coverage to 4π (ref. 7.7).

Suitable detectors for this purpose are the MESD, (ref. 7.8)--ionization detectors employing silicon as a medium--that can operate under vacuum. Metallic electrodes of any shape can be deposited on the two sides of silicon crystals. In the present application, the cathode plane would be a continuous conducting layer and the anode plane would be thin strips one mm apart from one another. With the presently available technology, the impact point of a traversing ionizing particle can be located to an accuracy of up to $\simeq 50\mu$ by exploiting charge division between adjacent strips. Work is actively in progress to achieve better accuracies.

We show in Figure 7.1 a schematic layout of the left/right telescopes. Detectors 2L, 2R have a θ, ϕ sandwich at 3.5 m and a θ, ϕ sandwich at 5.5 m from the intersection. These detectors are run in a fourfold coincidence on either side. Detectors 1L and 1R have one θ-plane at 21m and one ϕ-plane at 24m and are run in twofold coincidence. An event is signaled by an overall left-right coincidence. Each detector plane is split into six 60° wide azimuthal sectors. The sectors of the θ-planes are located at slightly different distances from the interaction point in order to allow access to the sensitive elements. An artists conception of a θ-ϕ sandwich is shown on top of Figure 7.1 where also the θ, ϕ structure of the electrodes is indicated. The θ-electrodes are annular strips, the ϕ-electrodes are straight strips running parallel to the symmetry axis of the sector. Table 7.1 summarizes the main parameters of the detectors. The MESD will be located inside removable enlarged sections of the vacuum pipe, as sketched in Figure 7.2. The azimuthal sectors will be moved out radially during beam manipulations and be put back as close to the beams

as possible during the measurements. For these measurements all quadrupoles between the detectors and the intersection should be switched off. The expected beam divergence is <0.1 mr. In these conditions, we expect to be able to locate the detectors as close as a few mm from the beam (we assume 3 mm in Table 7.1) (ref. 7.9). This would allow tagging $\frac{d\sigma}{dt}$ down to $|t| \sim 2\times10^{-2}(GeV/c)^2$, and therefore limit the extrapolation factor needed to obtain $\frac{d\sigma}{dt}|_{t=0}$ to $\lesssim 1.5$. This can be seen by an inspection of Figure 7.3, where we have (boldly) extrapolated the pp elastic and single diffractive cross-section from the ISR to $\sqrt{s}$=2000 GeV. We also compare the minimum momentum transfer covered by a CERN collider experiment (UA4) with that of CDF. One sees that the CDF measurement should be as good as the CERN one.

At the ISR, the proton fragmentation cones were found to be well confined to angles $\theta\lesssim30°$. This would shrink down to $\theta\lesssim15$ mr if angles are scaled inversely to beam momentum. With a coverage of the MESD telescopes extending up to $\sim$ 14 mr (as defined by detectors 2B) we therefore anticipate an essentially 100% efficiency for detecting beam diffraction jets. However, single diffraction events might be lost because the not-fragmented proton could be lost at very small angles. This is anticipated to be a minor effect (Figure 7.3), and can be corrected for with an extrapolation procedure as for elastic events. Very inelastic events should be detected with an efficiency at least as good as at $|\theta|<30°$ at the ISR, where this efficiency was $\gtrsim$97% (ref. 7.8). Indeed the pseudorapidity coverage of each telescope is $\Delta\eta\simeq3$, and the average multiplicity should be about 9 tracks. (We recall that the particle density per unit rapidity is expected to increase with energy). We conclude that the method is feasible and should produce results of a similar accuracy as at the ISR ($\sim$2% systematic error). Once the method has been applied in a number of dedicated runs, relative monitors will be calibrated and will be used for luminosity monitoring at any later time and for any beam conditions. The forward MESD telescopes will then

serve as normal components of the experiment, extending the trigger and tracking capability of the detector down to essentially zero angle.

7.2 VERTEX MINI-DETECTORS

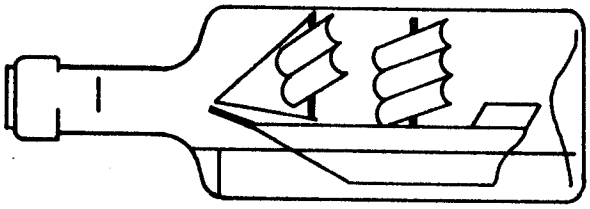

The desire to search for new particles with CDF points at the importance of augmenting the standard design with additional detectors for particle identification. With this problem in mind, the central calorimeter modules have been made removable such that, in the future, large acceptance spectrometers could be assembled on either side of the detector outside the magnet coil. Performing dE/dx measurements in the central tracking chamber in association with TOF measurements is another possibility. A very interesting possibility is also to insert miniaturized dE/dx and tracking detectors in the space (a cylindrical volume about 20 cm in diameter) that is available inside the central tracking chamber around the intersection point. We discuss here one possible system employing telescopes of multi-electrode silicon detectors (MESD). Although MESD have never been used under our expected conditions, enough is already known about this rapidly developing technique to sketch a realistic design for measuring dE/dx of single particles with a resolution sufficient to separate charge 1/3e and charge 2/3e from charge le particles. Since MESD can operate under vacuum, they can be installed very near the beam line. The proposed layout has the additional feature that it is reasonably efficient in detecting secondary vertices from decays of long lived particles.

The use of telescopes of MESD under vacuum around the intersection of a colliding beam machine has been considered at CERN, and a realistic vacuum chamber design (Ref. 7.9) has been studied by vacuum experts. We have scaled this design to the CDF beam pipe size. Fig. 7.4 shows a section of the collider pipe. It is assumed to be 5 cm in radius. Over a distance of 1.5 m around the interaction region, the pipe is 0.1 mm thick Al that is slightly bent to a hyperbolic profile to better support the outside pressure. Outside this region, the pipe is 1 mm thick Al. The thin insertion is the inner wall of an annular volume about 5 cm in width in which the MESD are located. The vacuum inside this volume may be relatively poor, say a few torr, such as can be maintained by a distant pump connected through a thin plastic pipe.

Fig. 7.5 shows the structure of the frame supporting the outer vacuum pipe insertion (1 mm thick corrugated Al, 10 cm in radius, 1.5 m long). Three 1 mm thick ribs are connected to the pipe to insure longitudinal stability of the inner thin insertion. The outer pipe section can be disconnected and moved longitudinally away from the center in order to give access to the active part. Fig. 7.6 shows a possible array of MESD. There are 12 telescopes in a ring with four crystals each, covering the full azimuth. The crystals are 5 cm long and 1 mm thick. Their width varies with the distance from the beam from 27 to 43 mm. These limited sizes allow the use of standard, commercially available crystals. The longitudinal (parallel to the beam) electrodes on one face are .1 mm wide and .9 mm distant from each other. On the opposite face perpendicular θ strips are 4.5 mm wide and .5 mm apart. This granularity will be sufficient to correlate one track in the MESD telescope to a specific track reconstructed in the central drift chambers. The ionization information will be collected on the ϕ electrodes, whose area of .5 cm^2 is sufficiently small to make multiple hits unlikely. The basic parameters of the large angle MESD array are summarized in Table 7.2.

Assuming that the event vertex is reconstructed by the central drift chamber, the position of the θ strip that was hit determines the effective thickness traversed by the particle. Since each telescope covers about 1 unit of rapidity and 1/12 of the full azimuth, the chance that more than 1 particle traverses the same telescope in an event is small, perhaps 1/3 on average. However, even if a few particles traverse one telescope, the θ - ϕ ambiguity will in general be resolved using the correlated pulse heights in the θ - ϕ strips. The system involves a total of 2160 strips, which are fed to ADC's through low noise preamplifiers. The solid angle is 1/3 of 4π. The coverage can of course be increased by putting, for instance, two identical arrays in a row. The preamplifiers would have to be located as near as possible to the MESD. There are already miniaturized versions of such preamplifiers that would not produce an important increase of material around the intersection. In general, the amount of material on the particle trajectories is very limited; the equivalent thickness of four crystals plus the beam pipes is about 5 percent of a radiation length. In the off-line analysis the majority of photon conversions in this material could be recognized and corrections to the event pattern applied.

The primary ionization released in silicon is large, and MESD are excellent dE/dx detectors. As such, they have already been used in a number of cases in high energy physics, for example, the NA1 experiment at CERN (Ref. 7.8). Tests with minimum ionizing particles traversing telescopes of MESDs can be used to predict the response of four 1 mm thick detectors to particles of charge 1/3 e, 2/3 e, and 1 e (Ref. 7.10). The expected response is shown in Fig. 7.7, where it is assumed that all particles are minimum ionizing. Recent tests with the central CDF hadron calorimeter have shown that a time-of-flight resolution of about 1.2 ns can readily be obtained. This time resolution is sufficient to preserve the particle separation indicated in Fig. 7.7.

An array of MESD like the one sketched in Fig. 7.6 can also be employed in a search for secondary vertices produced by decay in flight of heavy relatively long-lived particles (heavy flavors, leptons, etc.). With thin strips (.1 mm wide, 1 mm apart from each other), a resolution of about 50 microns on the impact point of the traversing particle can be obtained by exploiting charge division between adjacent electrodes. Thus, the system would be sensitive to lifetimes in the range of 10^{-13} sec. Such resolutions, similar to the ones already achieved in tests, would allow an appreciable fraction of charm decays to be observed. Moreover, studies are in progress in order to improve the detector precision and thus increase the sensitivity to short lifetimes.

References

1. CERN SPSC/78-06, p. 115.

2. G. Bellettini, et al, Endcap calorimeters--luminosity--forward angles, CDF 56.

3. S.R. Amendolia, et al, Measurements of ISR beam profiles with a spark chamber-counter telescope, Proc. of the 1973 Int. Conference on Instrumentation for High En. Physics, Frascati 1973, pg. 397.

4. L. Evans and R. Shafer, SPS/ABT/TR/LE/79.4; A. Barish et al, SPS/AC/LE/Rep. 173.

5. V. Amaldi, et al, Nuclear Phys. B 145 1978 (367).

6. G. Bellettini, et al, Luminosity and very small angle physics, CDF 59.

7. The method will be similar to the one employed in the R801 experiment at the ISR, S.R. Amendolia et al, Nuovo Cimento 17A, 735 (1973).

8. S.R. Amendolia et al, NIM 176, 457 (1980).

9. C. Bradaschia, et al, Feasibility of operating silicon detectors inside the collider vacuum pipe, CDF 60.

10. D.S. Ayres, et al, Thoughts on the implementation of a dE/dx system for CDF, CDF 78; R. Diebold, Time of flight possibilities, CDF 87.

11. NAl + CDF Pisa Groups, dE/dx with a silicon vertex detector, CDF-85.

TABLE 7.1

Main parameters of the forward MESD telescopes

(during measurements all detectors extend to a radial distance of 75mm from the beam. All wafers are 1mm thick)

Detector	distance from interaction	distance from beam of inner edge (during measurements)	electrode spacing	space resolution	number of channels per side
1θ	21 m	3 mm	1 mm	$\sim 50\mu$	426
1ϕ	24 m	3 mm	1 mm	$\sim 50\mu$	444
$2\theta F$	3.5 m	10 mm	2 mm	$\sim 100\mu$	204
$2\phi F$	3.5 m	10 mm	2 mm	$\sim 100\mu$	219
$2\theta B$	5.5 m	10 mm	2 mm	$\sim 100\mu$	204
$2\phi B$	5.5 m	10 mm	2 mm	$\sim 100\mu$	219

Total number of channels: 3432

TABLE 7.2

Main parameters of the large angle MESD Telescopes

(pitch of ϕ electrodes, 1 mm; pitch of θ-electrodes 5 mm; 12 wafers in each ring)

Ring	distance from beam	size of wafers	number of ϕ-channels	number of θ-channels
1	50 mm	27x50 mm^2	27	10
2	60 mm	32x50 mm^2	32	10
3	70 mm	38x50 mm^2	38	10
4	80 mm	43x50 mm^2	43	10

Total number of channels 2160

Figure Captions

7.1 Schematic layout of the 12 MESD rings around the interaction point (lower), and artist's view of one θ and one ϕ-plane (upper).

7.2 Expanded vacuum pipe insertion where the MESD rings are located. The MESD sectors are moved away from the beams during beam manipulations.

7.3 The differential cross section $d\sigma/dt$ of forward elastic and diffracted protons, qualitatively extrapolated from ISR energies to $\sqrt{s}$=2000 GeV.

7.4 Sketch of the annular vacuum insertion where MESD telescopes can be located around the intersection.

7.5 Support structure of the annular vacuum insertion.

7.6 Schematic lay-out of the large angle array of MESD telescopes.

7.7 Expected shape of the dE/dx distribution of minimum ionizing particles of various charges traversing the large angle MESD telescopes.

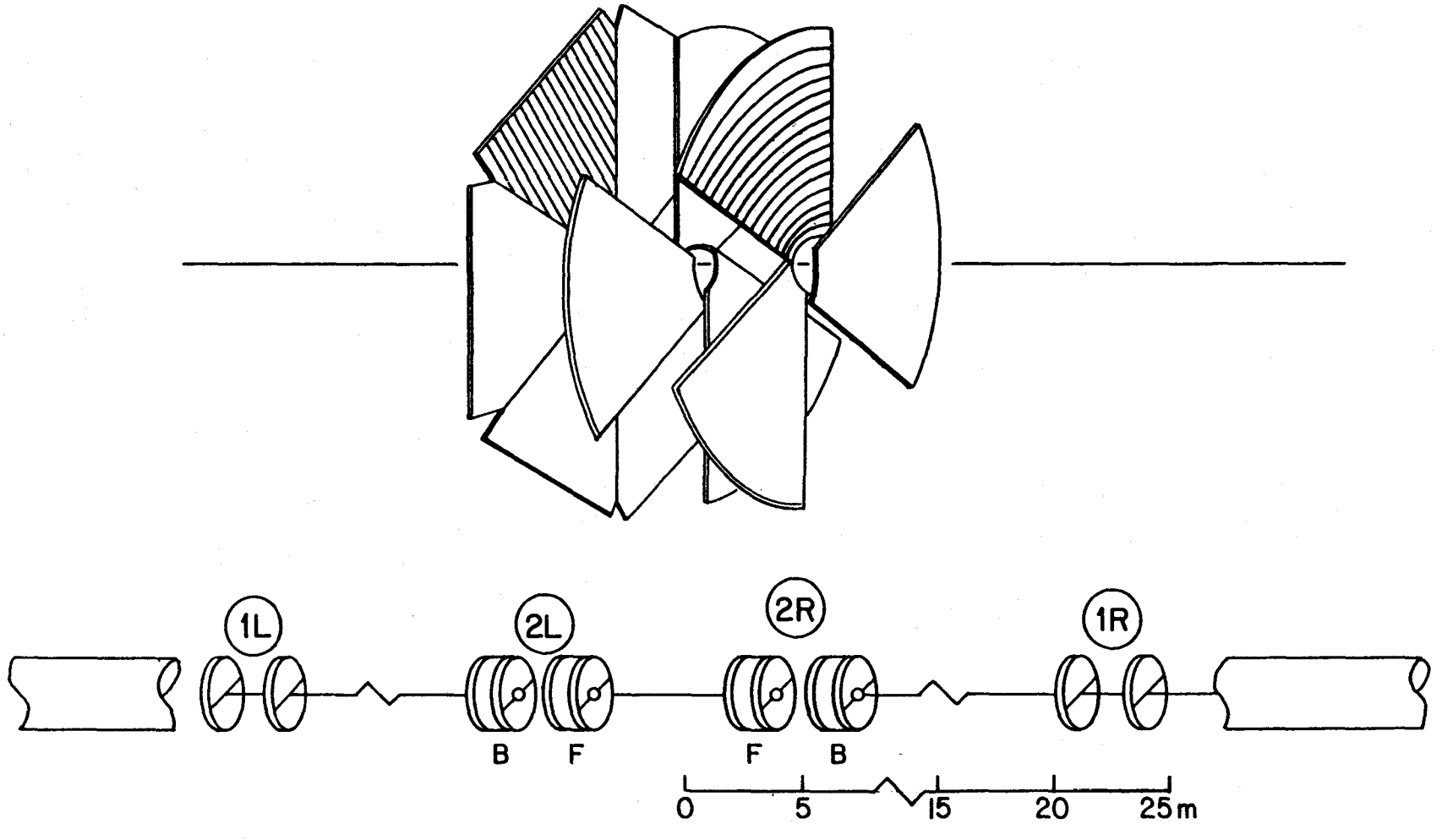

FIG. 7.1

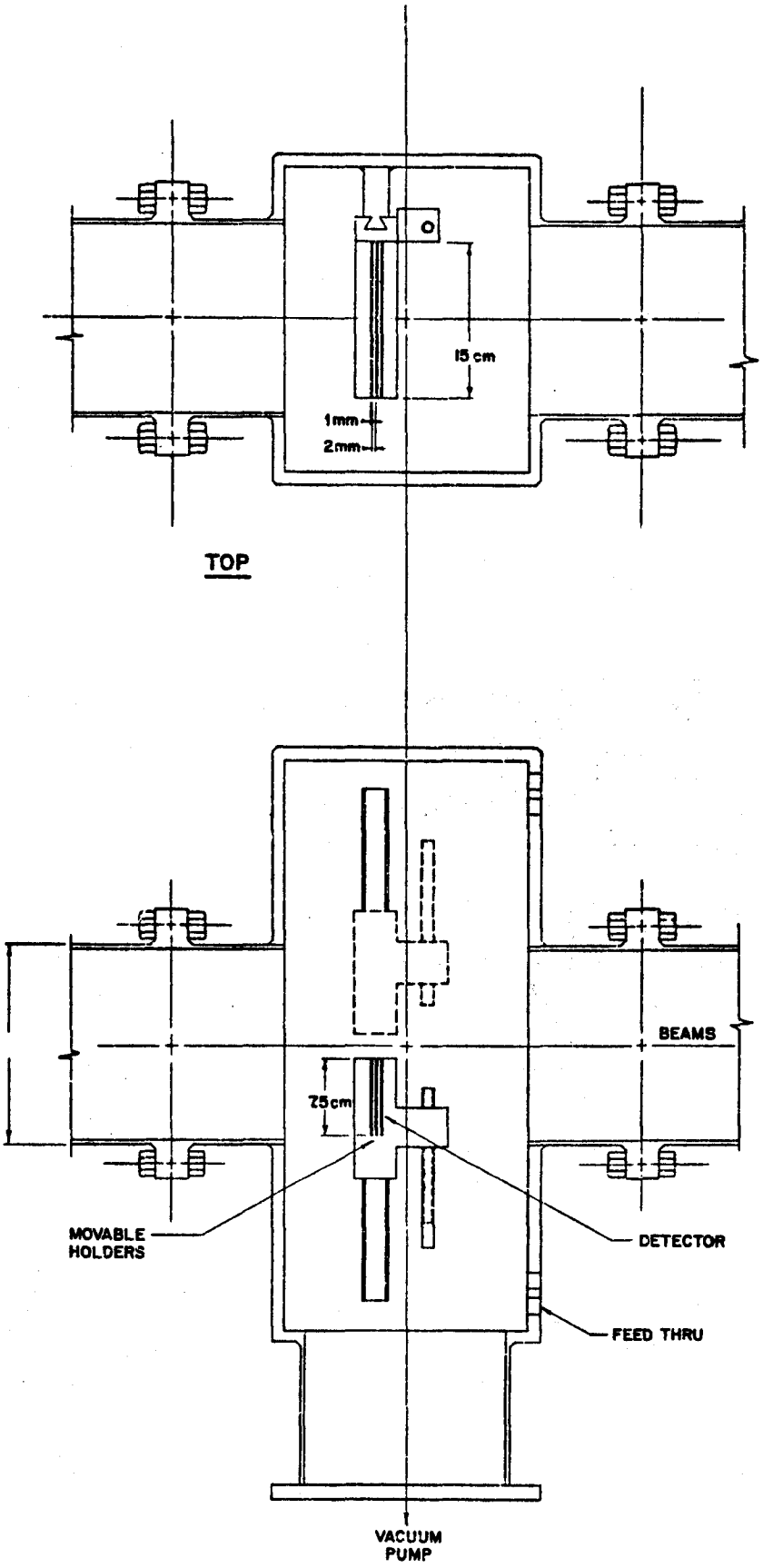
15 cm
1mm
2mm
TOP
BEAMS
7.5cm
MOVABLE HOLDERS
DETECTOR
FEED THRU
VACUUM PUMP
SIDE

FIG. 7.2

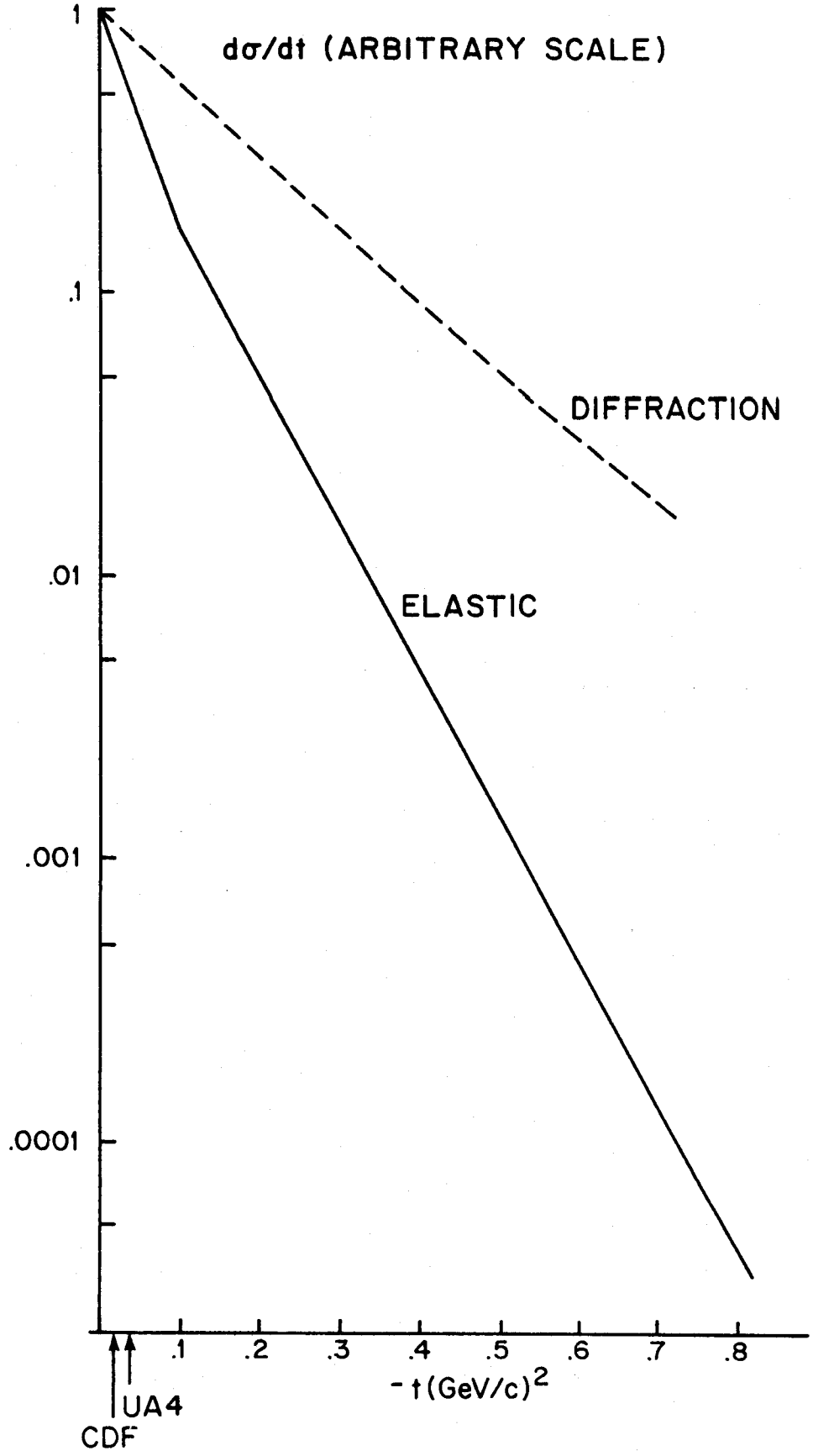
1
dσ/dt (ARBITRARY SCALE)
.1
DIFFRACTION
.01
ELASTIC
.001
.0001
.1
.2
.3
.4
.5
.6
.7
.8
-t(GeV/c)²
UA4
CDF

FIG. 7.3

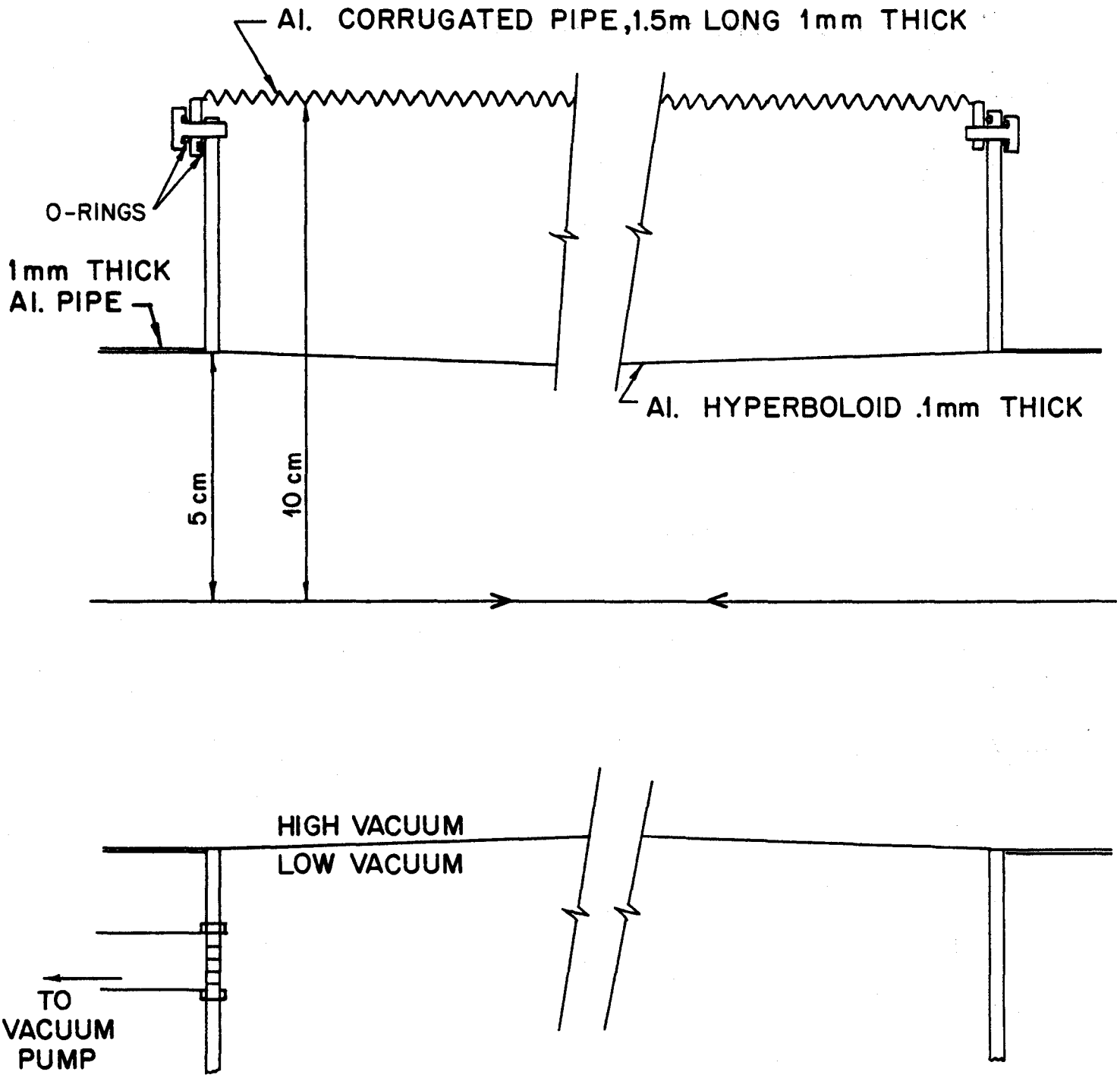
Al. CORRUGATED PIPE, 1.5m LONG 1mm THICK
O-RINGS
1mm THICK
Al. PIPE
Al. HYPERBOLOID .1mm THICK
5 cm
10 cm
HIGH VACUUM
LOW VACUUM
TO
VACUUM
PUMP

FIG. 7.4

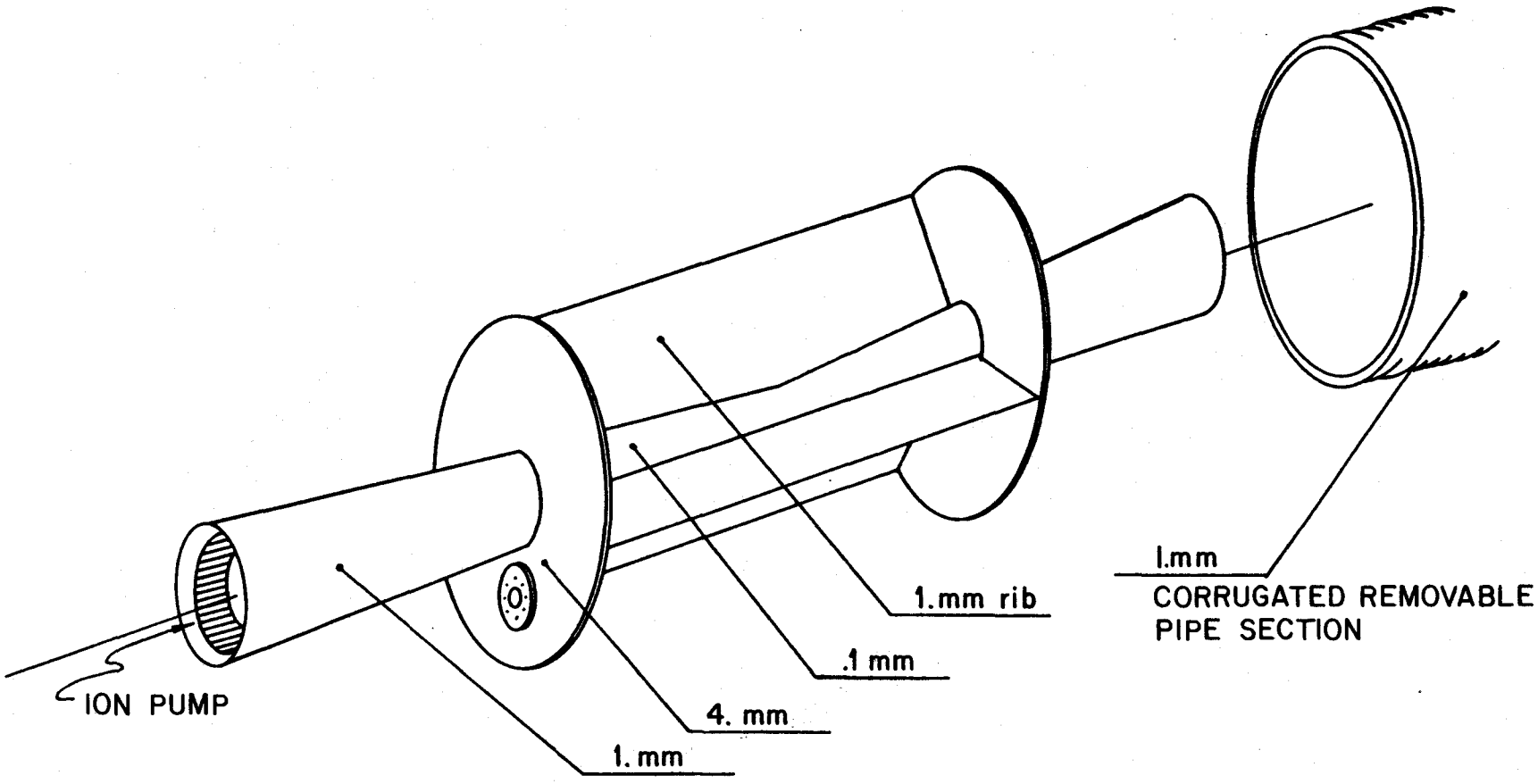
ION PUMP
1. mm
4. mm
.1 mm
1.mm rib
1.mm
CORRUGATED REMOVABLE
PIPE SECTION

FIG. 7.5

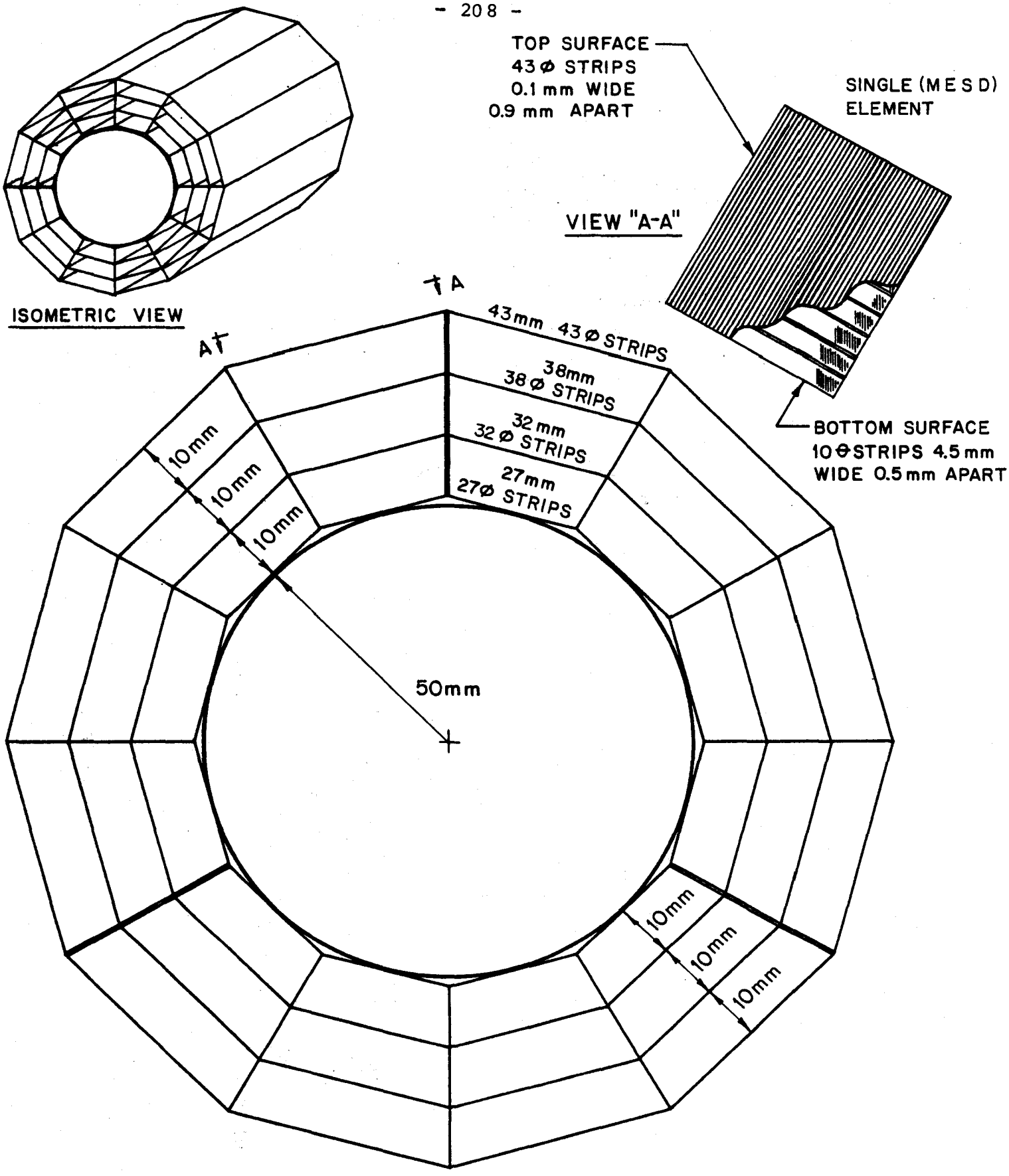
TOP SURFACE
43 ø STRIPS
0.1 mm WIDE
0.9 mm APART
SINGLE (M E S D)
ELEMENT
VIEW "A-A"
ISOMETRIC VIEW
BOTTOM SURFACE
10 ø STRIPS 4.5 mm
WIDE 0.5 mm APART
43mm 43 ø STRIPS
38mm
38 ø STRIPS
32 mm
32 ø STRIPS
27mm
27ø STRIPS
10mm
10mm
10mm
50mm
10mm
10mm
10mm

FIG. 7.6

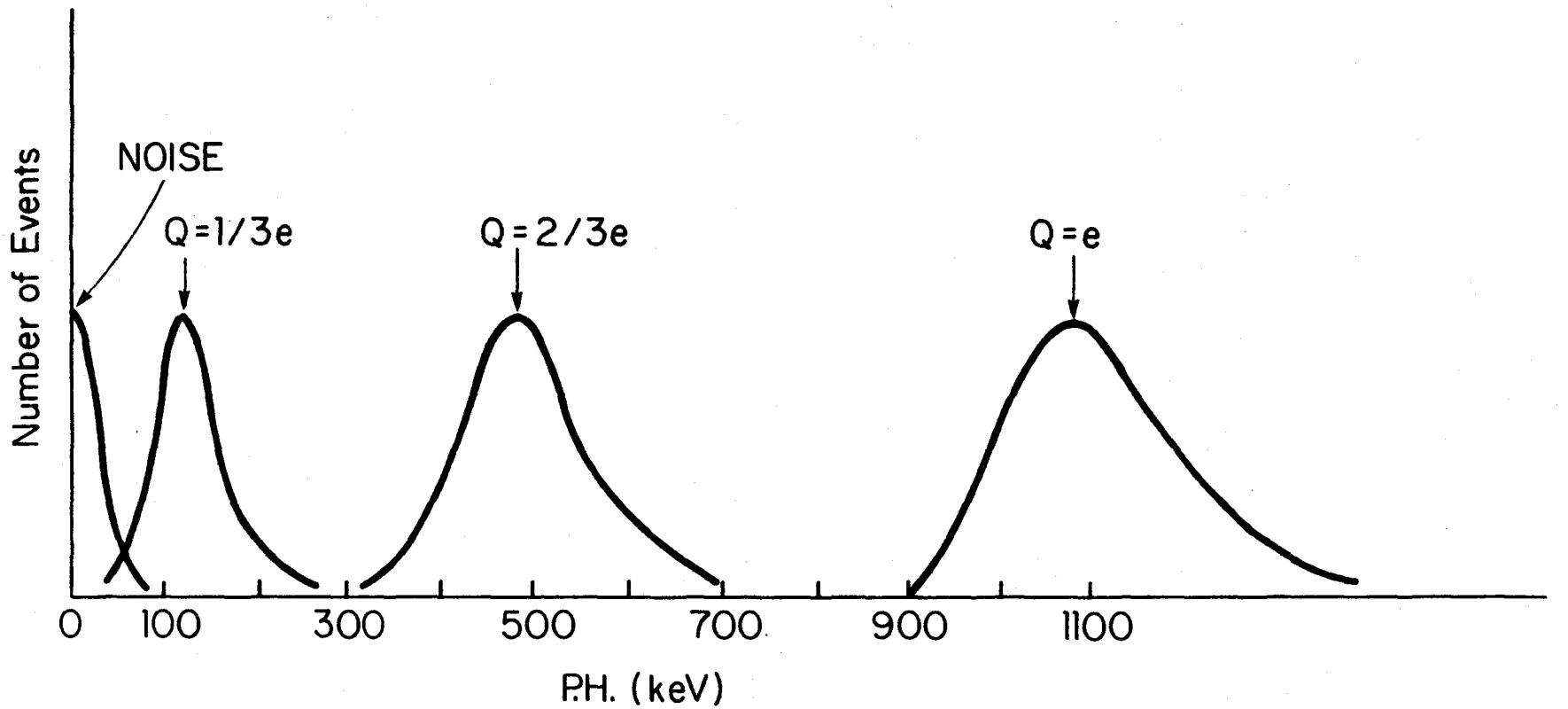
NOISE
Q=1/3e
Q=2/3e
Q=e
Number of Events
0
100
300
500
700
900
1100
P.H. (keV)

FIG. 7.7

Chapter 8

TRIGGER CONSIDERATIONS

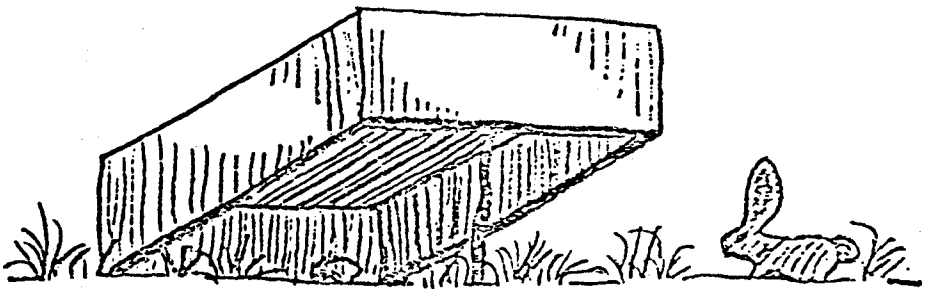

8.1 GENERAL CONSIDERATIONS

The problem presented by the trigger is: at a 50 kilocycle interaction rate, with a typical multiplicity of 50 particles per event, in an environment with unmeasured backgrounds, to pick out the signatures of interesting events in a completely new energy domain. Two additional considerations are that the physics of interest may change during the lifetime of the detector, and that the detector will grow in capability by the addition of new detector technology.

The design philosophy is to design a trigger scheme that has the capability of triggering efficiently on signatures from known physics, and that has sufficient sophistication to allow both proper rejection for backgrounds or unwanted events and a good recognition capability for specific signatures.

The trigger is designed to exploit the real strength of the detector--its finely segmented calorimetry. The segmentation in both the electromagnetic and hadronic calorimeters allows triggers which have a high degree of specificity in the signatures.

The signatures of 'known physics' for which the trigger must be selective and efficient are:

a) $W^{\pm} \rightarrow \mu^{\pm}\nu$, $W^{\pm} \rightarrow e^{\pm}\nu$
b) $Z^{o} \rightarrow \mu^{+}\mu^{-}$, $e^{+}e^{-}$
c) $q\bar{q} \rightarrow \mu^{+}\mu^{-}$, $e^{+}e^{-}$ (Drell-Yan)
d) 'jets' from the hard scattering of constituents
e) 'jets' from the decays of heavy quarks, such as 'top' decay
f) single particle high p_T inclusive trigger

To enable the triggering on 'unknown physics', building blocks containing several fundamental variables are available in the trigger. To name a few:

a) large E_T
b) large E_T imbalance
c) large hadronic/electromagnetic energy imbalance
d) large cluster invariant mass (may have a different

E_T threshold)

e) multilepton events

f) combinations of leptons and jets

g) combinations of multiplicities and energies

This is by no means an inclusive list--the point is that such capabilities exist without hardware changes. As the luminosity of the machine grows, one can reject unwanted events as needed.

8.2 DESCRIPTION OF THE TRIGGER

The trigger electronics is designed as a multi-level system. At each level the trigger rate must be low enough so that the deadtime produced by the next level is not significant. Within this constraint, the trigger requirements at each level are as loose as possible, leaving the more restrictive decisions to higher levels where more information from the detector is available and where there is a longer decision time allowed per event. The increased time permits the use of systems in which the trigger criteria are not hard-wired in and, therefore, can be modified as we learn about the physics at E_{cm} = 2000 GeV (3.2 ergs!).

Table 8.1 shows, for each trigger level, what information is available from the detector and the length of time allowed before a decision must be made. The maximum cross-section that can be accepted at each level, as well as the maximum trigger rate, are also shown. It should be noted that each level can pass on approximately 10% of the events presented to it. Moreover, even at the highest luminosity, 0.2% of all interactions can be passed to the level 3 hardware, where all the detector information is available and where more than one millisecond can be taken before a final decision is made to write the event onto the magnetic tape.

Table 8.1

Level	Information Available	Decision Time	Maximum Cross-Section Passing Trigger Requirement [MAXIMUM TRIGGER RATE] $L = 10^{28}$	$L = 10^{$
1	-Beam crossing	250 nsec	>100 mb	5 mb
			[5000/sec]	
	-Beam-beam counters			
	-Barrel counters (Stage 1 only)			
	-# of calorimeter towers above P_T threshold			
	-Total E_T in calorimeters			
1 MU	-Central detector μ chambers	1.0 μsec		
2 (A)	-Energy clusters in calorimeters	<7 μ sec	>100 mb	1.5 mb
			[1500/sec]	
	-Tracks in μ chambers			
(B)	-Match clusters & muons with tracks in central tracking chambers	20 μ sec	10 mb	100 μb
			[100/sec]	
3	-Full readout of detector	>1 msec	100 μb	1 μb
			[$\sim$1/sec limited by tape writing]	

We have assumed that the machine will operate with 12 bunches, that is, a time between beam crossings of 1.747 μsec. If in fact the machine operates with 3 bunches as may be necessary, there would be 7.0 μsec between crossings. Level 2 will be designed to be faster than this, and if possible, faster than 3.5 μsec in case one has 6 bunches. If the beam crossing time turns out to be one of the larger two numbers, the system is deadtimeless for Level 2 decisions to reset, and Level 1 and Level 2 merge into a single level.

A description of each level is given in the following sections:

(1) Level 1 (See Figure 8.1)

A Level 1 decision must be made in 1.25 μsec in order to allow 500 nsec for a fast reset of the TDCs and ADCs from the tracking chambers and calorimeters before the next crossing. At the initial luminosity of 10^{28}, the interaction rate is low enough that all beam-beam interactions can be accepted by Level 1.

At high luminosity, 10% of beam-beam interactions can be accepted by the level 1 logic. The decision will be based on transverse energy deposition in the calorimeters and data from the muon detectors. The pulse height from each calorimeter tower will be compared with a predetermined P_{Tmin} level. The number of towers with $P_T > P_{Tmin}$ will be available at this level. The magnitude of the transverse momentum in all towers will be added to give the total transverse energy (E_T). If E_T is greater than some E_{Tmin}, a level will be set.

A preliminary trigger will be available from the detector planes in the forward muon toroids indicating the likely presence of a large P_T muon.

One problematic topology is an event in which little is seen anywhere in the detector except for muons in the central detector. In this case, if two or more planes of muon chambers are hit (level 1μ), then the event is held for the level 2 processor. Otherwise a clear is sent to all channels.

(2) Level 2

The Level 2 hardware will determine the general topology of the event including energy clusters in the electromagnetic and hadronic calorimeters and muons in either the central detector or forward toroids.

The input to the cluster finding hardware is an array of pulse heights from the sections of electromagnetic and hadronic calorimeters. This is pictured below where the calorimeter modules have been folded open onto the pseudorapidity-azimuthal angle plane.

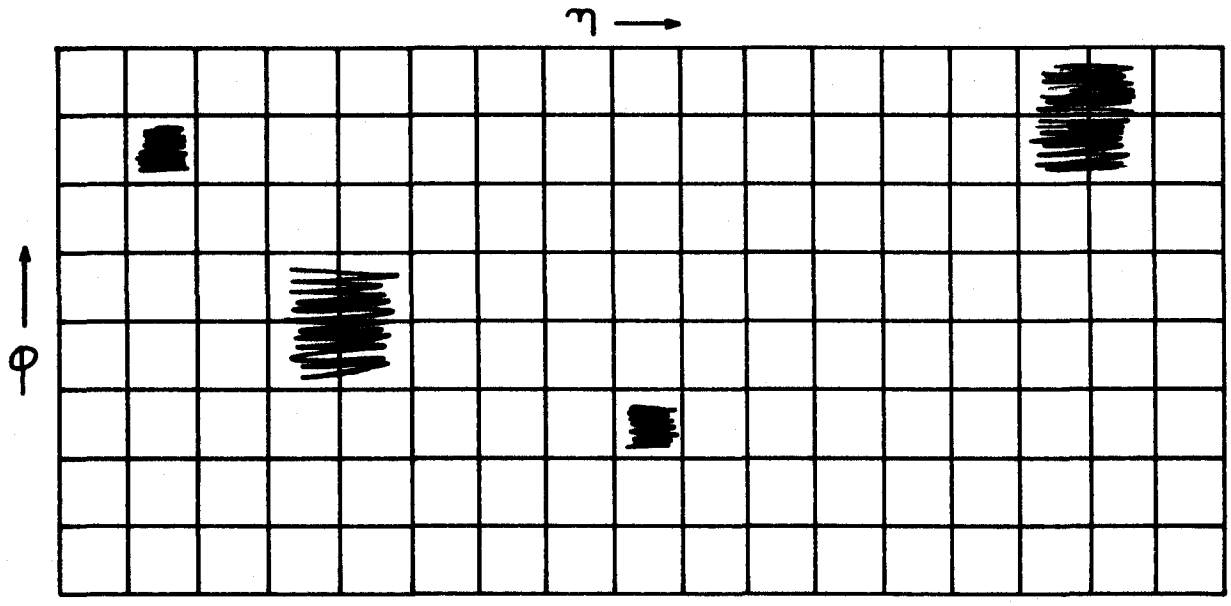

The hardware finds the energy clusters and produces a table containing the mean pseudorapidity and width, the mean azimuthal angle and width, and the transverse momentum for each cluster found in the electromagnetic calorimeter and each cluster found in the hadronic calorimeter.

The cluster finder will be built using analog or digital techniques. One possible scheme (CDF-93) is shown in Fig. 8.2.

The device uses the analog pulse height from each module and a digital level from each module indicating which modules have $P_T > P_{Tmin}$. The circuit finds a group of connected modules all of which are above the minimum P_T level. It records the size and location of the cluster in each direction and determines P_T by adding the analog signals from these modules.

Muon candidates in the central detector are kept at this level if the track in the muon chambers has a trajectory consistent with a high p_T muon coming from the interaction region. Similarly, by this time the forward muon system has determined whether a muon candidate has an acceptable trajectory which passed through all three detector planes.

If the number of moderate and high P_T clusters, and/or the number of muons exceeds the required value, the second part of the level 2 processing (2B) is initiated. Otherwise a clear is sent to the entire detector.

By level 2B, results are available from the inner tracking system, where the fast hit latches of 10 planes are connected to a hard-wired high P_T track finding device.

The central tracking, cluster, and muon data are used to determine particle type. If the ratio (R) of the electromagnetic P_T to hadronic P_T in a cluster is very large, and a central track points to the cluster, the particle is considered an electron. If R is very large, yet no track points to the cluster, the particle is labeled a π^o. If R is not very large, the cluster is considered a jet. The central tracking information is also used to refine the high-P_T muon identification.

After particle type is determined, we have a list of electrons, π^o's, jets, and muons, and the magnitudes and directions of their P_T vectors. This allows a set of trigger criteria to be established based on the number and P_T of leptons and jets. One can also be sensitive to particularly interesting topologies such a large P_T imbalance or heavy quark candidates which might consist of high P_T jets and leptons close to each other.

Because the time available at this level is relatively long, the list of criteria can be programmable. This will permit us to modify the trigger requirements as we learn which events are interesting at E_{cm} =2000 GeV.

If the level 2 trigger is satisfied, the full readout of the detector is initiated.

(3) Level 3

At this point, all information about the event is stored in a event buffer. The level 3 processors must decide whether or not the event is to be written onto magnetic tape. This will be done using the VAX or other high speed digital processors.

In addition to this major trigger scheme, there will also be special calibration triggers run at a prescaled level to monitor the operation of all the elements in the detector and measure such parameters as gains and pedestals.

8.3 RATES

The trigger rates have been estimated using the Monte Carlo predictions described in CDF-68 by S. Miyashita and K. Ogawa. The cross section for quark-quark scattering, W and Z production, etc. are derived therein from the quark distribution of Owens and Reya, with QCD corrections as prescribed by Buras and Gaemers. The actual trigger rates depend, for example, on the resolution of the calorimetry, on the decay path for pions and kaons, and on the detailed performance of the central tracking chambers. We present here rates for a minimal trigger scheme to show that the power of the detector is such that, at the luminosities we hope for, the trigger rates are reasonable.

All rates are estimated at a luminosity of 10^{30} cm^{-2} sec^{-1}. Comments on individual triggers are listed below, and the trigger rates are summarized in Table 8.2 (at the end of this section).

A. Single muon trigger - central detector

The muons from pion decay and hadrons which punch through the rather thin calorimeter dominate the muon trigger (CDF-57). The trigger rate is thus governed by the hadronic cross sections at large P_T rather than by any true lepton signal. On the order of 100 muons per sec emerge from the calorimeter at level 1. Using a P_T cut one gets on the order of 4 muons/sec at level 2. This should be easily handled by the readout system, which can find and cut on the true P_T of the associated track.

B. Single-muon rates - forward arm

The estimate of muons satisfying a three plane trigger in the forward toroid system is about 0.5/second. There are two main contributions. The first is two low momentum pions faking a high P_T muon; the second is a decay of a pion producing a muon which triggers. Both of these can be reduced at levels 2 and 3.

C. Single electrons

The trigger for moderate P_T single electrons is essentially defined in level 2 as a match between a charged track and a cluster of large electromagnetic energy but small hadronic energy. One has two constraints: a) that the energy as measured by the calorimeter be compatible with the momentum of the measured track, and b) the spatial matching of the track and the energy deposited. Major background will be the overlap of a π^o with another charged particle (or the confusion of several softer particles with a stiff track).

For W and Z decays the P_T cut in the central electromagnetic calorimetry alone is enough to reduce the rate to 10/sec at a P_T of 10 GeV/c. The additional identification of a stiff charged track which points to the sharply defined electromagnetic shower will identify the particle as an

electron rather than a photon or π°.

A track of P_T equal to 10 GeV/c has a sagitta of 1.2 cm, approximately the cell size of the chamber. We intend to bring out hit latch signals for 10 layers of wires (approximately 3000 wires) for the level 2 trigger to avoid confusion from the large multiplicity. How low a P_T one can reach, and for how small an angle in the forward and backward directions the π^o/charged particle overlap allows electron identification, are detailed problems under Monte Carlo investigation.

D. $Z \rightarrow \mu^+\mu^-, e^+e^-$

The rate for each Z dilepton decay channel is about 3×10^{-4} per second. Requiring that both leptons go into the central barrel detector gives a detection efficiency of only 15%, but if we include the angles down to 10° we get 80% of the decays with both leptons detected. The background from beam-beam interactions for this is, at the trigger level, so small as to be negligible.

E. Jets

The integral cross section for the production of a QCD constituent jet above a given P_T versus P_T is shown in Fig. 8.3. The effect of the calorimeter resolution is to blur the P_T threshold (CDF-89).

To get an unbiased spectrum at a given P_T , then, one has to lower the nominal P_T threshold and thus increase the trigger rate. For a hadronic calorimeter resolution of $0.65/\sqrt{E}$, this factor is approximately 10 at P_T = 10 GeV/c, 4 at 20 GeV/c and 2 at 70 GeV/c (CDF-89). For example, to get a P_T spectrum above a P_T of 20 GeV/c which is not biased by the threshold, one would need a P_T threshold at 14 GeV to be 2σ away from the threshold. The trigger rate would then be a factor of 4 higher than the true integrated rate above 20 GeV/c. The trigger rate for an unbiased spectrum above a given P_T is also shown in

TABLE 8.2

Leptonic Channels

Process	Kinematic Region	Particles Detected	p_T Cutoff	Reference	Production Rate (per second)	Background Process	Level 2 Expected Trigger Rate	Reference-Comment
$W^{\pm}\rightarrow\mu^{\pm}\nu$	central (30°-150°)	one μ	25 GeV/c	S.Miyashita K. Ogawa, CDF-68	6×10^{-4} sec^{-1}	π decay, punchthrough	4/sec	
	toroids (5°-30°)	one μ	10		3×10^{-4}	π decay, 2 μ's	$\leq$1/sec	
$W^{\pm}\rightarrow e^{\pm}\nu$	central	one e	25		6×10^{-4}	π/e confusion π° + charged	$<2\times10^{-3}$	
	endwall + plug (10°-30°)	one e	25		2×10^{-4}	π° + charged π/e confusion	?	
$Z^{\circ}\rightarrow\mu^{+}\mu^{-}$	central	one μ	25		1.5×10^{-4}	π decay, punchthrough	see W decay	
	toroids	one μ	10		1×10^{-4}	π decay, 2 μ's	see W decay	
	central	both μ's				cosmic rays 2π decays, punchthrough	.01/SEC	
	central+toroids	both μ's					2×10^{-4}	
$Z^{\circ}\rightarrow e^{+}e^{-}$	central	one e	25		1.5×10^{-4}			
	endwall + plug	one e	25		1×10^{-4}			
	central	both e's						
	central + ends	both e's						

Figure 8.3.

F. New things (Centauros, etc.)

Centauro events would appear as large amounts of hadronic energy with little associated electromagnetic energy. The trigger scheme we propose gives a rapid survey of this information and allows a software controlled choice of cuts on the difference or ratio.

8.4 BACKGROUNDS

None of the background rates are known, except that for cosmic rays. We try to discuss possible ways of dealing with each background in turn, but only measurements in the real situations will tell us what is required.

A. Cosmic rays

The raw cosmic ray rate penetrating the detector is 10 kHz, about 1/5 of the interaction rate at a luminosity of $L = 10^{30}$ cm^{-2}-sec^{-1}. Discrimination against cosmic rays is obtained in time resolution (muons, if real, should come during the beam crossing) and in spatial resolution (the muons should come from a point inside the beam).

Given a 1 μsec sensitive time on the μ chambers, the level 1 rate without timing from the barrel calorimetry would be about 7 kHz. With the calorimeter signals ($\sigma_t \sim 1.2$nsec) one should be able to reduce the resolving time to less than 15 nsec. This lowers the rate to 100/sec after level 1, where one has the hit information on the central chambers and the position information from the muon chambers. At this point one should gain a factor of 10 in time resolution, and a factor of 10^3 from the P_T cut and the impact parameter cut (CDF-57). We are thus at or below .01/sec.

B. Beam-gas or beam-wall collisions

Measurements from the Main Ring (ref. 8.1) show that in general counting rates near the beam pipe are relatively low, but there is a significant level of 'rogue buckets', in which a large number of correlated particles, presumably from an interaction far upstream, arrives in time over a large area. The rate in the Main Ring in 1977 was about one bucket in 30. We do not know what the analogous background will be in the Doubler. The Main Ring, however, may be circulating particles for about one third of the cycle, and there certainly will be background associated with it as well. These events will have a distinct time signature in scintillators in the forward and backward arms and can be rejected before the next crossing.

We propose to have two scintillator counter arrays in each arm, each the size of the tunnel (approximately 8' high x 10' wide). These would be located on either side of the distant toroids in the backward arm, and in the symmetric place in the forward hall. The full length of the 721' level is thus available for shielding against hadronic debris. Muons travelling with the beam would arrive at times before the interaction, and with relative times in the two banks indicating a particle going the wrong way. This information would be correlated with the muon and calorimeter information of the detector proper to see if the event should be rejected at the level 2 trigger.

C. Multiple interactions per crossing

At a luminosity of 10^{30} $cm^{-2}sec^{-1}$ with a crossing interval of 1.75 μsec, 1% of all crossings (and 7% of all crossings with interactions) have two or more events in them. This has little effect on the trigger rates of already rare events, but probably will dominate multiplicity or very crude E_T triggers. (The problem with accepting such triggers would be that the neutral particles cannot be associated with their parent event.)

The present plan is to use the current division in the central tracking chambers at Level 2 or 3 to reject events with multiple vertices. (In the early days of the machine, high luminosity will not be a problem!) Processors exist at present at Fermilab (ref. 8.2) which can separate multiple vertices in a cylindrical geometry, and which are fast enough to function at Level 2.

8.5 TRIGGER SPECIFICS

A. What signals are needed

1. Hadronic and electromagnetic calorimetry. In each of these there are 24 divisions in ϕ by 46 divisions in θ in the main detector. The signal from each of these divisions is formed and balanced at the detector, and is brought directly upstairs for the level 1 trigger.

   Total: 2208 analog signals.

2. Muon counters, central detector barrel.

   Total: 1900 wires (one half the number of drift wires)

3. Central tracking chamber.

   a) 10 layers of fast hit latches (DC levels).

   Total: 3000 twisted pairs.

   b) 4 layers of current division. This should be done directly at the detector, and can be put out as a dc level.

   Total: 1200 wires.

4. The forward calorimetry. 24 divisions in ϕ by 8 in θ x 2 arms for electromagnetic and for hadronic calorimetry.

   Total: 768 analog signals.

5. Toroid muon chambers. 6 sectors x 126 cells x 2 toroid assemblies

   Total: 1512 DC levels (twisted pairs)

B. The location of the trigger logic electronics

The master logic of Level 1 is located in the lowest counting room (See Figure 8.4), which is 40 feet (as a shaped-charged crow files) from the centerline of the top of the detector. The electronics for the summing and calibration of the signals to form the 24 x 46 logical block sums sits directly on the detector.

The Level 1 trigger must be formed quickly enough such that the fast clear generated if the crossing has not satisfied a Level 1 trigger fans out to all modules within 1.25 μsec. A list of the delays in the trigger system is given in Table 8.3.

The level 1μ trigger, however, requires 1 μsec to be formed because of the drift time in the tubes. The level 1 trigger has returned from upstairs at this point and is waiting for the μ counters. If there is a muon, the 1 μ trigger intercepts the reset at 1.1 μsec and no reset is applied at the 1.25 μsec time.

The electronics for the barrel calorimeters, which are the fastest elements in the system, are located on the Roman arches. The slowest elements in the level 1 trigger are the gas calorimetry of the endplug (the backward and forward calorimeters are 50 feet (75ns) further away, but do not have any Lorentz force correction to drift times): the summing of signals in the endplug into logical block sums is done directly

on the back of the plug (i.e., the electronics moves with the plug). The sums are then brought by cable to racks located high on the endwall face of the forward end of the detector. This minimizes signal transit time, and leaves access to the end plug clear above and below. The endwall could either be treated this way, or all signals could be brought up to the high racks.

C. Cabling for the trigger-moving the detector

The signals needed for the trigger from the central detector amount to approximately 3000 analog pulse signals, and 4200 DC levels. They all can be brought up on twisted pairs: at 16 pairs/ribbon cable, this amounts to 450 flat cables. The muon chamber signals, necessary for Level 2, require another 120 ribbon cables.

The cables emerge from a common point at the top of the detector to minimize transit time. They run at the level of the top of the detector to slots alongside the door on the East side. From there they go directly up into the counting room. The simplest solution to the detector motion may be to disconnect these cables when moving.

D. Staging

The trigger described above lends itself well to staging the detector. For the early nonmagnetic stage the addition of scintillators around the interaction region inside the calorimetry would probably be an immensely valuable diagnostic tool. These would be included in the Level 1 trigger.

Table 8.3

Trigger Delays at Level 1

Element	Breakdown of Delay	Total Delay
central calorimetry	60 nsec width, 40 nsec tube delay, 20 nsec propagation	(120 nsec)
endwall + plug calorimetry	300 nsec drift, 100 nsec summing, etc.	400 nsec
forward calorimetry	300 nsec drift + 100 nsec extra transit	(400 nsec)
forward muons	<300 nsec drift + 75 nsec extra transit	(400 nsec)

a)	detector delay		400 nsec
b)	transit on detector	<50 feet	75 nsec
c)	transit to counting room	80' to counting, 20' in counting room	150 nsec
d)	transit of reset back to detector	70' of hardline	75 nsec
e)	fan out of reset on detector		300 nsec
		Total	1.00 μsec

This leaves 250 nsec for the Level 1 logic.

References

8.1 R. Loveless, 1977 Summer Study, Vol. 1, p. 187.
8.2 E. Barsotti, IEEE proceedings.

Figure Captions

Fig. 8.1 Schematic of the Level 1 trigger logic.

Fig. 8.2 The cluster finder described in CDF-93.

Fig. 8.3 The integral rate into the detector acceptance for a luminosity of $10^{30}cm^{-2}sec^{-1}$.

Fig. 8.4 Elevation view of the detector and counting rooms.

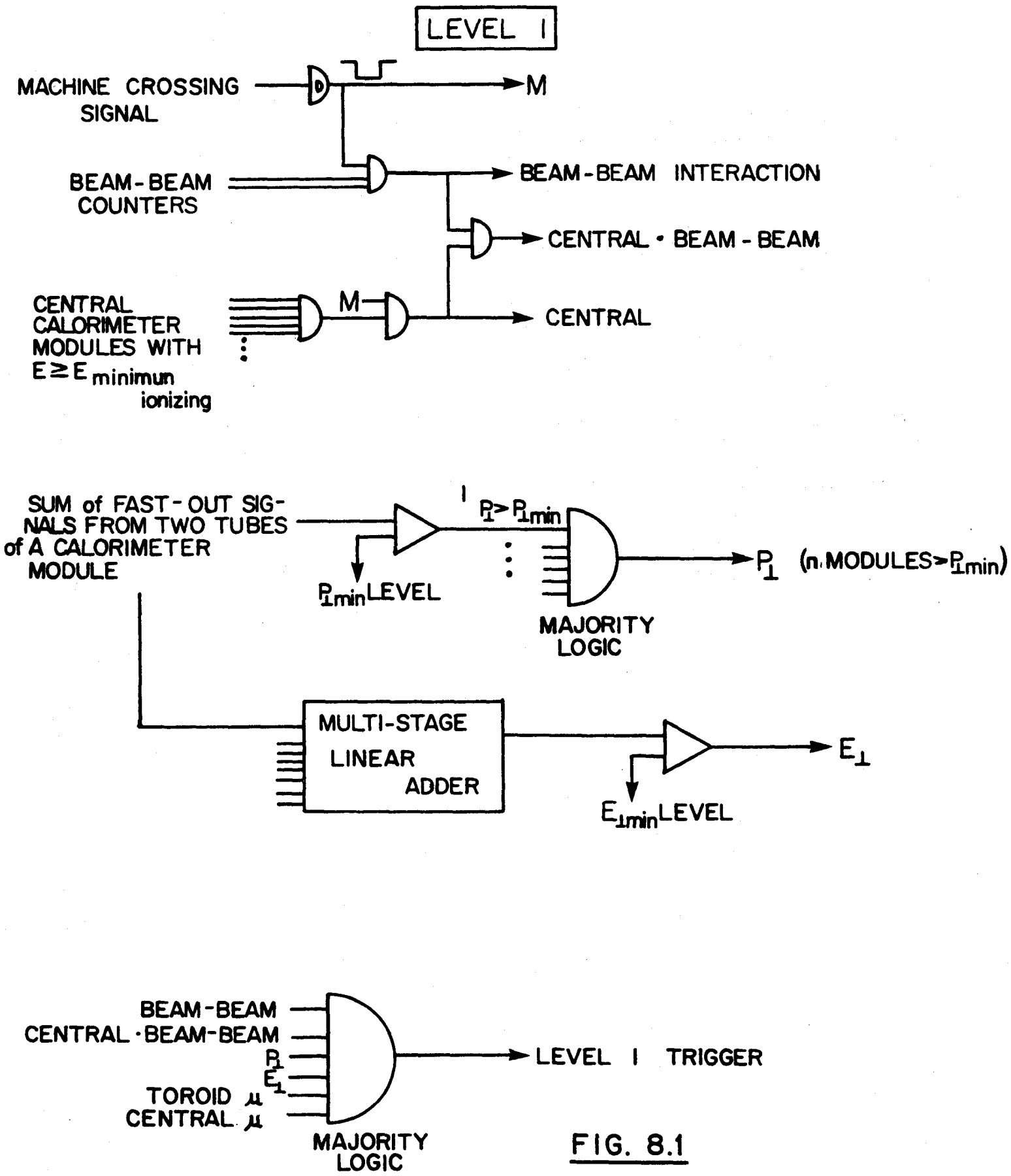
LEVEL 1
MACHINE CROSSING SIGNAL
M
BEAM-BEAM COUNTERS
BEAM-BEAM INTERACTION
CENTRAL · BEAM-BEAM
CENTRAL CALORIMETER MODULES WITH E ≥ E minimun ionizing
M
CENTRAL
SUM of FAST-OUT SIGNALS FROM TWO TUBES of A CALORIMETER MODULE
1
P⊥ > P⊥min
P⊥min LEVEL
P⊥ (n MODULES > P⊥min)
MAJORITY LOGIC
MULTI-STAGE LINEAR ADDER
E⊥
E⊥min LEVEL
BEAM-BEAM
CENTRAL · BEAM-BEAM
P⊥
E⊥
TOROID μ
CENTRAL μ
MAJORITY LOGIC
LEVEL 1 TRIGGER

FIG. 8.1

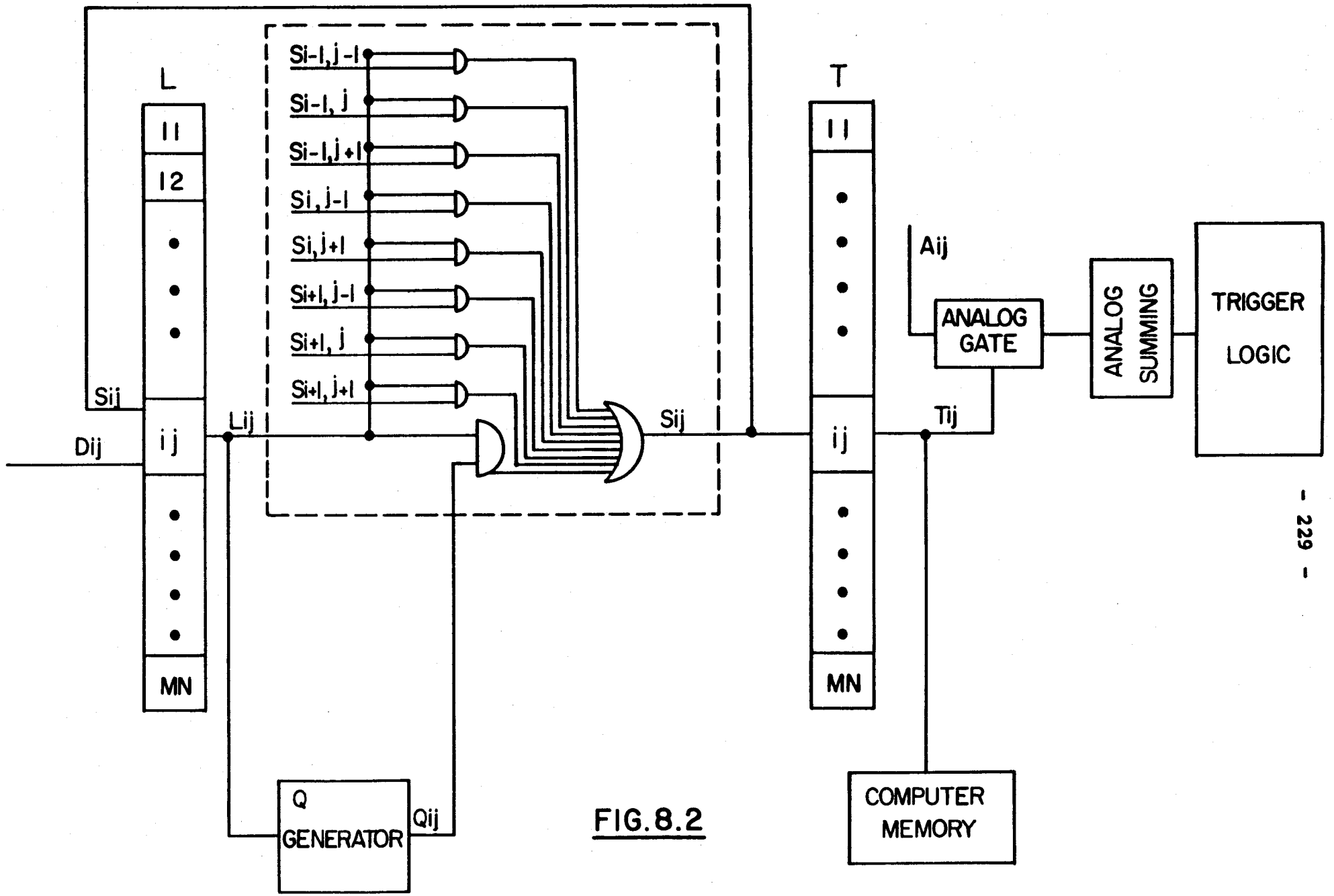
L
11
12
MN
Sij
Dij
ij
Lij
Si-1,j-1
Si-1, j
Si-1,j+1
Si, j-1
Si,j+1
Si+1, j-1
Si+1, j
Si+1, j+1
Sij
T
11
MN
ij
Aij
Tij
ANALOG GATE
ANALOG SUMMING
TRIGGER LOGIC
Q GENERATOR
Qij
COMPUTER MEMORY

FIG.8.2

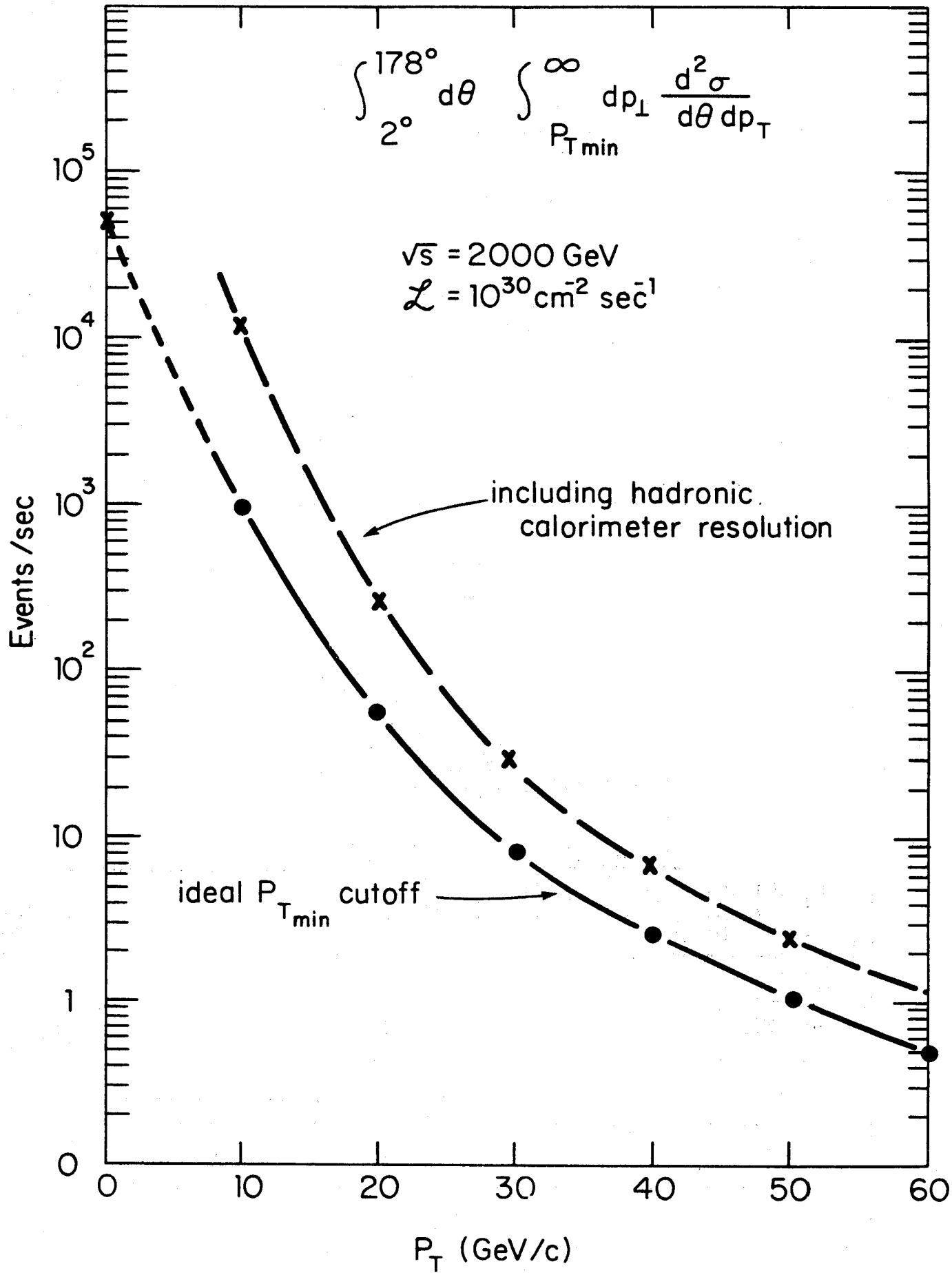
$\int_{2°}^{178°} d\theta \int_{P_{T\,min}}^{\infty} dp_\perp \frac{d^2\sigma}{d\theta\, dp_T}$
$\sqrt{s}$ = 2000 GeV
$\mathcal{L} = 10^{30} cm^{-2} sec^{-1}$
including hadronic calorimeter resolution
ideal $P_{T\,min}$ cutoff
Events /sec
P_T (GeV/c)
0
1
10
10^2
10^3
10^4
10^5
0
10
20
30
40
50
60

FIG. 8.3

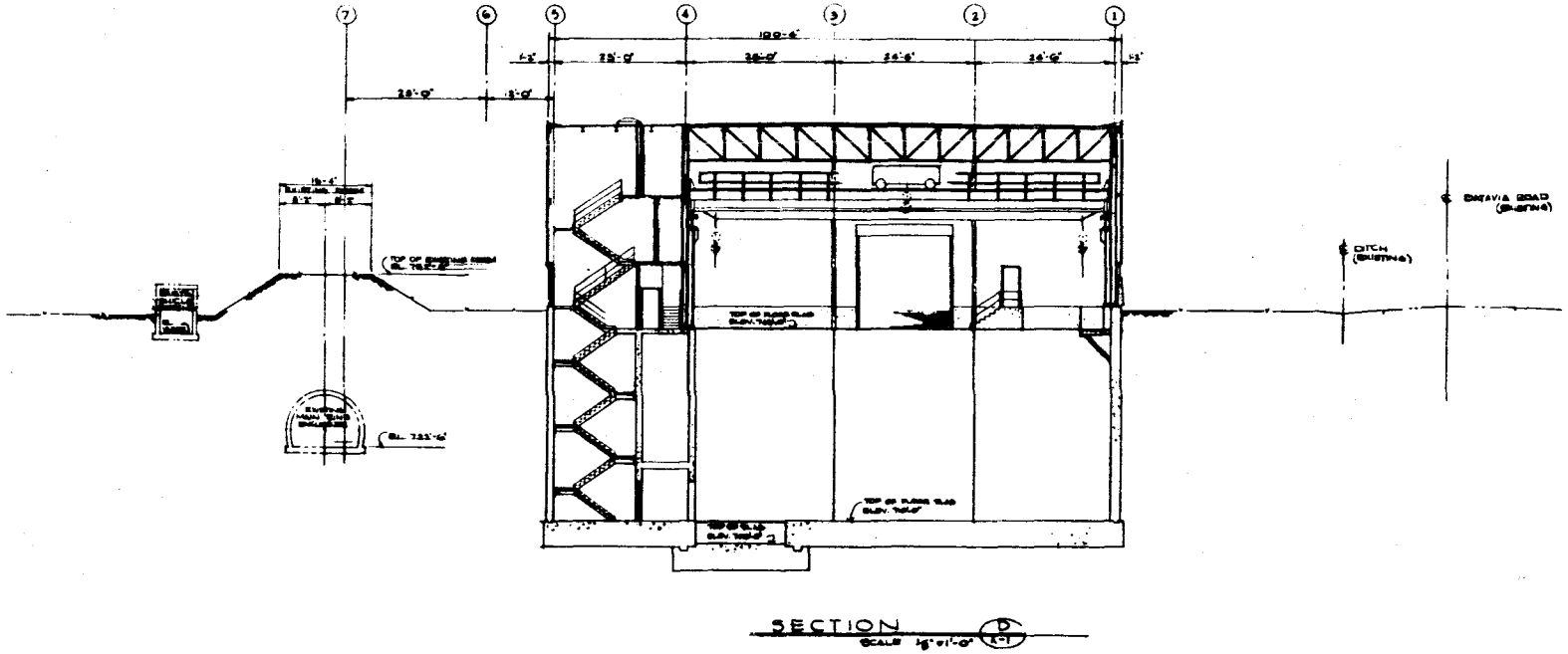

SECTION

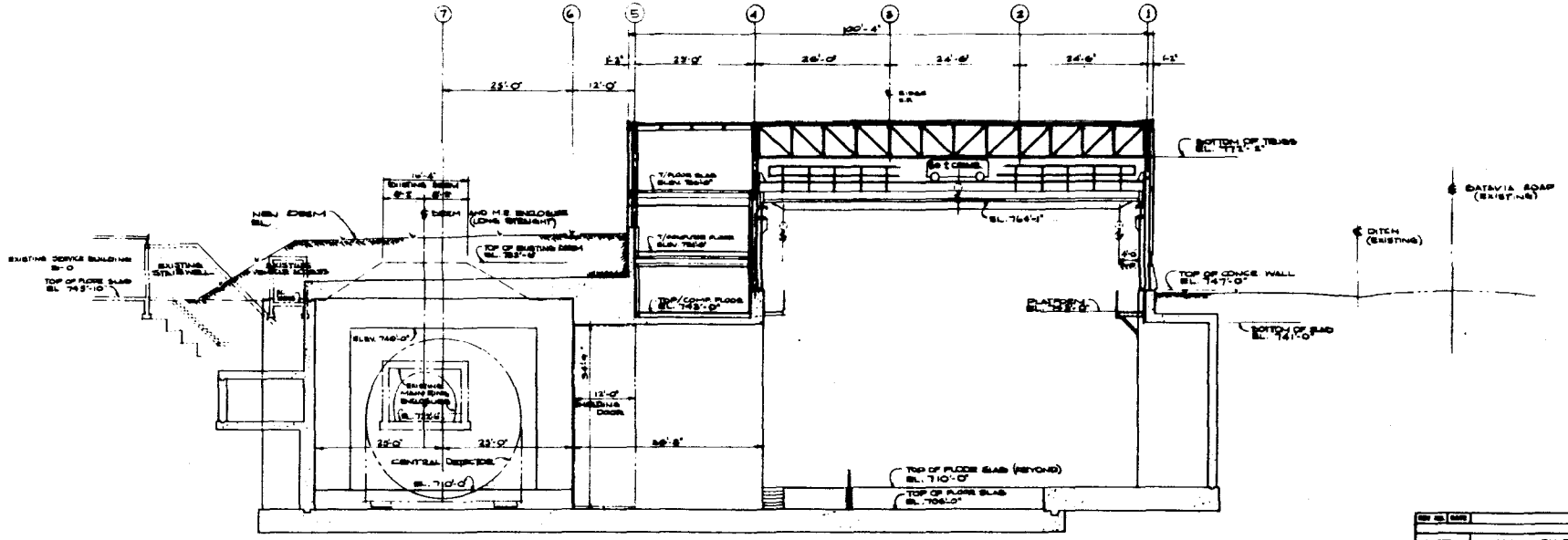

SECTION

DESIGNED	W.W. KRSTANOVIC	
DRAWN	J.T. HACKEMEIER	
CHECKED		
APPROVED		
SUBMITTED		

FERMI NATIONAL ACCELERATOR LABORATORY
UNITED STATES DEPARTMENT OF ENERGY

B-0 COLLIDING BEAM FACILITY
CROSS SECTIONS

MAY 1981

FIG. 8.4

Chapter 9

DATA ACQUISITION

The CDF Data Acquisition System is of necessity a complex one, due to the number of channels in the detector and the potential complexity of the physics we wish to investigate. It needs to cope with very high data rates, to select the data sample to write on tape, to monitor the performance of the detector and to maintain calibrations in a virtually automatic manner. It must still remain inexpensive. In addition, it is important for the data acquisition system to grow in a sensible manner as the luminosity of the machine increases.

Section 9.1 outlines the requirements on the system and the tasks it must perform. Section 9.2 provides an overview of the various pieces of the system, describing the components that will accomplish the tasks listed in section 9.1. Section 9.3 discusses certain decisions already made (relative to FASTBUS, the VAX, and front-end modules), dealing with the specific ways we intend to implement these components in CDF. Section 9.4 gives more details on various parts of the system, and in particular discusses the amounts and kinds of processing power needed in each component. Section 9.5 describes ongoing projects.

9.1 SYSTEM REQUIREMENTS

The tasks of the data acquisition system are:

1. Data logging: Writing the events onto magnetic tape. The assumption is that we will not attempt to accumulate data any faster than the speed of a 6250 bpi tape drive. This is both to avoid a difficult hardware and software project on developing a faster means of accumulating data, and because of the belief that any more data than that would

totally saturate our ability to analyze the data offline.

2. Preprocess the data: These tasks range from simple ones such as only selecting channels above some threshold and subtracting pedestals, to such complex ones as track-finding and jet-finding.

3. Event selection: The data acquisition system must filter the events, selecting only the ones of greatest physics interest to write onto tape. This implies the eventual presence in the system of a considerable amount of processing power that is programmable in high-level languages, so that on-line triggers can be understood, changed, and checked.

4. Monitoring: The system must provide automatic checks on the performances both of the various detector elements and of the data acquisition system itself.

5. Calibration: The system must provide for automatic calibration of the large number of channels in the system and maintain tables and histories of the calibration constants.

6. Interaction: The system must make it easy for physicists to hook into the detector at any level, from simple counts of hits per channel to complex physics analysis.

In somewhat more specific performance terms, the requirements on the system are:

1. The ability to deal with up to 100,000 channels, while keeping total electronics costs down to under $50 per channel.

2. The ability to process up to 1000 events/second and to select roughly 10 events/second for logging on tape.

3. The capability of turning the detector on in a gradual manner, with provisions appropriate for a low-luminosity machine at early stages, evolving into the complex system necessary for a higher-luminosity experiment later on.

9.2 SYSTEM OVERVIEW

The flow of data is shown in Figure 9.1 and a block diagram is given in Figure 9.2. The components of the system are:

1. Fast trigger: This provides the trigger for the data acquisition system. It is fully discussed in a separate chapter of this report. Important points to bear in mind are that the data acquisition system should be prepared to cope with up to 1000 fast triggers per second, and that the fast trigger is made using information that has an entirely separate path from the standard readout path.

2. Front-End Modules: These modules, primarily TDC's and ADC's, convert the electronic signals from the detector into voltage levels or digitized signals. There are of order 75,000 channels in the entire detector.

3. Scanner/Digitizers: These modules read through a crate (or a few crates) of front-end modules, digitize any undigitized data, scan to select only those channels above pedestal or above some preset threshold value, subtract off the pedestal, and write the data into an output buffer available to later stages of the system.

4. Processors: These modules perform a variety of functions on the output of the scanners to make the data more accessible to higher level processors and to perform special tasks for which there is not sufficient processing power available at higher levels. These tasks may include reformatting of the data, time/distance or pulse-height/energy conversions using tables of calibration constants, tabulation of high statistics monitoring information on an event-by-event basis, and reading additional channels nearby to the ones already read out. The processors may also make computations on the portion of the event available to them that can be used in later trigger decisions.

5. Minicomputers: These computers provide independent control over a subset of the data acquisition system, typically one or more crates of scanners and processors. These computers function as the primary data acquisition computer during checkout of independent subsystems and also form an integral part of the overall system, providing diagnostic and monitoring software that can be run on command from higher level machines or run independently of the rest of the system.

6. Event Builders/Bulk Memory: These devices (which in the early stages are likely to be merely a piece of software in one of the higher level processors) are responsible for collecting the entire event from the many buffers filled by the scanners and processors and for putting the event as a whole into a memory for further processing.

7. Trigger Filters: These are computers which do complex physics related calculations on the event as a whole to select which events will actually be logged onto magnetic tape.

8. High level computer complex: These computers run the whole system. The complex will contain one or more powerful 32-bit processors together with additional CPU's to act as front ends. Its jobs include data logging onto magnetic tape, overall performance monitoring, overall system control, event analysis, event display, data base management, etc.

As many as possible of these components will be assembled from commercially available CPUs and standard software so that our limited resources can be focused on the pieces of the problem that cannot be solved with commercially available equipment.

9.3 SETTLED ISSUES

Several important decisions have already been made about the implementation of certain pieces of the data acquisition system. These are:

1. VAX: The high level CPU will be a VAX.

2. FASTBUS: The various processors in the system will be linked via the FASTBUS, and most data transfers in the system will be block transfers from one FASTBUS memory to another.

3. Front End Modules: There is an overall requirement on the Front-End Modules that they deliver their data into FASTBUS memories within 0.5-1.0 milliseconds.

Considering these in turn:

1. VAX

This decision requires little further discussion. The VAX is clearly the 32-bit computer of choice, particularly in view of the maturity of its software. The VMS operating system is well matched to the multi-task on-line program needed for CDF. We have already acquired a VAX-11/780.

Note that this does not necessarily imply that tape logging will be done on the VAX, nor does it imply that there will be extensive real-time interrupt driven operations on the VAX. It may prove to be convenient to off-load certain of these functions onto smaller dedicated front-end CPU's, reserving the VAX for overall system management, analysis, and monitoring functions. The list of important non-real-time tasks that can only be performed on the VAX is a long one, including physics analysis of incoming events, maintaining data bases of past histories of performance of detector components, error logging, calibration, and graphic event displays. It would be easy to lose the capability to perform some of these functions by overloading the VAX too heavily with real-time tasks, particularly due to the relatively poor real-time responsiveness of such a large system. The precise division of tasks between the VAX and satellite CPU's has yet to be determined, and in fact may very well change as the system evolves.

2. FASTBUS

This decision merits some discussion. First, it is important to recognize what this does not imply. In particular, we put no requirement on the packaging of front-end modules, and we do not require commercial manufacturers to redesign electronics to fit the FASTBUS

standard. Rather, we are adopting FASTBUS as the standard for high speed interprocessor communications.

Simply put, the CDF system requires a standard that allows for high speed block transfers of data and provides for multiple processors all contending for the same bus. FASTBUS meets these requirements with relatively low overhead, as well as bringing the additional advantages of 32-bit addressing (allowing every channel in the detector to be addressed individually, impossible in a CAMAC system), commercial availability of crates and power supplies, and development of pieces of use to CDF (interfaces, bulk memory, software, etc.) by other groups, both at Fermilab and elsewhere. In general a broad range of FASTBUS support, both hardware and software, is likely to become available within the community, as has been the case with the CAMAC standard.

Note that it is likely that there will be an additional communications link (for example DECNET) between high level processors in the system for lower rate control information. The FASTBUS will almost exclusively be used for block transfers from one memory to another, a function for which it is very well suited.

3. Front End Modules

The front end modules have to be highly reliable, since it is intended to locate them inside the shielding wall close to the detector. This is crucial to avoid having 75,000 cables, all of which pass through the shielding wall and must move when the detector is moved from the assembly area to the collision area. Redundancy and remote diagnosis of faults are important considerations. Physical dimensions will in many cases be determined by the amount and shape of space available on the detector.

Electronic requirements on the front end modules come from two directions: the fast trigger and the (relatively) slow standard read-out. Again, note the important implicit assumption here. The fast trigger is entirely separate from the standard read-out path. This is to keep the bulk of the electronics as simple and inexpensive as possible. A requirement that every channel has its data available rapidly enough to be used in the fast trigger would add greatly to the complexity and cost of the electronics.

Thus, the primary requirement on the front end modules for all channels is for the standard read-out. The modules must be able to deliver their digitized data into FASTBUS memories in 0.5-1.0 milliseconds after receiving a fast trigger. In addition, some 10% of all channels are used in the fast trigger. These have the additional requirement of a separate fast output (and separate cable) for use in the trigger.

9.4 DETAILS ON SYSTEM COMPONENTS

Scanners

The scanners perform the functions of digitization (if not already done by the front end modules), sparse data scan, and pedestal subtraction, filling up a FASTBUS output buffer with the data. They are required to read through all attached channels in 0.5-1.0 milliseconds. This limits an individual scanner to handling roughly one crate containing roughly 1000 channels. Thus there are a total of order 100 scanners in the entire system.

One reasonably well worked out scheme for the scanners is under design by Tom Droege's group. This scheme consists of two modules, a remote scanner (called EWE-2) which lives at the detector in the same crate as the front end modules, and a

scanning controller (called TDS, or table driven scanner) which lives in a FASTBUS crate in the counting house. The two modules are connected by a cable with a specially defined protocol.

The system works as follows: The TDS contains tables of addresses, pedestals and thresholds. It sends an address and a threshold value to the EWE-2. The EWE-2 does a digital-to-analog conversion on the threshold value and performs an analog comparison of the data with the threshold. If that channel is indeed above threshold it goes on to perform a high precision analog-to-digital conversion on the data, and then sends the digitized data back to the TDS where the pedestal is subtracted and the data, together with a channel label, is put into an output buffer. It is expected that this system will require roughly 500 nanoseconds per channel that is below threshold, and 3 microseconds per channel that is above threshold, resulting in a total time of 800 microseconds for a crate of 1000 channels with a 10% hit rate.

Processors

As described above, the processors perform a wide variety of functions, falling into the general categories of data formatting and compaction, monitoring, and calculations for later trigger decisions. Different components of the detector will require widely differing amounts of processing at this level, as will the same components of the detector at different stages in the evolution of the system.

This ranges from a few operations per data word (for a simple calibration correction), or even no operations if the "raw" data from the scanner is to be sent directly on to the next level of processing, up to tens of operations per word if calculations are to be performed. Since a single scanner puts out up to 1000 100-word events per second, the output of an individual scanner can require anywhere from 2×10^5 to 5×10^6 operations per second at this level.

Thus a single processor may be attached to a single scanner, or to an entire crate of scanners, depending on the amount of processing needed. The processors may be either conventional micro-computers (PDP 11/23, for example), somewhat more specialized microprocessor based systems (e.g., Intel 8086 or Motorola 68000), or even home-built special purpose processors, again depending on the processing needs. The programs at this level will not be changed often, so it is not vital for these processors to be general purpose CPU's. However, it will be important to prevent the proliferation of lots of different types of devices and to optimize the use of scarce designing talent by making maximum use of commercially available products. The exact design of the processors will be specified gradually as the processing needs of the various subsystems become clearer. In any case, the early stages of the system will not need processors, or at most will have some of this functionality performed by various general purpose CPU's elsewhere in the system.

Minicomputers

These computers have two different functions at different stages in the evolution of the detector. First, when the subsystems are separated and are being brought up individually (possibly in widely separated locations), these computers are the primary data acquisition computers for the subsystems. Thus they are required to be a fairly standard CPU/software package, for example a PDP-11/23 or 34 running RT MULTI.

Second, in the context of the overall system, they continue to perform an important role in monitoring the performance of the subsystems. While not in the direct path of data between the detector and mag tape, they sit off to the side examining a subsample of the events. Jobs on these CPU's can be initiated locally or on command from a terminal attached to a higher level CPU via DECNET, for example.

There are no crucial speed requirements for these computers. Instead, it will be appropriate to have one per major detector subsystem, or one per crate of scanners and processors, and thus a total of order 10 for the entire system. They also do not need extensive peripherals, as program development for them will be done on the VAX.

Event Builder

If the event builder is a single device, it represents the high rate node in the system, processing 10^7 words/second. Its function, however, is a simple one, since it merely acts as a funnel, gathering blocks of data from various memories in the scanners and processors and collecting them in a single bulk memory. Two possible implementations of the event builder are under consideration:

1. A single high speed device. This would be a special device with a very simple instruction set that can do FASTBUS block transfers very efficiently.

2. A multitude of separate devices, or more likely, software in each of the individual trigger filter CPU's. This will require development of a switching network to route the events one at a time to whichever event builder/trigger filter is ready to receive an event.

9.5 ONGOING PROJECTS

Present efforts are concentrated on those areas of the system which are required to be ready at the earliest stages, in particular the front-end modules, scanners, human interface computers, and the VAX. Some of the projects underway now are:

1. Evaluation of prototype TDC systems (from both Tom Droege's group and from LeCroy).

2. Evaluation of prototype ADC systems.

3. Design of the EWE-2/TDS Scanner/Digitizer system.

4. Development of FASTBUS interfaces and software.

5. Development of a Multi system for the VAX (and specification of a future system to provide physicist interface with the event data in the actual data acquisition system).

6. Development of a serial CAMAC facility for the VAX.

Figure Captions

Fig. 9.1 Logical data flow during normal data acquisition.
Fig. 9.2 Block diagram of the CDF data acquisition system.

DATA FLOW

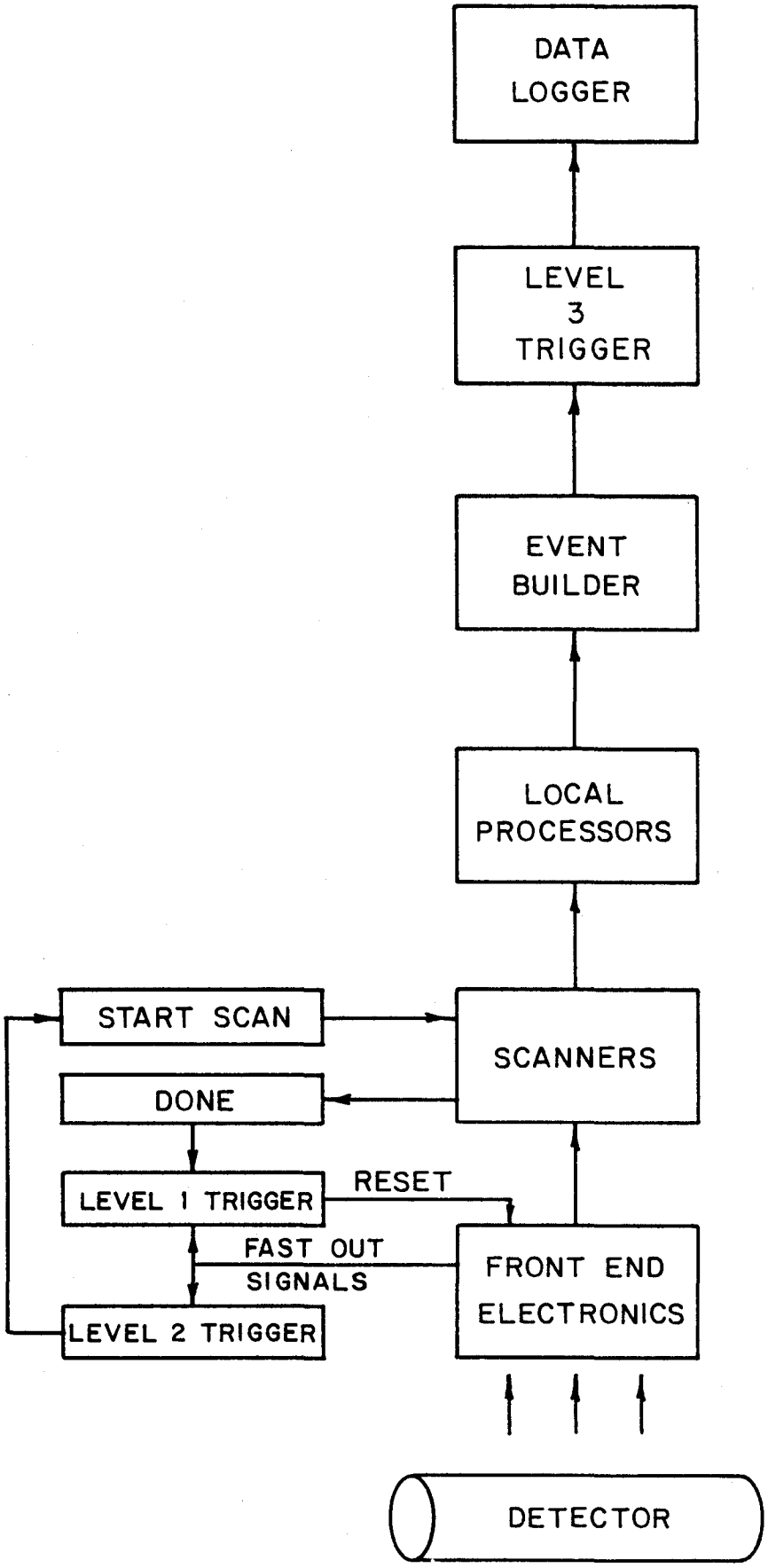

FIG. 9.1

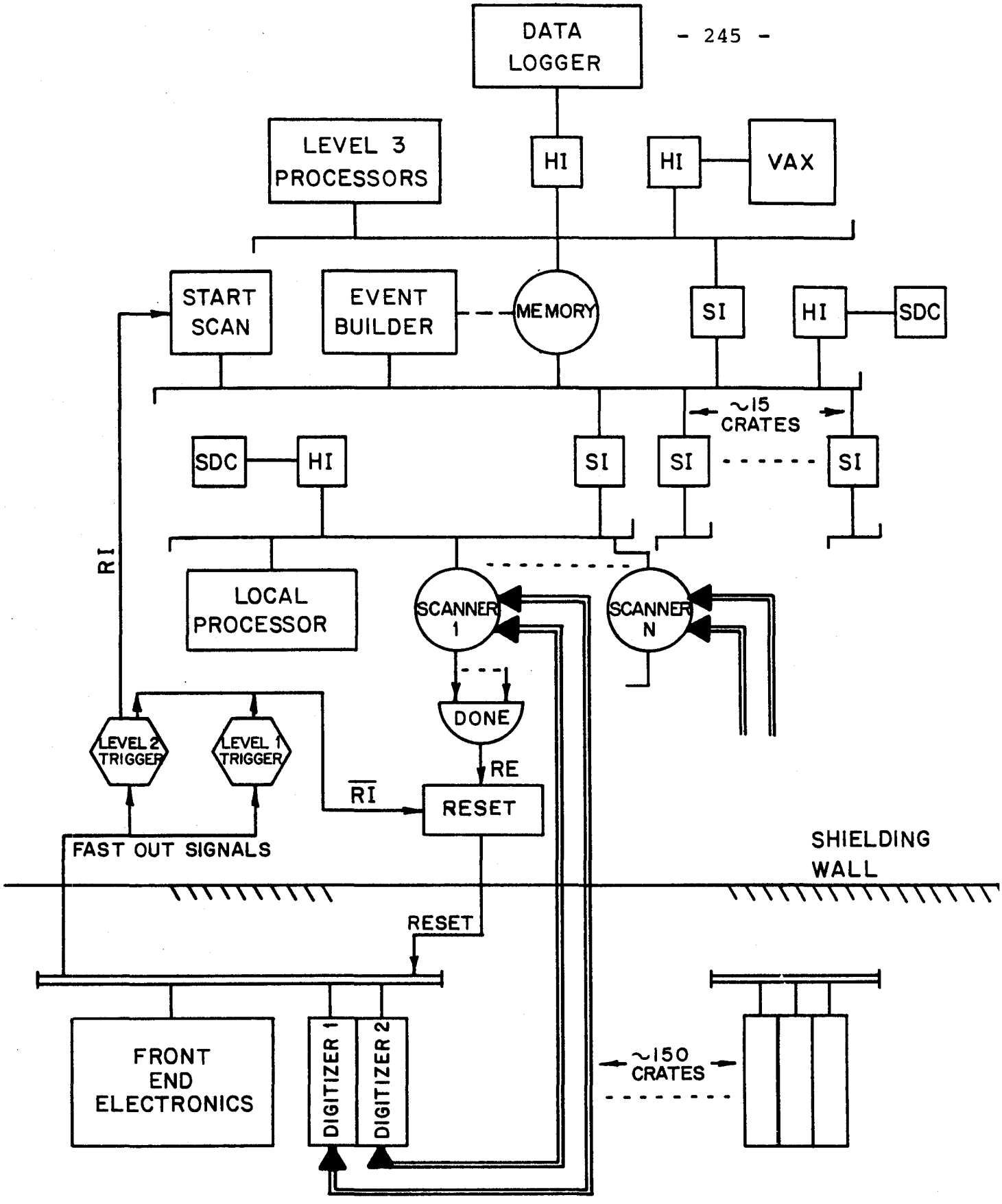

RE RESET ENABLE
RI RESET INHIBIT
HI HOST INTERFACE
SI SEGMENT INTERCONNECT
SDC SERVICE AND DIAGNOSTIC COMPUTER

FIG. 9.2

Chapter 10

DETECTOR PERFORMANCE

In this chapter we come back to the physics of Chapter 1 but with the details of the detector in hand. We describe here how the detector is expected to perform on several specific experiments. Much of the following of course depends on the models used for both the signal and the background; no claim is made for the truth of any of the model predictions, but we have tried to be consistent in order to illustrate the capabilities and limitations of the detector. More detailed studies are continuing.

Section 10.1 discusses the detection of the leptonic decays of the W and the Z, and the discrimination of these leptons from backgrounds from parton jets, c, b, and t quark semileptonic decays, and leptons from the Drell-Yan process. Section 10.2 briefly discusses the measurement of the transverse momentum spectra for jets. Finally, in Section 10.3 the identification of the top (T) meson in the hadronic and semileptonic decay modes is discussed.

10.1 LEPTONIC DECAYS OF THE INTERMEDIATE VECTOR BOSONS $W^{\pm}$ AND Z°

The results to be discussed in this section are based on Monte Carlo studies that incorporate realistic simulation of the detector. Data from beam tests of our prototype calorimeters were used to obtain a parameterization for the energy resolution, the partition of energy between electromagnetic and hadron calorimeters as well as between adjacent towers, and energy leakage. We were able to analyze the equivalent of several million Monte Carlo generated background jet events by performing track reconstruction only on those events with at least one charged particle of momentum

above 15 GeV/c. This is justified because track reconstruction studies, summarized in Appendix V, show that the probability of reconstructing a low momentum track as a very high momentum track is small.

Rates: Signal And Background

We expect 20,000 W bosons of each sign and 10,000 Z°'s to be produced in an integrated luminosity of 10^{36} cm^{-2} (see Chapter 1 and Reference 1.7). The branching ratio for $W^{\pm}\rightarrow\ell^{\pm}\nu$ is estimated to be 8%. We thus anticipate about 1600 each of the decays $W^{+}\rightarrow e^{+}\nu_e$, $W^{+}\rightarrow\mu^{+}\nu_\mu$, $W^{-}\rightarrow e^{-}\bar{\nu}_e$ and $W^{-}\rightarrow\mu^{-}\bar{\nu}_\mu$. The angular distribution of the leptons is shown in Figure 1.2 of Chapter 1. The branching ratio for $Z^{\circ}\rightarrow\ell^{+}\ell^{-}$ is 3% for each lepton type, so that 300 $e^{+}e^{-}$ and 300 $\mu^{+}\mu^{-}$ pairs will be produced.

The distinctive W or Z signature which we exploit is the presence of an isolated large P_T lepton. The major backgrounds are from jets produced by the hard scattering of the incident partons of the p and $\bar{p}$. These jets are predicted to occur 10^4 times as copiously as the leptons from W decay at a P_T of 35 GeV/c, and 10^6 times at a P_T of 15 GeV/c. Figure 10.1 shows the predicted $d^2\sigma/dydP_T$ at y=0 versus P_T for jets, inclusive charged hadrons, and leptons from W decay.

There are other backgrounds, such as single leptons from c, b and t decay, and pairs of leptons from the Drell-Yan process. The spectra of single leptons from both these reactions are also shown in Figure 10.1.

Triggering

The rates for "single electron" triggers, as defined below, are shown in Figure 10.2. The curves labelled A through C are the integrated rates of triggers above a threshold energy E_T from QCD jets after the following progressively tighter cuts:

(A) At least one electromagnetic tower has energy above threshold.

(B) The total energy in the nine hadron towers adjacent to or behind the EM tower is less than 10% of that of the trigger EM tower.

(C) There is a track with P_T above 5 GeV/c.

Criteria (A) and (B) select predominantly isolated π^o's; criterion (C) requires an energetic particle to be charged, thus suppressing the π^o's. The off-line programs then deal with the remaining sample of events.

With reference to the discussion in the trigger chapter (Chapter 8) criteria A and B could be implemented in trigger level I and criterion C in level II.

We observe that this electron trigger with a p_T threshold of 10 GeV/c, using criteria A, B and C gives a trigger rate of 0.3 Hz. Studies with Monte Carlo generated events that contain single electrons and beam jets have shown that the trigger efficiency is 80% for those electrons with energies 10% above threshold, and the efficiency increases to more than 95% at an energy 1.5 times threshold. The major loss near threshold in this simple implementation of the trigger is due to leakage into neighboring towers. The cluster finder described in Chapter 8 should provide much better performance near threshold.

A "single muon" trigger can be implemented over the central barrel ($50°<\theta<130°$), and in the region covered by the toroids ($150°<\theta<175°$). The muon requirements are an energy deposition in the calorimetry consistent with a minimum ionizing particle, penetration to the appropriate muon chamber depth, and a high P_T track in the chambers. We find from the Monte Carlo that we have a 57% trigger efficiency for $W^{\pm}\rightarrow\mu^{\pm}\nu$. For the $Z^o\rightarrow\mu^+\mu^-$ the detection efficiency is 58%. In this case the triggering is on one muon only, but both muons must be detected. For both the W and the Z^o the major loss is in the end cap on the side which is without toroid coverage.

$W^{\pm} \rightarrow e^{\pm}\nu$ Event Recognition

Our Monte Carlo studies show that the most serious off-line background to $W^{\pm} \rightarrow e^{\pm}\nu$ events is from single charged hadrons, even though π°'s and not charged hadrons dominate the trigger rate. Of particular interest is therefore the total off-line rejection of this background. The situation is illustrated in Figure 10.3, where the upper curve is the total jet cross section before triggering. The effect of the three following cuts is also shown:

(E1) Isolated charged particle requirement
The high P_T electron candidate must have no other energetic particles nearby. This is implemented by requiring that the adjacent calorimeter towers contain only a small amount of energy (typically 1 GeV or less) and that there be no reconstructed energetic tracks nearby. Figure 10.3 shows the rate of isolated charged particles, roughly one fourth of the total charged particle spectrum. At a P_T of 20 GeV/c this criterion causes a rejection factor of 300 in the jet rate, and is 99% efficient for W decays. The loss is due to overlap of the electron with "beam jet" particles of average density $dn/dy = 9$.

(E2) Electron identification criteria
The electron candidate must behave like an electron, i.e., leave almost all of its energy in the EM tower, have an E/p close to 1.0, and satisfy the strip chamber requirements, see section 4.1. At a P_T of 20 GeV/c, these criteria bring an additional rejection factor of about 400 with a 90% efficiency for real electrons. A larger rejection factor is possible if one is willing to accept lower efficiency.

(E3) P_T imbalance
We have studied the expected angular correlation between two QCD jets, one of which gives rise to the background electron candidate. About 1% of the oppositely-directed jets will lie within the uninstrumented region of our detector. At high p_T ($p_T \geq 15$ GeV/c) the rejection factor is therefore about 100.

About 90% of the events with electrons from W decays satisfy these three criteria. The combined rejection factor against the jet background is 300 x 400 x 100 or about 12,000,000 at a p_T of 20 GeV/c, see Figure 10.3 and Reference 10.1. As seen in the figure, the background has been eliminated by these cuts above a p_T of 15 GeV/c.

In the angular region $3° \leq \theta \leq 10°$ the momentum resolution in the solenoid is very poor. The charged hadron rejection is consequently worse by a factor of about 5. The expected signal and background are shown in Figure 10.4.

Other backgrounds for electrons are:

1) $\pi°$ background--e^+e^- pairs can be generated either in $\pi°$ Dalitz decays or by external conversion of the γ-rays, for instance in the beam pipe. The detector discrimination against this background comes from the E/p cut (the other photon from the $\pi°$ decay lands very close to the electron in the shower counter), and from detecting the other electron. From the Monte Carlo studies we estimate this background to be about an order-of-magnitude smaller than the charged particle background in the central region.

2) overlap of an energetic $\pi°$ and a low energy charged hadron--our Monte Carlo studies show that this background is much less than either one of the above backgrounds in the central region (again the E/p cut discrimates strongly).

3) electrons from heavy quark decays (c, b, t)--the estimated cross section for these electrons, shown in Figure 10.1, is clearly small. Detection of associated jet particles on either side (E1 and E3) reduces this background to levels below the charged hadron background.

4) electrons from the Drell-Yan process--this cross section is also shown in Figure 10.1. The detection of the second electron reduces this already small background to considerably below the charged hadron background.

$W^{\pm} \rightarrow \mu^{\pm} \nu$ Event Recognition

Again the dominant background is from charged hadrons from jets. The first requirement (M1) is that the particle be an isolated charged particle, just as in the electron case. The second requirement (M2) is that the particle act muon-like. This requires that the electromagnetic shower and hadron calorimeter towers at which the track points have minimum ionizing signals and that there be a satisfactory track in the outer muon chambers. The probability of π, $K \rightarrow \mu$ decay in flight plus the probability of hadronic punch-through is approximately 1/200 at p_T = 20 GeV/c, comparable to the probability of a hadron faking an electron. The final cut (M3) is a P_T imbalance cut exactly as in the electron case.

Figure 10.5 shows the muon signal from W decays compared with the expected background after the above cuts. The combined rejection factor at a P_T of 20 GeV/c is 300 x 200 x 100 or 6,000,000, half as good as the combined rejection in the electron case.

The Charge Asymmetry in W Decay

Figures 1.2, 1.3, and 1.4 of Chapter 1 show clearly the charge asymmetry in the leptonic decay of the W. At low values of p_T there is a preponderance of ℓ^- in the proton hemisphere. At large p_T for angles away from 90° the asymmetry reverses.

A two dimensional plot of the number of leptons of each sign produced in a given angular range and a given P_T bin is given in Table 10.1. The upper entry in each bin is the number of beam sign leptons (e.g. positrons in the proton hemisphere) produced in an integrated luminosity of 10^{36} cm^{-2}. The lower entry is the number of opposite sign leptons. No effects of detector resolution or efficiency are included in Table 10.1.

The region where the asymmetry is large, and where the background rejection might be adequate is roughly described by the intervals 15 GeV/c $\leq P_T \leq$ 35 GeV/c and $2° \leq \theta \leq 20°$, as indicated in Table 10.1. In this region, there are 116 ℓ^- and 29 ℓ^+ (there are equal numbers with opposite signs on the other side).

The muon toroids cover this region of phase space (on one side) with an 17% momentum resolution and fundamentally high efficiency. Table 10.2 shows the effects of the momentum resolution. In the contour shown, there are 99 ℓ^- and 35 ℓ^+, still a very significant asymmetry (CDF-64).

In Table 10.3, we show the same asymmetry with the electron resolution folded in. We also show in Table 10.3 the contour for sign determination in the solenoid. The region of large asymmetry is unfortunately beyond the limit of sign determination.

However the addition of two sets of chambers of the same design as the intermediate tracking close to the beam pipe allow a sign determination at a P_T=35 GeV/c with 100% efficiency at 10° and 60% at 5°. In the 5°-10° region we expect 7 electrons and 43 positrons in the backward detector; the forward arm would see the same with the signs reversed. If we put in a (somewhat arbitrary but pessimistic) detection efficiency of 60%, we are left with an asymmetry of ∿8 beam sign and ∿52 opposite sign leptons.

Table 10.1

$P\bar{P} \rightarrow W^+ X, W^+ \rightarrow \ell^+ \nu$ $(W^- X, W^- \rightarrow \ell^- \bar{\nu})$ WITHOUT SMEARING Unit: 10^{-36} cm^2

P_T (GeV/c)	0^o-5^o	5^o-10^o	10^o-15^o	15^o-20^o	20^o-25^o	25^o-30^o	30^o-35^o	35^o-40^o	40^o-140^o
0-5	1.63 (8.17)	0.73 (2.91)	0.42 (1.58)	0.15 (1.53)	0.04 (0.49)	--- (0.82)	--- (0.23)	--- (0.45)	
5-10	0.91 (8.63)	1.87 (5.44)	1.64 (4.30)	1.09 (3.63)	0.46 (2.67)	0.13 (1.61)	0.29 (2.60)	0.10 (0.82)	11.9
10-15	0.50 (8.65)	1.69 (10.10)	2.81 (6.85)	2.37 (4.81)	1.92 (3.52)	0.70 (2.59)	0.42 (5.65)	1.13 (5.14)	23.0
15-20	0.37 (7.29)	1.37 (10.10)	1.85 (5.74)	2.53 (7.51)	2.53 (2.96)	2.62 (4.66)	2.23 (3.56)	1.72 (5.25)	59.8
20-25	0.20 (4.07)	1.23 (12.9)	1.75 (7.72)	2.50 (4.13)	3.18 (3.58)	3.58 (6.47)	4.86 (4.45)	4.82 (6.73)	79.8
25-30	0.25 (2.37)	1.44 (9.83)	2.25 (12.37)	4.31 (10.2)	5.46 (6.68)	5.03 (8.41)	8.11 (4.02)	7.28 (5.34)	109.5
30-35	0.33 (0.88)	2.60 (9.87)	5.69 (10.65)	8.43 (10.0)	10.0 (7.05)	10.2 (7.52)	10.3 (9.53)	9.58 (8.49)	141.5
35-40	0.12 (0.13)	7.62 (6.11)	16.0 (12.3)	19.0 (11.8)	18.1 (12.1)	18.9 (12.5)	17.8 (13.0)	16.5 (11.4)	225.0
40-45	--- (---)	0.35 (0.17)	1.13 (0.60)	1.16 (0.67)	1.25 (0.72)	0.93 (0.57)	0.80 (0.94)	0.91 (0.65)	13.8

The number of $W^{\pm} \rightarrow \ell^{\pm}\nu$ events produced in an integral luminosity of 10^{36}cm^{-2} binned in 5 GeV/c bins in p_T and 5^o bins in polar angle. The upper line of each bin is the number of beam sign leptons (e.g. positrons in the proton hemisphere); the lower line is the opposite sign.

Table 10.2

$P\bar{P} \rightarrow W^+X \hookrightarrow \mu^+\nu$ $(W^-X) \hookrightarrow \mu^-\bar{\nu}$ WITH SMEARING UNIT: $10^{-36}CM^2$

$\theta \rightarrow$ WITH RESPECT TO THE PROTON

P_T (GeV/c)	0°-5°	5°-10°	10°-15	15°-20°	20°-25°	25°-30°	30°-35°	35°-40°	40°-140°
0-5	1.68 (7.61)	0.55 (3.91)	0.44 (1.48)	0.21 (1.17)	0.05 (0.52)	0.01 (0.46)	0.01 (0.16)	0.004 (0.45)	
5-10	0.87 (9.05)	1.93 (6.41)	1.79 (4.84)	1.70 (4.61)	0.57 (2.95)	0.31 (2.72)	0.30 (2.01)	0.10 (0.83)	
10-15	0.51 (9.38)	2.04 (8.87)	2.37 (7.61)	2.21 (4.50)	2.19 (2.71)	0.93 (2.62)	0.68 (5.37)	1.20 (5.48)	
15-20	0.35 (6.79)	1.22 (10.0)	2.30 (8.02)	2.32 (6.59)	2.77 (3.54)	2.90 (2.67)	3.69 (5.46)	2.27 (5.01)	
20-25	0.29 (3.53)	1.81 (11.7)	2.66 (7.80)	3.69 (9.22)	4.52 (4.20)	5.05 (9.52)	6.99 (3.99)	6.39 (7.35)	
25-30	0.23 (2.28)	2.19 (10.4)	4.21 (10.6)	5.17 (8.02)	6.79 (6.92)	6.31 (9.19)	9.54 (4.98)	7.87 (6.03)	
30-35	0.19 (1.09)	2.79 (7.68)	6.42 (8.62)	9.48 (8.07)	9.87 (7.30)	10.1 (6.41)	9.57 (8.94)	8.48 (8.20)	
35-40	0.14 (0.35)	3.19 (5.32)	6.52 (7.89)	8.22 (6.26)	9.54 (7.18)	9.04 (4.81)	6.30 (6.51)	9.72 (6.26)	
40-45	0.05 (0.08)	2.18 (2.25)	3.98 (3.49)	6.08 (4.26)	4.31 (2.55)	4.9 (4.77)	5.19 (5.15)	4.26 (3.87)	

$\Delta P/P = 17\%$
$0.2\% \times P_T/\tan^2\theta$
$0.2\% \times P_T$

$2^\circ \leq \theta \leq 30^\circ$
$30^\circ \leq \theta \leq 45^\circ$
$45^\circ \leq \theta \leq 135^\circ$

±15% Statistics

The same plot as Table 10.1, but including the detector resolution for muons.

Table 10.3

$\bar{P}P \rightarrow W^+X \hookrightarrow e^+\nu \quad (W^-X) \hookrightarrow (e^-\bar{\nu})$ WITH SMEARING UNIT: $10^{-36}CM^2$

P_T (GeV/c)	0°-5°	5°-10°	10°-15°	15°-20°	20°-25°	25°-30°	30°-35°	35°-40°	40°-140°
0-5	1.63 (7.77)	0.73 (3.08)	0.42 (1.58)	0.09 (1.41)	0.05 (0.49)	0.01 (.083)	0.01 (0.16)	--- (0.47)	0.94
5-10	0.91 (9.19)	1.81 (5.08)	2.02 (4.30)	1.37 (4.23)	0.46 (2.69)	0.30 (2.34)	0.30 (2.11)	0.10 (7.97)	12.1
10-15	0.49 (8.27)	1.77 (10.1)	2.44 (6.84)	2.39 (4.74)	1.97 (2.90)	0.56 (1.80)	0.70 (5.37)	1.16 (5.16)	24.1
15-20	0.37 (7.40)	1.32 (10.2)	1.70 (6.76)	2.24 (6.11)	1.54 (3.38)	2.69 (4.35)	1.96 (4.46)	1.72 (5.16)	59.9
20-25	0.20 (4.11)	1.26 (12.9)	7.02 (6.81)	2.61 (5.91)	3.29 (3.90)	3.55 (6.75)	5.85 (4.17)	5.51 (5.60)	79.3
25-30	0.25 (2.49)	1.50 (10.1)	2.08 (11.5)	4.43 (8.95)	5.33 (7.12)	5.01 (8.36)	7.34 (4.43)	6.71 (6.45)	104.4
30-35	0.33 (0.83)	2.69 (9.74)	5.91 (12.2)	8.10 (10.5)	9.79 (6.49)	10.6 (7.78)	10.6 (8.73)	9.13 (9.41)	147.3
35-40	0.12 (0.13)	7.26 (5.87)	15.1 (11.3)	18.5 (11.4)	17.6 (11.3)	17.8 (11.2)	16.1 (13.2)	16.1 (10.3)	215.4
40-45	--- (---)	0.86 (0.24)	1.90 (0.86)	2.00 (1.08)	1.95 (1.48)	1.58 (1.71)	2.04 (1.41)	1.58 (0.87)	22.6

LIMIT OF SIGN DETERMINATION IN SOLENOID.

The same plot as Table 10.1, but including the detector resolution for electrons.

$Z^0 \rightarrow e^+e^-$ and $Z^0 \rightarrow \mu^+\mu^-$

We have determined the background to the electron pair signal from Z decays by applying the E1 and E2 cuts to events with a pair of jets. Figure 10.6 shows that the background is negligible. The expected mass resolution for electron pairs with a mass of 90 GeV/c^2 is 1.5 GeV/c^2 rms.

Figure 10.6 also shows the expected muon pair signal from Z decays in the central region. The background is comparable to the electron pair background shown. The major difference is that the mass resolution is appreciably worse.

10.2 JET PHYSICS

Jets are the manifestation of the quarks and gluons which are the fundamental objects in the hard scattering processes underlying high P_T events. Jets are also the realization of the light quarks at the end of the decay chains of heavier particles such as the T meson, and the W and Z^0 vector bosons. The detection of jets is consequently very important, and has determined the tower structure of the detector as described in Chapter 2. Studies have been made both of isolated jets (CDF-41, 44, and 66), and multiple jets (CDF-6, 70, and 77). In particular, algorithms have been developed to group detected particles into the parent jets (see, for example, CDF-70, 77, and 97).

In order to determine the dependence of the hard scattering cross sections on the kinematic variables s and t one must measure the direction as well as the energy of the resulting jets. The jet angular size decreases with the energy of the jet. Jet cone half angles, in which on average 50%, 80%, and 90% of the jet energy falls, are shown in Figure 10.7. Half of all jets of 200 GeV, for example, have 80% of their energy within a cone of half-angle of 5°.

The calorimeter information from the detector was used to reconstruct the jet direction from 50 GeV jets in the central region. Using the signals from the two phototubes in a central calorimeter tower, the ϕ direction was found to be measured to an accuracy of $\pm$ 1 degree. From energy sharing between adjacent modules the resolution in η is approximately .02.

Of particular interest is the shape of the spectrum in p_T. To investigate the effect of the energy resolution on this measurement, we have folded our measured resolutions (see Chapter 4) with an assumed spectrum of slope $E\frac{d\sigma}{d^3p} \sim 1/p_T^{6.5}$. The resulting spectrum has a local power of 6.94 in the range $20 \leq p_T \leq 40$ GeV/c. Unfolding the calorimeter resolutions will improve this already satisfactory measurement. If in fact the naive Berman-Bjorken-Kogut p_T^{-4} spectrum is in force we will measure it quite accurately with the machine running at only one energy (x_T is .1 at p_T=100 GeV/c so that all of the spectral shape is in the p_T dependence)

There is a great deal of physics which can be confronted in the investigation of jets in the p_T range 100-400 GeV/c. In particular we mention jet multiplicity, angular correlations and perhaps discrimination among heavy quark, light quark, and gluon fragmentations. Detailed Monte Carlo studies of much of this physics with a realistic simulation of the detector are just beginning; the role of jets in identifying heavy quark decays (i.e. top quarks) is discussed in the next section.

10.3 PRODUCTION AND DETECTION OF TOP QUARKS

We have considered various techniques for detecting top quarks. In standard QCD models the top quark production cross section depends strongly on the quark mass and the optimum detection technique is consequently mass-dependent. From the results at PETRA, it is unlikely that the top quark mass is less than 18 GeV/c^2. To be definite, we have considered a reference top quark with a mass of 25 GeV/c^2.

I. Production

We have used the QCD production calculations of Dechantsreiter, Halzen, and Scott (Ref. 10.2). They consider the sum of $q\bar{q}$ annihilation, two gluon, and three gluon contributions to $0(\alpha_s^2)$. Quark structure functions are taken from Owens and Reya (scale-violating) but the gluon structure function is taken to be $(1-x)^3$, to be consistent with measured prompt photon production. The total cross section for associated $t\bar{t}$ production is shown in Figure 1.8. For masses near 25 GeV/c^2:

$$\sigma_{t\bar{t}}^{TOT} = 6 \times 10^{-32} \text{ cm}^2 \left(\frac{m_t}{25 \text{ GeV}}\right)^{-4.4}$$

For an integrated luminosity of 10^{36} cm^{-2}, this corresponds to 6×10^4 events.

II. Quark Decay and Signatures

We assume that the t quark, once formed, will decay via a flavor cascade. More specifically the bare t quark fragments in such a way that the heavy meson formed by the t quark and a light quark carries off most of the momentum of the original bare quark. The t quark in the heavy meson then undergoes a weak decay to a b quark and a virtual W, unaffected by the presence of the bound light quark (i.e., the "Spectator" model). The flavor cascade proceeds for example by one of the following decay chains:

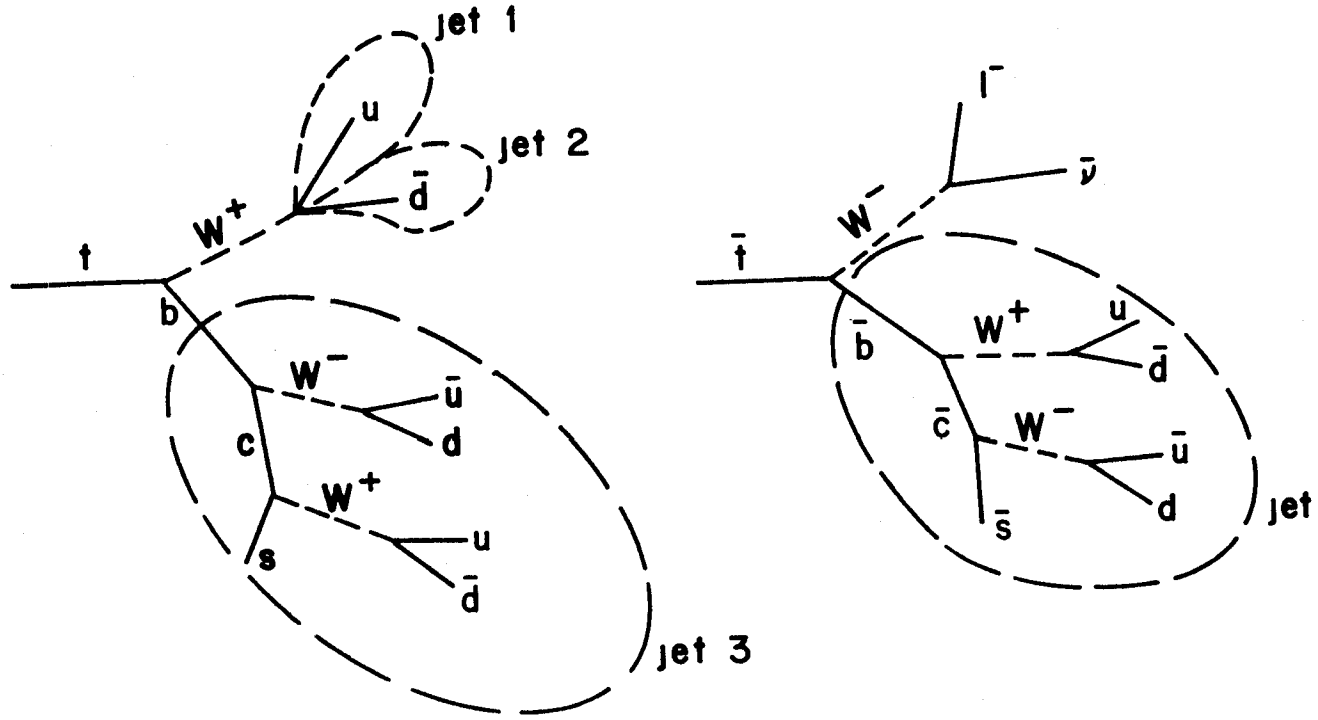

The branch of the decay chain emanating from the b quark is likely to appear as a single jet since none of the subsequent quark masses is so large compared to the ordinary transverse momenta of hadronic fragmentation as to produce distinct sub-jets. This situation is contrasted with the original t quark decay where the t quark masses considered here ($\geq$25 GeV/c^2) are quite sufficient to separate the sub-jets. We are led to consider topological signatures for t decay consisting of either three distinct jets or a jet together with a distinct lepton, depending on how the first virtual W decays.

It is further useful to divide the three-jet topology into two categories. If any decay in the b quark cascade proceeds semi-leptonically the undetected energy carried off by the neutrino will prevent an accurate reconstruction of the t quark mass. For the remaining three-jet events the mass can be reconstructed to within the accuracy of the calorimetry and the jet-finding algorithm. With this justification, we consider the following:

Category	Topology	Approximate Branching Ratio
A	3 jets, no leptons	40%
B	1 jet, separated leptons	30%
C	3 jets, leptons imbedded in one jet	30%

III. Background

Before proceeding to a rate calculation, some consideration of the background is in order since cuts which discriminate against background will also reduce the efficiency for detecting the signal. We anticipate two classes of background - low p_T processes associated with the spectator quarks and large p_T processes involving hard QCD scattering of light quarks and gluons.

a) Low p_T background

The obvious technique for discriminating against this background is a cut on minimum p_T. The scale for such a cut is given by the t quark mass, since $p_T \lesssim m_t$ will leave many of the decay products in the small-angle "beam jet" region. As shown in Figure 10.8 the p_T-spectrum for t quark production is expected to drop only a factor of 10 at $p_T \simeq 2m_t$. For the light t quark case, we choose a cut $p_T > 2\ m_t = 50$ GeV.

b) High p_T backgrounds

If large p_T were the only criteria for t quark production the signal would be completely overwhelmed by the background of hard QCD scattering of gluons and light quarks. The best discrimination against such processes is a cut on the reconstructed mass. Indeed it would be hard to have confidence in the discovery of t quark jets without a peak in the mass distribution.

These considerations then suggest the following strategy for isolating top quark jets:

1. "Lepton tag"

Search for events with an isolated lepton and a single jet in the same hemisphere. A cut on the minimum transverse momentum between the lepton and the associated jet will be necessary to reject lighter quark decays. An angular cut to remove beam jet fragments will also be required. For these events, select a subset with three jets in the opposite hemisphere with total p_T>50 GeV/c and reconstruct the three-jet effective mass.

2. "6-jet signature"

Make a strong p_T cut, p_T > 50 GeV/c, together with an angular cut around the beam direction to remove "beam jet" fragments. Select events with 6 jets; three each in opposing hemispheres. Reconstruct the three-jet effective mass.

Rates

The differential cross sections for t quark production are shown in Figure 10.8. It is clear that a severe cut in p_T is expensive in the rate of real events. For the relatively clean region

$$p_T > 50 \text{ GeV/c}$$
$$45° \leq \theta \leq 135°$$

the integrated cross section is

$$\int_0^{2\pi} d\phi \int_{45°}^{135} d\theta \int_{50Gev}^{\infty} dp_T \frac{d^2\sigma}{dp_T d\Omega} = 1.6 \times 10^{-33} \text{ cm}^2$$

This corresponds to 1600 $t\bar{t}$ pairs for our standard experiment $\int Ldt = 10^{36}$ cm^{-2}. These events now divide among the categories according to the various branching ratios as shown in Table 10.4. The efficiency for pattern recognition cuts is included to produce the final number of reconstructed top jets. These cuts are described in detail in CDF-70.

Table 10.4. Effect of cuts

Topology	Combined branching ratio	Pattern recognition efficiency	Remaining t quarks
Lepton tag	2 x .3 x .4 = .24	.3 x .85 = .25	100
6 jet	.4 x .4 = .16	.3 x .3 = .09	50

Backgrounds

We first discuss the background for the lepton tag case since it is the cleanest. The most serious background comes from inclusive (mostly gluon) jets produced at large transverse momentum just as in the $W^{\pm} \to \ell^{\pm}\nu$ case discussed in section 10.2. The background from charm and bottom production is much lower. For the same p_T and angular cuts

$$p_T > 50 \text{ GeV/c}$$
$$45° \leq \theta \leq 135°$$

the integrated cross section for jet production (from Fig. 1.13) is 4.6 x 10^{-31} cm^2. For our standard experiment, this corresponds to 4.6 x 10^5 events, or about 300 times the top production rate.

For a real top decay, the lepton from the first step in the flavor cascade will usually carry off a substantial transverse momentum with respect to the remaining jet axis (by virtue of the t mass) and will also have a large total momentum (because of the $p_T > 2\ m_t$ requirement). If we adopt as a signature the requirement that the lepton be within a 30° cone of the associated jet and also carry off at least 3 GeV/c of momentum transverse to the jet axis, we lose only about 15% of the real top decays.

For an ordinary gluon jet to mimic such a signature, it must first either fragment to produce a secondary with large transverse momentum (probability < .05 for p_T > 3 GeV/c) or must accidentally pick up a particle from the beam jet (probability <.06 for $\theta_{jet} < 30°$, $p_T > 3$ GeV/c). If a particle should pass these cuts it must still fake a lepton in the particle identification algorithms. The probability for such a misidentification is less than .01, and for electrons (where the momentum is measured in the magnet) can be less than 10^{-3}. The combined rejection factor for the lepton tag is better than 10^3.

Finally to contribute as background, the recoil gluon jet must both pass the 3-jet pattern recognition criterion and reconstruct to the top mass. Fox (CDF-70) has estimated the broadening of the jet mass to all orders in QCD. He finds a probability of .04 for reconstructing from a gluon jet a mass of (25±2.5) GeV/c^2. The probability of passing the pattern recognition cuts is more difficult to estimate, but is certainly less than the efficiency for real top jets, so we may very conservatively use that number (0.3). The total rejection factor is better than 8×10^4. When applied to the original sample of 4.6×10^5 events, we are left with only 6 events under a peak of 100 top quark events. We show the result of such a Gedanken experiment in Figure 10.9. What if real life is much worse than our assumptions? If the background turns out to be much worse than we have calculated, we can increase the rejection factor dramatically by increasing the p_T requirement

for the lepton with respect to the associated jet in the lepton tag without losing many real decays. For example, increasing that cut from 3 GeV/c to 5 GeV/c reduces the background by at least a factor of 10 and costs only 30% of the real top decays. If the signal for real tops is much less than we have estimated, the fall-back would be a reduction in the p_T requirement for top production. For example, reducing the cut from 50 GeV/c to 30 GeV/c increases the rate by a factor of 5. Alternatively, we could relax the requirement that the jet algorithm find exactly 3 jets since the mass calculation will still be correct even if two jets merge or the algorithm manufactures an extra jet. Relaxing this cut doubles the efficiency for real events.

We now consider the background to the 6 jet signature. The joint probability for an ordinary gluon jet to both pass the 3 jet pattern recognition requirements and reconstruct to a heavy mass is hard to estimate as noted above. We again use Fox's estimate (from CDF-70) of the total probability for a gluon to reconstruct to a heavy mass and assume that the corresponding pattern recognition efficiency is less than that for real top decays. The combined probability, .04 x .3 = .012, should be a conservative upper limit. We now make use of the fact that for real top decays the 3 jets in opposing hemispheres should reconstruct to the same mass to within the detector resolution. The combined rejection factor is approximately $(.012)^{-2} \approx 7000$ at 25 GeV/c^2 mass, so the signal-to-background is about one-to-one.

The result of a simulated experiment is shown in Figure 10.10. With the conservative background rejection factors that have been used, the evidence for top production in this signature is clearly tenuous.

In conclusion the signal in the lepton tag signature looks so clean that we are reasonably confident that if the top exists with a mass near 25 GeV/c^2 we will see it.

Very Heavy Top Quarks

What if the mass of the top quark is very large, m_t = 150 GeV/c^2 say? The total cross section for the associated production of a pair of 150 GeV/c^2 top quarks in the model used above is about 20 x 10^{-36}cm^2. The signatures for such events are likely to be distinctive. We conclude that an integrated luminosity greater than 10^{36}cm^{-2} is required for their detection, unless the cross section is larger than that given by the particular model used.

References

10.1 The true level of background rejection is clearly dependent on quantities as yet unknown. For example, in our jet background studies, we have (we hope pessimistically) assumed that the jets fragment according to the Field-Feynman procedure, rather than a QCD fragmentation which is expected to give softer spectra and thus smaller backgrounds. Much of our background rejection factor, however, depends on the details of the true jet fragmentation. Other uncertainties include the jet cross section and the distribution of particles from spectator beam jets.

10.2 Dechantsreiter et al., University of Wisconsin preprint DOE-ER-00881-202 (1981), to be published in Phys. Rev. D. For earlier work, see Pakvasa et al., Phys. Rev. D20, 2862 (1979).

Figure Captions

Fig. 10.1 The differential cross section

$$\left.\frac{d^2\sigma}{dp_T d_y}\right|_{y=0}$$

versus p_T for electrons from W decay. Also shown are the (background) cross sections for jets, single inclusive charged hadrons, electrons from heavier quark decays, and single electrons from the Drell-Yan process.

Fig. 10.2 The trigger rates for jets above a given E_T threshold for the central region ($40° < \theta < 140°$). The effects of the criteria listed in the text are shown.

Fig. 10.3 The effect of the electron cuts (see text) on the backgrounds for electrons from W decay.

Fig. 10.4 The differential cross section $d\sigma/dp_T$ versus p_T for the angular range $3° \leq \phi \leq 140°$. The effects of the criteria listed in the text are shown.

Fig. 10.5 The effect of the muon criteria on the backgrounds from jets, and the muon signal from W decay.

Fig. 10.6 The mass spectrum of dilepton pairs from Z decay, and of dihadron pairs before and after electron cuts.

Fig. 10.7 Jet opening angles for Field-Feynman Jets with internal transverse momentum of particles with respect to the jet axis given by the prescription of Fox (CDF-37). Half of the jets have a greater

fraction of their energy within the angles shown and half have less.

Fig. 10.8 Differential cross sections for heavy quark production for $\sqrt{s}$=2 TeV as a function of p_T.

Fig. 10.9 Reconstructed 3-jet mass distribution for a simulated experiment of $\int Ldt = 10^{36}$ cm^{-2} using the lepton tag signature.

Fig. 10.10 Reconstructed 3-jet mass distribution for a simulated experiment of $\int Ldt = 10^{36}$ cm^{-2} using the 6-jet topological signature.

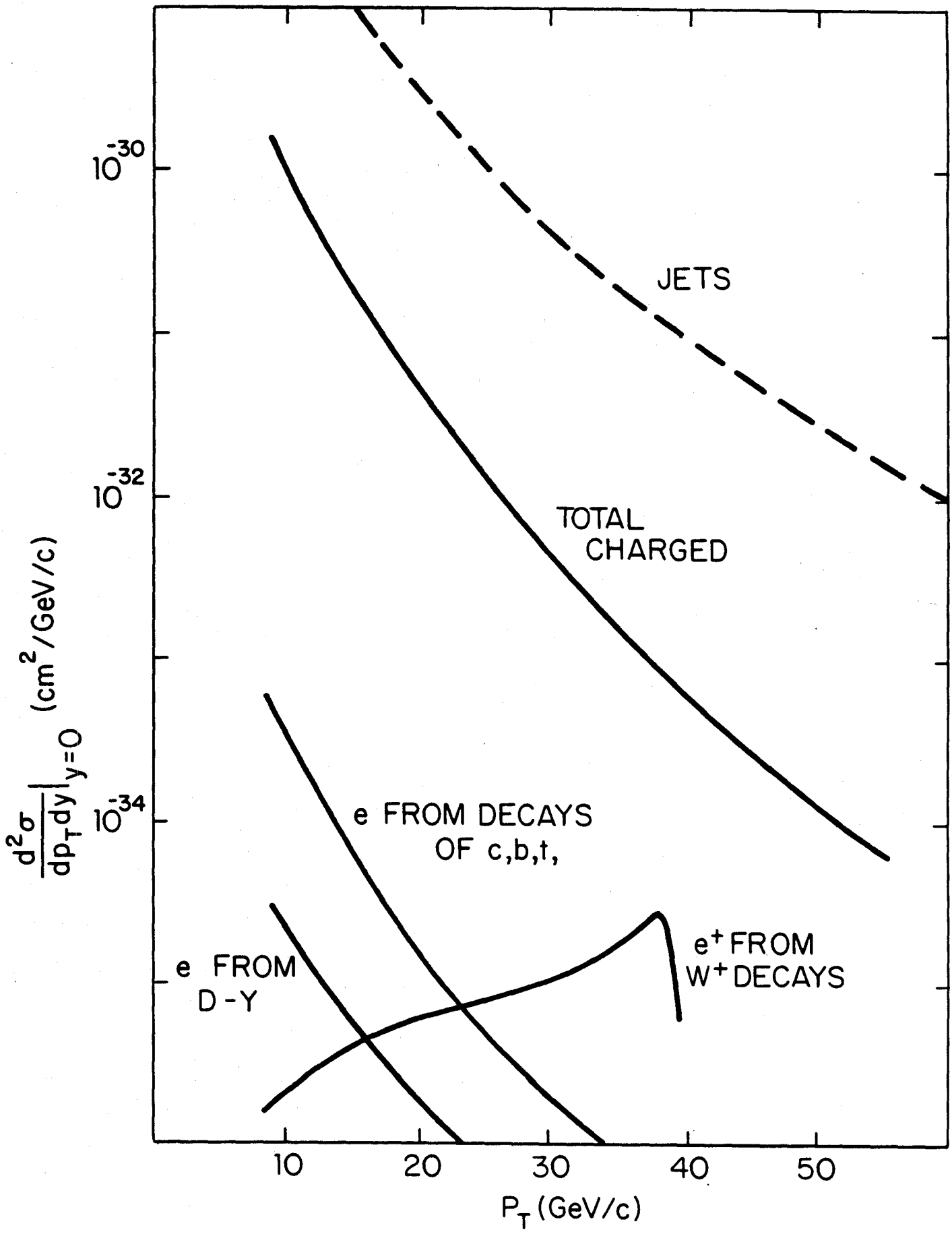
10^{-30}
10^{-32}
10^{-34}
$\frac{d^2\sigma}{dp_T dy}\Big|_{y=0}$ (cm^2/GeV/c)
JETS
TOTAL CHARGED
e FROM DECAYS OF c,b,t,
e FROM D-Y
e$^+$ FROM W$^+$ DECAYS
10
20
30
40
50
P_T (GeV/c)

FIG. 10.1

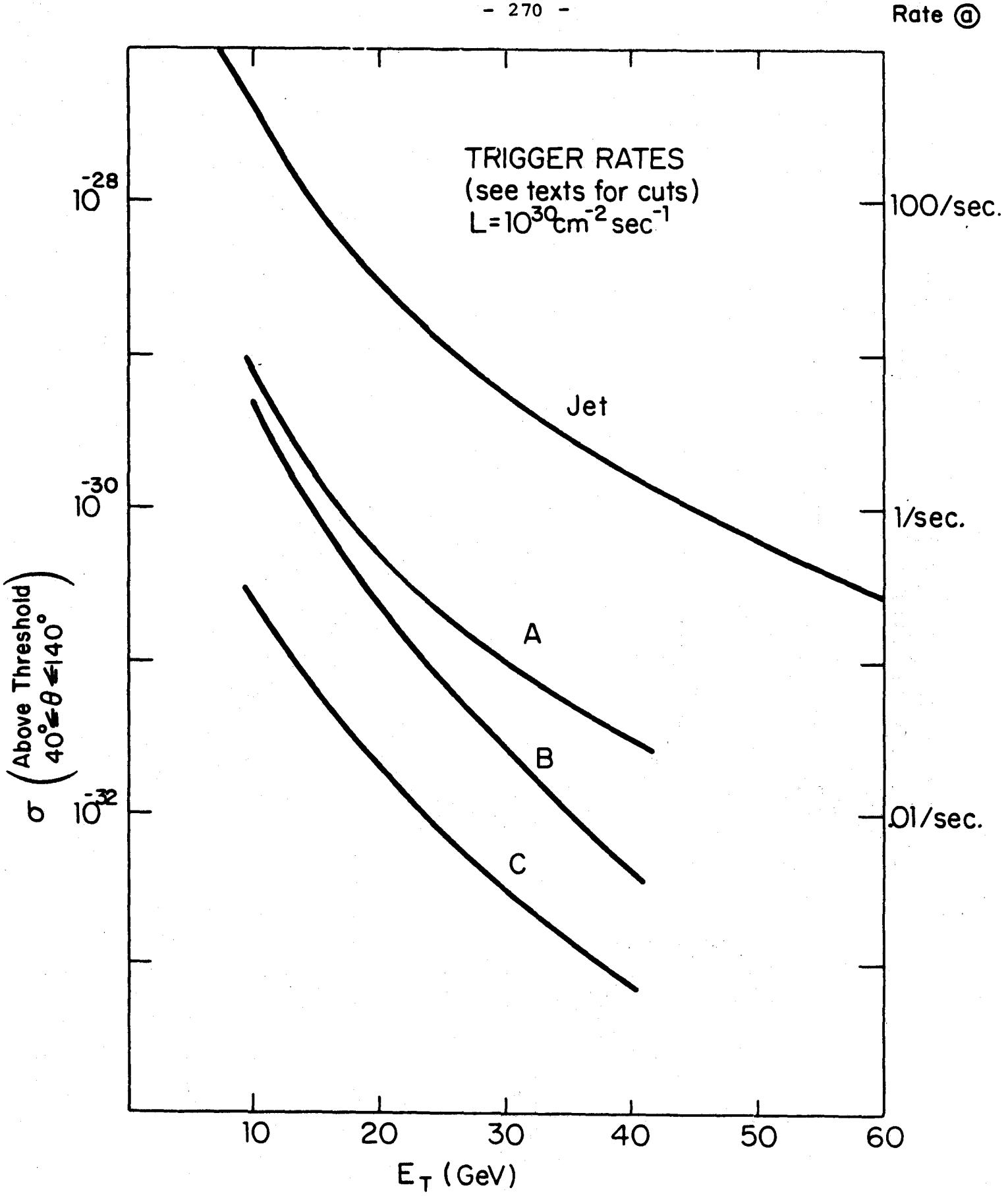
Rate @
TRIGGER RATES
(see texts for cuts)
L=10^30 cm^-2 sec^-1
10^-28
10^-30
10^-32
100/sec.
1/sec.
.01/sec.
Jet
A
B
C
σ (Above Threshold 40°≤θ≤140°)
10
20
30
40
50
60
E_T (GeV)

FIG. 10.2

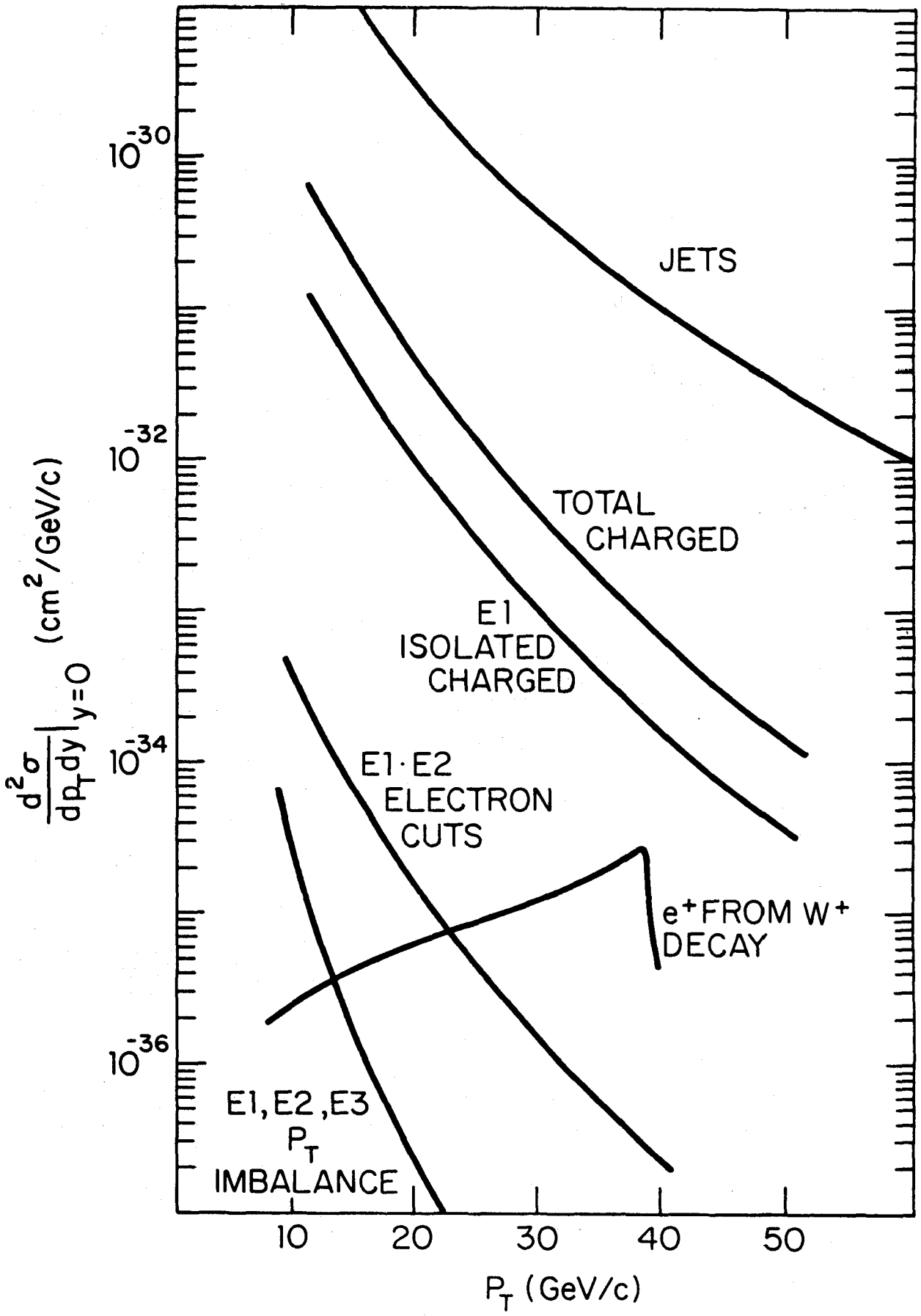
10^{-30}
10^{-32}
10^{-34}
10^{-36}
$\frac{d^2\sigma}{dp_T dy}\Big|_{y=0}$ (cm²/GeV/c)
JETS
TOTAL CHARGED
E1 ISOLATED CHARGED
E1·E2 ELECTRON CUTS
e⁺FROM W⁺ DECAY
E1, E2, E3 P_T IMBALANCE
10
20
30
40
50
P_T (GeV/c)

FIG. 10.3

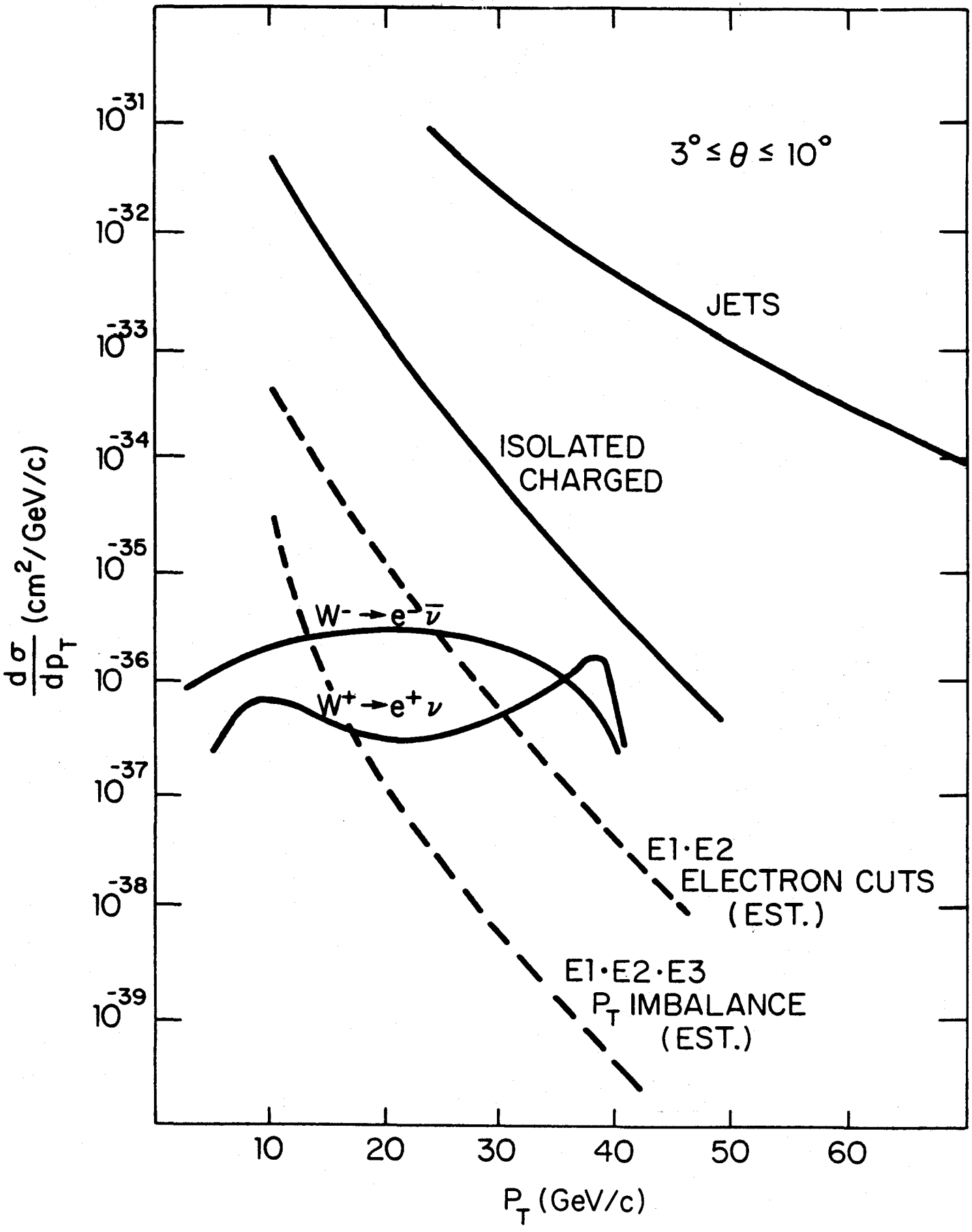
$3° \leq \theta \leq 10°$
JETS
ISOLATED CHARGED
$W^- \rightarrow e^- \bar{\nu}$
$W^+ \rightarrow e^+ \nu$
E1·E2 ELECTRON CUTS (EST.)
E1·E2·E3 P_T IMBALANCE (EST.)
$\frac{d\sigma}{dp_T}$ (cm²/GeV/c)
10^{-31}
10^{-32}
10^{-33}
10^{-34}
10^{-35}
10^{-36}
10^{-37}
10^{-38}
10^{-39}
10
20
30
40
50
60
P_T (GeV/c)

FIG. 10.4

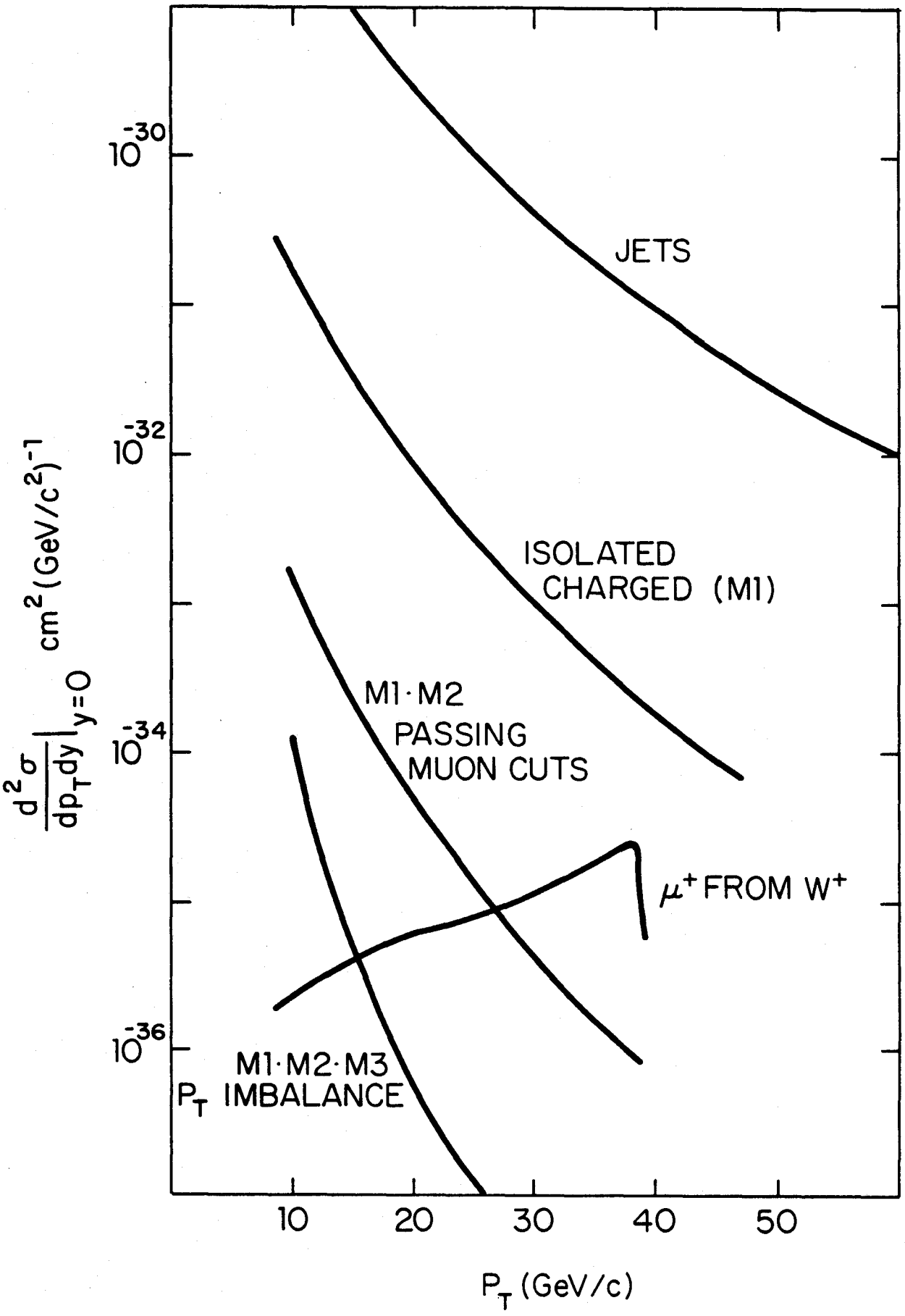
10^{-30}
10^{-32}
10^{-34}
10^{-36}
$\frac{d^2\sigma}{dp_T dy}\Big|_{y=0}$ cm^2(GeV/c^2)$^{-1}$
JETS
ISOLATED CHARGED (M1)
M1·M2 PASSING MUON CUTS
μ^+ FROM W$^+$
M1·M2·M3 P_T IMBALANCE
10
20
30
40
50
P_T (GeV/c)

FIG. 10.5

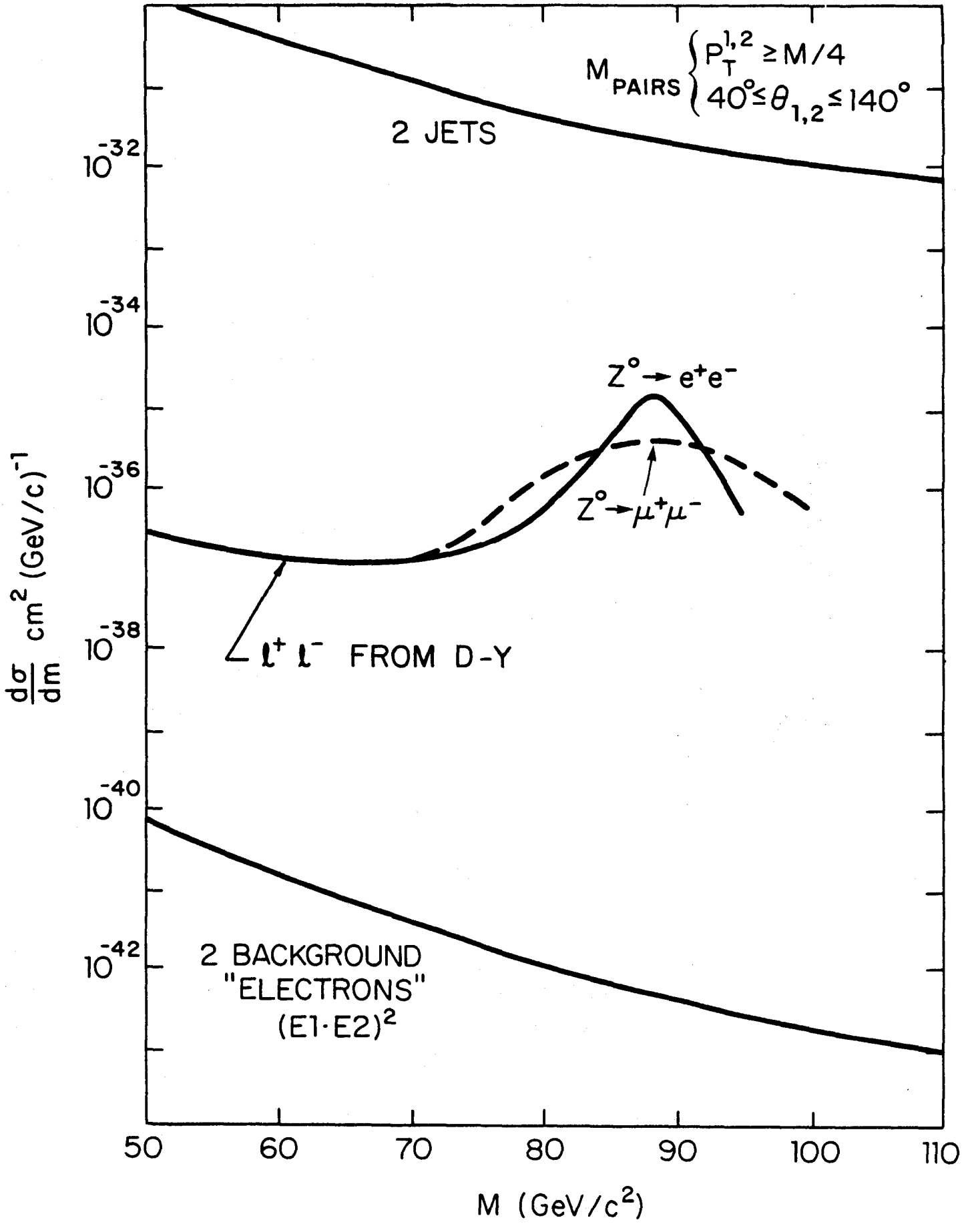
M_{PAIRS} $\begin{cases} P_T^{1,2} \geq M/4 \\ 40° \leq \theta_{1,2} \leq 140° \end{cases}$
2 JETS
$Z^0 \rightarrow e^+e^-$
$Z^0 \rightarrow \mu^+\mu^-$
$l^+ l^-$ FROM D-Y
2 BACKGROUND "ELECTRONS" $(E1 \cdot E2)^2$
$\frac{d\sigma}{dm}$ cm^2 (GeV/c)$^{-1}$
10^{-32}
10^{-34}
10^{-36}
10^{-38}
10^{-40}
10^{-42}
50
60
70
80
90
100
110
M (GeV/c^2)

FIG. 10.6

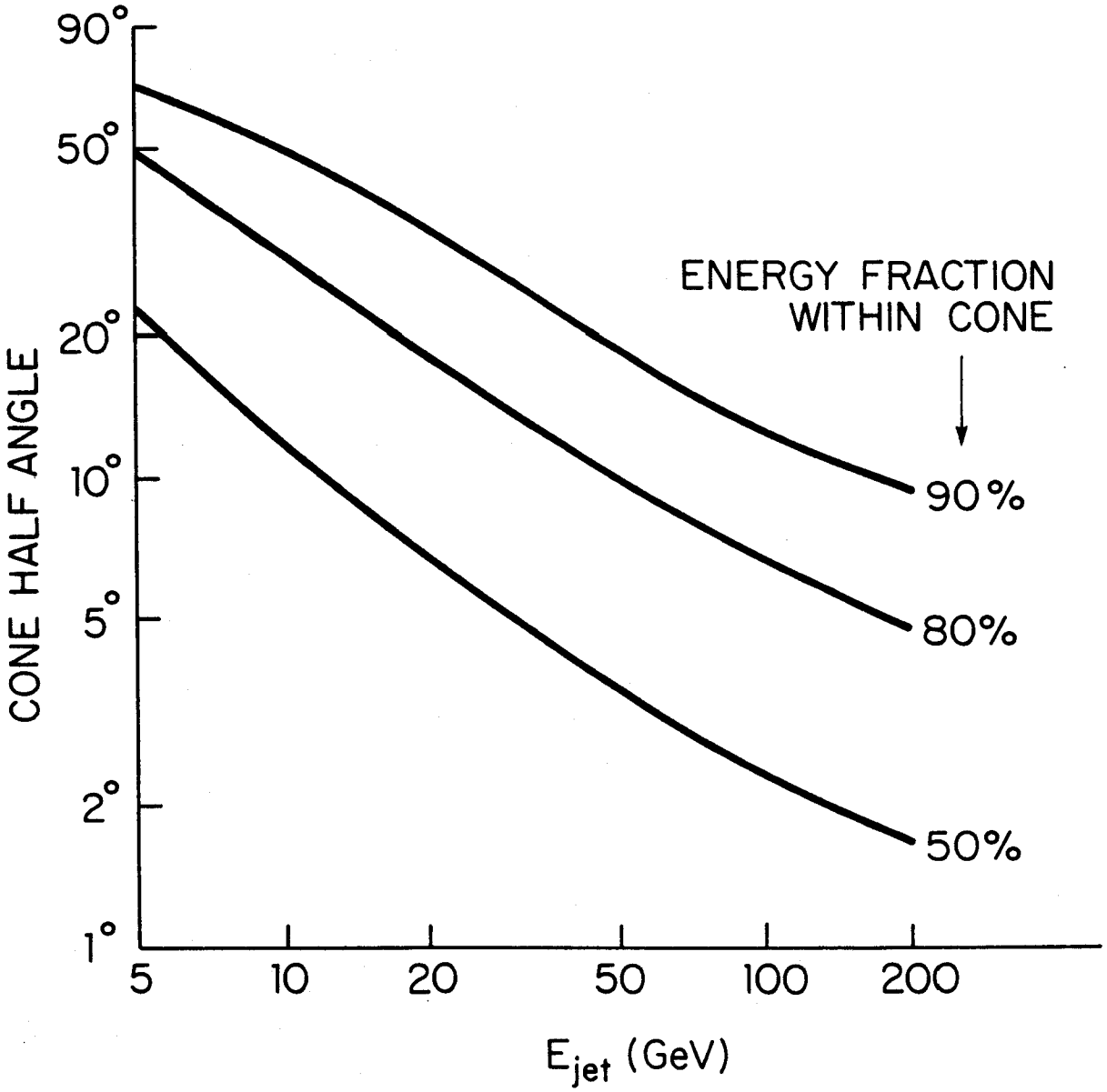
90°
50°
20°
10°
5°
2°
1°
CONE HALF ANGLE
ENERGY FRACTION
WITHIN CONE
90%
80%
50%
5
10
20
50
100
200
E_{jet} (GeV)

FIG.10.7

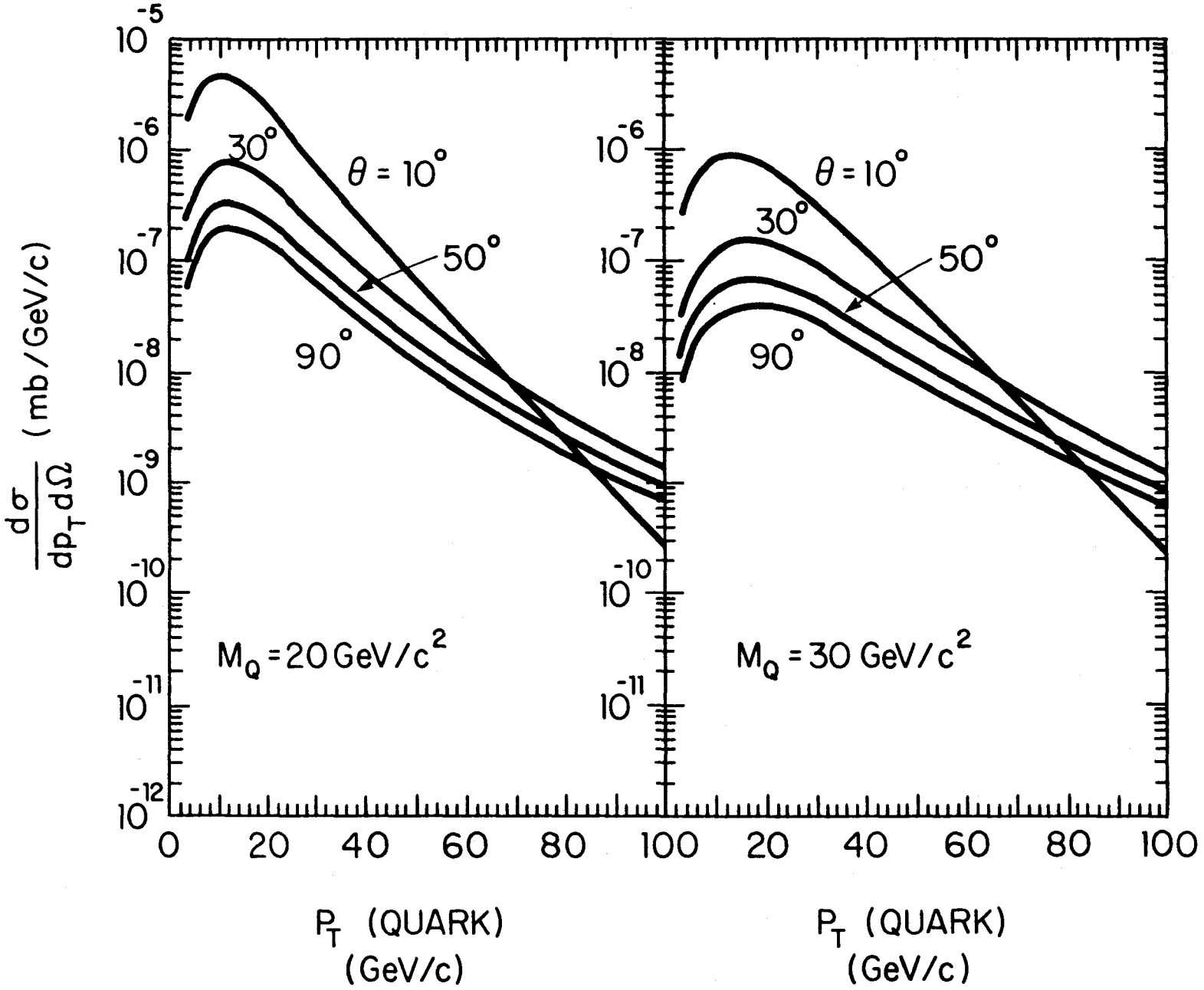
$\frac{d\sigma}{dp_T d\Omega}$ (mb/GeV/c)
10^{-5}
10^{-6}
10^{-7}
10^{-8}
10^{-9}
10^{-10}
10^{-11}
10^{-12}
$\theta = 10°$
30°
50°
90°
$M_Q = 20\,GeV/c^2$
$M_Q = 30\,GeV/c^2$
0 20 40 60 80 100
20 40 60 80 100
P_T (QUARK) (GeV/c)
P_T (QUARK) (GeV/c)

FIG. 10.8

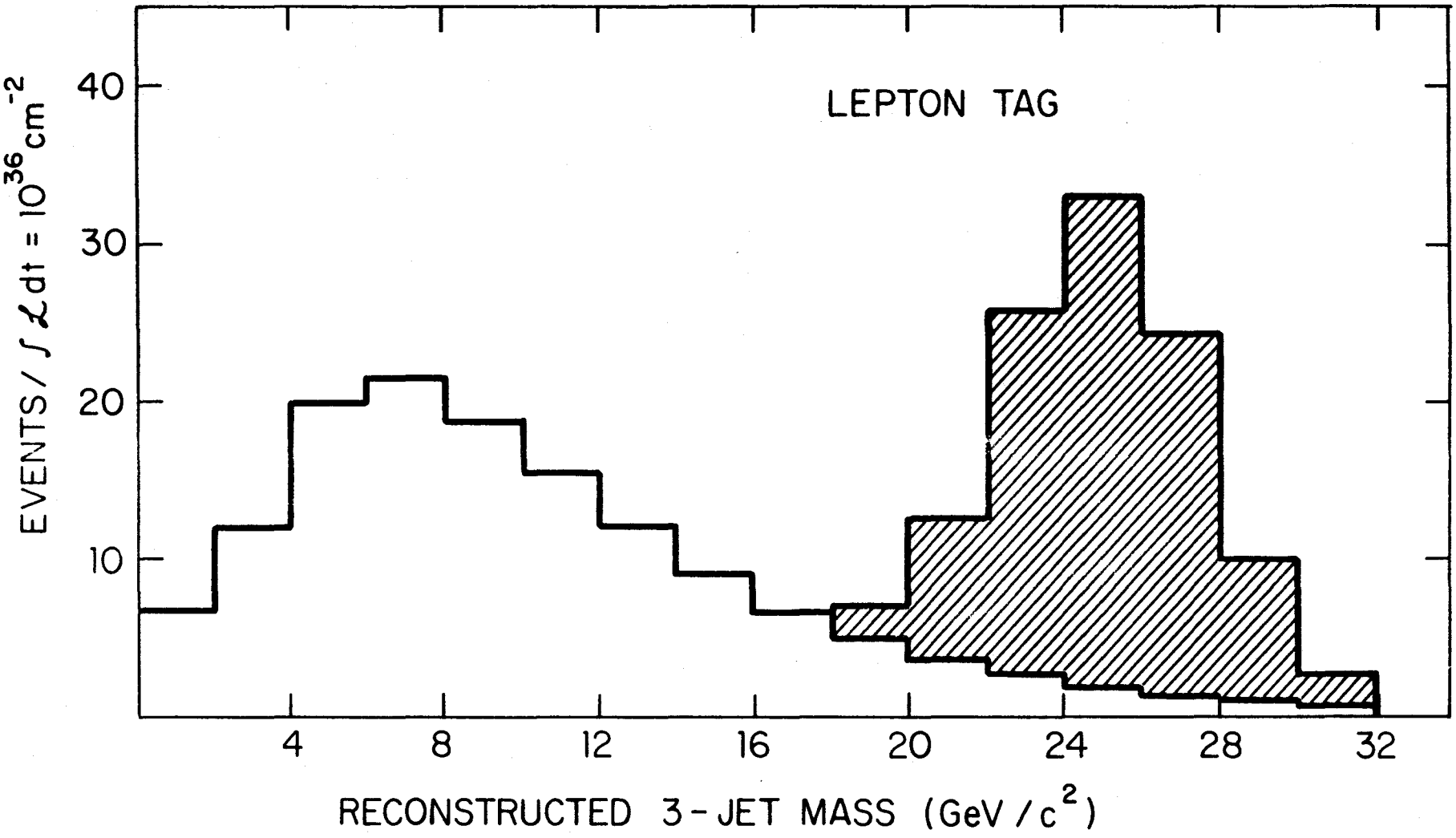
LEPTON TAG
EVENTS/ $\int \mathcal{L} dt = 10^{36} cm^{-2}$
40
30
20
10
4
8
12
16
20
24
28
32
RECONSTRUCTED 3-JET MASS (GeV/c^2)

FIG. 10.9

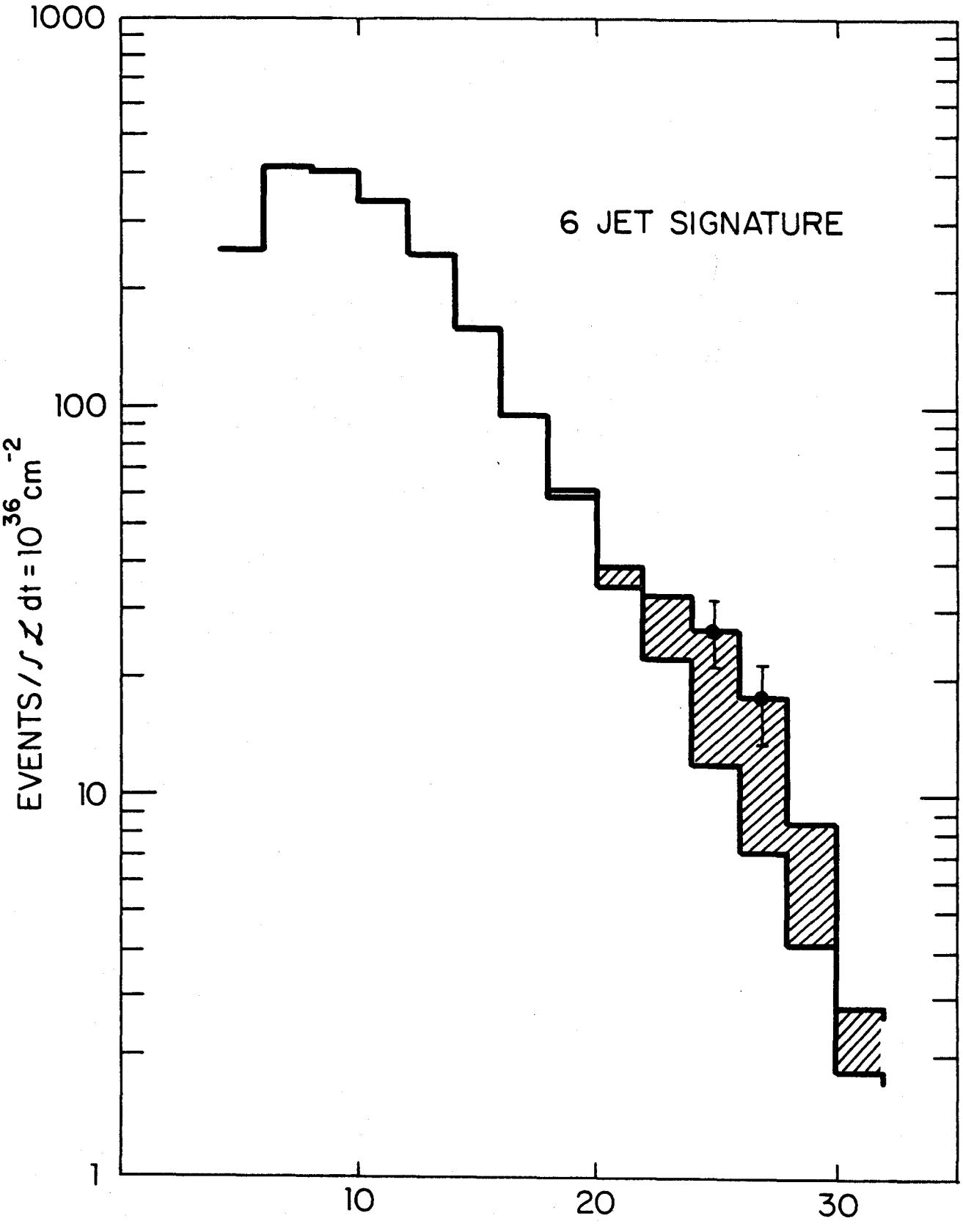
1000
100
10
1
6 JET SIGNATURE
EVENTS / ∫ℒ dt = 10^36 cm^-2
10
20
30
RECONSTRUCTED 3-JET MASS (GeV/c^2)

FIG. 10.10

Appendix I

CDF NOTES

CDF-1 Parameters of Colliding Beam Detector - J. K. Walker

CDF-2 New Kissing Parameters - R. Diebold

CDF-3 Track Detecting Bi-dimensional Drift Chambers - M. Atac

CDF-4 Back of the Envelope Energy Resolution for Jets - R. Diebold

CDF-5 Muon Background in Colliding Beam Detector Experimental Halls - (also TM-773) - K. W. Chen

CDF-6 Errors Caused by Jet Ambiguities - R. Diebold

CDF-7 Comparison of Solenoid Systems for $W^{\pm} \rightarrow \ell^{\pm} \nu$ - R. Diebold

CDF-8 A Comparison of Narrow State Resolutions for Two Different Solenoidal Magnets - R. Singer

CDF-9 Monte Carlo Results on Multiple Hits per Element in the C. B. Detector - R. Loveless

CDF-10 Comparison of a Large and a Small Solenoidal Detector - B. Musgrave

CDF-11 Preliminary Design of a Magnetic Detector Facility for Colliding Beams at Fermilab - CDF Group

CDF-12 Monte Carlo Results on Multiple Hits in the Non-Magnetic Detector Calorimeter - R. Loveless

CDF-13 A Preliminary Design of a Calorimetric Colliding Beam Detector for Fermilab - P. Limon

CDF-14 PROGRAM TRACKER: A Hit Simulator for a Solenoidal Detector for Fermilab - R. Singer

CDF-15 Notes on Detector Calorimeters - Bob Walker

CDF-16 Summary of Colliding Detector Facility Discussion on Colliding Beams Experimental Area

CDF-17 A Comparison of CB Areas/Moving Schemes from Discussion of August 17, 1978 - J. K. Walker, H. Kautzky, B. Musgrave, A. Weitsch, R. Loveless, S. Ecklund

CDF-18 Calorimeter Design Notes - M. Atac, R. Loveless, A. Weitsch, P. Limon, J. K. Walker, R. Walker, A. Garfinkel, H. Kautzky

CDF-19 Can We Detect π^{o}'s in the CDF Electromagnetic Shower Counter - R. Loveless

CDF-20 Mass Construction of Strip Chambers - A. Weitsch

CDF-21 Muon Detection Problem - L. Pondrom

CDF-22 Comments on Pondrom's "Muon Detection Problem" - C. Ankenbrandt

CDF-23 Dependence of Shower Counter Resolution on Counter Depth - B. Musgrave

CDF-24 Shower Counter Resolution - B. Musgrave

CDF-25 Electron-Hadron Separation Shower Development - R. Singer

CDF-26 Kissing Magnet Design for the pp Collider - R. Diebold, et al.

CDF-27 Design of the Central Electromagnetic Shower Counter Based on M5 Test-Beam Results - M. Atac, R. Diebold, R. Loveless, B. Musgrave, J. Sauer, R. Singer

CDF-28

CDF-29 Energy Leakage as a Function of Shower Counter Depth - B. Musgrave

CDF-30 Physics Capacity of a Staged Solenoid Detector - R. Diebold

CDF-31 Big p_T Trigger with Strips - R. Diebold

CDF-32 Identification of Electrons without a Magnet - R. Diebold

CDF-33 Strip Chamber Tests in ANL Beam 5 - L. Nodulman

CDF-34 A Fly's Eye Calorimeter for Fermilab Colliding Beams - R. Walker, G. C. Fox (CalTech)

CDF-35 Some Results from Extruded Proportional Tubes - M. Atac, R. Loveless, J. K. Walker

CDF-36 Further Analysis of the Scintillator/Lead Sheet Test Beam Data - J. Sauer

CDF-37 Spreading of Parton Jets at High Energy - G. C. Fox (CalTech)

CDF-38 Results from Lead-Plexipop Sandwich Shower Counters with Wave-Shifter Readout - R. Musgrave

CDF-39 Tests of an "Educational Prototype" for Hybrid Shower Counter Wire Chambers - L. Nodulman

CDF-40 The Possibility of Using Lead Glasses Electromagnetic Calorimeter - A. Maki, M. Mishina, F. Takasaki

CDF-41 Hybrid Shower Counter Simulation - L. Nodulman

CDF-42 Preliminary Considerations on Data Acquisition System for CDF - Y. Watase

CDF-43 QCD Corrected W-boson Production - L. Holloway

CDF-44 Single Jet Calorimeter Simulation Studies - I. Gaines

CDF-45 A New Approach for Tracking Drift Chamber Systems - M. Atac

CDF-46 Liquid Helium Logistics in the Colliding Beam Long Straight Sections - D. S. Ayres

CDF-47 Choreography and the Detector - D. S. Ayres, T. Collins, R. Johnson, H. Kautzky, S. Pruss, T. Toohig, R. Yamada

CDF-48 Vacuum Requirements for pp Collider Detector and Suggestions for How to Achieve Them - S. Pruss

CDF-49 A Comparison of the Measurement of $Z^o \to e^+e^-$ at High s Using Dipolar and Solenoidal Magnetic Fields - R. G. Kennett

CDF-50 Hybrid Central Shower Counters - D. S. Ayres, R. Diebold, B. Musgrave, L. Nodulman, J. Sauer

CDF-51 On the Lead Glass System - P. Giromini

CDF-52 On the Analysis of the Electromagnetic Calorimeters - H. Aoyama and L. Romans (as narrated by G. Fox)

CDF-53 Radial Wire Drift Chambers - M. Atac

CDF-54 January 1980 CDF Workshop - Summary of Tracking Group - M. Atac, A. Beretvas, S. Bertolucci, D. Bintinger, R. Eisenstein, H. Jensen, M. Ono, R. Raja, A. Sermoneta, K. Ueno

CDF-55 Machine/Area/Detector Interface - D. Ayres, T. Collins, R. Johnson, H. Kautzky, S. Pruss, T. Toohig, R. Yamada

CDF-56 Endcap Calorimeters/Luminosity/Forward Angles - G. Bellettini, R. DelFabbro, D. Gustafson, L. Jones, L. Nodulman, D. Cline, K. Kondo

CDF-57 Muon Detection for the Colliding Beam Experiment - G. Ascoli

CDF-58 The Criterion for Avoiding Hot Spots in Calorimeters - W. Selove

CDF-59 Luminosity and Very Small Angle Physics - G. Bellettini, C. Bradaschia, A. Menzione

CDF-60 Feasibility of Operating Silicon Detectors Inside the Collider Vacuum Pipe - C. Bradaschia, T. Collins, A. Menzione

CDF-61 Prototype Pad Chamber Hadron Calorimeter - M. Ono and R. Yamada

CDF-62 Endcap Hadron Calorimeters - G. Bellettini, R. Bertani, R. Del Fabbro, G. Gennaro, A. Scribano

CDF-63 Hybrid Shower Counters for CDF - L. Nodulman

CDF-64 Conceptual Design of a Forward Detector for the Antiproton-Proton Collider - G. Bauer et al.

CDF-65 A Study of Electric Field and Electrostatic Forces in a Large Drift Chamber - M. Atac and R. Bertani

CDF-66 Effects of Scintillator Attenuation in the Central Calorimeter - R. Diebold and I. Gaines

CDF-67 Shower Counter Lab Tests - B. Kustom, R. Diebold, B. Musgrave, L. Nodulman, G. Walschon

CDF-68 Tevatron Collider Monte Carlo - Physics and Results - S. Miyashita and K. Ogawa

CDF-69 On Magnetic Field Calculations for the Central Detector of the Colliding Beams Facility at Fermilab - K. Gamadia and J. Rhoades

CDF-70 A Longer Note on Top Quarks - G. Fox and L. Romans

CDF-71 An Idea for a General Purpose Detector for the Fermilab Colliding Beams - G. Fox, R. Kennett, R. L. Walker

CDF-72 Electron Identification in Jets - R. Diebold and J. Sauer

CDF-73 Material Procurement Report for the FNAL pp Forward Detector's Toroids and Cosθ Dipole Magnets - D. Cline, R. Morse, I. Orosz, L. C. Thomas

CDF-74

CDF-75 Large Angle Hadron Calorimeter Prototype - S. Bertolucci, M. Cordelli, P. Giromini

CDF-76 Time of Flight Counters for CDF - I. Gaines and R. W. Kadel

CDF-77 Six-Jet Reconstruction of $\bar{T}T$ - R. Diebold

CDF-78 Thoughts on the Implementation of a dE/dx System for CDF - D. S. Ayres and R. Diebold

CDF-79 Comments on the Effectiveness of the Return Flux as an Aid to Separating Primary Muons from Background - G. Blaylock and B. Eisenstein

CDF-80 Gas Sampling Hadron Calorimetry - P. Giromini

CDF-81 Detecting the Next Heavy Neutrino - G. L. Kane and J. P. Leveille

CDF-82 Lepton Pair Production by Drell-Yan and γ-γ Interactions at the Fermilab Collider - R. Tripiccione

CDF-83 Photon and π^0 Production at the FNAL $\bar{p}p$ Collider - I. Hinchliffe and R. L. Kelly

CDF-84 Test of Prototype Towers for the Endcap Hadron Calorimeter - G. Bellettini, R. Bertani, C. Bradaschia, R. Del Fabbro, A. Scribano, G. Terreni

CDF-85 dE/dx with a Silicon Vertex Detector - NAl + CDF Pisa Groups

CDF-86 Can We Test Large Solenoid Coils Safely Without Yoke - R. Yamada

CDF-87 Time of Flight Possibilities - R. Diebold

CDF-88 Report from the CDF Workshop Group on New Particles - R. Diebold

CDF-89 Detector Resolution Effects on High $p_\perp$ Trigger - L. Ristori

CDF-90 First Results from the Central Shower Counter Prototype - R. Diebold, L. Nodulman, J. Sauer, R. Wagner

CDF-91 Drift Chamber Electronics - Prototype - J. E. Elias

CDF-92 Simulation of the Central Tracking System - F. Bedeschi, M. Ono, J. Yoh

CDF-93 A Fast Cluster Finder Using Digital Logic - J. Freeman

CDF-94 Development of Resistive Plastic Cathode for Proportional Chamber - FNAL/KEK/Tsukuba Group

CDF-95 A Wire Chamber Photon Calorimeter - R. L. Walker, E. Brooks, W. Friedler, and B. Newport

CDF-96 Angular Acceptance for the Forward Spectrometer - P. McIntyre

CDF-97 The Drell-Yan Process at the Fermilab Collider - R. Tripiccione

CDF-98 Construction and Staging of the Shower Counter for the Full Scale CDF Central Calorimeter Prototype - L. Nodulman

CDF-99 Central Muon Detection - G. Ascoli and B. Eisenstein

CDF-100 Asymmetry in the $W^{\pm} \to \ell\nu$ Decays - H. Frisch

CDF-101 Scan Results from the Full Scale Central Calorimeter Prototype Tests - L. Nodulman, V. E. Barnes, R. Bertani, S. Bertolucci, M. Cordelli, R. Diebold, A. F. Garfinkel, P. Giromini, H. Kautzky, A. Laasanen, A. Menzione, J. Sauer, R. Wagner, J. Wilson, A. B. Wicklund

CDF-102 Parametrization of the Longitudinal and Transverse Development of the Hadronic Cascade in an Absorbing Medium - R. Bertani and R. Del Fabbro

CDF-103 Chamber Response in the M5 Test of the Barrel Shower Counter Prototype - L. Nodulman, A. B. Wicklund, R. Diebold, J. Sauer, R. Wagner

Appendix II

B0 Experimental Area

The B0 experimental area was designed specifically to house the detector. Both the depth of the building and its overall width are determined by the transverse dimensions of the central detector. The area is divided into two distinct regions, the collision hall, where the experiment is actually performed, and the assembly area, where the entire apparatus will be constructed and serviced, and where the central detector will be stored during operation of the Tevatron fixed-target program. A bypass is provided around the outside of the collision hall for traffic servicing the Main Ring and the Tevatron. The building is a concrete structure; the floor which carries the detector is a concrete mat about 4 ft. thick. It should be noted that the engineering challenge posed by the weight of the detector and the earth pressure on the walls of this underground area is unique in the history of Fermilab. Plan and elevation views of the B0 area are shown in Figs. II.1 and II.2, and Fig. II.3 has the detector in two positions in B0.

The central volume of the Collision Hall which houses the central detector is 50 ft. long by 50 ft. wide and at its deepest point 40 ft. high, dimensions set directly by the detector and its requirements for in-place servicing. Forward-backward detectors sit in the volumes at either end of the collision area. Since these devices are smaller transversely than the central detector, these sections are 35 ft. wide by 30 ft. high and 25 ft. long; their floor level is raised 4 ft. from the central region.

The assembly area is separated from the collision hall by a 35 ft. long tunnel whose transverse size is the minimum needed for passage of the central detector. When the accelerator is operating, the tunnel is plugged at the collision hall end by a retractable 12 ft.-thick concrete wall.

This thickness of radiation shielding is sufficient to allow people to work in the assembly area while the Tevatron is running for fixed-target physics.

The assembly area consists of three parts: an underground assembly area at the same level as the collision hall, an above-ground construction area, and two floors of electronics, computer and control rooms for the detector on the side closest to the collision hall. The area is served by a 50 ton crane that runs the entire length of the building.

The size of the below-ground assembly area is set by the space needed to construct the central detector and to service the central detector while constructing the forward-backward detectors. As in the collision hall, there are two levels which differ by 4 ft. The central detector sits at the lower level on its own transporter; the forward-backward detectors will be assembled on the higher level and transported to the collision hall on a special transfer cart. The two bays at the entrance to the tunnel are at the lower elevation and can both accept either the transfer cart or the concrete shield wall. A labyrinth with a movable plug allows passage for people and light equipment between the assembly area and the collision hall.

The above ground section of the assembly building will be used for offices and fabrication of the individual components of the detector. The experiment electronics and control rooms are placed as close to the collision hall as possible to reduce the time delays from cable lengths to a minimum.

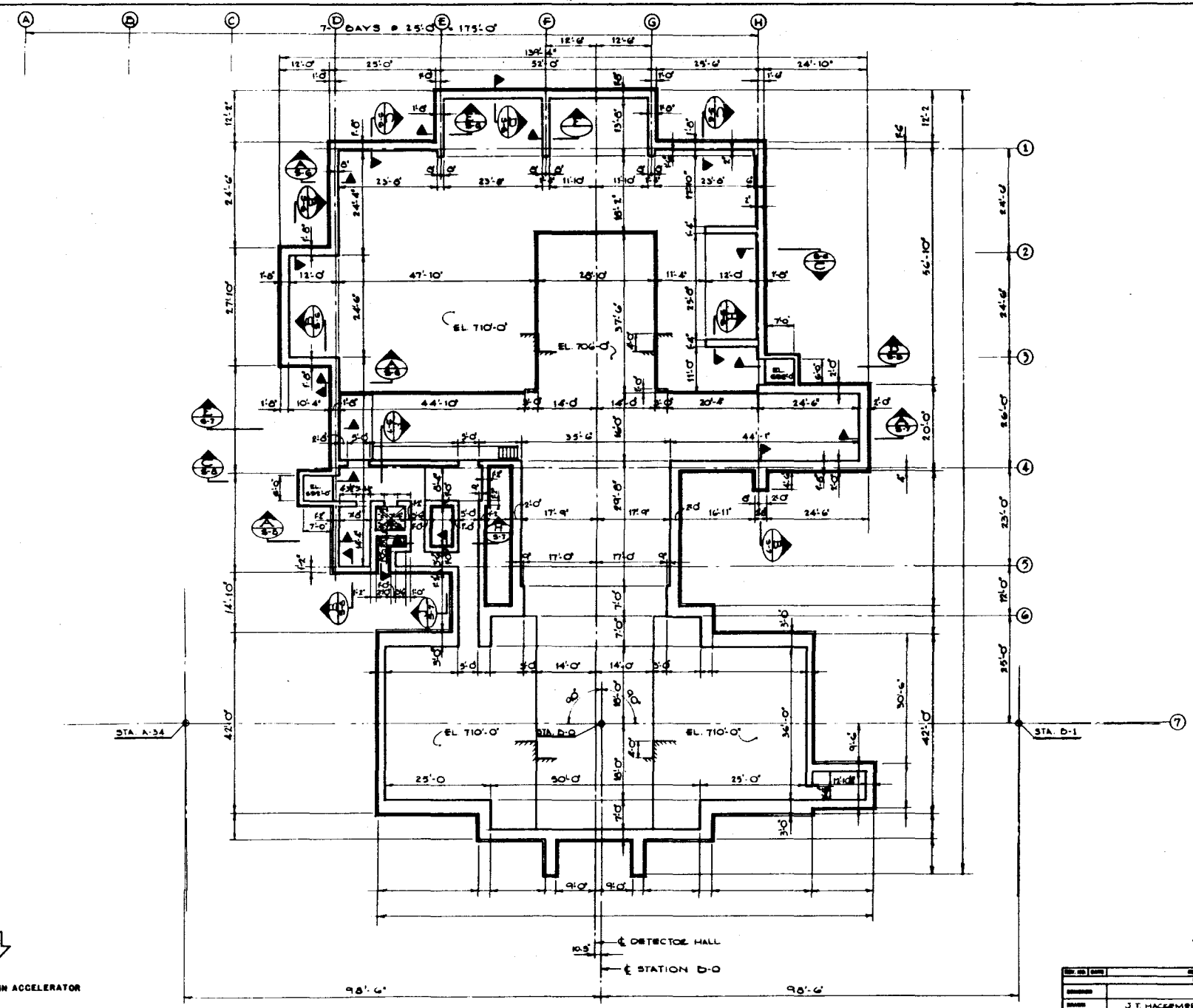

PLAN AT ELEVATIONS 706 & 710

FIG. II.1

J.T. HACKERMOD

FERMI NATIONAL ACCELERATOR LABORATORY

B-0 COLLIDING BEAM FACILITY

PLAN AT ELEVATIONS 706 & 710

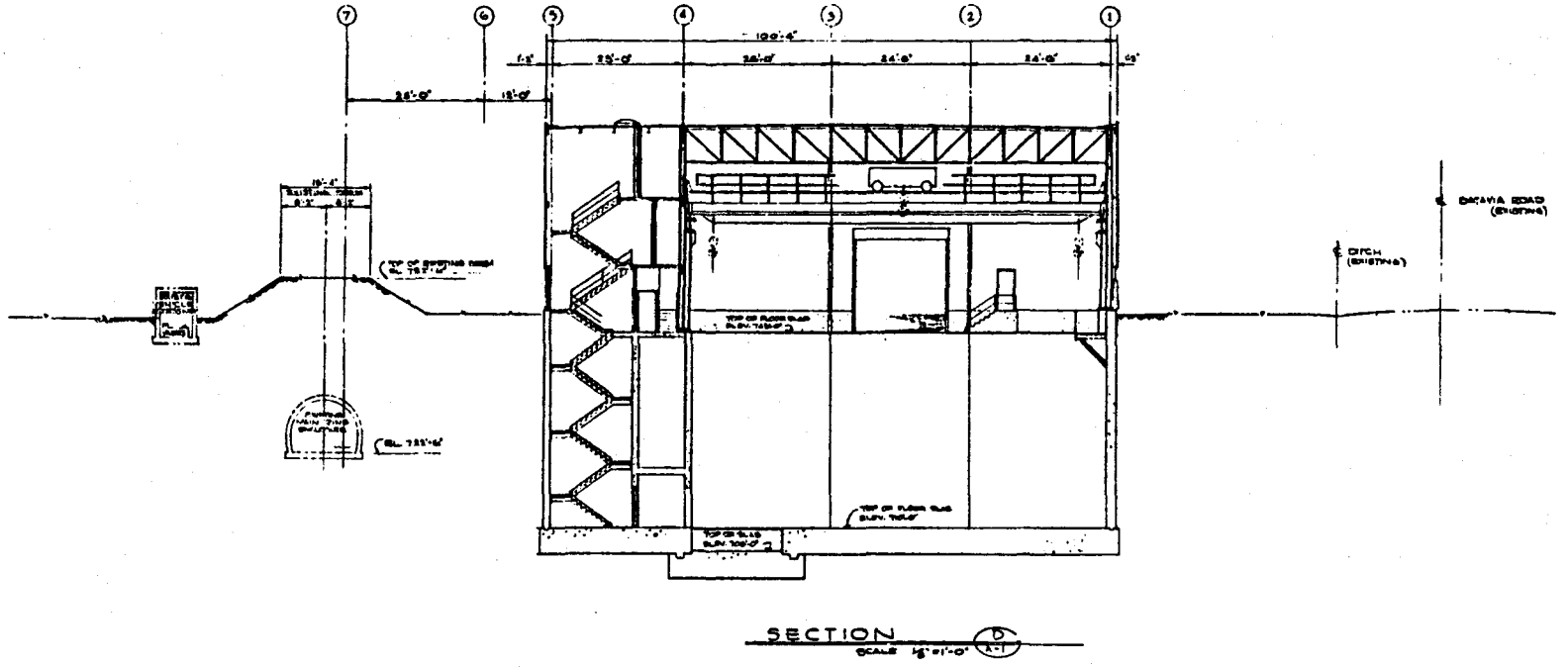

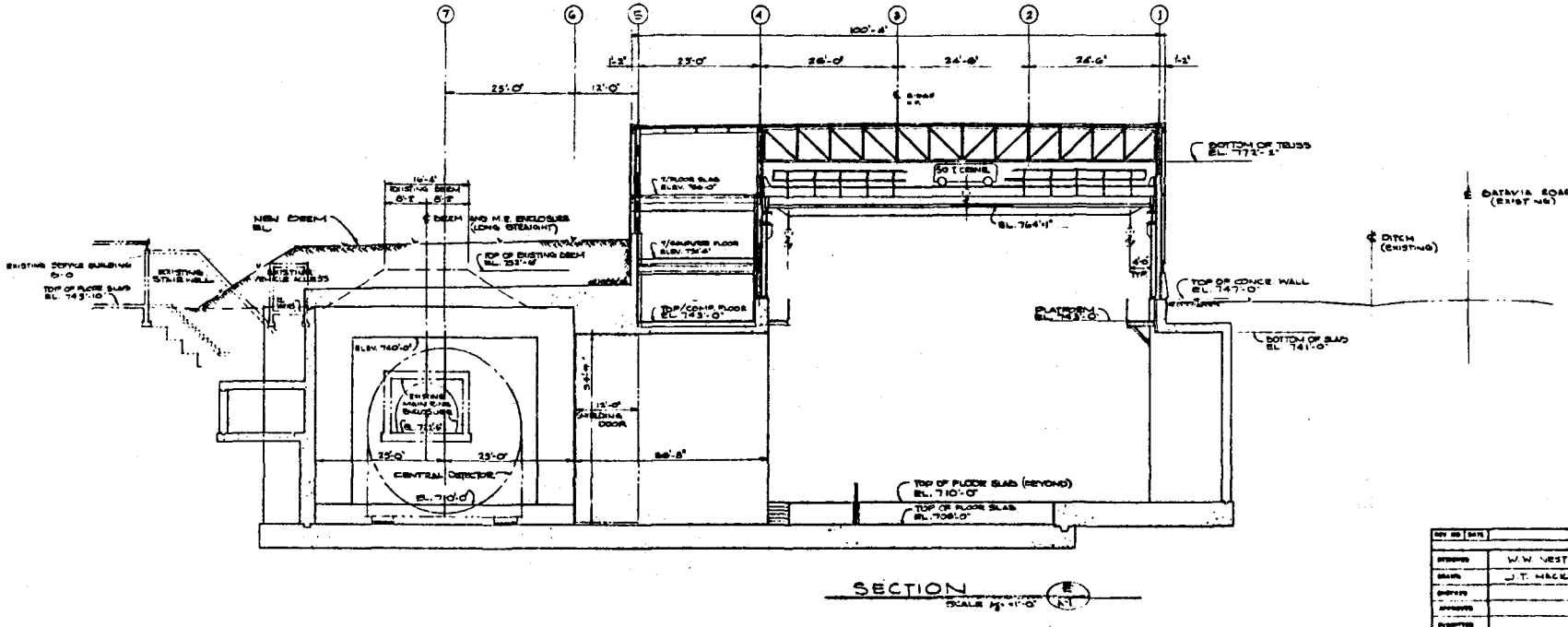

FIG. II.2

DRAWN	W.W. WESTANDER
TRACED	J.T. MACKEMER

FERMI NATIONAL ACCELERATOR LABORATORY
B-0 COLLIDING BEAM FACILITY
CROSS SECTIONS
8-1-37

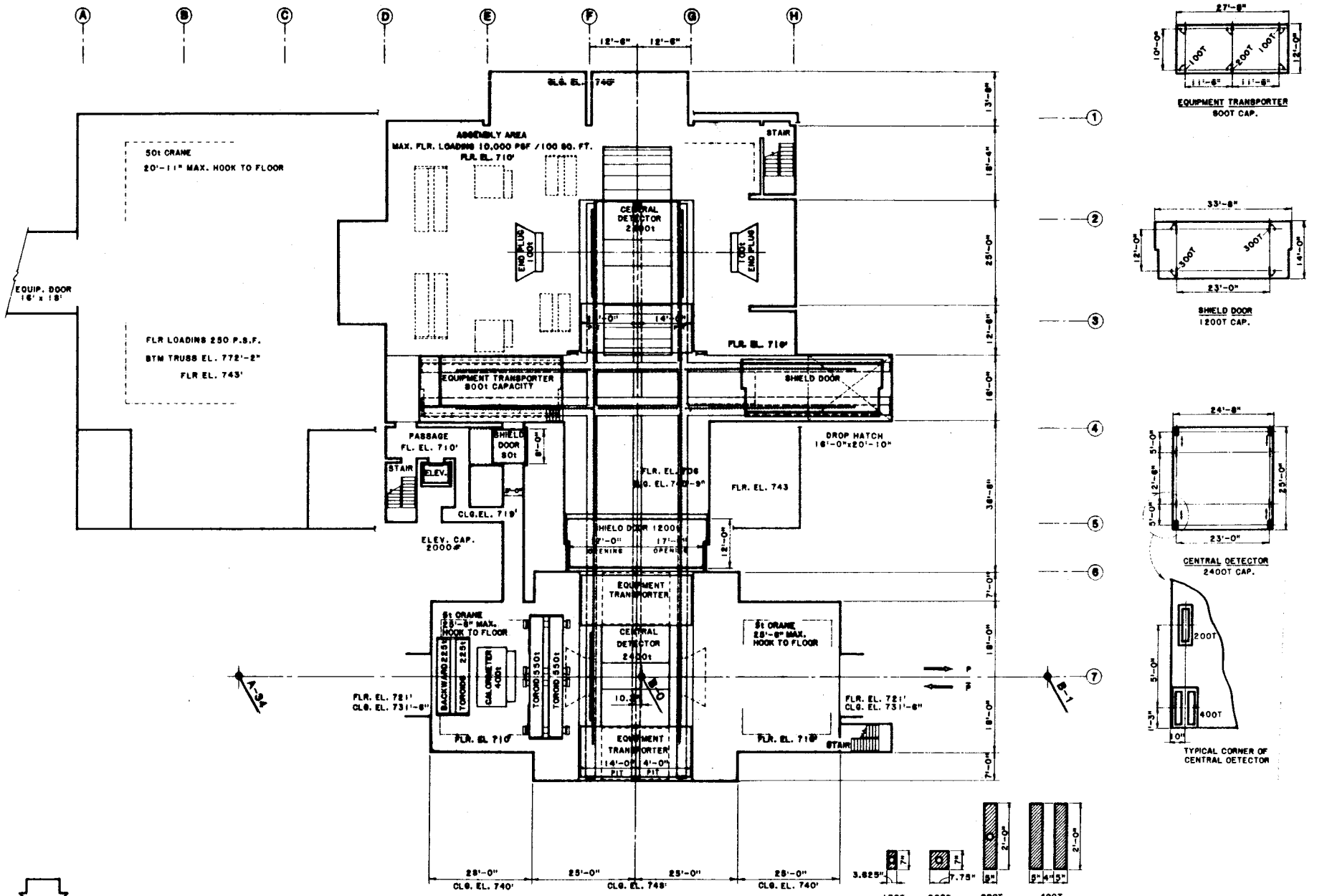

FIG. II.3

LEGEND

2"x2'-4" FLOOR TRACKS W/INDEXING HOLES ELEV. 706'-0"

.5"x2'-0" FLOOR TRACKS ELEV. 706'-0"

DESIGNED	W.W. NESTANDER
DRAWN	J.T.HACKEMER

FERMI NATIONAL ACCELERATOR LABORATORY

UNITED STATES DEPARTMENT OF ENERGY

B-0 COLLIDING BEAM FACILITY

EQUIPMENT LOADS & POSITIONS

FLOOR PLAN ELEV. 706 & 710

Appendix III

Model Solenoid and its Test Results

A model solenoid, which is one meter in diameter and one meter long, was designed, constructed, and tested by Japanese collaborators at the University of Tsukuba and KEK, using the Hitachi Company.

The structure of the coil is like that of the CELLO Solenoid, and its superconductor is stabilized with pure aluminum (Ref. 1.) The superconductor is metallurgically bonded to the aluminum stabilizer by Hitachi's EFT method. The conductor is wound on a 10 mm thick aluminum bobbin, covered with an insulator layer and a layer of aluminum banding is wound with pretension over the conductor with another insulation layer between them. The cooling pipe with liquid helium flow in it is wound and glued on the surface of the banding. A radiation shield cooled with liquid nitrogen, covers the whole surface of the coil. The detailed design and construction reports are given in a series of Status Reports (Ref. 2) and Hitachi's Engineering Reports (Ref. 3). Magnetic field distribution and forces were calculated and reported (Ref. 4).

This model solenoid was tested at the Hitachi Company in Japan this April. After the first quench at 4 kA, it reached 4.5 kA successfully, which is the designed operating point. This current would give a magnetic field of 1.5 Tesla at the center if there were an iron yoke around it.

The magnet does not seem to go through any training after the first quench and the test results indicate strongly that this coil is very stable against quenches. In the first quench an estimated energy of about 1.3 MJ was unintentionally dumped into the magnet, while the stored magnetic energy was about 440 kJ. No hint of any physical damage was observed with the solenoid. The characteristics of the magnet cooling system were monitored from room temperature to liquid helium

temperature, and the system seemed to function as designed.

During this test run it was tried to raise the maximum quench current above 4.5 kA, but a thermal short inside prevented higher currents. It was estimated that the temperature of the conductor was about 6.5 K at some point, while it was designed to operate below 5 K. This thermal defect will be corrected and with some minor modifications the magnet will be tested again in the near future. It is expected to go above 5 kA.

The propagation speed of the normal zone was tested as a function of excitation current using a heater embedded into the coil. The observed speed in the perpendicular direction to the winding direction was around 0.12 m/sec at 3.5 kA and estimated about 0.3 m/sec at 4.5 kA. This relatively fast propagation speed made the coil very safe when the coil quenched. The quench mode has been studied using the program QUENCH, and it was found that the full scale magnet is stable during a quench with such parameters as were found with this test. (ref. 5)

References

1. "Conceptual Design of a Large, Thin Coil Superconducting Solenoid Magnet for Colliding Beam Experiments at Fermilab," D. Cline et al., TM-826, October 25, 1978.

2. "Status Report on the R&D Superconducting Solenoid Magnet for the $\bar{p}p$ Colliding Beam Detector (1) to (6)," by S. Mori, from July 31, 1980 to April 27, 1981.

3. Hitachi's Engineering Reports 1423 series. From HES-1 (Nov. 1979) to HES-41 (March 1980).

4. "Can We Test Large Solenoid Coils Safely Without Yoke", by R. Yamada, CDF-86, January 26, 1981.

5. "Quench Properties of Superconducting Solenoid Magnet for Fermilab Colliding Beam Experiments," by H. Hirabayashi et al., Tsukuba-HEAP-1, December 12, 1980.

Appendix IV

Angular Granularity of Towers and η-ϕ Coverage

This is a compilation of the granularity of towers in the various calorimetric elements of our detector with a tentative nomenclature. A table of rapidity intervals is also given. c = central, w = end wall, p = end plug, and f = forward.

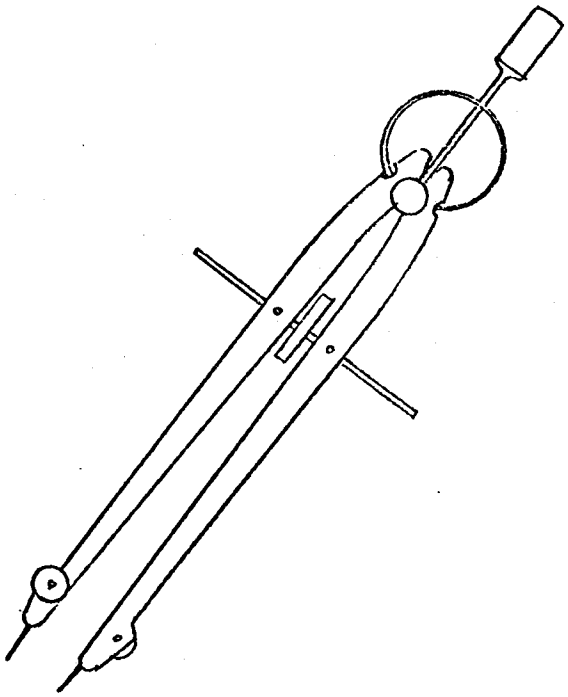

Hadron	Angle		Pseudorapidity			
Tower	From	To	From	To	$\Delta\eta$	$\Delta\phi$
1c	90	82.53	0.	.131	.131	15°
2c	82.53	75.30	.131	.259	.128	15°
3c	75.30	68.52	.259	.384	.125	15°
4c	68.52	62.31	.384	.503	.119	15°
5c	62.31	56.74	.503	.616	.113	15°
6c	56.74	51.79	.616	.723	.107	15°
7c	51.79	47.44	.723	.822	.101	15°
7w	51.79	47.44	.723	.822	.101	15°
8c	47.44	42 ↶	.822			15°
8w	47.44	43.83	.822	.910	.088	15°
9w	43.84	40.40	.910	1.	.090	15°
10w	40.40	36.82	1.	1.1	.1	15°
11w	36.82	33.52	1.1	1.2	.1	15°
12w	33.52	30.49	1.2	1.3	.1	15°
13p	30.49	27.71	1.3	1.4	.1	5°
14p	27.71	25.16	1.4	1.5	.1	5°
15p	25.16	22.83	1.5	1.6	.1	5°
16p	22.83	20.71	1.6	1.7	.1	5°
17p	20.71	18.77	1.7	1.8	.1	5°
18p	18.77	17.01	1.8	1.9	.1	5°
19p	17.01	15.41	1.9	2.	.1	5°
20p	15.41	13.96	2.	2.1	.1	5°
21p	13.96	12.65	2.1	2.2	.1	5°
22p	12.65	11.45	2.2	2.3	.1	5°
23p	11.45	10.37	2.3	2.4	.1	5°

E.Mag.	Angle		Pseudorapidity			
Tower	From	To	From	To	$\Delta\eta$	$\Delta\phi$
1c	90	82.53	0.	.131	.131	15°
2c	82.53	75.30	.131	.259	.128	15°
3c	75.30	68.52	.259	.384	.125	15°
4c	68.52	62.31	.384	.503	.119	15°
5c	62.31	56.74	.503	.616	.113	15°
6c	56.74	51.79	.616	.723	.107	15°
7c	51.79	47.44	.723	.822	.101	15°
8c	47.44	43.62	.822	.915	.092	15°
9c	43.62	40.27	.915	1.	.085	15°
10c	40.27	35 ≈	1.			15°
11p	36.82	33.52	1.1	1.2	.1	5°
12p	33.52	30.49	1.2	1.3	.1	5°
13p	30.49	27.71	1.3	1.4	.1	5°
14p	27.71	25.16	1.4	1.5	.1	5°
15p	25.16	22.83	.1.5	1.6	.1	5°
16p	22.83	20.71	1.6	1.7	.1	5°
17p	20.71	18.77	1.7	1.8	.1	5°
18p	18.77	17.01	1.8	1.9	.1	5°
19p	17.01	15.41	1.9	2.	.1	5°
20p	15.41	13.96	2.	2.1	.1	5°
21p	13.96	12.65	2.1	2.2	.1	5°
22p	12.65	11.54	2.2	2.3	.1	5°
23p	11.45	10.37	2.3	2.4	.1	5°

Hadron or E. Mag. Tower	Angle From	Angle To	Pseudorapidity From	Pseudorapidity To	$\Delta\eta$	$\Delta\phi$
23f	11.45	10.37	2.3	2.4	.1	5°
24f	10.37	9.39	2.4	2.5	.1	5°
25f	9.39	8.50	2.5	2.6	.1	5°
26f	8.50	7.69	2.6	2.7	.1	5°
27f	7.69	6.96	2.7	2.8	.1	5°
28f	6.96	6.30	2.8	2.9	.1	5°
29f	6.30	5.70	2.9	3.0	.1	5°
30f	5.70	5.16	3.0	3.1	.1	5°
31f	5.16	4.67	3.1	3.2	.1	5°
32f	4.67	4.22	3.2	3.3	.1	5°
33f	4.22	3.82	3.3	3.4	.1	5°
34f	3.82	3.46	3.4	3.5	.1	5°
35f	3.46	3.13	3.5	3.6	.1	5°
36f	3.13	2.83	3.6	3.7	.1	5°
37f	2.83	2.56	3.7	3.8	.1	5°
38f	2.56	2.32	3.8	3.9	.1	5°
39f	2.32	2.10	3.9	4.0	.1	5°

Appendix V

PRELIMINARY STUDIES OF CYLINDRICAL DRIFT CHAMBER TRACK RECONSTRUCTION

We have studied the track reconstruction efficiency in the central drift chambers using a "road" algorithm. We present here some preliminary results on the performance for jets and for events with high P_T leptons. The reconstruction efficiency is good for isolated tracks. For tracks in the core of a high P_T jet, some tracks are lost with the current algorithm. An improved tracking algorithm should reduce the inefficiency.

CENTRAL DRIFT CHAMBER SCHEMES STUDIED

Two drift chamber schemes were studied:

(A) A scheme similar to the one described in chapter 5 with 22 axial planes in 11 sets of half-cell-staggered doublets supplemented by 10 small angle stereo planes (versus 8 for the scheme discussed in chapter 5). Note that information from charge division is not used in the trackfinding algorithm as yet. The 32 planes have a total of 11,200 wires.

(B) A scheme with 13 axial planes and 12 small angle stereo planes equally spaced radially; this is a simple extension of the CLEO geometry of 9 axial and 8 small angle stereo planes. The total number of wires is 8348.

DESCRIPTION OF TRACK RECONSTRUCTION ALGORITHM

The "road" algorithm we have used so far is a modified version of the algorithm written by Karl Berkelman for the CLEO collaboration. This algorithm has been used for physics at CLEO during the last 18 months. Tracks are reconstructed first

in the r-ϕ view using only the axial layers. These r-ϕ tracks are then extended to 3-dimensional tracks using the small-angle stereo layers.

For scheme A, the hits from the two adjacent planes of a doublet are still treated as independent in the algorithm; we expect that trackfinding could be improved significantly if the correlation information is used. Thus, our studies probably underestimate the power of scheme A.

MONTE CARLO EVENT GENERATION AND DRIFT CHAMBER SIMULATION

The result presented here are based on studies of events with single high P_T leptons along with stray particles (4 particles per unit rapidity) from "beam jets" (other particles from the same event presumably from soft scattering of the spectator partons) and events with one high P_T jet fragmenting into multi-hadrons according to the Field-Feynman procedure. The drift chamber simulation includes inefficiencies (3%), random noise hits (3 per layer), and position smearing (200 microns). A 15 kG uniform solenoidal magnetic field and a linear space-time relationship are assumed. Single hit electronics is assumed (i.e., only the track closest to the sense wire is recorded in case two tracks cross the same cell).

TRACKFINDING FOR SINGLE HIGH p_T LEPTONS

The reconstruction results for events with a charged lepton with P_T of 10 to 40 GeV/c (expected from W and Z decays) and including stray particles from "beam jets" are shown in Figures V.1 and V.2. Figure V.1 shows the comparison of reconstructed P_T vs. generated P_T for the leptons for scheme A. All leptons were successfully found. Figure V.2 shows the distribution in $\Delta p_T/p_T^2$ for leptons, with the solid curve for scheme A and dashed curve for scheme B. Perfect reconstruction with all the hits found and ambiguities correctly resolved should give a $\Delta p/p$ of 0.2% p_T in agreement with the peak

observed. For scheme B, there is a significant tail in the distribution due to reconstructed tracks with some wrong hits or wrong left-right ambiguities. These tracks typically have only 8 or 9 of the 13 axial planes hit, with the remaining planes missing either due to inefficiency or overlap. For scheme A, the number of misreconstructed tracks is reduced by an order of magnitude by demanding more than 12 axial planes with a hit. Resolution in $\cot(\theta)$ is about .003. Leptons were studied at both 90 degrees and at 45 degrees in polar angle with similar results. Thus, we conclude that the reconstruction efficiency with proper resolution should be better than 98% for single isolated high P_T tracks event in the presence of stray beam jet particles.

The expected value of $\Delta p_T/p_T^2$ is 0.2% x p_T using only the tracking information from r =30 cm to r=140 cm. The resolution should be better in our detector for several reasons--(i) the interaction vertex could be used to improve momentum resolution since many other tracks should exist for the same event; however, experience at other solenoidal detectors show that the improvement will probably be degraded by beam pipe multiple scattering; (ii) the addition of high resolution vertex detectors will improve the resolution.

TRACKFINDING EFFICIENCY FOR EVENTS WITH JETS

For jet reconstruction, we have studied Field-Feynman jets produced at $\theta=90°$ with total momenta of 30, 50, and 70 GeV/c. The average charged multiplicity is about 9; we have used the u quark fragmentation with average P_T w.r.t. the jet axis of .7 GeV/c. While the reconstruction efficiency for individual particles is good (typically 95%) in the lower momentum jets, the efficiency for particles with high P_T in higher momentum jets is lower due to overlapping of tracks in the jet core, (which contains the highest momentum tracks) and due to the tighter jet collimation for higher energy jets. For example, for a layer with 200 cells, a cell will contain 2 or more hits

typically 20 % of the time. Figures V.3, V.4 and V.5 show the comparison of generated and reconstructed jet total charged momentum for 200 jets each of 30, 50, and 70 GeV/c total momentum using scheme A. 30 GeV/c jets are reconstructed successfully most of the time; only 5% of the jets have jet total charged momentum incorrectly measured by more than 15%, mostly by missing some tracks. For 50 and 70 GeV/c jets, a larger fraction of jets are mis-reconstructed. For 70 GeV/c jets, 80% of the jets are reconstructed with total charged momentum within 15% of the the generated value. The cases of mis-reconstruction are almost entirely due to some tracks not being found. Figure V.6 shows the reconstructed vs. generated momenta for individual charged tracks for the 70 GeV/c jets. Out of a total of about 1800 tracks, only a few tracks are reconstructed with wrong momentum. However, 5 % of the tracks are not reconstructed due to overlapping in the jet core. The current criteria for acceptable tracks could be modified to improve the efficiency and thus ameliorate this problem. Note that for scheme B, the inefficiencies are worse; in addition, many tracks are reconstructed with wrong momenta.

ASSESSMENT AND PLANS FOR FUTURE STUDIES

These preliminary results are extremely encouraging. The comparison of the two schemes clearly favors scheme A and shows the need for many axial planes to enable efficient and correct pattern recognition, especially in the jet core. We will continue to study the performance as a function of the number of planes, wire arrangement, cell size, and algorithm. In particular, we are adapting the "tree" algorithm to our chamber configuration. This algorithm, being used at TASSO, may be better at trackfinding inside the jet core than the "road" algorithm. Another approach we are investigating is how to decide purely from the reconstructed information that we may have missed some tracks. Special second stage algorithms may be used when two reconstructed tracks are overlapped or when

there are many extra hits near a reconstructed track. Some fraction of doubtfully reconstructed jets may have to be thrown out. We believe that with our current design, this could be kept to less than 5%.

Figure Captions

V.1 Reconstructed versus generated momentum for leptons in scheme A. The background included particles from "beam jets".

V.2 Distributions of (p_T generated - p_T reconstructed)/p_T^2 for leptons in scheme A and B.

V.3 Reconstructed versus generated total charged momentum for 30 GeV/c jets.

V.4 Same as Figure V.3 for 50 GeV/c jets.

V.5 Same as Figure V.3 for 70 GeV/c jets.

V.6 Reconstructed versus generated transverse momentum for individual charged particle in 70 GeV/c jets. The entries with reconstructed p_T of zero correspond to tracks that were not reconstructed.

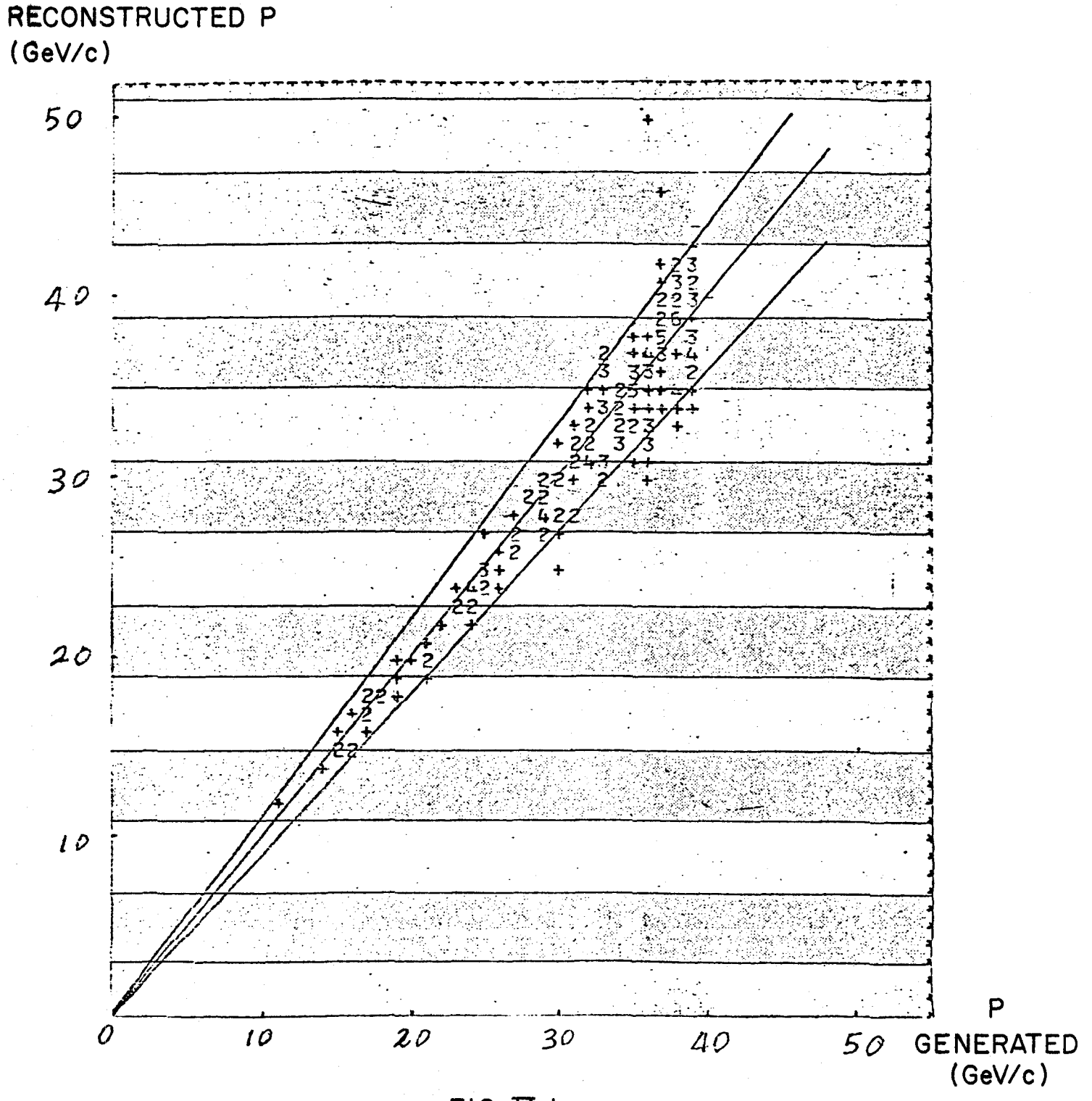

FIG. V.1

LEPTON WITH BEAM jets

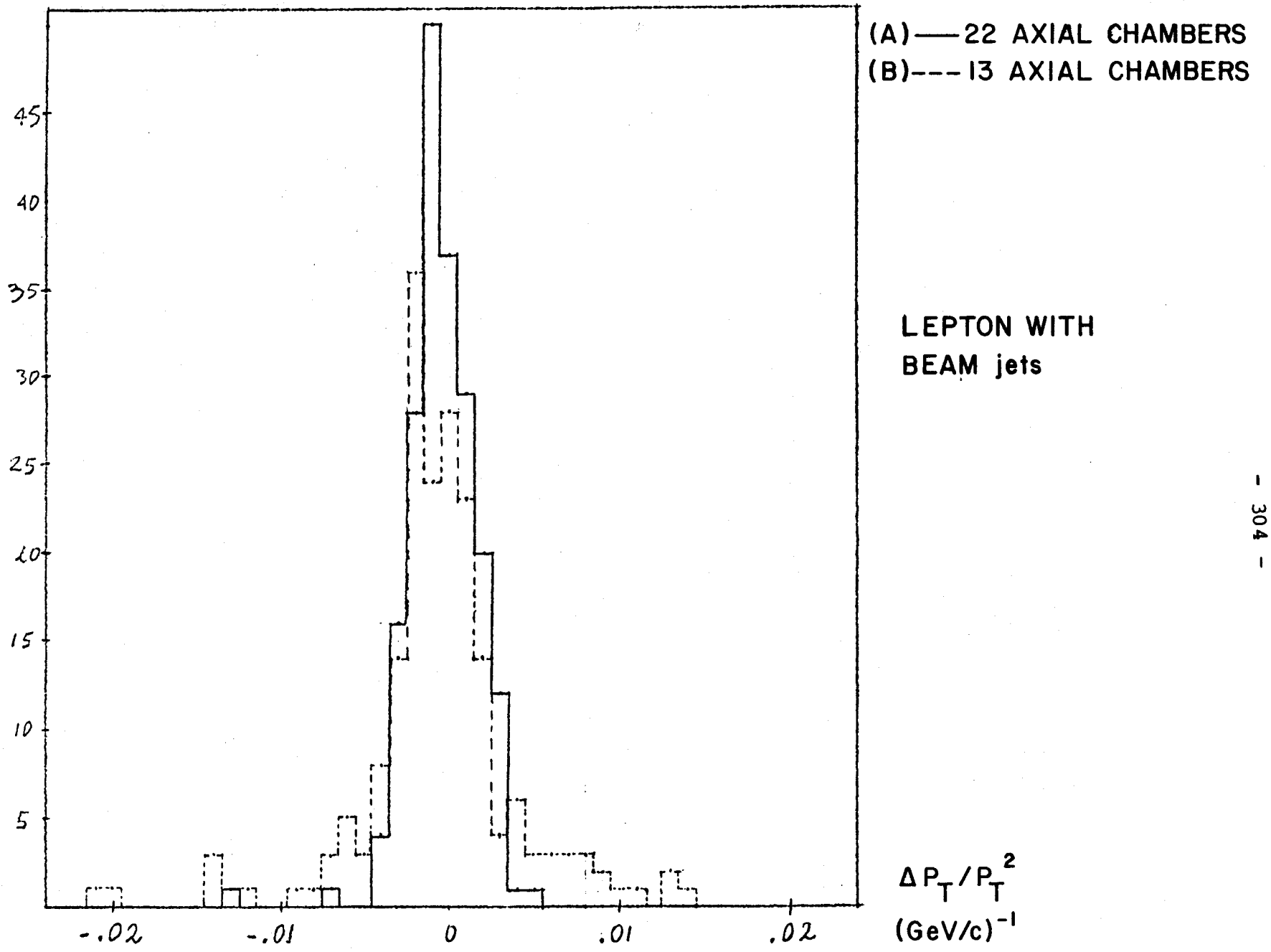
(A)——22 AXIAL CHAMBERS
(B)---13 AXIAL CHAMBERS
LEPTON WITH
BEAM jets
45
40
35
30
25
20
15
10
5
-.02
-.01
0
.01
.02
$\Delta P_T / P_T^2$
$(GeV/c)^{-1}$

FIG. V.2

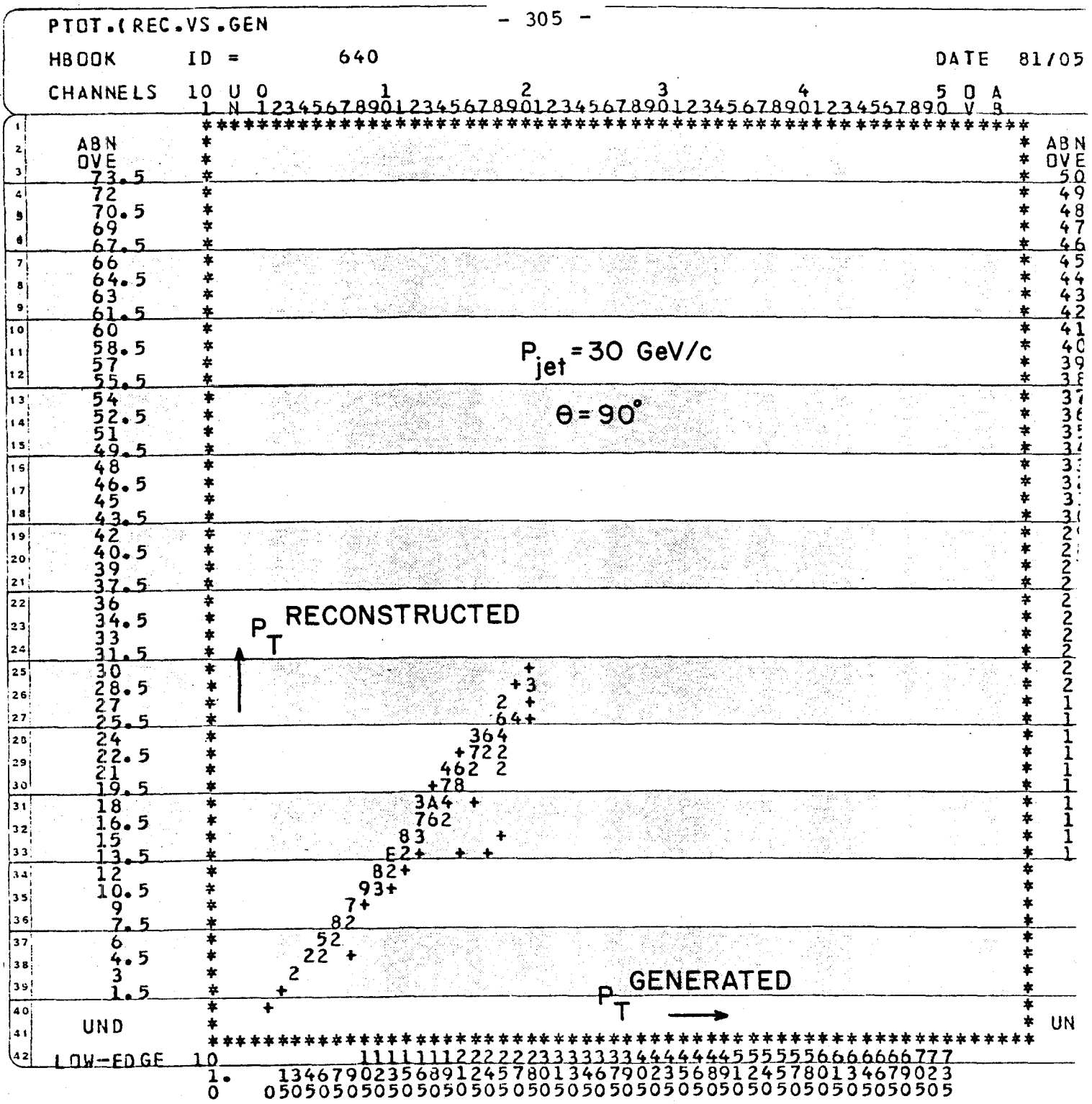
PTOT.(REC.VS.GEN
HBOOK ID = 640
DATE 81/05
CHANNELS
ABN OVE
UND
LOW-EDGE
P_{jet}=30 GeV/c
θ=90°
P_T RECONSTRUCTED
P_T GENERATED
ENTRIES = 199
SATURATION AT= 31
SCALE .,+,2,3,.,.,., A,B,
STEP = 1 * MINIMUM=0
PLOT STATISTICS
199

FIG. V.3

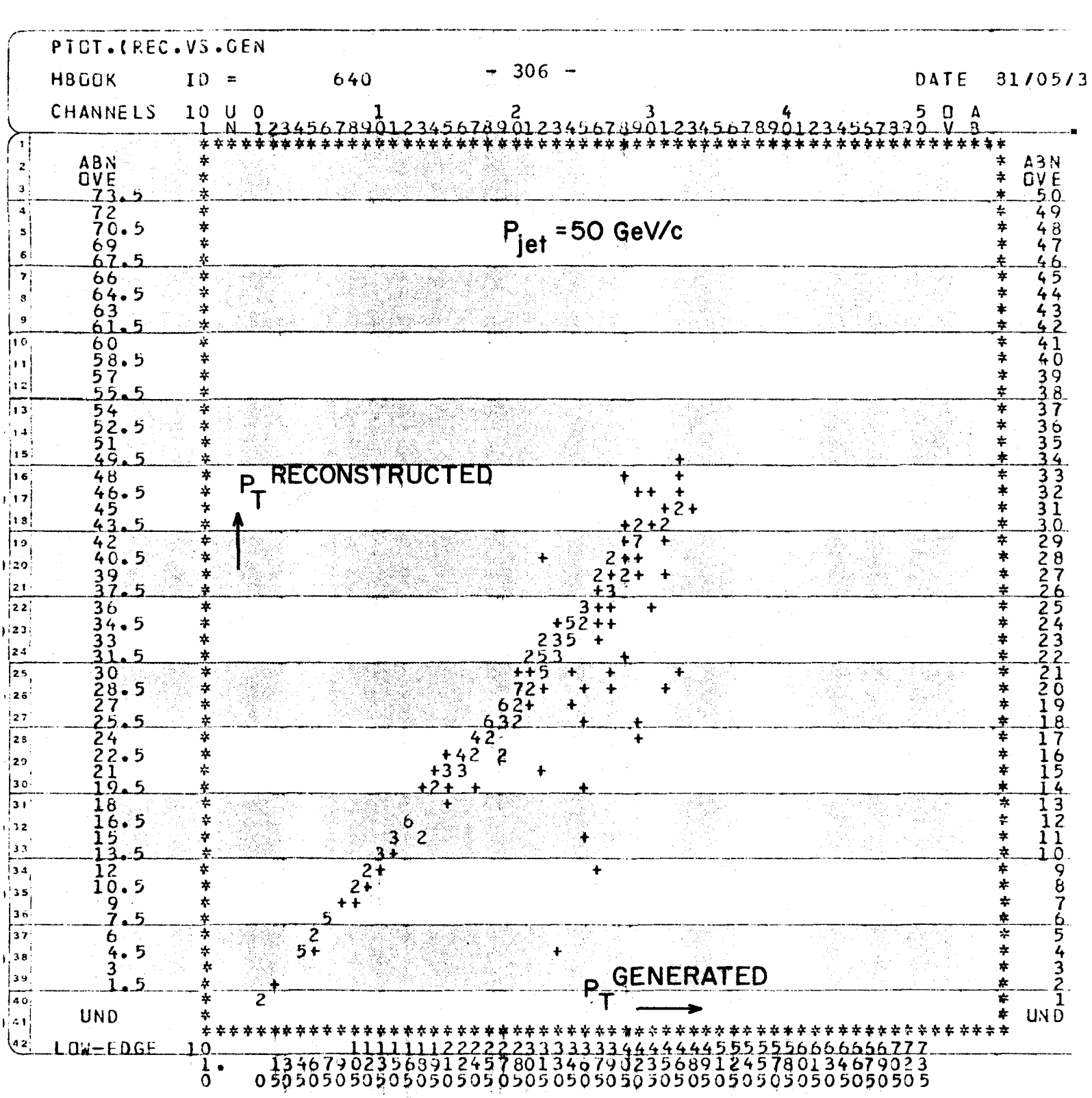
PTOT.(REC.VS.GEN
HBOOK ID = 640
DATE 81/05/3
CHANNELS
ABN OVE
UND
LOW-EDGE
P_{jet} = 50 GeV/c
P_T RECONSTRUCTED
P_T GENERATED
ENTRIES = 198
SATURATION AT= 31
SCALE .,+,2,3,.,.,.,A,B,
STEP = 1
* MINIMUM=0
PLOT STATISTICS
198

FIG. V.4

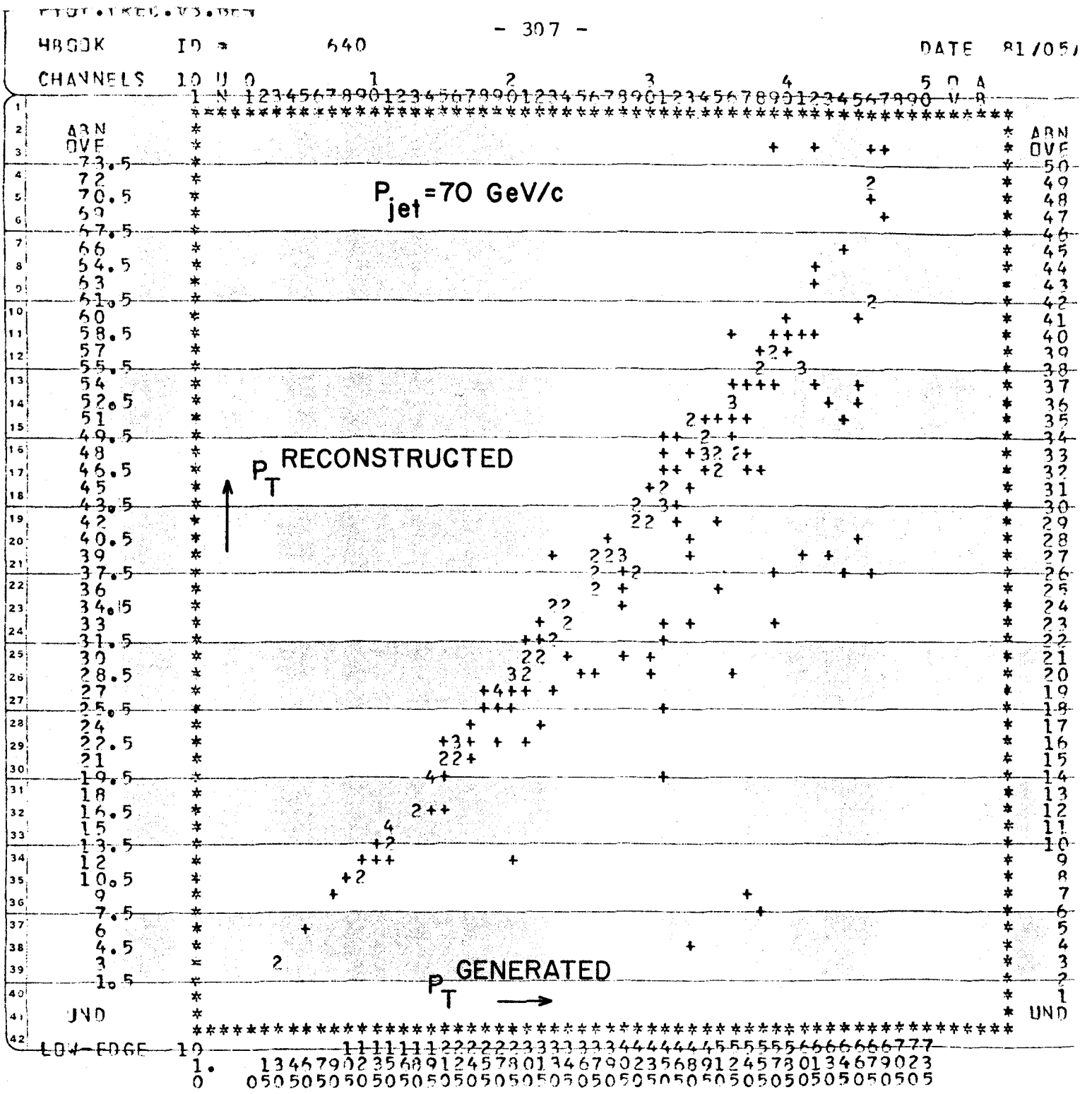
HBOOK ID = 640
DATE 81/05/
CHANNELS 10 U 0 1 2 3 4 5 O A
P_{jet}=70 GeV/c
P_T RECONSTRUCTED
P_T GENERATED
P_T →
ENTRIES = 200
SATURATION AT= 31
SCALE .,+,2,3,...,A,B,
STEP = 1 * MINIMUM=0
PLOT STATISTICS
4
196

FIG. V.5

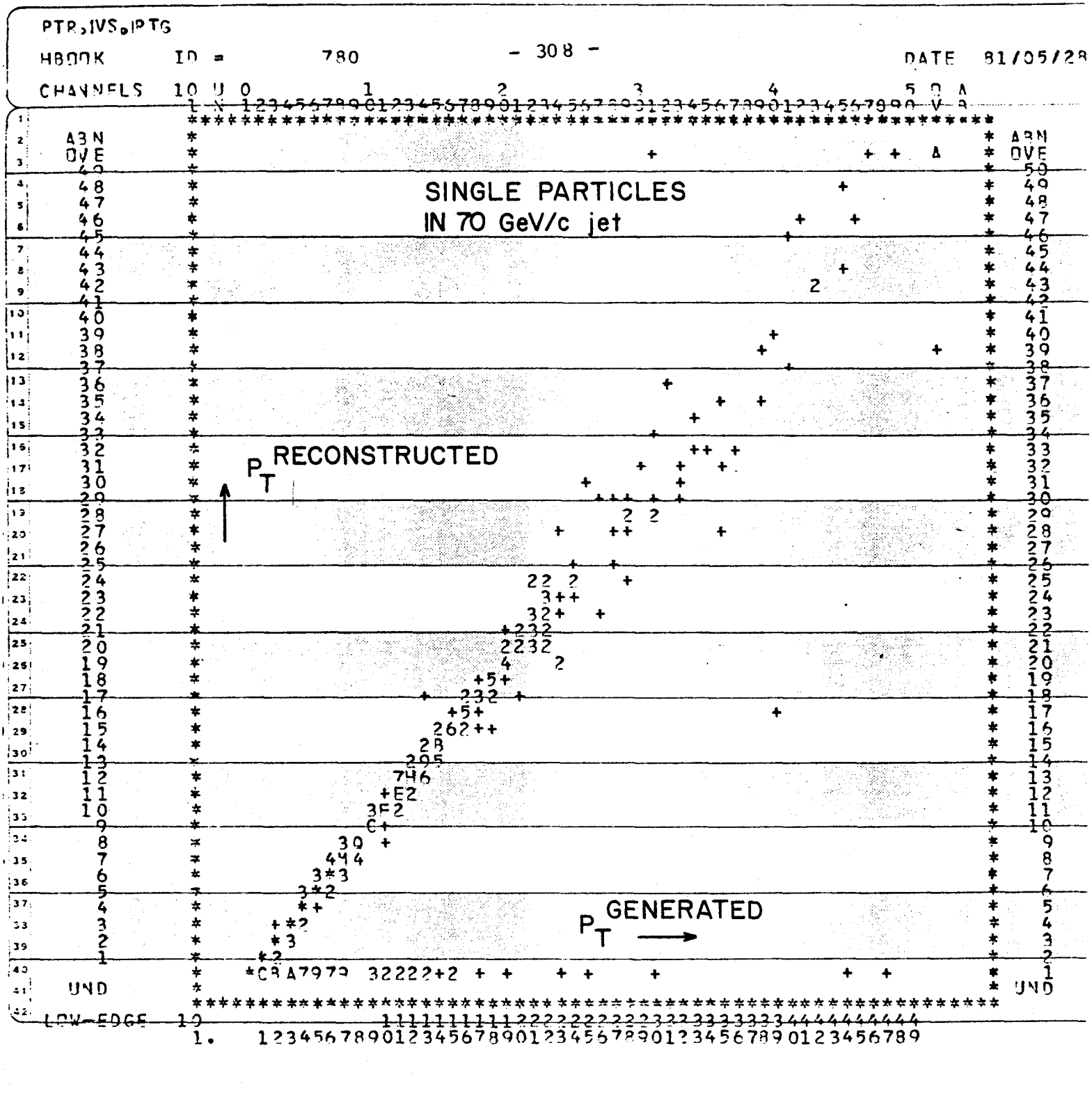
PTR,IVS,IPTG
HBOOK ID = 780
DATE 81/05/28
SINGLE PARTICLES
IN 70 GeV/c jet
P_T RECONSTRUCTED
P_T GENERATED
ENTRIES = 1491
SATURATION AT= 31
SCALE .,+,2,3,.,., A,B,
STEP = 1 * MINIMUM=0
PLOT STATISTICS

FIG. V.6

Appendix VI

THE END WALL HADRON CALORIMETERS

Contribution to the Design Report

G. Gennero and A. Menzione

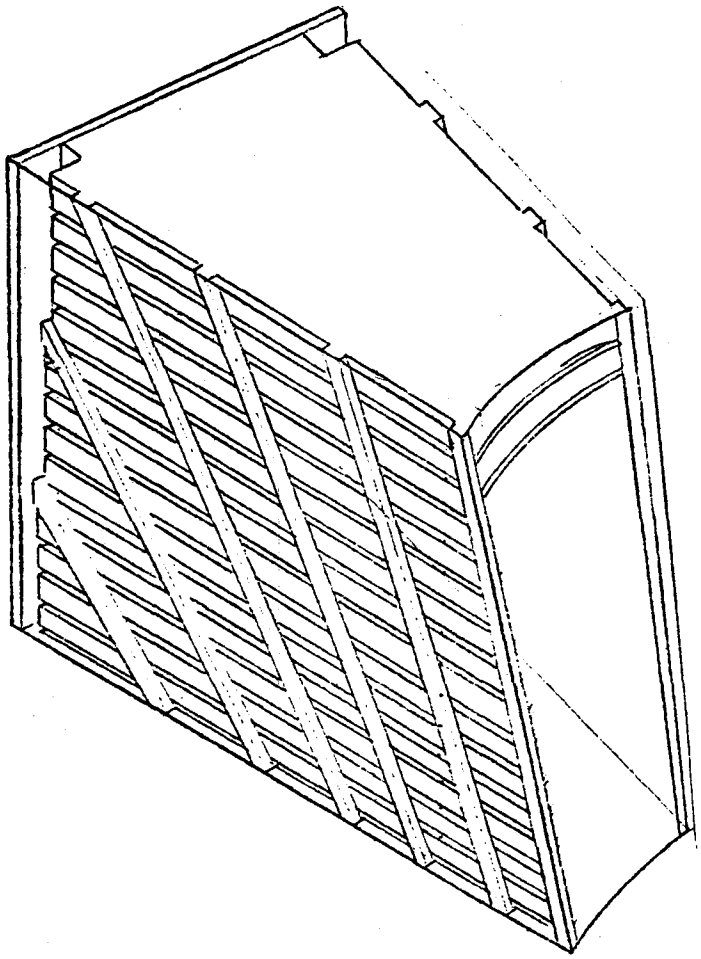

We present working principles, scheme of construction and assembly of the iron, layout of light pipes and photomultipliers, list of material dimensions, and weights.

Characteristics

1. The modularity is the same as in the central hadron calorimetry (24 equal azimuthal modules in each wall).
2. The tower structure of central calorimetry is extended in the wall.
3. The read out technique is the same as in central calorimetry, see Fig. 1. This allows us to predict performances from our test beam results.
4. The sampling is 2 in. iron. Reasons for this choice are mainly: The higher energy of secondaries in this region and the use we intend to do of the iron in bringing return flux.
5. No easy access to the inert part of these modules is planned, but all photomultipliers, dividers, and cables are easy to access.

Fig. 2 shows the tower structure in the context of central calorimetry and of the magnet. The proposed way of holding modules in the wall is also sketched.

In order to work out all equal modules and provide room for a number of ribs (eight in this hypothesis) needed to give stiffness to the wall plate and deliver forces from the plug, a slightly off-center geometry has been chosen. Specifications of that are given in Fig. 3.

Fig. 4 shows the assembly of iron parts: Plates, covers, and fixtures. Of course, details of the construction depend upon which workshop is going to manufacture the parts.

Layout of light pipes and photomultipliers are given in Fig. 5 and the detail of the up-right corner in Fig. 6.

Fig. 7 shows the detail of the PM housing, shielding, and divider. The light adapter to the PM is also shown in the same figure.

Three examples of scintillator planes are given in Fig. 8. Scintillator 1 cm thick PMMA base is supposed to be laser cut to the right shape with an accuracy of a fraction of millimeter.

Fig. 9 shows a possible fixture that, with the help of the two crane hooks, allows, in the garage, to put all modules in the right position.

Table 1 is the list of dimensions of iron plates (preliminary) with weights.

Table 2 gives the list of the other relevant materials.

Table 1

IRON PLATES

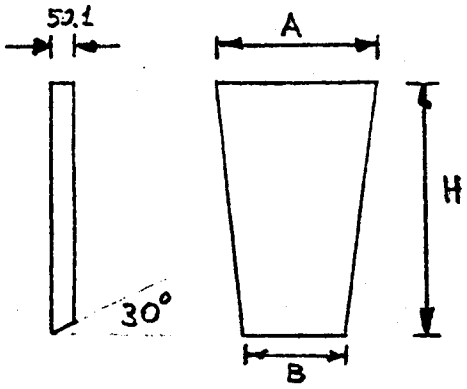

	A (mm)	B (mm)	H (mm)	S (cm^2)	W (Kg)
Plate No. 15	784.1	492.5	1,132.9	7,231	283.81
14	784.1	482.5	1,171.4	7,419	291.18
13	784.1	472.6	1,209.9	7,602	298.4
12	784.1	462.7	1,248.4	7,783	305.5
11	784.1	452.8	1,286.9	7,959	312.4
10	784.1	442.9	1,325.4	8,131	319.2
9	784.1	433.0	1,363.9	8,300	325.8
8	784.1	423.1	1,402.3	8,465	332.2
7	784.1	413.2	1,440.8	8,626	338.6
6	784.1	403.3	1,479.3	8,783	344.7
5	784.1	393.4	1,517.8	8,937	350.7
4	784.1	383.5	1,556.3	9,086	356.6
3	784.1	373.5	1,594.8	9,231	362.3
2	784.1	363.6	1,633.3	9,373	367.9
1	784.1	353.7	1,671.8	9,511	373.3
Total 1 module				135,949	5,336.
Total 48 modules				6,525,600	256,128.

Table 2

Scintillators

Total surface	660	m^2 + 20% inefficiency
Total volume	7.92	m^3
Total weight	9.5	tons
Naphthaline	760	Kg
Buthyl BPD	95	Kg
POPOP	950	gr

72 pieces/mod x 48 mod = 3456 pieces

BBQ

(800 x 10 x 5) x 2 x 1500 = 3000 pieces

(500 x 10 x 5) x 2 x 2000 = 4000 pieces

Total volume 220 ℓ + 20% inefficiency

Total weight 317 Kg

PMMA

Rods	20 x 15 x 1300	= 100 pieces
	20 x 25 x 500	= 100 pieces
	30 x 25 x 500	= 100 pieces
Plate	10 x 75 x 1500	= 400 pieces
	10 x 60 x 1000	= 100 pieces
	10 x 40 x 500	= 100 pieces
Adaptors	20 x 30 x 60	= 400 pieces

Total volume 780 ℓ + 20% inefficiency

Total weight 1123 Kg

Number of light pipes 576

Photomultipliers

Dividers

Housings

(2 sides x 6 towers x 48 modules) = 576

+ spare units = 600

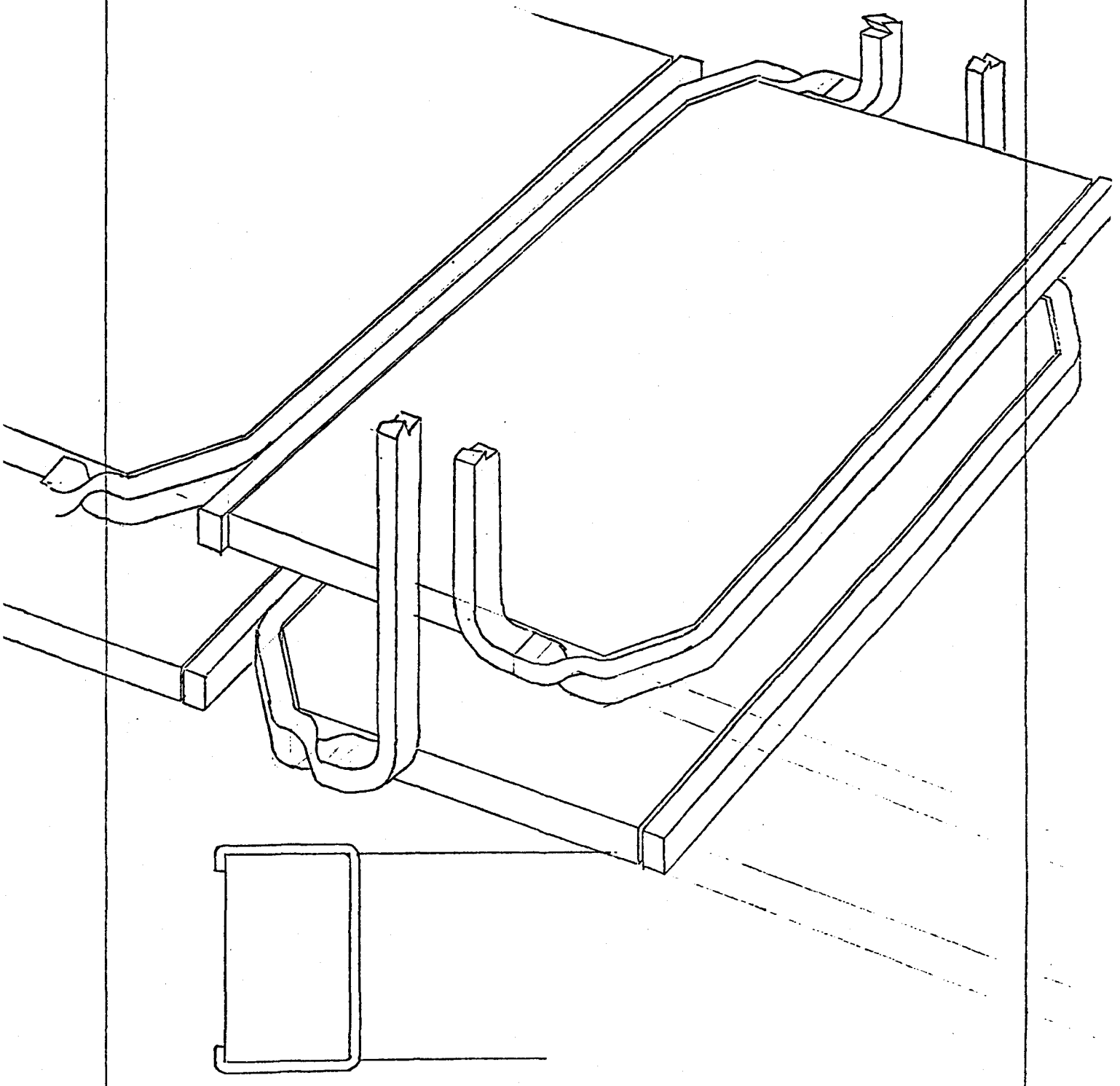

Fig. 1

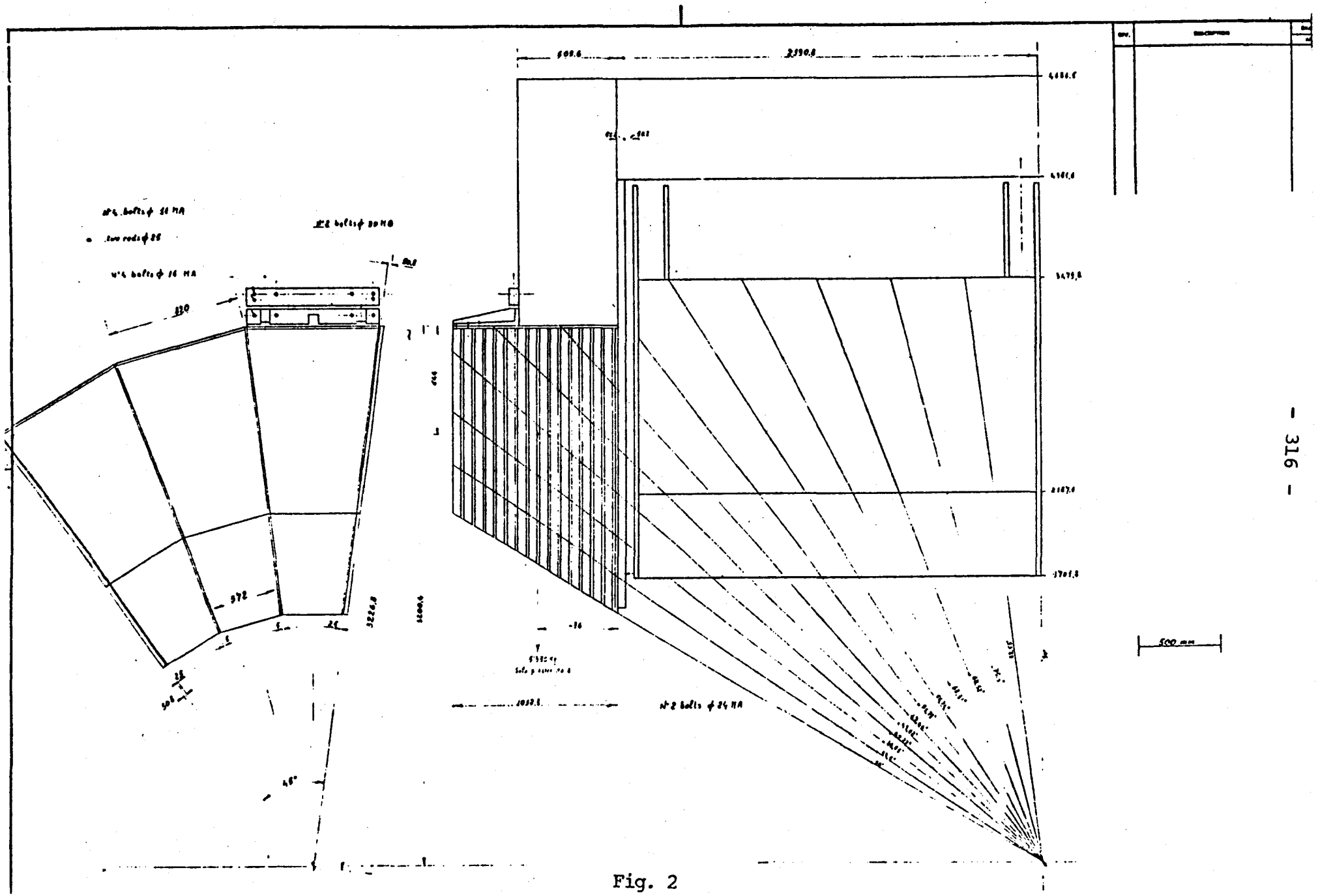

Fig. 2

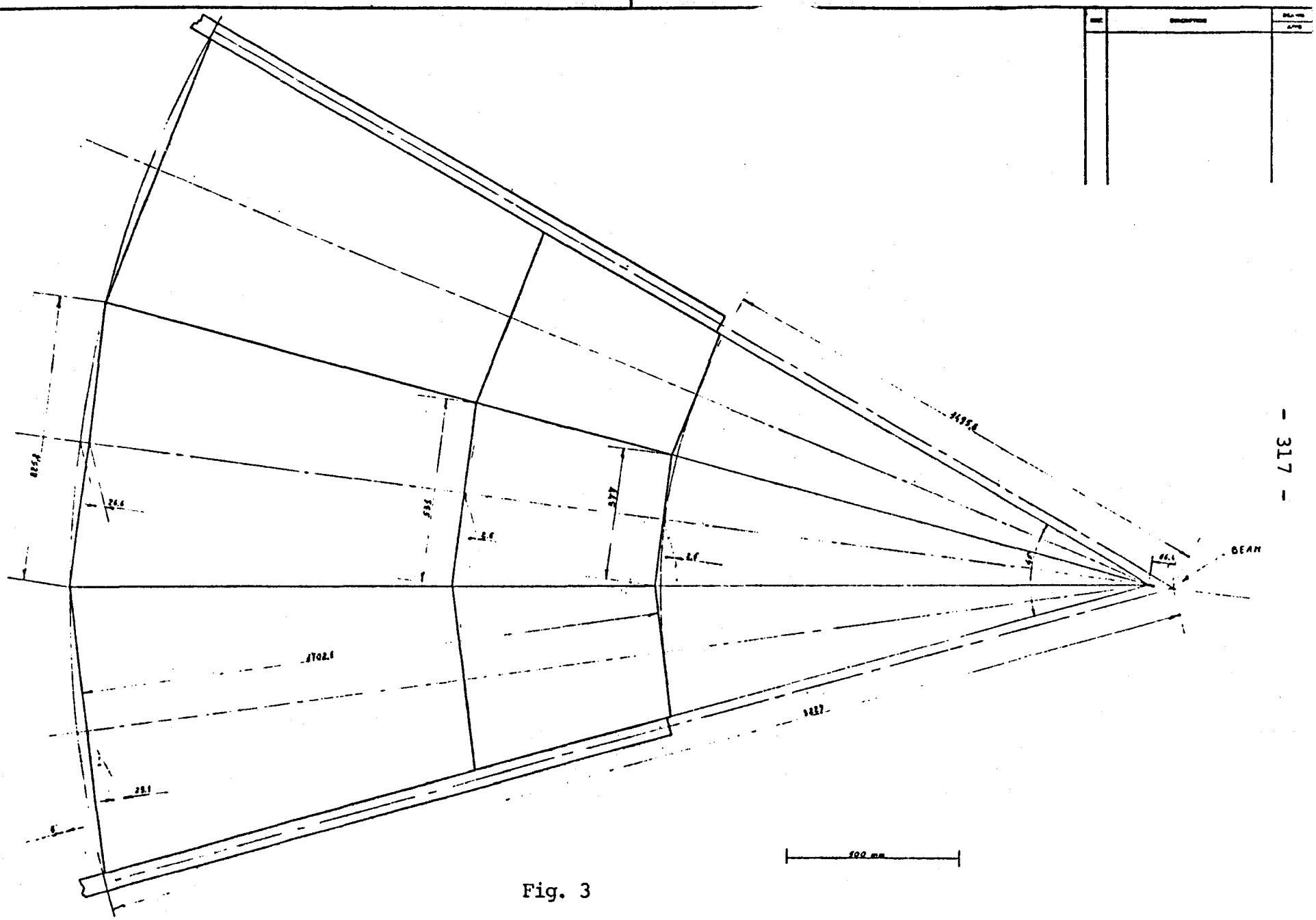

Fig. 3

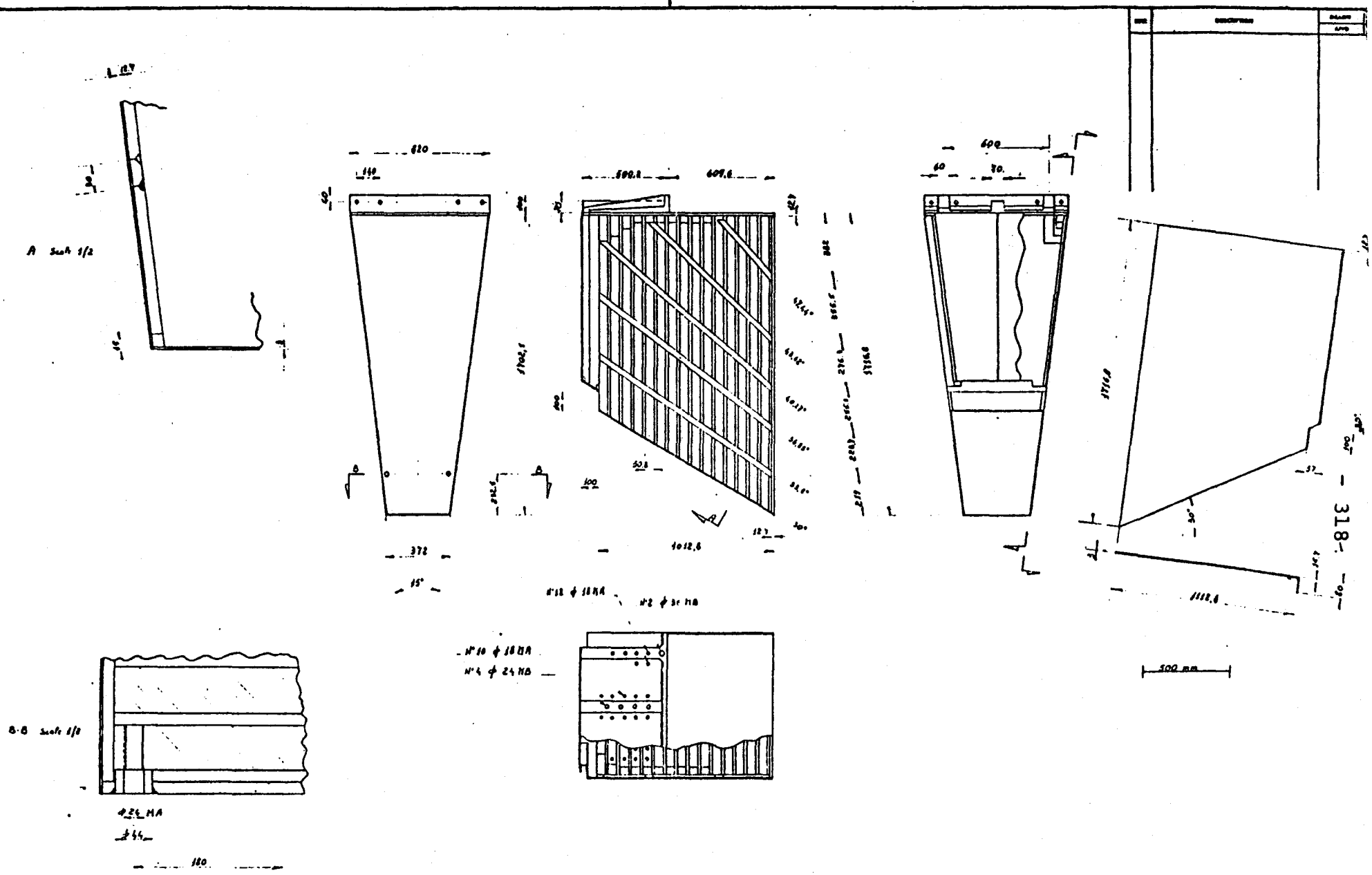

Fig. 4

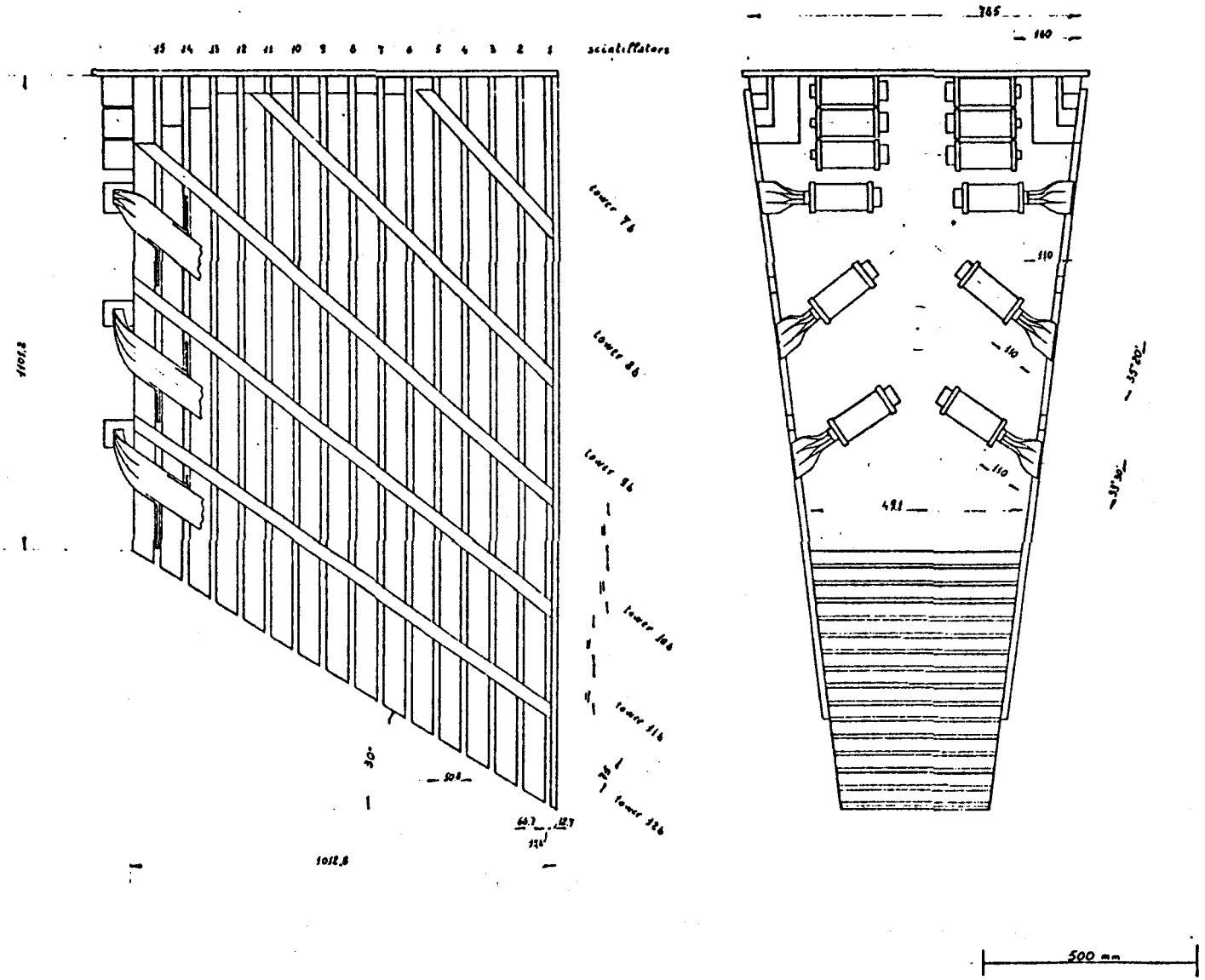
scintillators
lower Ta
lower Sb
lower Sb
lower Sb
lower Sb
lower Sb
1012.8
365
110
110
110
110
491
500 mm

Fig. 5

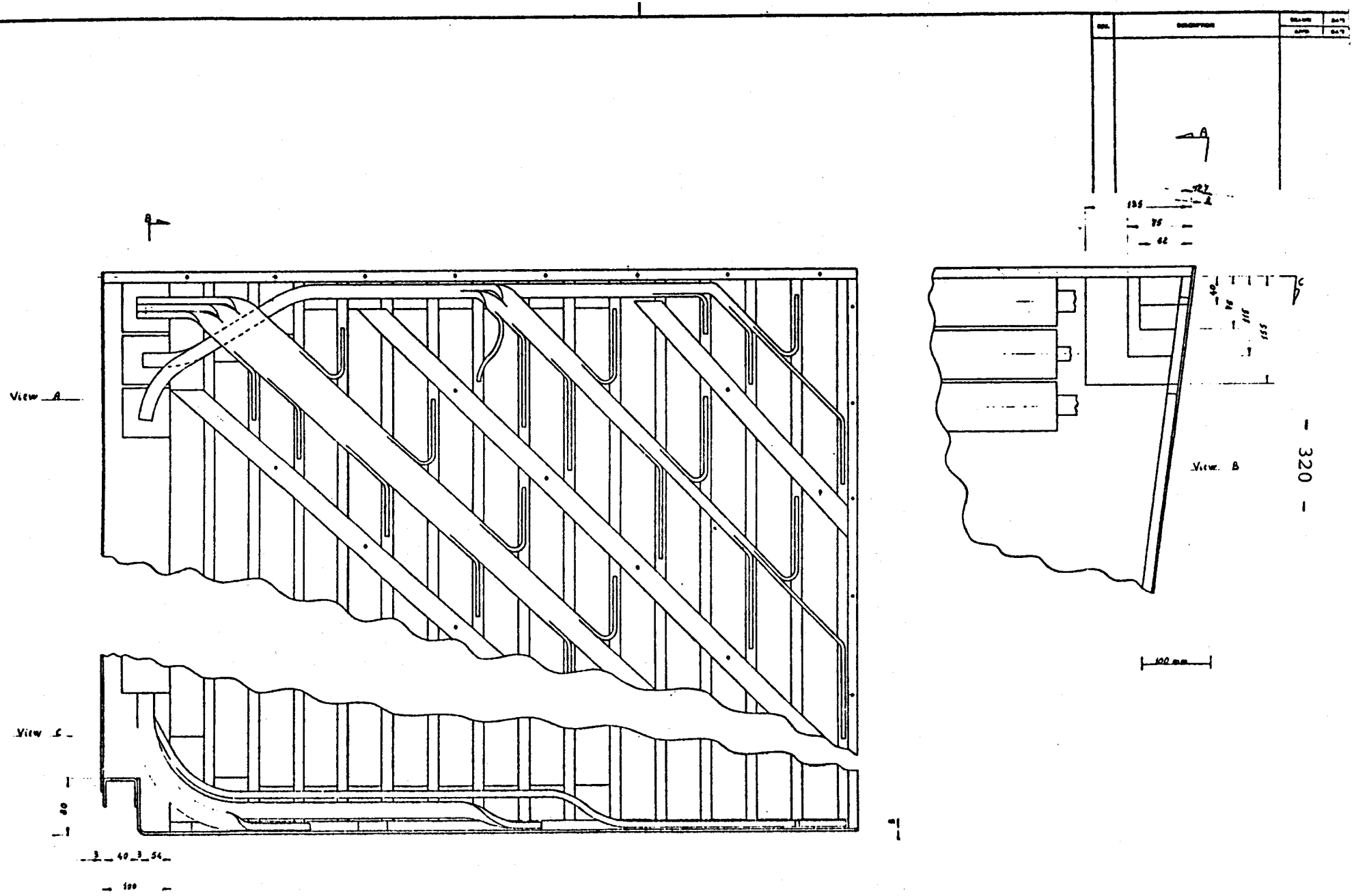

Fig. 6

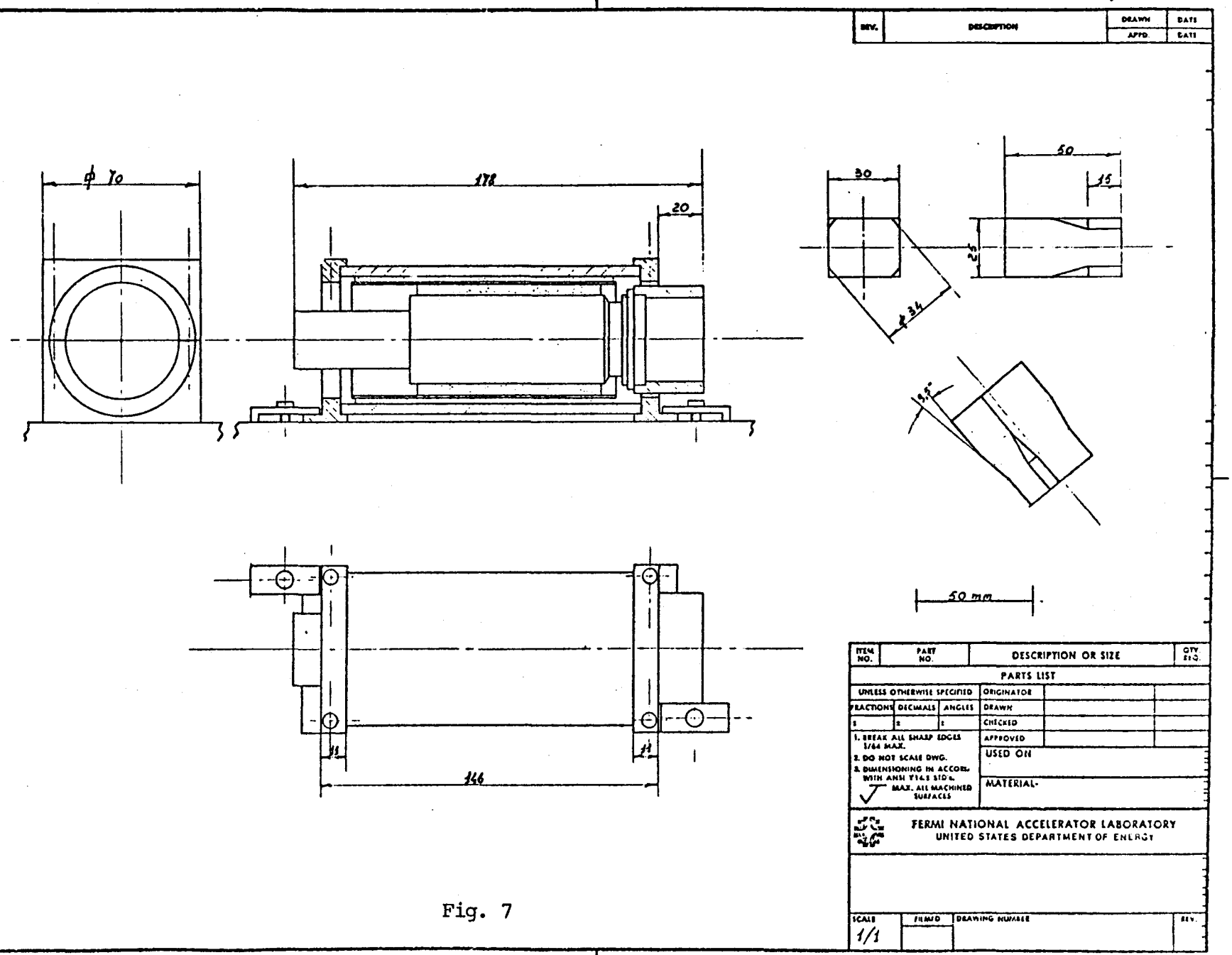
REV.
DESCRIPTION
DRAWN
DATE
APPD.
DATE
ϕ 70
178
20
30
50
15
25
ϕ 34
95°
50 mm
ITEM NO.
PART NO.
DESCRIPTION OR SIZE
QTY REQ.
PARTS LIST
UNLESS OTHERWISE SPECIFIED
FRACTIONS
DECIMALS
ANGLES
1
2
1
1. BREAK ALL SHARP EDGES 1/64 MAX.
2. DO NOT SCALE DWG.
3. DIMENSIONING IN ACCORD. WITH ANSI Y14.5 STD.
MAX. ALL MACHINED SURFACES
ORIGINATOR
DRAWN
CHECKED
APPROVED
USED ON
MATERIAL-
FERMI NATIONAL ACCELERATOR LABORATORY
UNITED STATES DEPARTMENT OF ENERGY
SCALE
1/1
FILMED
DRAWING NUMBER
REV.
11
11
146

Fig. 7

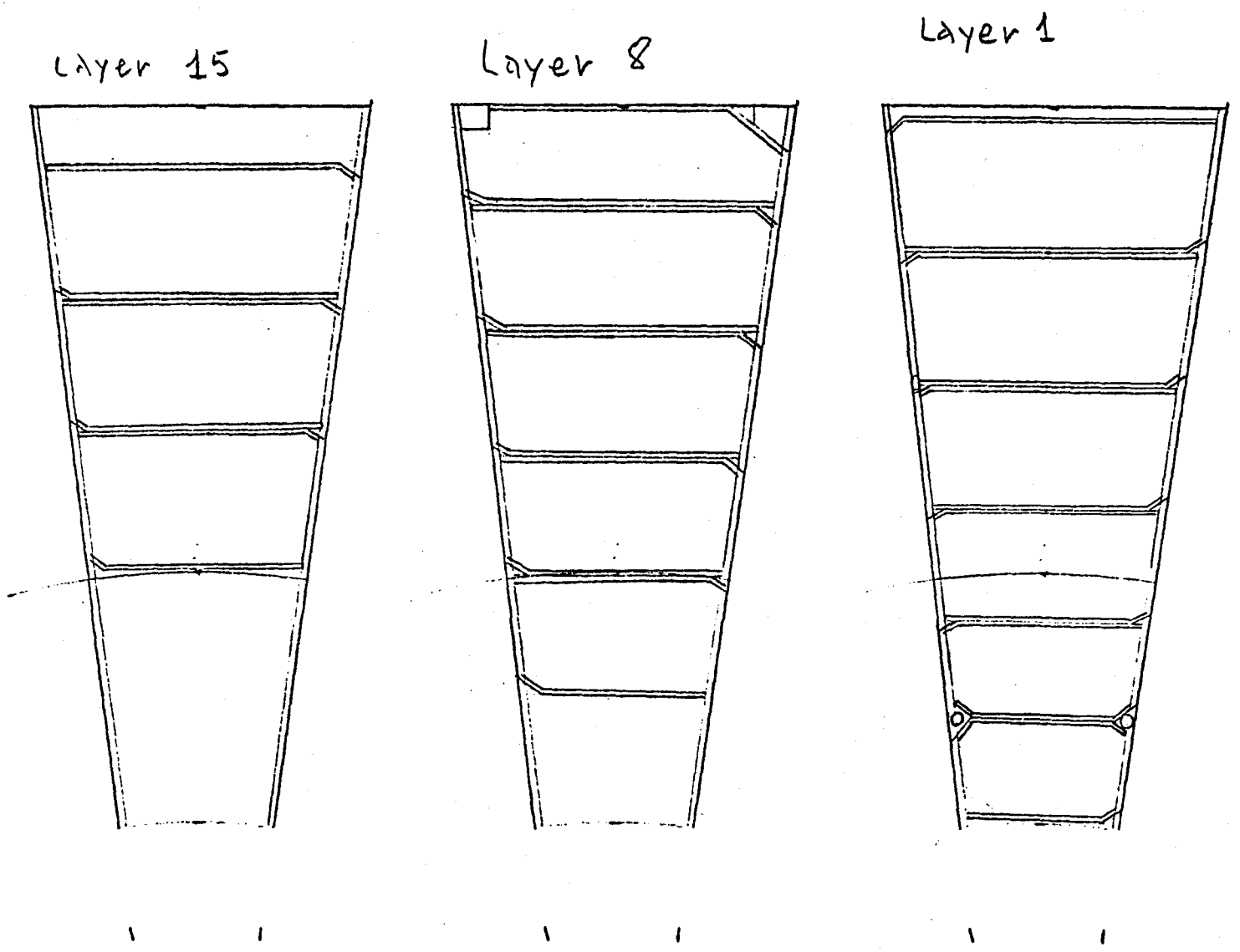

fig.

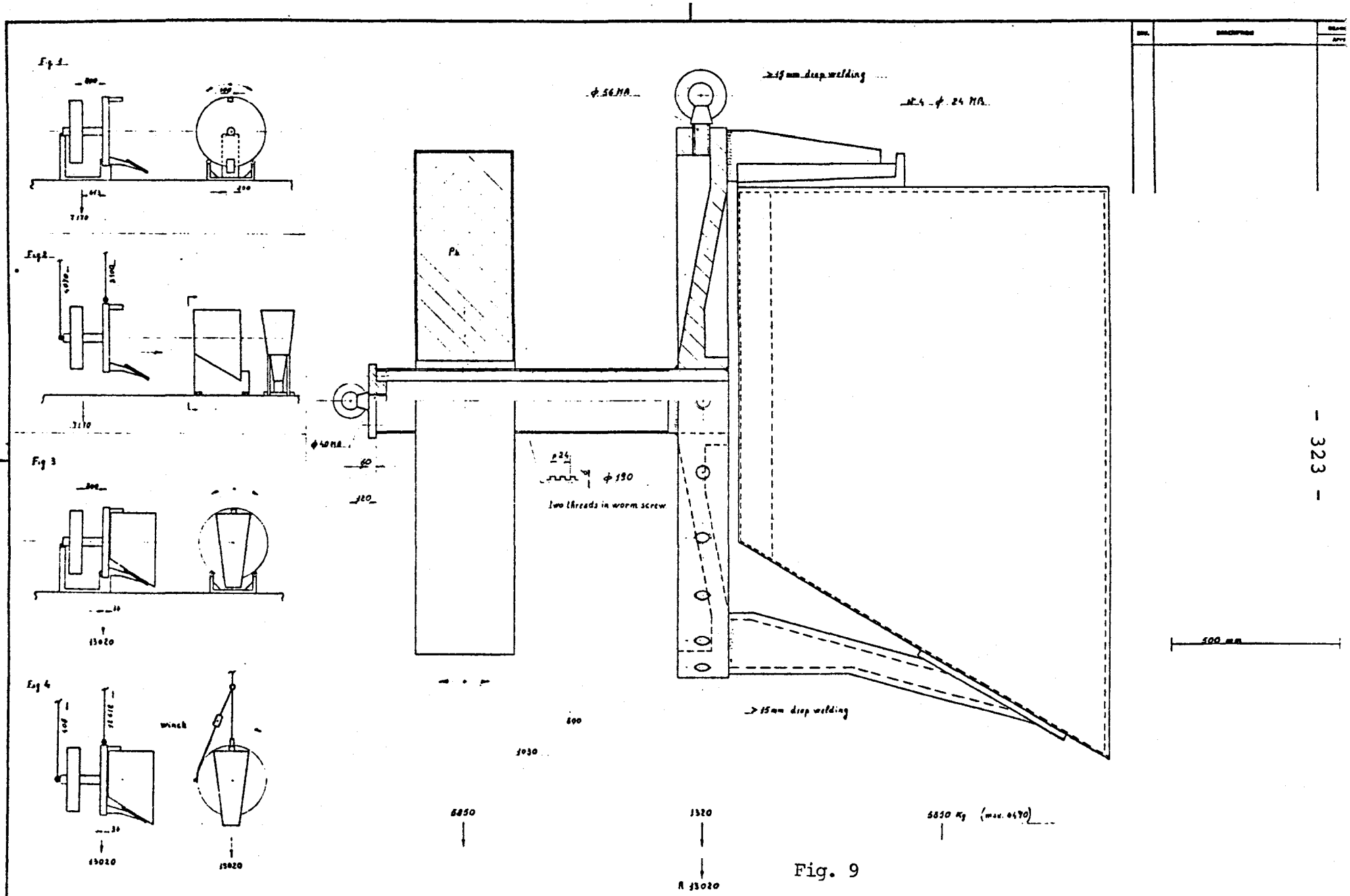
Fig 1
Fig 2
Fig 3
Fig 4
winch
≥ 15 mm disp. welding
Φ 56 MB
Φ 24 MB
Φ 40 MB
Φ 190
Two threads in worm screw
≥ 15 mm disp. welding
6850
1320
6850 Kg (max. 6470)
R 13020
500 mm

Fig. 9

Appendix VII

DESIGN AND CONSTRUCTION OF THE TOROID SYSTEM

a. Toroid Design

The toroids are shown in place in the BO collision area in Figures VII.1 and VII.2. The toroids must move both transversely to the beam line as well as longitudinally, they therefore must be split in half.

The design of the muon toroids has been initiated. The design is very similar to that of other large toroids constructed for Fermilab neutrino experiments. The toroid spectrometer is composed of four toroids, each of outer radius 4.4 m, thickness 1 m. Each toroid is composed of five pancakes eight inches thick, and each pancake is constructed from six pieces. The pieces are flame-cut to size and the interior mating surfaces are machined. Stainless-steel spacers placed between the pieces of each pancake establish 0.2 cm gaps for insertion of field-measuring probes. The toroids are mounted on a common structure, separated magnetically from their supports by 2.5 cm of aluminum. The structure and magnet can be moved on commercial transporters.

b. Toroid Construction and Moving Mechanism

Figures VII.3 --- VII.5 show the construction technique for the base of the toroids. The sequence of construction is as follows:

1. Iron slabs are pre-selected from stock at Fermilab or steel company with special emphasis put on uniformity of thickness, width, and straightness.

2. Slab locations in magnets are pre-determined.

3. Slabs are delivered to a commercial shop where they are marked for finished surfaces.

4. The shop flame cuts lengths, radii, and through holes taking into account finished machined surface locations.

5. The shop flame cuts scarfing for weld purposes.

6. Optional - Blocks may be machined flat with a 50% or 75% clear up to give a more predictable magnet thickness.

7. Five blocks are welded together including lifting ears and plates. The block formed becomes a single magnet layer and remains intact as a single block throughout.

8. Some machine shop machines all surfaces required to be machined with flatness, squareness, and dimensional tolerances maintained.

9. The machine shop bores out large holes in the bottom blocks for through rods.

10. The machine shop bores out small flame cut hydraulic cylinder holes or spade drills through block if holes not flame cut earlier.

11. The machine shop machines through rods to dimension.

12. Finished blocks are delivered to assembly site.

13. Blocks are placed in position using lifting ears to partially align and when fine aligned are welded adequately to resist earthquark forces. Lifting lugs and plates may be removed if necessary.

14. Through rods, cylinders, and casters are assembled to magnets.

15. Hangers, catwalks, mounts, support rods, etc. are installed before moving magnet to location.

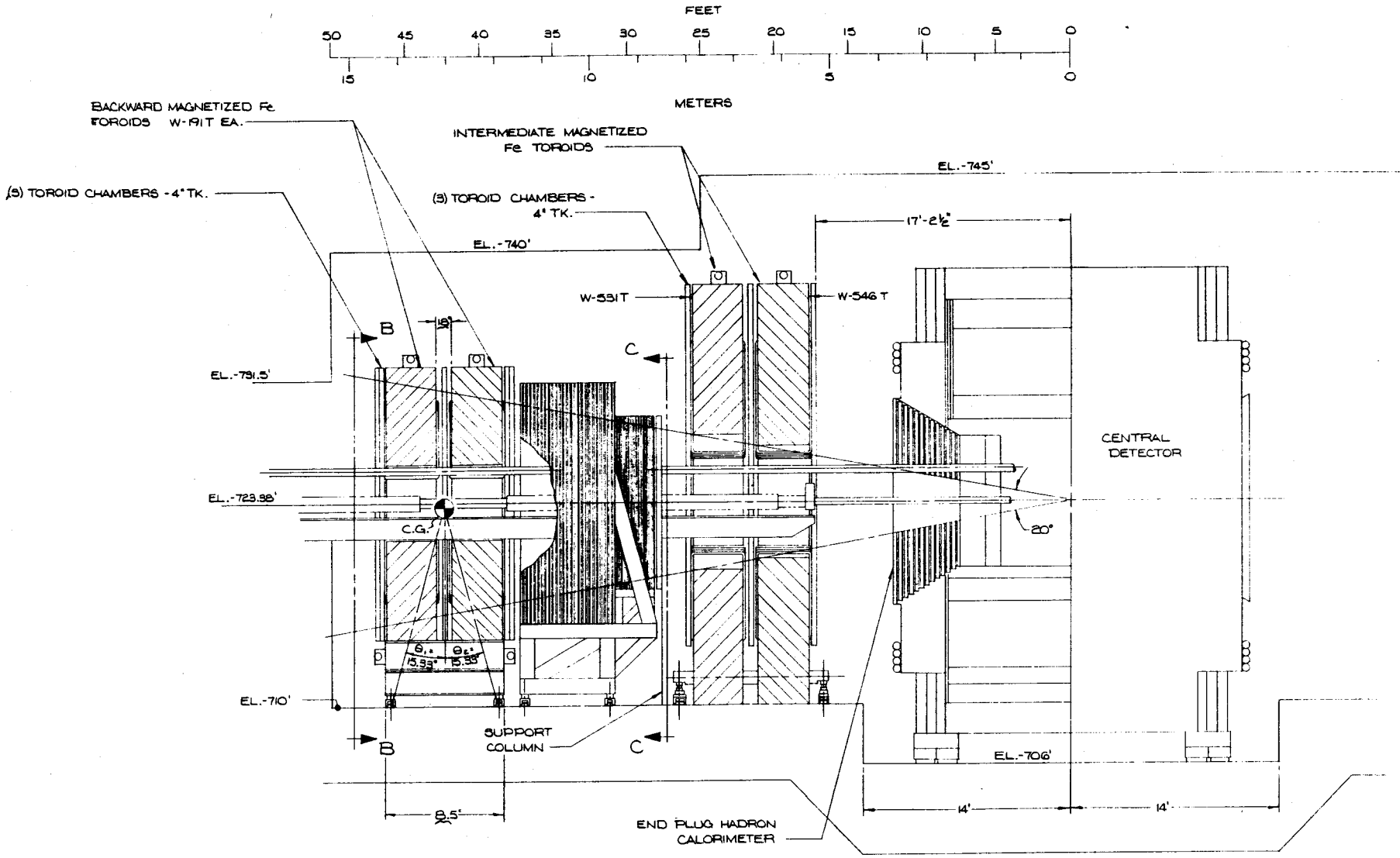
FEET
50 45 40 35 30 25 20 15 10 5 0
15 10 5 0
METERS
BACKWARD MAGNETIZED Fe TOROIDS W-191T EA.
INTERMEDIATE MAGNETIZED Fe TOROIDS
(3) TOROID CHAMBERS - 4" TK.
(3) TOROID CHAMBERS - 4" TK.
EL.-745'
EL.-740'
17'-2½"
W-531T
W-546T
B
C
EL.-731.5'
CENTRAL DETECTOR
EL.-723.98'
C.G.
20°
EL.-710'
SUPPORT COLUMN
EL.-706'
14'
14'
END PLUG HADRON CALORIMETER

FIG. VII .1

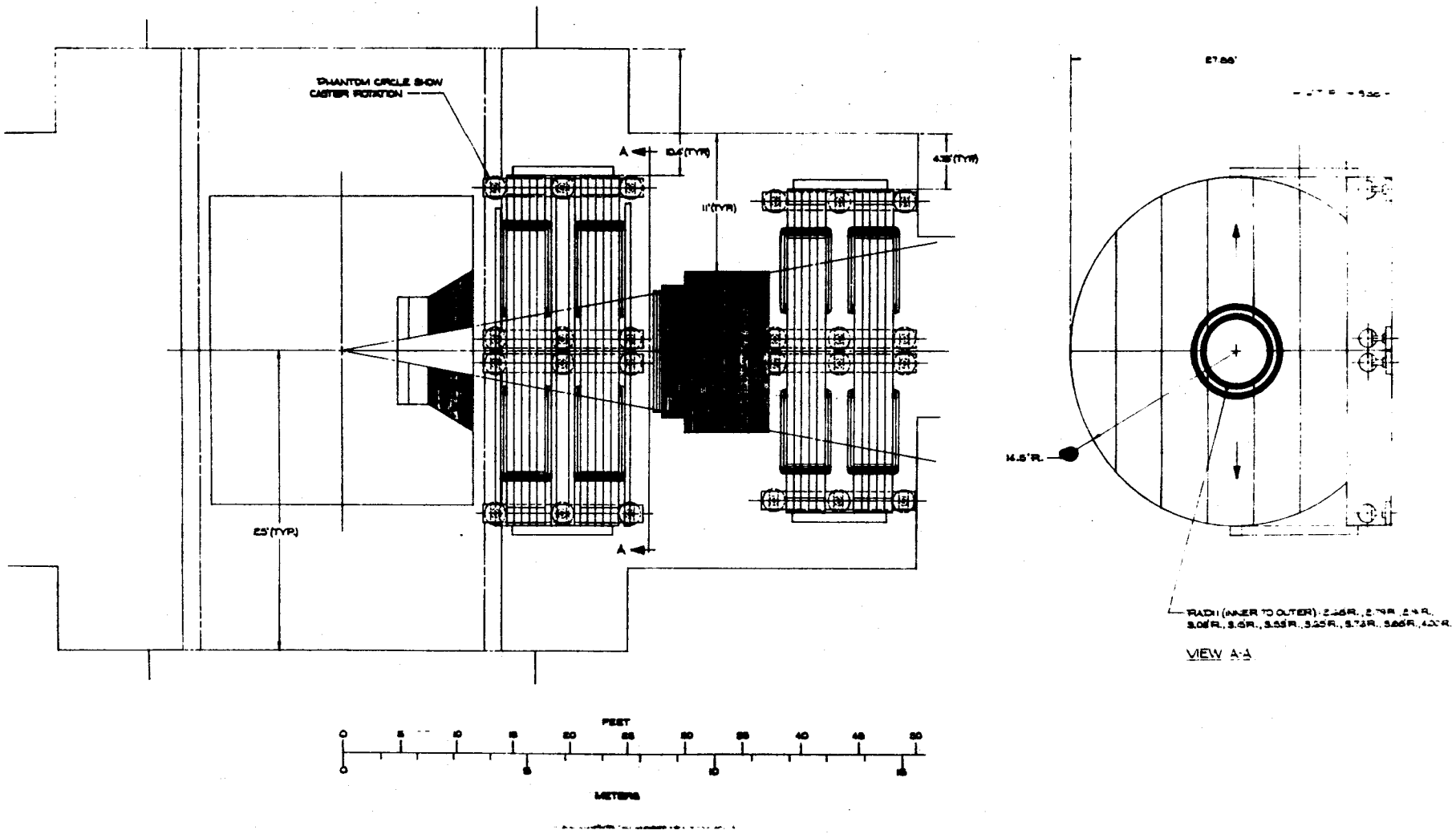
PHANTOM CIRCLE SHOW
CASTER ROTATION
A
A
11'(TYP)
25'(TYP)
14.5'R.
VIEW A-A
FEET
METERS

FIG. VII.2

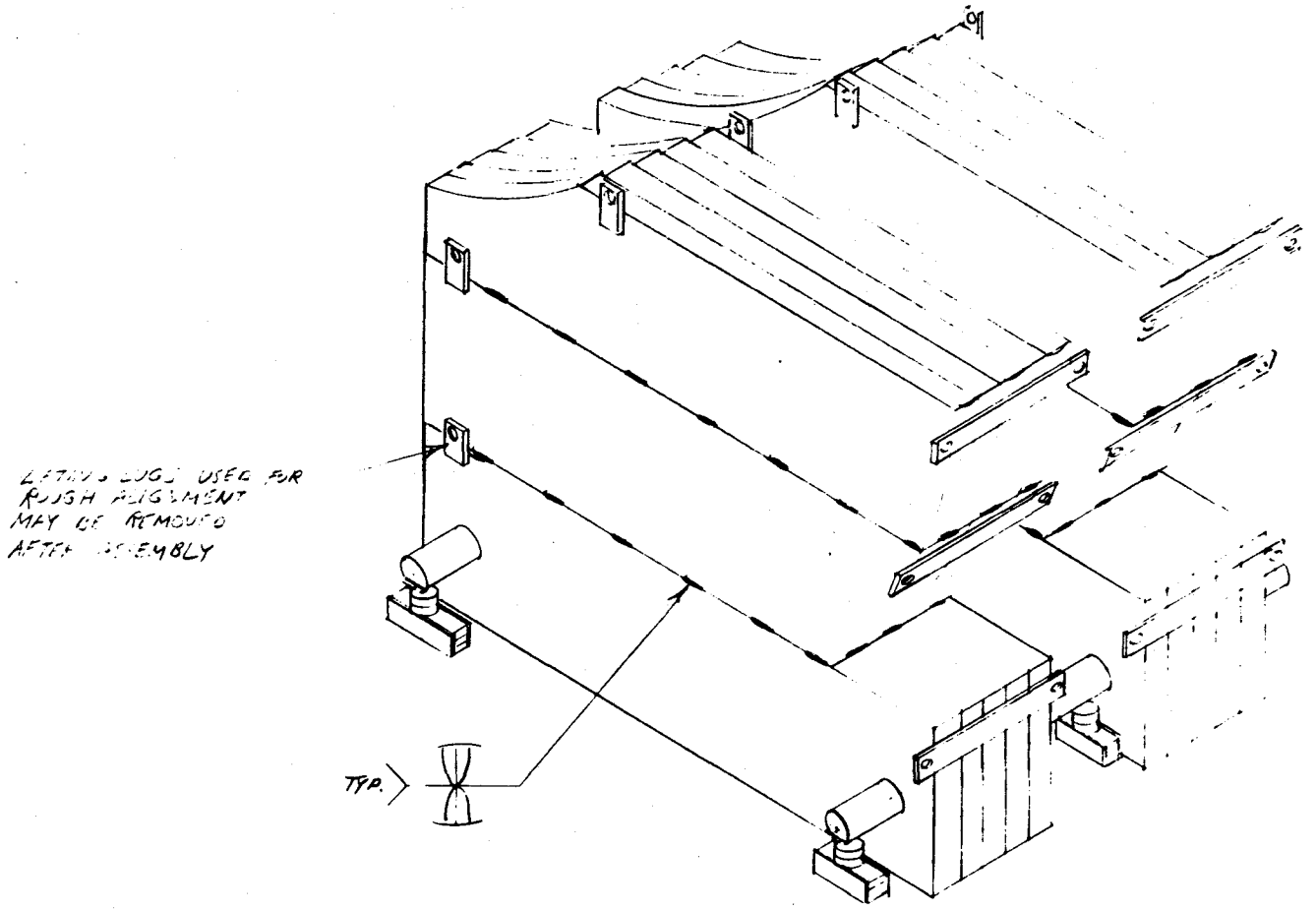

DO NOT SCALE DRAWING

PHYSICAL SCIENCES LABORATORY
UNIVERSITY OF WISCONSIN

FIG VII.3

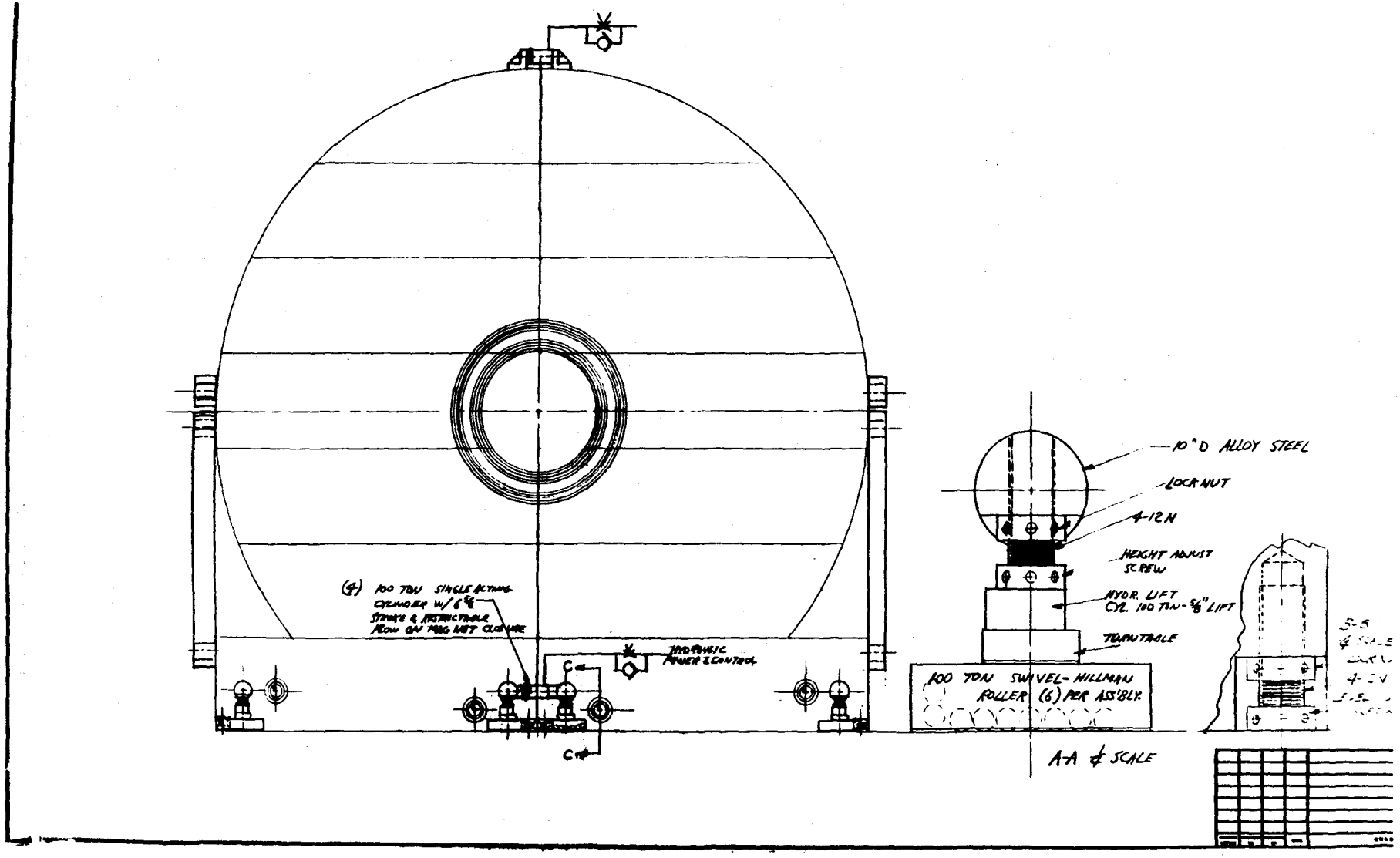
(4) 100 TON SINGLE ACTING CYLINDER W/ 6" ϕ STROKE & ADJUSTABLE FLOW ON HEAD END CLOSURE
HYDRAULIC POWER & CONTROL
10" D ALLOY STEEL
LOCK NUT
4-12 N
HEIGHT ADJUST SCREW
HYDR. LIFT CYL. 100 TON - 5/8" LIFT
TRUNNION
100 TON SWIVEL-HILLMAN ROLLER (6) PER ASS'BLY.
A-A ϕ SCALE

FIG. VII .4

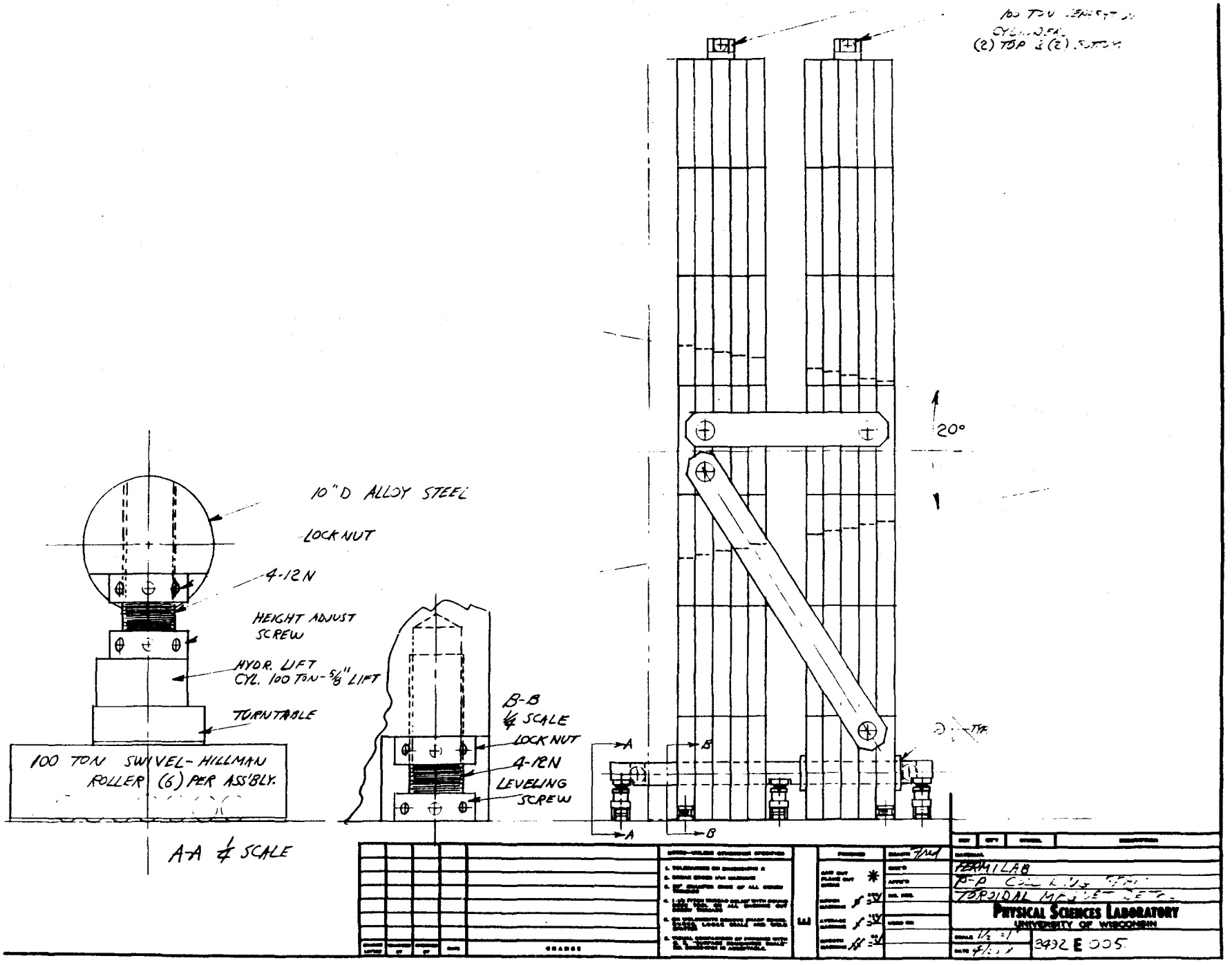
10" D ALLOY STEEL
LOCK NUT
4-12 N
HEIGHT ADJUST SCREW
HYDR. LIFT CYL. 100 TON - 5/8" LIFT
TURNTABLE
100 TON SWIVEL - HILLMAN ROLLER (6) PER ASS'BLY.
A-A ¼ SCALE
B-B ¼ SCALE
LOCK NUT
4-12 N
LEVELING SCREW
20°
PHYSICAL SCIENCES LABORATORY
UNIVERSITY OF WISCONSIN
3492 E 005

FIG III-5